THE THEORETICAL MODELLING OF CIRCULAR SHALLOW FOUNDATION FOR OFFSHORE WIND TURBINES

by

LAM NGUYEN-SY

A thesis submitted for the degree of
Doctor of Philosophy
at the University of Oxford

Brasenose College
Michaelmas Term 2005

ABSTRACT

The theoretical modelling of circular shallow foundation for offshore wind turbines

A thesis submitted for the degree of Doctor of Philosophy

Lam Nguyen-Sy
Brasenose College, Oxford
Michaelmas term 2005

Currently, much research is being directed at alternative energy sources to supply power for modern life of today and the future. One of the most promising sources is wind energy which can provide electrical power using wind turbines. The increase in the use of this type of energy requires greater consideration of design, installation and especially the cost of offshore wind turbines. This thesis will discuss the modelling of a novel type of shallow foundation for wind turbines under combined loads. The footing considered in this research is a circular caisson, which can be installed by the suction technique. The combined loads applied to this footing will be in three-dimensional space, with six degrees of freedom of external forces due to environmental conditions. At the same time, during the process of building up the model for a caisson, the theoretical analyses for shallow circular flat footing and spudcans also are established with the same principle.

The responses of the soil will be considered in both elastic and plastic stages of behaviour, by using the framework of continuous plasticity based on thermodynamic principles. During this investigation, it is necessary to compare the numerical results with available experimental data to estimate suitable values of factors required to model each type of soil. There are five main goals of development of the model.

Firstly, a new expression for plasticity theory which includes an experimentally determined single yield function is used to model the effects of combined cyclic loading of a circular footing on the behaviour of both sand and clay. This formulation based on thermodynamics allows the derivation of plastic solutions which automatically obey the laws of thermodynamics without any further assumptions. A result of this advantage is that non-associate plasticity, which is known to be a proper approximation for geotechnical material behaviour, is obtained logically and naturally. A FORTRAN source code called ISIS has been written as a tool for numerical analysis.

Secondly, since there are some characteristics of the geometric shape and installation method which are quite different from that of spudcans and circular flat footing, another objective of this study is to adapt the current model which has been developed in ISIS for spudcans to the specific needs of caissons.

The third goal of this research is the simulation of continuous loading history and a smooth transition in the stress-strain relationship from elastic to plastic behaviour. The model is developed from a single-yield-surface model to a continuous plasticity model (with an infinite number of yield surfaces) and then is discretized to a multiple-yield-surface model which can be implemented by numerical calculation to be able to capture with reasonable precision the hysteretic response of a foundation under cyclic loading. This can not be described by a conventional single-yield-surface model.

Fourthly, as a method to simplify the numerical difficulties arising from the calculation process, a rate-dependent solution will be introduced. This modification is implemented by changing the dissipation function derived from the second law of thermodynamics.

Finally, in order to control the model to capture the real behaviour, many parameters are proposed. A parametric study will be implemented to show the effects of these parameters on the solution.

ACKNOWLEDGEMENT

I would like to express my deep gratitude and appreciation to my supervisor, Professor Guy Houlsby, who gave me invaluable guidance and were always accessible with friendly support throughout my time in Oxford.

I would like to thank the Vietnamese Government for their financial support. My thanks also go to the Peter Wroth Memorial funding from civil engineering academic staff.

Thanks to John Pickhaver, Paul Bonnet, Oliver Cotter and Anthony Corner for your comments and proof reading my thesis with care. I also like to thank all my friends who had made my time in Oxford such an unforgettable memory.

I wish to dedicate this thesis to my father and my mother whose lifetimes have been devoted to my education.

I thank my beloved wife, Dung, who had to withstand time and long distance in almost three long years. Your love means so much to me.

TABLE OF CONTENTS

ABSTRACT 0-1

ACKNOWLEDGEMENT

TABLE OF CONTENTS

LIST OF SYMBOLS

CHAPTER 1. INTRODUCTION 1-1

- 1.1 Shallow foundation for offshore wind turbines 1-1
- 1.2 Numerical modelling of circular shallow foundation of offshore structures 1-5
- 1.3 Application of plasticity models based on Thermodynamic principles 1-9
- 1.4 Outline of this thesis 1-12

CHAPTER 2. LITERATURE REVIEW AND BACKGROUND 2-1

- 2.1 Introduction 2-1
- 2.2 Conventional elastic solutions 2-2
  - 2.2.1 Elastic solutions for circular flat footing and spudcan 2-2
  - 2.2.2 Elastic solution for caisson footing 2-5
  - 2.2.3 Elastic shear modulus 2-6
- 2.3 Bearing capacity formulations 2-9
  - 2.3.1 Bearing capacity formulations for circular flat footing and spudcan 2-10
  - 2.3.2 Installation of caisson footing and vertical bearing capacity of caisson footing 2-16
    - 2.3.2.1 Installation of caisson footing on clay 2-17
    - 2.3.2.2 Installation of caisson footing on sand 2-20
- 2.4 Conventional plasticity models for shallow foundation for offshore structures 2-22
  - 2.4.1 Conventional plasticity model for circular shallow foundation on clay 2-23
  - 2.4.2 Conventional plasticity model for circular shallow foundation on sand 2-23
- 2.5 Plasticity models based on thermodynamic framework 2-25
  - 2.5.1 Single-yield-surface hyperplasticity 2-26
    - 2.5.1.1 Energy function and internal variables 2-26
    - 2.5.1.2 Dissipation and yield function 2-27
    - 2.5.1.3 Incremental response 2-29
  - 2.5.2 Multiple-yield-surface hyperplasticity and continuous hyperplasticity 2-31
    - 2.5.2.1 Rate-independent solution 2-31
    - 2.5.2.2 Rate-dependent solution 2-33
  - 2.5.3 Application of the hyperplasticity theory to a force resultant model 2-35
- 2.6 Summary 2-36

CHAPTER 3. SINGLE-YIELD-SURFACE HYPERPLASTICITY MODEL FOR CIRCULAR SHALLOW FOUNDATION 3-1

- 3.1 Introduction 3-1
- 3.2 Conventions for a foundation 3-2
- 3.3 Single-yield-surface hyperplasticity model using rate-independent behaviour 3-4
  - 3.3.1 Free energy function and definitions of internal state variables for the foundation using the macro element concept 3-5
  - 3.3.2 Yield function 3-9
    - 3.3.2.1 Yield function of circular flat footing and spudcan 3-10
    - 3.3.2.2 Yield function of caisson footing 3-15
  - 3.3.3 Flow rule 3-17

3.3.4 Incremental response 3-20
3.3.4.1 Elastic response 3-21
3.3.4.2 Plastic response 3-23
3.4 Single-yield-surface hyperplasticity model using rate-dependent behaviour 3-25
3.4.1 Flow potential function 3-26
3.4.2 Incremental stress-strain response 3-27
3.5 Application of the vertical bearing capacity of caisson in ISIS model 3-28
3.5.1 Modification of the vertical bearing capacity of caisson footing 3-28
3.5.2 Analysis of the suction assisted penetration in ISIS model 3-33
3.6 Numerical illustrations 3-35
3.6.1 Simulations of the behaviour of circular flat footing and spudcan on both clay and sand using rate-independent hyperplasticity 3-36
3.6.2 Installation of caisson with and without suction assistance 3-46
3.6.3 Rate-dependent solution 3-48
3.7 Discussion 3-50
3.8 Concluding remarks 3-52

CHAPTER 4. CONTINUOUS HYPERPLASTICITY AND THE DISCRETIZATION FOR NUMERICAL ANALYSIS 4-1
4.1 Introduction 4-1
4.2 Continuous hyperplasticity formulation 4-2
4.2.1 Free energy functional and internal variable functions 4-2
4.2.2 Yield functional 4-8
4.2.3 Flow rule and incremental response using rate-independent solution 4-10
4.2.4 Incremental response using rate-dependent solution 4-15
4.3 Discretization formulation – Multiple-yield-surface model (ISIS) 4-18
4.3.1 Discretization of free energy functional and internal variable functions 4-18
4.3.2 Yield functions 4-22
4.3.3 Modification for the yield functions 4-23
4.3.4 Flow rule and incremental response using rate-independent solution 4-25
4.3.5 Flow rule and incremental response using rate-dependent solution 4-27
4.4 Application of hardening rules to the model 4-30
4.4.1 Possibilities of hardening rules 4-30
4.4.2 Discussion 4-33
4.5 Numerical illustrations 4-35
4.5.1 Advantages of the multiple-yield-surface model compared with single-yield-surface model 4-36
4.5.1.1 Numerical examples for circular flat footings 4-37
4.5.1.2 Numerical examples for spudcan footings 4-45
4.5.1.3 Numerical examples for caissons 4-51
4.5.1.4 Summary 4-59
4.5.2 Capturing the real behaviour of caissons 4-59
4.6 Discussion 4-71
4.7 Concluding remarks 4-73

CHAPTER 5. PARAMETER SELECTION AND PARAMETRIC STUDY 5-1
5.1 Introduction 5-1
5.2 Shape of the yield surface 5-2
5.2.1 Variations of the shape parameters corresponding to the ratio of L/D 5-2
5.2.2 Discussion 5-9

- 5.3 Association factors 5-10
  - 5.3.1 Association factors for circular flat footing and spudcan in single-yield-surface model 5-11
  - 5.3.2 Association factors for a caisson footing in single-yield-surface model 5-15
  - 5.3.3 Effects of the association factors on the solutions using multiple-yield-surface model 5-17
- 5.4 Initial distribution of the yield surfaces 5-25
- 5.5 Effects of kernel functions on the distribution of plastic displacements 5-30
- 5.6 Relationship between viscosity, time increment and loading step in rate-dependent solution 5-36
  - 5.6.1 Accuracy and stability conditions of the simplest one-dimensional kinematic hardening rate-dependent model 5-37
  - 5.6.2 Accuracy and stability conditions for ISIS model 5-45
    - 5.6.2.1 Stability conditions for ISIS model 5-46
    - 5.6.2.2 Accuracy conditions for ISIS model 5-48
  - 5.6.3 Discussion and advice for the use of rate-dependent solution 5-49
- 5.7 Concluding remarks 5-50

CHAPTER 6. MODEL APPLICATIONS 6-1
- 6.1 Introduction 6-1
- 6.2 Application for the analysis of a monopod caisson 6-4
  - 6.2.1 Installation 6-4
  - 6.2.2 Horizontal and rotational responses 6-7
  - 6.2.3 Numerical results 6-9
- 6.3 Application for the analysis of a quadruped caisson 6-11
  - 6.3.1 Installation 6-12
  - 6.3.2 Horizontal and rotational responses 6-13
  - 6.3.3 Numerical results 6-18
- 6.4 Effect of the simulation of suction installation on the solution 6-20
- 6.5 Effect of the tensile capacity factor on the caisson response 6-24
- 6.6 Effect of the heave on the caisson response 6-28
- 6.7 Confirmation for cyclic behaviour 6-31
- 6.8 Concluding remarks 6-36

CHAPTER 7. CONCLUDING REMARKS 7-1
- 7.1 Introduction 7-1
- 7.2 Main Findings 7-1
- 7.3 Suggestions for future research 7-3
- 7.4 Conclusion 7-4

REFERENCES

LIST OF SYMBOLS

Soil parameters

c	Cohesion of soil
I_r	Rigidity index
K	Earth pressure coefficient
q	Overburden pressure
R_D	Relative density
G	Elastic shear modulus of soil (in terms of effective stress)
G_R	Elastic shear modulus of soil at the depth R (in terms of effective stress)
p_a	Atmospheric pressure
s_u	Undrained shear strength
s_{um}	Undrained shear strength at mudline
α	Dimensionless exponential factor depending on the soil type
δ	Interface friction angle
ϕ	Friction angle of soil
γ	Unit weight of soil
γ'	Effective unit weight of soil
γ_w	Unit weight of water

Bearing capacity parameters

a	Pressure factor
a_0	Empirical factor
a_1	Emperical factor
a_2	Empirical factor
f_{ins}	Spreading factor inside the caisson
f_{out}	Spreading factor outside the caisson
k_f	Ratio between k_{ins} and k_{out}
k_{ins}	Permeability factor inside the caisson
k_{out}	Permeability factor outside the caisson
N_c	Cohesion factor
N_q	Overburden factor
N_γ	Self weight factor
N_c^*	Cohesion factor of the circular flat footing with diameter D_{ins}

N_q^*	Overburden factor of the circular flat footing with diameter D_{ins}
N_γ^*	Self weight factor of the circular flat footing with diameter D_{ins}
s	Suction pressure
$s_{ultimate}$	Limit value of suction pressure
V_0	Vertical bearing capacity
α_{ins}	Adhesion factor inside the caisson
α_{out}	Adhesion factor outside the caisson
σ_1	Vertical average stress inside the caisson
σ_2	Vertical average stress outside the caisson
$\sigma_{Vins}^{'}$	Vertical effective stress inside the caisson
$\sigma_{Vout}^{'}$	Vertical effective stress outside the caisson
τ_{ins}	Friction stress inside the caisson
τ_{out}	Friction stress outside the caisson
ζ_c	Dimensionless shape factor corresponding to N_c
ζ_q	Dimensionless shape factor corresponding to N_q
ζ_γ	Dimensionless shape factor corresponding to N_γ
ζ_{ci}	Dimensionless inclination factor corresponding to N_c
ζ_{qi}	Dimensionless inclination factor corresponding to N_q
$\zeta_{\gamma i}$	Dimensionless inclination factor corresponding to N_γ

Footing parameters

A	Plan area of footing
$A^{'}$	Effective plan area of footing under eccentric load
B	Width of rectangular footing
$B^{'}$	Effective width of strip footing
B^*	Effective width of circular footing
d	Distance from the load reference point to the soil surface level
D	Footing diameter
D_{ins}	Inside diameter of caisson
D_{out}	Outside diameter of caisson
D_m	Diameter of the effected area outside caisson
D_m	Diameter of the non-effected area inside caisson
e	Eccentricity
L	Length of rectangular footing or length of caisson
$L^{'}$	Effective length of rectangular footing

L^*	Effective length of circular footing
R	Footing radius
m, m_L, m_B	Empirical parameters involving the footing shape factor
t	Thickness of the caisson's skirt
z	Depth considered

Load parameters

V	Vertical load
V_R	Vertical load at load reference point (LRP)
H	Horizontal load in plane problem
H_R	Horizontal load in plane problem at LRP
H_2	Horizontal load in 2-axis
H_{2R}	Horizontal load in 2-axis at LRP
H_3	Horizontal load in 3-axis
H_{3R}	Horizontal load in 3-axis at LRP
M	Moment in plane problem
M_R	Moment in plane problem at LRP
M_2	Moment about 2-axis
M_{2R}	Moment about 2-axis at LRP
M_3	Moment about 3-axis
M_{3R}	Moment about 2-axis at LRP
Q	Inclined load (chapter 2)
Q	Torsion moment
Q_R	Torsion moment at LRP

Displacement parameters

w	Vertical displacement
w_R	Vertical displacement at LRP
u	Horizontal displacement in plane problem
u_R	Horizontal displacement in plane problem at LRP
u_2	Horizontal displacement in 2-axis
u_{2R}	Horizontal displacement in 2-axis at LRP
u_3	Horizontal displacement in 3-axis
u_{3R}	Horizontal displacement in 3-axis at LRP
θ	Rotational displacement in plane problem
θ_R	Rotational displacement in plane problem at LRP

θ_2	Rotational displacement about 2-axis
θ_{2R}	Rotational displacement about 2-axis at LRP
θ_3	Rotational displacement about 3-axis
θ_{3R}	Rotational displacement about 3-axis at LRP
q	Rotational displacement about 1-axis
q_R	Rotational displacement about 1-axis at LRP

Hyperplasticity parameters (Hyperplasticity theory and ISIS model)

d	Dissipation function
f	Helmholtz free energy
g	Gibbs free energy
G	Shear modulus
h	Enthalpy
H_i	Kernel function (for hardening rule)
k_i	Dimensionless elastic stiffness coefficient
K_i	Elastic stiffness factors
u	Internal energy
w	Flow potential
y	Yield function
z	Force potential
α_{ij}	Internal state variable
α_i	Plastic displacement
ε_{ij}	Strain
ε_i	Total displacement
θ	Temperature
η	Internal coordinate
λ, Λ	Multipliers
μ	Viscosity factor
ρ_{ij}	Back stress
ρ_i	Back force
σ_{ij}	Stress
σ_i	Force
$\chi_{ij}, \overline{\chi}_{ij}$	Generalised stress
$\chi_i, \overline{\chi}_i$	Generalised force

CHAPTER 1

INTRODUCTION

1.1 Shallow foundations for offshore wind turbines

There are many onshore wind turbines which have been used in few countries. However, there is a lot of controversy associated with this option for renewable energy generation. As mentioned in Byrne and Houlsby (2003), the main reason for this is the aesthetic effect of the onshore wind farm on the landscape. Moving wind turbines offshore could be a solution for this problem. Moreover, by using offshore wind turbines, larger wind turbines can be constructed which therefore supply much more power and can be more economically efficient.

In the development of offshore wind turbines, the foundations usually are a significant fraction of the overall installed cost. They are about from 15 % to 40% of the total cost of a unit (see Houlsby and Byrne, 2000). Consequently, the designers of the foundation for offshore wind turbines also face the challenges of finding an economical solution for this problem. In recent designs of foundations for offshore structures, there are five main types: piled, gravity bases, mudmats used as temporary supports of piles, spudcan foundations for jack-up units and caissons. These forms are mostly used for offshore structures in the field of the oil and gas industry. Obviously, there is wide knowledge of these foundations which can be used for their design. The design of a foundation for the offshore wind industry, in some important aspects, is quite different from that of offshore foundations within the oil and gas industry, the differences are briefly:

- The vertical loading is typically much smaller than that in oil and gas industry.

- As a result of above, the effects of horizontal and moment loading are much larger. Thus, the dynamic influences of environmental loading, such as wave, current and wind, are different from those that dominate in the design of oil and gas structures.
- The water depth at the installation location is typically much smaller.
- The requirements for mass-production and multiple installations are higher, leading to a need for economical designs.

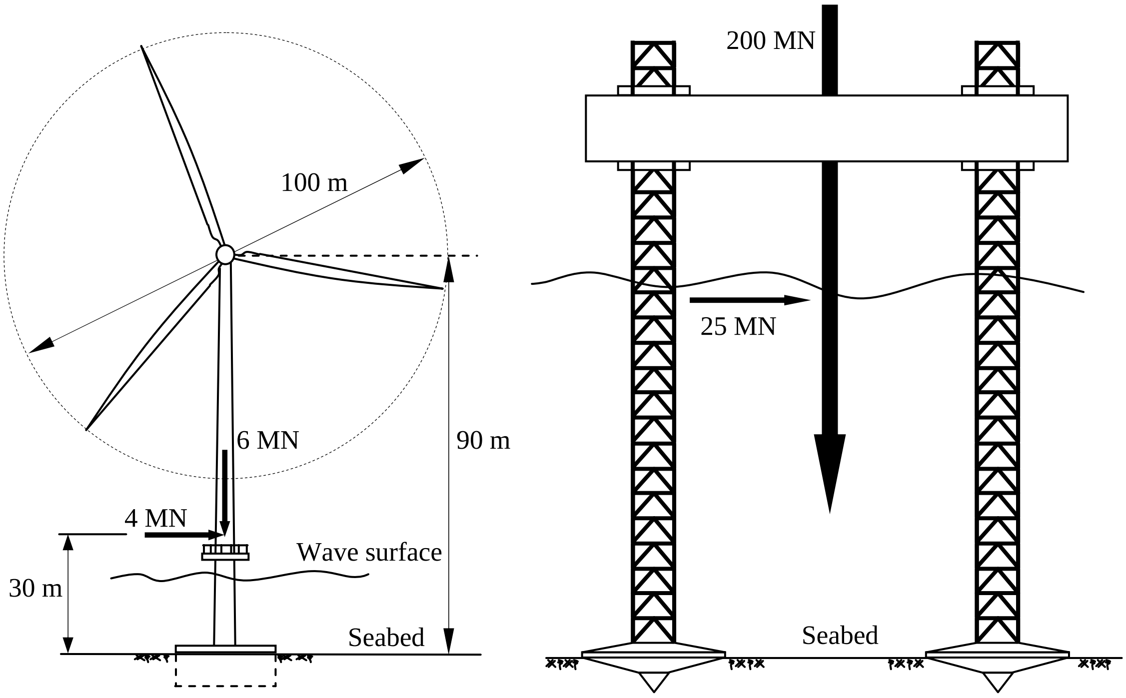

Figure 1.1 Typical sizes and loadings of an offshore wind turbine and a jack-up rig drawn in the same scale, after Byrne and Houlsby (2003)

For instance, for a given 3.5 MW offshore wind turbine, the maximum load may be about 6 MN, the applied horizontal load, located at about 30m above the seabed, is about 4 MN. In Figure 1.1, a comparison between a typical wind turbine and a jack-up unit is presented to illustrate the differences in serviceability conditions.

The monotonic behaviour of shallow foundations of offshore soil and gas structures is well established. However, as mentioned above, the effects of environmental loadings on offshore wind turbines differ from those of oil and gas designs. Thus, it might be unsuitable to transfer directly the previous results to the designs of offshore wind turbine foundations. It is therefore necessary to explore a new concept for the designs of the foundations for offshore wind turbines, instead of extending previous concepts from the oil and gas industry. This work can offer another choice for engineers to create both technically and economically improved designs. So far, almost all offshore wind farms are installed in shallow water close to the shore, and there are few of them. Large-diameter monopile and gravity base foundations have been used for these offshore wind turbines. In this research, a novel form of shallow foundation, called a suction caisson, is considered which can provide an economical choice for the design (see Byrne *et al.*, 2000). This foundation essentially consists of two parts, a circular plate and a perimeter skirt connected together. The whole foundation is installed by the combination of gravity and suction. Firstly, the caisson footing is pushed down to an initial depth in the seabed by its self-weight. Afterwards, applying suction pressure to pump the water out of the caisson carries on the installation process. The pressure differentials between the inside and the outside of the caisson, which are created by the suction process, not only play the role of further vertical forces but also, in sand, reduce the vertical bearing capacity of the soil at the tip level of the caisson's skirt. Once the inside volume of the caisson is fully occupied by the soil, which is considered as full penetration, the installation process is finished. Figure 1.2 shows the principle of the suction assisted installation.

There are two main possibilities for a caisson foundation for an offshore wind turbine: single-caisson foundation and multi-caisson foundation.

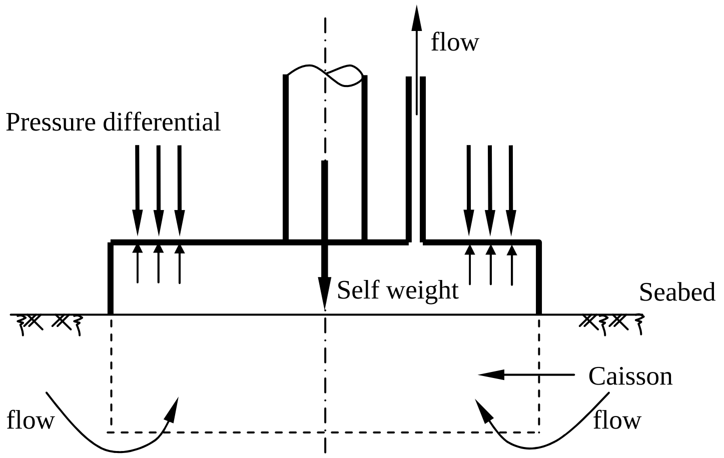

Figure 1.2 Installation of caisson with suction assistance

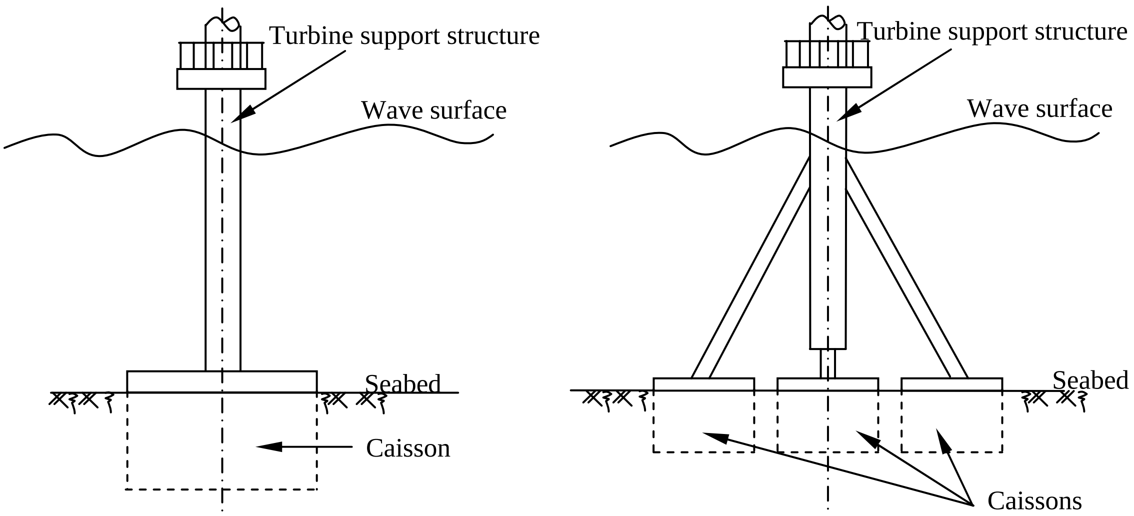

(a) Single caisson foundation

(b) Multi caisson foundation

Figure 1.3 Caisson foundation for wind turbine

Figure 1.3 shows the outlines of these two kinds of foundation for offshore wind turbine structures. In case of a single-caisson foundation, vertical and horizontal forces as well as overturning moments are resisted directly. Meanwhile, in a multi-caisson foundation, which often consists of three (tripod) or four (quadruped) caissons, the moment resistance is provided by the combination of tension and compression capacities on upwind and downwind legs. The vertical and horizontal forces are also distributed over the whole system of caissons. Thus, the caissons in a multi-caisson footing are often smaller than those of a single footing. However, the single-caisson foundation offers a great advantage of simplicity (see Houlsby and Byrne, 2000). It can be used for wind turbine structures which are perhaps constructed on the seabed with the water depth up to approximately 40 m. In addition, this foundation can easily be removed after the end of the life of the structure, although it has been very expensive to do this with the previous types of offshore foundations.

1.2 Numerical modelling of circular shallow foundations for offshore structures

There has been a lot of research describing shallow foundation behaviour under combined loadings. Traditionally, geotechnical solutions established have been based on the estimation of bearing capacity and the use of some ad hoc procedures using emprical factors such as the method proposed in Meyerhof (1953) or in Brinch Hansen (1970) and Vesic (1973). These methods are appropriate to the prediction of the failure of foundation. They include a series of empirical factors which must be modified to evaluate capacity for horizontal and moment loading during the calculation, but this process can not be implemented in a numerical analysis program. Moreover, these methods also do not pay attention to the plastic response in the pre-failure stage, which has many effects on the stability of foundations and structures.

Another approach which is used to investigate the foundation behaviour under combined loading is to discretise the soil media into many elements and solve the problem using the Finite Element method. Although this approach can allow consideration of details such as a complicated constitutive law, soil characteristics and geometry; the requirements of a large computer memory, large data storage capacity, excessive running time and the need for an experienced analyst to carry out the work are still obstacles for the user.

A requirement exists to understand the foundation behaviour within the structural analysis. In addition, it is necessary to find a practical calculation method for engineers. Both these requirements lead to the need to develop a “force-resultant” model encapsulating the generalised behaviour of the foundation purely in terms of the resultant forces and the corresponding displacements through a reference point. This concept is also called a “macro-element”. The key advantage expected from this model is that it can be implemented easily and accurately in a program which is able to analyse the foundation-structure interactions. In a similar way to the use of force resultants and nodal displacements in the conventional analysis of beams or columns, the soil media and the footing are combined together and considered as a “macro-element”. The behaviour of this element will be reflected through applied loads from the structure and corresponding displacements of the foundation. By using this concept, some models have been developed, on the basis of work hardening plasticity theory, to describe the shallow foundation behaviour. Among others, Nova and Montrasio (1991) and Gottardi and Butterfield (1995) have described the strip footing behaviour on sand. Martin and Houlsby (2001) have proposed the model B for a spudcan footing on clay. Cassidy (1999), Houlsby and Cassidy (2002) and Cassidy *et al*. (2002) have given the solution for circular shallow foundation on loose sand which is called model C.

Extensive tests have been done at the University of Oxford to develop the models based on this “macro-element” concept. So far, there have been two models which are constructed and verified, Model B and Model C. These models are based on a convenient framework using work hardening plasticity theory. Model B and Model C address directly the response of a foundation through the variation of displacements under applied loading without considering the complicated stress states in the soil beneath the foundation. The most important factor of these models is to determine an experimental yield surface in load space. Figure 1.4 shows the shape of this yield surface, in which, V_0 is the vertical bearing capacity of the foundation at a certain depth.

Particularly, model B is a plasticity model applying for the analysis of clay under a spudcan footing in a 2-dimension problem (V, M, H). This model was originally proposed in Houlsby and Martin (1992). It focuses on two main issues of spudcan foundation assessment on clay.

Firstly, the preloading in the installation process is considered. This process may involve large penetrations of the foundation in the soil. The magnitude of penetration in soft clay is very large, for instance, 30m penetration of a 15m-diameter spudcan is not unusual (see Martin, 1994). This requires an analysis accounting for shear strength, which increases with depth of the clay.

The second issue addressed in model B is the performance of a spudcan foundation under combined loading which includes three components: vertical, horizontal and moment load. In simple analysis procedures, the jack-up structures are assumed to transfer only two components of load to their foundations: vertical and horizontal loads. However, the moment loads also have some significant effects in the performance of structure and foundation as shown in Figure 1.5. Therefore, it is necessary to take into account the moment loads in the analysis for more accuracy and safety.

Model C is also a theoretical model based on work hardening plasticity theory. The motivation of this model, again, is the performance of a spudcan foundation under the extreme conditions of environmental loads such as wave and wind. By using this model, the behaviour of a circular footing on sand subjected to an arbitrary combination of drained vertical, horizontal and moment loading has been described (see Cassidy, 1999).

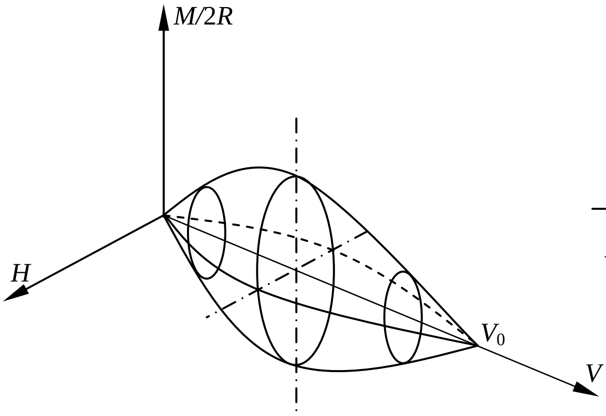

Figure 1.4 Shape of the yield surface

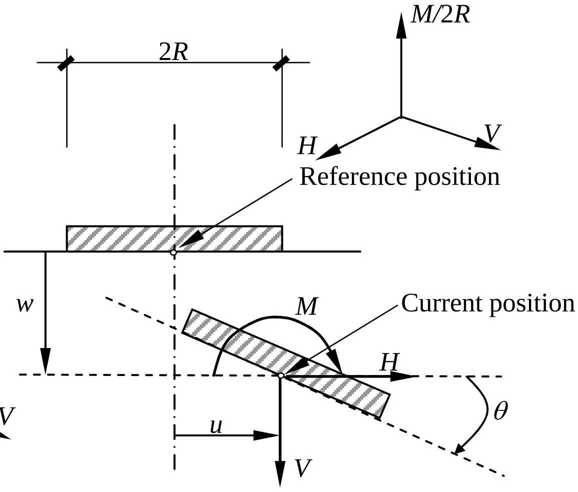

Figure 1.5 Loads and displacements of the foundation

It is clear that the foundation behaviour has to be investigated in a six-degree-of-freedom system of cyclic loading with displacement response evaluated. It should be noted that the directions of environmental forces such as wave and wind do not usually coincide. Both Model B and Model C, however, just address three degrees-of-freedom with a planar applied loading (V, H, M). These models are focussed on monotonic failure with a single-yield surface but, for offshore wind turbines, it is necessary to investigate the case of cyclic loading in a six degrees-of-freedom system.

Furthermore, during the cyclic loading, hysteresis occurs in the unloading-reloading processes. In the single-yield-surface model, the response which is obtained from the unloading will be much stiffer than the actual behaviour since it is just an elastic unloading response and cannot reflect the hysteresis, which makes the stress-strain curve softer in the unloading-reloading process.

In addition, the single-yield-surface models using macro-element concept, such as Model B and Model C, have been developed for circular flat footings and spudcan footings. However, in the case of caisson footings, there are some special characteristics related to geometry and installation techniques which have not been considered.

Therefore, in this research, in order to simulate correctly the cyclic effects of loading, the three-dimensional performance of the offshore wind turbine foundation and the special features of caisson, the two models, B and C, will require developments. The method used will be an approach to plasticity theory based on thermodynamics which is called continuous hyperplasticity, modified for the caisson footing. An overview of the continuous hyperplasticity formulation will be given in the following section.

1.3 Application of plasticity models based on thermodynamic principles

A framework for the derivation of plasticity theory based on thermodynamic principles has been proposed in Houlsby and Puzrin (2000). This framework is originally derived from the works of Ziegler (1977). Corresponding to this framework, the derivation of constitutive behaviour of elastic-plastic materials will be established in strict accordance with the first and the second laws of thermodynamics. The key feature of this approach is to specify fully the constitutive behaviour of materials by using only two scalar potential functions, which are called the free energy function and the dissipation function, following the two laws of thermodynamics. The incremental constitutive behaviour of materials is derived from these functions. These incremental responses therefore always automatically obey the two laws of thermodynamics. This is the feature that some conventional plasticity models cannot take into account. In fact, obeying the two laws of thermodynamics also is an important motivation for the establishment of models based on thermodynamic framework, which are called hyperplasticity models. The advantages of this approach, which have been pointed out in Collins and Houlsby (1997), Houlsby and Puzrin (2000) and Puzrin and Houlsby (2001), are outlined briefly below.

Firstly, as mentioned above, the hyperplastic approach guarantees that incremental derivation of plasticity will strictly obey the Laws of Thermodynamics. It allows the description of any constitutive behaviour just by using two scalar functions, the free energy function and either the dissipation or the yield function. The problem of choosing a non-associate flow rule for plastic responses of geotechnical materials is therefore formulated easily and automatically without any further potential functions which are usually used in conventional plasticity theory. This convenience is the result of the use of generalised stresses, which depend on the plastic state of the model, and the existence of the true stress terms in either the dissipation function or the yield function. A detailed demonstration of this characteristic of generalised stress space in hyperplastic models is given in Collins and Houlsby (1997).

The second advantage of the hyperplastic model results from the use of internal variables in the case of cyclic loading. Using these variables, no distinction is necessary between the case of cyclic loading and monotonic loading. This is because the past history of the loading-unloading process represented by a strain state is always reflected clearly through the state of the internal variables. This is very convenient for the computational analysis, especially in the case of offshore construction because of the cyclic feature of environmental loads such as winds and waves.

Continuous hyperplasticity, disceretised by Puzrin and Houlsby (2001a), is the next step in the development of the hyperplastic model. The motivation for this improvement is to increase the abilities of constitutive models to capture fully the irreversible strains in materials under the applied loads. In fact, in many types of geotechnical materials, especially in soil, irreversible strains appear very soon when the value of loading is still very low. The increase of irreversible strain occurs continuously and smoothly during the loading-unloading process. This implies that there is almost no stage of purely elastic behaviour of materials and the elasto-plastic behaviour will be taken into account as soon as the loads are applied. Furthermore, it should be noted that, by using continuous plasticity, elastic-plastic behaviour should also occur on unloading which can not be explained by a conventional single-yield-surface model. The hysteresis is therefore expressed more logically and clearly. In the continuous hyperplastic model, the internal variables which, in this case, represent the irreversible parts of the total strains are developed into internal functions. Consequently, the two scalar potential functions become the two scalar potential functionals, which can be defined as the functions of functions. The most important feature of the continuous hyperplastic model is the choice of internal functions, which play on the role of internal variables in the hyperplastic model. These functions must be chosen to fit the curves of the stress-plastic deformation relationship well, which are derived from the results of experiments.

It is necessary to bear in mind that there could be some numerical difficulties arsing in the application of the continuous plasticity model. Particularly, when using the rate independent behaviour of materials, the adjustment for the load point to lie on the surface of a system of infinite number of yield surfaces could require some very complicated numerical procedures. In order to avoid this obstacle, a further development that will be considered in this thesis is rate-dependent behaviour. Originally, rate-dependent plasticity models derived from hyperplasticity have been proposed in Houlsby and Puzrin (2001b). Once the rate-dependent behaviour is applied, the dissipation function no longer serves as a purely scalar energy potential function. It will be divided into two parts known as force potential and flow potential function. The relationship between these parts is expressed mathematically by a Legendre-Fenchel transformation. Based on this methodology, the rate-dependent solution for shallow foundation for offshore wind turbines is established. Rate-dependence plays a role not just in removing the numerical difficulties but also may be the base for future research on the model which takes into account the rate effects of materials.

In order to validate this theoretical model, the last core issue is integrating the model into a numerical program. Afterward, a number of numerical examples are implemented to compare the results with those of experiments or other models available. For this reason, the continuous plasticity model derived in this paper is discretized to a multiple-yield-surface model which has a finite number of yield surfaces to be able to implement a numerical implementation. A FORTRAN program named ISIS is built during the investigation process. This program is based on an earlier first version, which has been written by Professor Guy T. Houlsby (Oxford University) using the conventional plasticity theory with macro-element concept to validate model B and model C.

1.4 Outline of this thesis

The strategy of this research is to build a theoretical model combined with programming for the numerical analysis step by step. Firstly, the conventional single-yield-surface models (model B and model C) are used as the starting point. Then, these models are converted to the single-yield-surface hyperplasticity model. Afterwards, the multiple-yield-surface hyperplasticity model is developed from its single-yield-surface version. A step-by-step approach has therefore been adopted. In each step, there will be some numerical illustrations to validate the current version of the model. The outline of this thesis is expressed by the following structure.

Chapter 2: Literature review and background

This chapter will describe briefly the theoretical background and conventional solutions concerned with this research.

Chapter 3: Single-yield-surface hyperplasticity model

This chapter discusses the following issues:

- Development of a hyperplasticity model with single yield function based on those of both model B and model C.
- Consideration of the special features of models for caisson foundations.
- The rate-dependent solution is introduced to prepare for further developments.

Chapter 4: Continuous hyperplasticity and the discretization for numerical analysis

This chapter includes the following discussions:

- Theoretical development of continuous hyperplasticity model using rate-independent materials for circular rigid foundation under combined loading in a three-dimensional problem.
- Theoretical development of continuous hyperplasticity model using rate-dependent materials for a circular rigid foundation under combined loading in three-dimension problem.

- Discretization of rate-dependent continuous hyperplasticity model for numerical analysis.

Chapter 5: Parametric study

This chapter presents the investigation of the relationship among the factors and the suitable values of parameters given in the model.

Chapter 6: Model applications

This chapter presents the applications of the model to predict the behaviour of real caissons.

Chapter 7: Concluding remarks

This chapter discusses the final results of the research, the lesson learned, the experiences obtained and the achievements gained.

CHAPTER 2

LITERATURE REVIEW AND BACKGROUND

This chapter briefly presents the developments of theoretical analyses of circular foundations for offshore wind turbines and the motivation behind the development of a novel model based on thermodynamic principles.

2.1 Introduction

In order to establish a model predicting the response in the pre-failure stages of loading of the foundation, there are three issues which must be considered: the elastic behaviour, the boundary of the elastic region which is the so-called yield surface and the incremental plastic response which is affected by the expansion, contraction and movement of the yield surface in stress space during loading-unloading processes.

In addition, in the prediction of the behaviour of the soil under a circular footing of an offshore structure, there are two main analyses that must be undertaken separately. Firstly, the pre-loading process (footing penetrations during the installation process) has to be analysed. Secondly, the effects of environmental loads, represented by the cyclic combined loadings (storm, wind and wave) have to be simulated as accurately as possible. In the case of foundations for offshore wind turbines, the serviceability of the structure in extreme natural conditions is much more important than the ultimate vertical bearing capacity. Therefore, this study mainly considers the behaviour of a circular foundation under cyclic combined loading. The background of the vertical bearing capacity calculation and of the elastic response of foundations used here is based on the experimental and theoretical results of previous researchers.

The previous investigations, based on plasticity theory for offshore foundations, such as model B and model C, will be used as the starting point for this research. Thus, the review of previous plasticity models will focus on developments from Model B and Model C to the introduction of the hyperplasticity model which is the main focus of this research.

2.2 Conventional elastic solutions

The installation of shallow foundations for offshore structures on the seabed always causes plastic deformations and remoulding of the soil surrounding the footings. Furthermore, during the operation of the structures, additional plastic deformations happen under the combined loadings which are caused by the environmental conditions. However, before going to the plasticity models, it is necessary to mention the elastic solutions as the beginning of any mechanical behaviour.

2.2.1 Elastic solutions of circular flat footing and spudcan

Poulos and Davis (1974) proposed a solution for the deflection of a rigid circular footing on the surface of a homogeneous elastic medium:

$$V = \left(\frac{4GR}{1-\nu}\right)w\,;\; H = \left(\frac{32GR(1-\nu)}{7-8\nu}\right)u\,;\; M = \left(\frac{8GR^3}{3(1-\nu)}\right)\theta \qquad (2.1)$$

where the loads and displacements are defined in Figure 2.1b. G and ν are the shear modulus and Poisson’s ratio of the soil and R is the footing radius. There are some investigations confirming that equations (2.1) are exact solutions in the case of a rough footing on incompressible soil ($\nu = 0.5$), such as Poulos (1988) and Bell (1991). These solutions have often been applied to an embedded footing, although they are originally derived for a surface footing.

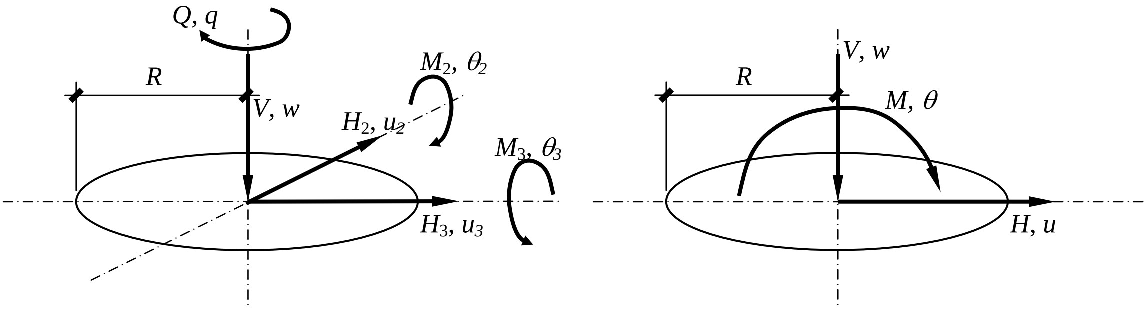

(a) Six degrees of freedom (b) Three degrees of freedom

Figure 2.1 Combined loading of a circular footing and corresponding displacements

Investigations about the cross-coupling terms between horizontal and rotational displacements have been carried out by Butterfield and Banerjee (1971) and Gazetas *et al.* (1985). In research using three-dimensional finite element analysis, Bell (1991) has confirmed these terms for ratios of penetration depth and footing radius such as 0.25, 0.5, 1.0, and 2.0. Endley *et al.* (1981) pointed out that, in practice, these ratios rarely exceed the value of 2.5. Ngo-Tran (1996) has extended the work of Bell (1991) with some further details on the shape of spudcan footing.

In this research, the elastic responses are based on the solutions of previous research such as Bell (1991), Ngo-Tran (1996). These elastic solutions for 2D analysis can be described in matrix form as follows:

$$\begin{Bmatrix} V \\ M \\ H \end{Bmatrix} = \begin{bmatrix} K_1 & 0 & 0 \\ 0 & K_2 & K_4 \\ 0 & K_4 & K_3 \end{bmatrix} \begin{Bmatrix} w \\ \theta \\ u \end{Bmatrix} \tag{2.2}$$

Where V, M and H are vertical load, moment load and horizontal load respectively. The corresponding displacements are w, θ and u. These solutions have been used in Model B (Martin, 1994) and Model C (Cassidy, 1999). K_1, K_2, K_3 and K_4 are the dimensionless stiffness coefficients for elastic behaviour.

$$K_1 = 2GRk_1;\ K_2 = 8GR^3k_2;\ K_3 = 2GRk_3;\ K_4 = 4GR^2k_4 \tag{2.3}$$

in which k_1, k_2, k_3 and k_4 are the stiffness coefficients of soil (see Ngo-Tran, 1996). They depend on the embedment depth of the footing, the radius of the footing, the Poisson's ratio, the cone angle of the footing (spudcan) and the property of the surface of the footing. The closed forms of these factors which have been derived from a variety of elastic solutions, such as Bycroft (1956), Gerrard and Harrison (1970), Poulos and Davis (1974), were conducted by Bell (1991) and were modified by Ngo-Tran (1996).

The elastic solutions of Bell (1991), Ngo-Tran (1996) and their applications in Model B (Martin, 1994) and Model C (Cassidy, 1999) are considered only in 2D problems. However, this study is concerned with 3D analysis. Thus, it is necessary to expand these above elastic solution for a 3D problem. In the first version of the ISIS program, Houlsby proposed an expansion of the elastic solution for both model B and model C as follows:

$$\begin{Bmatrix} V \\ H_2 \\ H_3 \\ Q \\ M_2 \\ M_3 \end{Bmatrix} = \begin{bmatrix} K_1 & 0 & 0 & 0 & 0 & 0 \\ 0 & K_3 & 0 & 0 & 0 & -K_4 \\ 0 & 0 & K_3 & 0 & K_4 & 0 \\ 0 & 0 & 0 & K_5 & 0 & 0 \\ 0 & 0 & K_4 & 0 & K_2 & 0 \\ 0 & -K_4 & 0 & 0 & 0 & K_2 \end{bmatrix} \begin{Bmatrix} w \\ u_2 \\ u_3 \\ \omega \\ \theta_2 \\ \theta_3 \end{Bmatrix} \tag{2.4}$$

The elastic response of the current model will be based on the above form. The additional stiffness factor K_5 was proposed by Houlsby (2003) to take into account the effect of torsion about the vertical axis. It can be calculated as:

$$K_5 = 8GR^3 k_5 \tag{2.6}$$

The convention for the loadings and corresponding displacements in a three-dimensional problem has been shown in Figure 2.1a.

2.2.2 Elastic solution for caisson footing

Based on a numerical study using the scaled boundary finite-element method, Doherty *et al.* (2004) have provided an accurate means of assessing the elastic behaviour of caisson footings (see Figure 2.2).

An elastic half-space representing the soil combined with shell finite elements has been used to represent the flexible caisson skirt, which has a significant influence on the elastic response of the foundation. The dimensionless elastic stiffness coefficients calculated have been expressed as functions of the relative stiffness of the caisson's skirt compared with the soil, the geometric shape of the caisson and the two extreme calculations, which are (a) the case of a rough rigid circular foundation at the soil surface and (b) the case of absolutely rigid caisson. This solution is briefly described in the following.

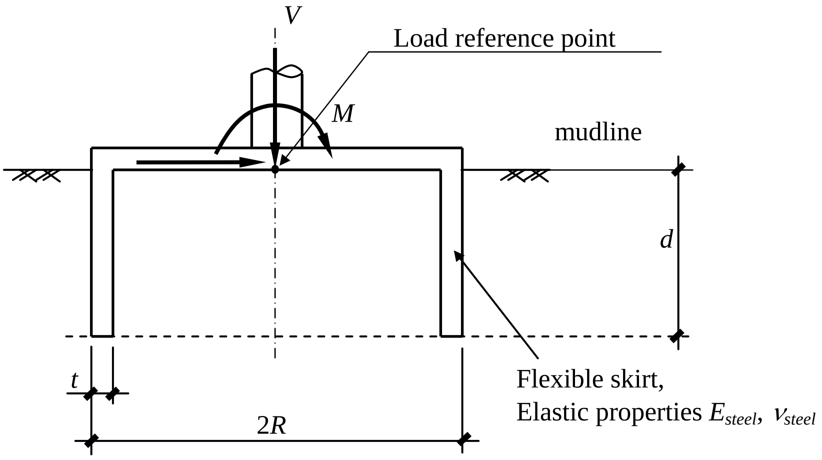

Figure 2.2 Caisson foundation with flexible skirt

The dimensionless elastic stiffness coefficients can be calculated as follows:

$$k_i(J) = \frac{k_{0i} + \left(\frac{J}{J_{mi}}\right)^{p_i} k_{\infty i}}{1 + \left(\frac{J}{J_{mi}}\right)^{p_i}} \tag{2.7}$$

where the subscript i represents 1, 2, 3, 4 and 5 as the indices of the elastic stiffness coefficients corresponding to those of Eqs. (2.3) and Eq. (2.6); J is a dimensionless parameter which represents the normalised bending stiffness of the caisson skirt; k_{0i} is the value of the stiffness coefficients k_i when J tends to zero, corresponding to the case of a circular flat footing; $k_{\infty i}$ is the value of k_i when J tends to infinity, corresponding to the absolutely rigid caisson. The form of J is expressed as follows:

$$J = \frac{E_{steel} t}{G_R R} \tag{2.8}$$

where G_R is the shear modulus of the soil at the depth equal to the value of the radius R, t is the thickness of the skirt, E_{steel} is the elastic modulus of the skirt. J_{mi} is the value of J at $k_i = (k_{0i} + k_{\infty i})/2$ and p is proportional to the gradient of the k_i curve at J_{mi}. The factors k_{0i}, $k_{\infty i}$, J_{mi} and p_i have been tabulated in Doherty *et al.* (2004). The general shape of the k_i curve is shown in Figure 2.4

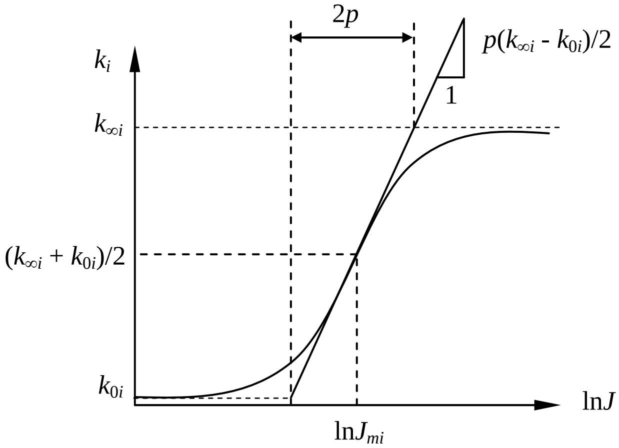

Figure 2.4 Stiffness coefficient variations (after Doherty *et al.*, 2004)

2.2.3 Elastic shear modulus

In the application of the elastic solutions, one of the most important factors, which strongly affects the accuracy of the results, is the choice of shear modulus G. The variations of shear modulus G that will be reviewed briefly in this section are in the case of clay (Model B - for a circular flat footing and spudcan), in the case of sand (Model C - for a circular flat footing and spudcan) and in the analysis of a caisson footing.

In the case of clay, the shear modulus is often determined from the undrained shear strength of soil s_u and an empirical rigidity index (I_r) defined as G/s_u. The value of G/s_u depends on the level of strain. In SNAME (1994), for the clay beneath the spudcan under extreme loading events, a value for G/s_u is suggested as 39. In the case of small strain problems, the value of G/s_u ranges from 150 to 200. For very small strain problems, such as in serviceability conditions, G/s_u can vary from 200 up to 800 (see Martin, 1994). It should be noted that the value of shear modulus must be an approximation because of the inaccuracy in the measurement of s_u. Therefore, it is necessary to pay attention as much as possible to reproduce the natural conditions and stress histories of soil specimens. In this thesis, a linear variation of undrained shear strength with depth is mainly used. The undrained shear strenth profile is shown in Figure 2.5 in which s_{um} is the undrained shear strength at mudline, R is the radius of footing, z is the depth of footing and ρ is a factor which typically has a value of about 2 kPa/m (see Martin, 1994).

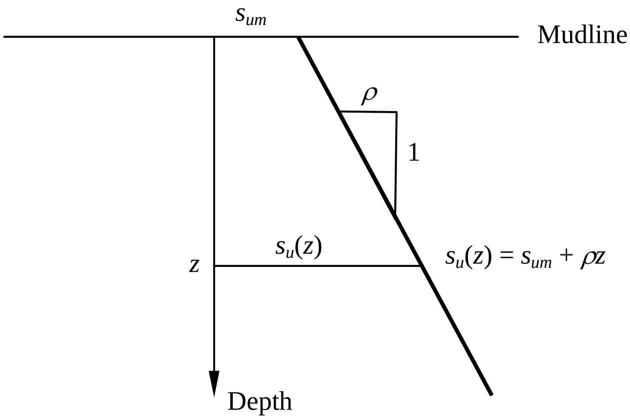

Figure 2.5 Undrained shear strength profile

In the case of sand, Wroth and Houlsby (1985) have pointed out that the variation of shear modulus depends not only on the depth of footing but also on the vertical stress level applied. Therefore, the form of shear modulus which is derived from the experimental observation (Wroth and Houlsby, 1985) is taken as follows:

$$G = p_a g \sqrt{\frac{\frac{V}{\pi R^2} + \gamma' R}{p_a}} \tag{2.9}$$

where p_a is atmospheric pressure, g is a non-dimensional shear modulus factor and γ' is the effective unit weight of the soil.

In an investigation of the effects of caisson stiffness behaviour in non-homogeneous soil, Doherty *et al.* (2004) have proposed a variation in the shear modulus as follows:

$$G(z) = G_R \left(\frac{z}{R} \right)^{\alpha} \tag{2.10}$$

where G_R is the shear modulus at a depth R. The value of G_R could be calculated by using the formulation of model B (for clay) or Eq. (2.9) (model C - for sand). α is the dimensionless factor depending on the soil type.

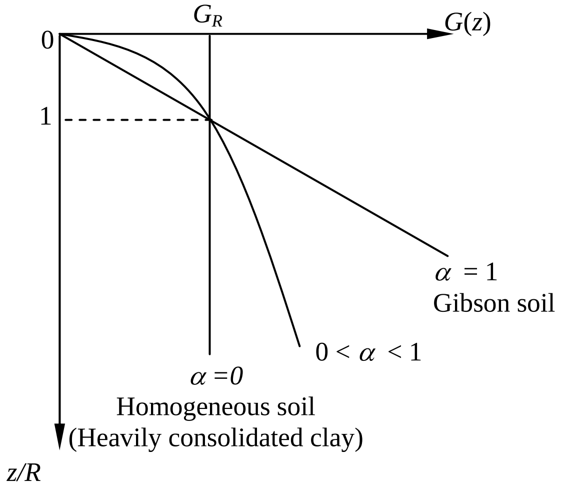

Figure 2.6 Variation of shear modulus with depth (after Doherty *et al.*, 2004)

This variation is chosen from the point of view that the shear modulus depends on the stress level which could increase with depth. Within the types of heavily consolidated clay which have very large overconsolidation ratios, there are not large variations of shear modulus with depth. The factor α is therefore close to zero. For normally overconsolidated clay, the value of α tends to unity, which is known as the α value of a "Gibson" soil. Other types of soil have α values varying from 0 to 1. For example, sands show an approximate value of α of 0.5 (see Doherty *et al.*, 2004). Figure 2.6 shows the variation of shear modulus with different kinds of soil.

2.3 Vertical bearing capacity formulations

In the analysis of shallow foundation for offshore structures, there have always been two issues which have to be considered and implemented: the installation process of the footing and the performance of the foundation under the environmental conditions during the lifetime of the foundation. Both these issues involve the calculation of bearing capacity. For clay, the undrained bearing capacity is the focus of interest. For sand, the drained or partially drained bearing capacity will be relevant. The size of the yield surface which is used in elastic-plastic analysis is also related to the bearing capacity. For instance, the size in V-axis of the yield surface in Model B (Martin, 1994) or in Model C (Cassidy, 1999) is determined by the bearing capacity.

There has been a lot of research published on the issue of bearing capacity of foundations. It is impossible to review all of them here. Therefore, in this section, it is appropriate to present briefly the solutions of the bearing capacity of circular footings and spudcans under purely vertical and combined loadings in offshore industry and introduce a proposed calculation procedure for the vertical bearing capacity of a caisson footing, which is the main goal of this research.

2.3.1 Bearing capacity formulations for circular flat footing and spudcan

Original vertical bearing capacity formulations

The solutions for the vertical bearing capacity under pure vertical load on cohesive soil generally accepted are the solutions of Meyerhof (1951, 1953), Brinch Hansen (1961, 1970) and Vesic (1975). From the solution of bearing capacity for strip footing on a weightless Tresca material, $V_0 / A = (\pi + 2)s_u$, Brinch Hansen (1970) has modified a formulation with some more empirical shape factors and depth factors to take into account the effects of footing geometries and the installation process. The circular footing is changed to an equivalent square footing with the size of $B = R\sqrt{\pi}$. Brinch Hansen's formulation can be expressed as follows:

$$V_0 = \left((\pi + 2)s_u \left(1.2 + 0.4\frac{z}{B} \right) + \gamma' z \right)A \qquad \text{with } \frac{z}{B} \le 1 \tag{2.11}$$

$$V_0 = \left((\pi + 2)s_u \left(1.2 + 0.4\tan^{-1}\left(\frac{z}{B} \right) \right) + \gamma' z \right)A \qquad \text{with } \frac{z}{B} > 1 \tag{2.12}$$

Vesic (1975) has modified the Hansen's formulation to get the smooth transition at $\frac{z}{B} = 1$. For a square footing, Vesic's formulation can be written as:

$$V_0 = \left((\pi + 2)s_u \left(1 + \frac{1}{\pi + 2} \right)\left(1.2 + 0.4\frac{z}{B} \right) + \gamma' z \right)A \qquad \text{with } \frac{z}{B} \le 1 \tag{2.13}$$

$$V_0 = \left((\pi + 2)s_u \left(1 + \frac{1}{\pi + 2} \right)\left(1.2 + 0.4\tan^{-1}\left(\frac{z}{B} \right) \right) + \gamma' z \right)A \qquad \text{with } \frac{z}{B} > 1 \tag{2.14}$$

Martin (1994) has proposed the bearing capacity for circular flat footing and spudcan on clay as follows:

$$V_0 = N_{c0}\pi R s_u \tag{2.15}$$

where N_{c0} is determined from the set of theoretical bearing capacity factors; R is the radius of the footing.

In the case of sand, Gottardi *et al.* (1999) has provided an empirical formulation for the bearing capacity of a circular flat footing based on test results as follows:

$$V_0 = \frac{k_p w_p}{1 + \left(\frac{k_p w_{pm}}{V_{0m}} - 2 \right) \left(\frac{w_p}{w_{pm}} \right) + \left(\frac{w_p}{w_{pm}} \right)^2} \tag{2.16}$$

where k_p is the elastic stiffness (or the initial plastic stiffness); w_p is the depth of footing; V_{0m} is the maximum vertical bearing capacity and w_{pm} is the value of w_p at this maximum bearing capacity. Numerical values of k_p, V_{0m} and w_{pm} are derived from experiments.

Cassidy (1999) and Houlsby and Cassidy (2002) have modified Gottardi's formulation to take into account the case when $w_p \to \infty$ as follows:

$$V_0 = \frac{k_p w_p + \left(\frac{f_p}{1 - f_p} \right) \left(\frac{w_p}{w_{pm}} \right)^2 V_{0m}}{1 + \left(\frac{k_p w_{pm}}{V_{0m}} - 2 \right) \left(\frac{w_p}{w_{pm}} \right) + \left(\frac{1}{1 - f_p} \right) \left(\frac{w_p}{w_{pm}} \right)^2} \tag{2.17}$$

where f_p is a dimensionless constant that describes the limiting value of vertical load of V_{0m}. Figure 2.7 shows the curve representing the Eq. (2.17).

By changing the magnitude of f_p, Eq. (2.17) can match the vertical bearing capacity curve in both cases of loose sand and dense sand. The dashed curve in Figure 2.7 shows the typical variation of the vertical bearing capacity of a circular footing on loose sand corresponding to the case when $f_p \to 1$ and $w_{pm} \to \infty$.

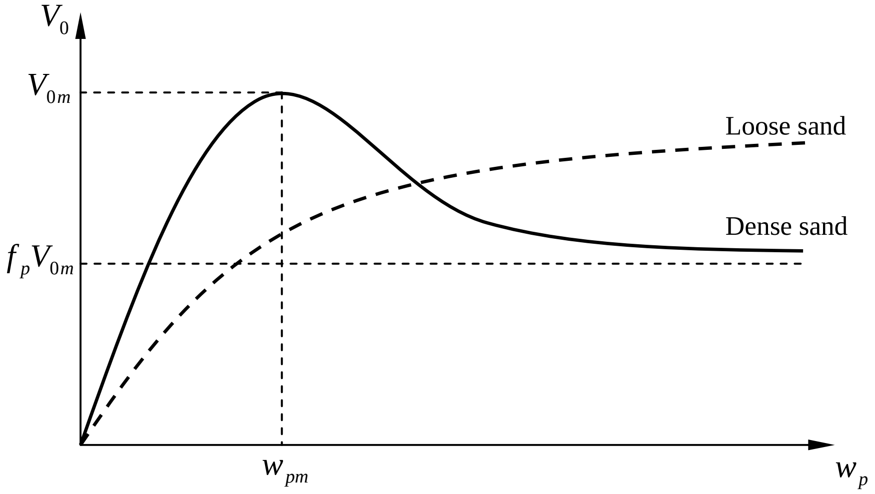

Figure 2.7 Vertical bearing capacity of a circular flat footing on dense and loose sand

Bearing capacity of foundation under combined loading

In the offshore industry, bearing capacity methods have been widely used to estimate the failure of a foundation under combined loading. Meyerhof (1951, 1953), Brinch Hansen (1961, 1970) and Vesic (1975) have given calculation procedures of the bearing capacity of foundations under inclined or eccentric load conditions. In general, a combined planar loading on a circular foundation can be transferred to a combination of an eccentric vertical load and a horizontal load as shown in Figure 2.8.

For a strip footing, Meyerhof (1953) has suggested an effective width as $B' = B - 2e$, in which e is the eccentricity of the applied loads. For a circular footing, the effective area is determined as that of the equivalent rectangle constructed so that its geometric centre coincides with the load centre of the original circular footing. The American Petroleum Institute (API, 1993) has recommended a formulation for determining the effective dimensions B^*, L^* for the circular footing as:

$$A' = B^* L^* = \pi R^2 - 2e\sqrt{R^2 - e^2} - 2R^2 \sin^{-1}\left(\frac{e}{R}\right) \text{ and } \frac{B^*}{L^*} = \sqrt{\frac{R+e}{R-e}} \qquad (2.18)$$

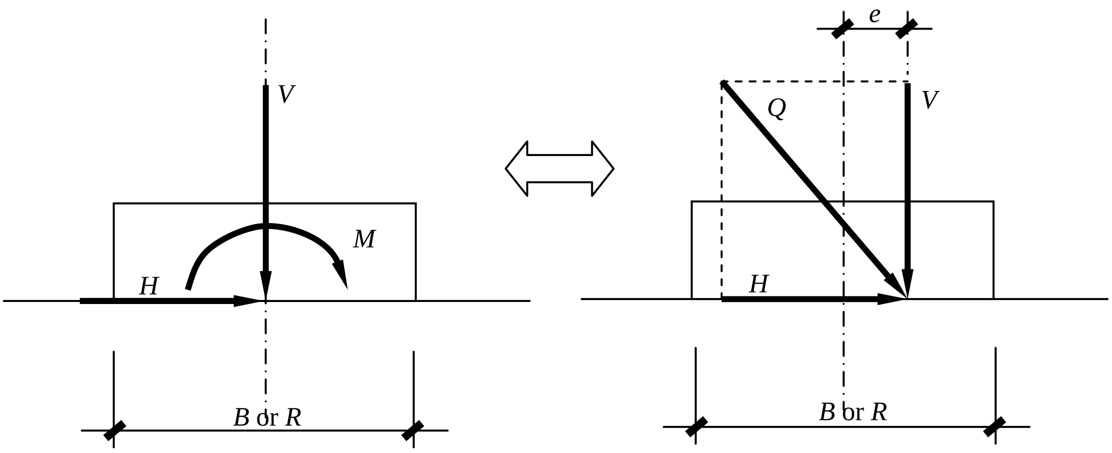

Figure 2.8 Equivalent force systems on rigid foundation

Meyerhof (1953) and Binch Hansen (1961) have introduced the inclination factors ζ_{ci}, ζ_{qi} and $\zeta_{\gamma i}$ to take into account the influence of the inclination and eccentricity on the vertical bearing capacity of the foundation. These factors are calculated by using the concept of effective area as can be seen from Figure 2.9. The vertical bearing capacity becomes:

$$V_0 = \left(cN_c\zeta_c\zeta_{ci} + qN_q\zeta_q\zeta_{qi} + \frac{1}{2}\gamma' BN_\gamma\zeta_\gamma\zeta_{\gamma i} \right) B' L' \qquad (2.19)$$

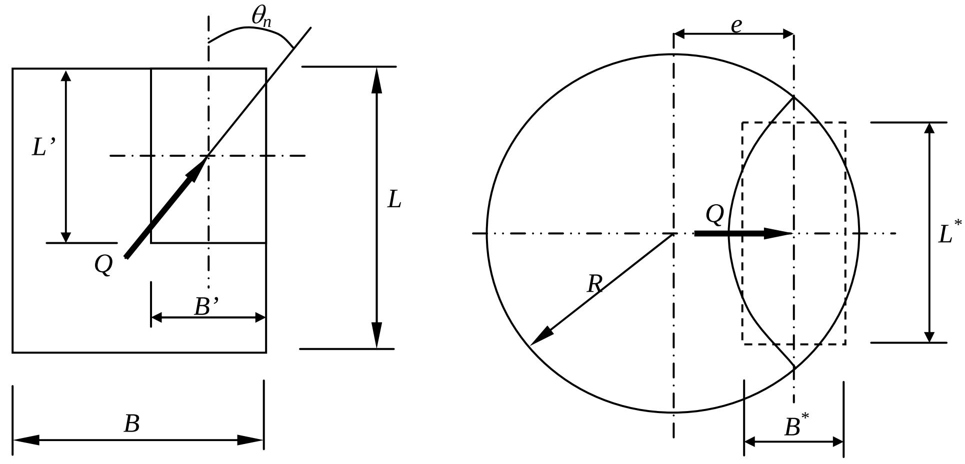

(a) Effective area of rectangular (b) Effective area of circular

Figure 2.9 Equivalent and effective areas of foundations

Alternative failure envelopes

The bearing capacity formulations under combined loadings discussed in the preceding paragraphs are mainly described in cases of using onshore shallow foundations which are just subjected to small effects from horizontal loading and moment. Meanwhile, the effects of lateral loading during the lifetime of the foundation of offshore wind turbines are relatively large. This shortcoming of conventional bearing capacity analyses leads to the need for a better solution. Another problem is that it is impossible to apply these formulations to numerical analysis because of their empirical characteristic. Therefore, the use of the concepts of plasticity theory and the exploration of the shape of the yield surface within three-dimensional load space (V: M: H) can overcome this obstacle to allow for the implementation of numerical analysis. This approach has been proposed firstly in Roscoe and Schofield (1956).

Some alternative failure envelopes are proposed in the (V: M: H) plane. Butterfield and Ticof (1979) have suggested a parabolic yield surface along the V axis. The sizes of their surface have been fixed within the range of dimensionless values of $M / BV_0 \approx 0.1$ and $M / BV_0 \approx 0.2$ where V_0 is the maximum vertical load known as the pre-consolidation load and B is the width of strip footing. Figure 2.10 shows the cigar shape of the failure envelope suggested by Butterfield and Ticof (1979).

This shape of the failure envelope has been verified and confirmed by Nova and Montrasio (1991). For conical footings and spudcan footings, research implemented at Cambridge University has shown the similar cigar-shaped failure surface. This investigation was done by Noble Denton and Associates (1987) and has been summarised by Dean *et al.* (1992). The proposed surface has the biggest cross section at $V / V_0 = 0.5$ and the corresponding ratios are $M / 2RV_0 = 0.0875$ and $H / V_0 = 0.14$.

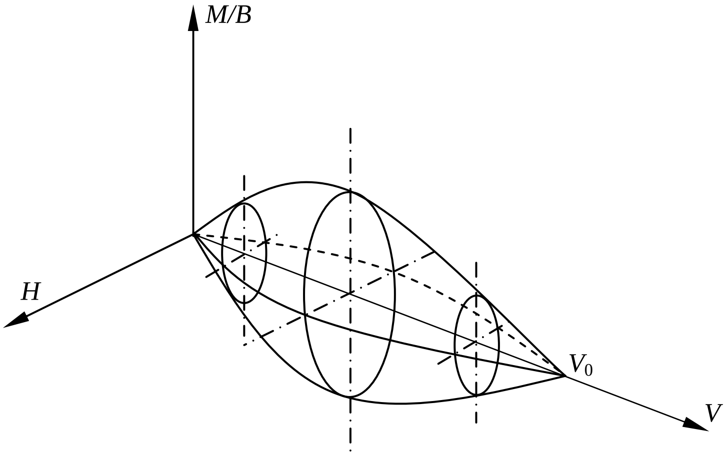

Figure 2.10 Cigar-shape of the failure envelope (After Buterfield and Ticof, 1979)

A modified cigar-shape yield surface similar to that of Butterfield and Ticof (1979) (see Figure 2.10) has been proposed in Martin (1994). Martin also pointed out that the shape of yield surface remains constant during expansion, which has been caused by the increase of penetration. This has allowed the definition of a normalised yield function with respect to only V_0, which is the pure vertical bearing capacity at the depth considered. The Model B yield function is defined as:

$$y(V,H,M,w_p)=\left(\frac{M}{M_0}\right)^2+\left(\frac{H}{H_0}\right)^2-2\bar{e}\left(\frac{M}{M_0}\right)\left(\frac{H}{H_0}\right)-\beta_{12}^2\left(\frac{V}{V_0}\right)^{2\beta_1}\left(1-\frac{V}{V_0}\right)^{2\beta_2}=0 \tag{2.20}$$

Where $M_0=m_0 2RV_0$; $H_0=h_0V_0$;

$$\bar{e}=e_1+e_2\left(\frac{V}{V_0}\right)\left(1-\frac{V}{V_0}\right);\ \beta_{12}=\frac{(\beta_1+\beta_2)^{\beta_1+\beta_2}}{(\beta_1)^{\beta_1}(\beta_2)^{\beta_2}}$$

The six parameter values obtained from experimental data (see Martin and Houlsby, 2001) are $m_0=0.083$, $h_0=0.127$, $e_1=0.518$, $e_2=-1.180$, $\beta_1=0.764$ and $\beta_2=0.882$.

In the case of a circular footing on dense sand, based on the experimental results, Gottardi *et al.* (1999) proposed an elliptical yield surface as follows:

$$y(V,H,M,w_p)=\left(\frac{M}{M_0}\right)^2+\left(\frac{H}{H_0}\right)^2-2a\left(\frac{M}{M_0}\right)\left(\frac{H}{H_0}\right)-4\left(\frac{V}{V_0}\right)^2\left(1-\frac{V}{V_0}\right)^2=0$$

(2.21)

The definitions of M_0 and H_0 are the same with those of Martin's formulations. The parameters are $m_0 = 0.09$, $h_0 = 0.1213$, a = -0.2225.

In the case of a spudcan on dense sand, Cassidy (1999) has proposed a yield function which has a similar form as that in Model B (Martin, 1994) as shown in Eq. (2.20). The six parameter values obtained from experimental data now become $m_0 = 0.086$, $h_0 = 0.116$, $e_1 = -0.2$, $e_2 = 0.0$, $\beta_1 = 0.9$ and $\beta_2 = 0.99$.

2.3.2 Installation and vertical bearing capacity of caisson footing

Since the suction caisson is a rather novel type of foundation for offshore structures, there are not many theoretical solutions established for the bearing capacity problem of caisson foundation. This section, therefore, only presents the calculation procedures suggested by Byrne and Houlsby (2004a and 2004b) to describe the installation of a suction caisson on single layer soils as the background for the establishment of the model investigated in this study. The evaluation of the vertical bearing capacity of a caisson will be based on the calculation procedure of the installation at the full depth.

The strategy of this calculation is that it uses the concepts of pile design, silo design and bearing capacity theory to conduct the estimation of vertical bearing capacity of caisson. The numerical illustrations for this theory will be shown in chapter 3 (for single-yield-surface model) and chapter 4 (for multiple-yield-surface model).

Since the contact area with the soil of the caisson varies from the beginning to the end of the installation process, there are two main stages which must be calculated separately: partial penetration and full penetration. In the partial penetration stage, the vertical bearing capacity of the caisson is caused by the friction inside and outside the part of the skirt contacting the soil medium as well as the end bearing capacity at the tip of the skirt. When the caisson reaches to the full penetration position, the vertical bearing capacity is calculated as the summation of the adhesion outside the perimeter skirt plus the end bearing capacity of a circular flat footing which has the same outside diameter as the caisson and is located at the depth of the tip of the skirt. The undrained condition is assumed for clay and the drained condition is the idealised case for sand. The calculations are described briefly in the following sections.

2.3.2.1 Installation of caisson footing on clay

Byrne and Houlsby (2004a) have proposed a calculation procedure for the installation of a suction caisson in clay. In this section, the calculation process will be reviewed briefly for more convenience in later uses.

Installation without suction - partial penetration

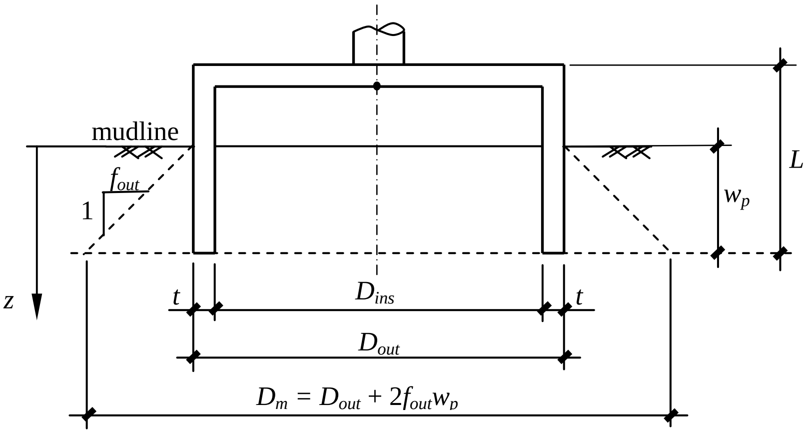

Figure 2.11 Outline of the caisson

Figure 2.11 shows the outline of a caisson with the notations that will be used in the following expressions. The vertical bearing capacity of a partially penetrated caisson without suction can be calculated by using Eq. (2.19) for the end bearing capacity of a strip footing with the width *t* and the friction forces along the skirt as:

$$V_0 = \int_0^{w_p} \alpha_{out} s_u(z)(\pi D_{out})dz + \int_0^{w_p} \alpha_{ins} s_u(z)(\pi D_{ins}) + (cN_c + qN_q + \gamma' N_\gamma)(\pi Dt) \quad (2.22)$$

where $s_u(z) = s_{um} + \rho z$ (as shown in Figure 2.5); α_{out} and α_{ins} are the adhesion factors outside and inside of the caisson; D_{out} and D_{ins} are the outside and inside diameters of the caisson skirt as shown in Figure 2.11; *D* is the average diameter: $D = \frac{D_{out} + D_{ins}}{2}$; w_p is the penetration depth of the caisson; *c* is the shear strength at depth w_p i.e. $c = s_{um} + \rho w_p$; *q* is the overburden pressure caused by the soil weight: $q = \gamma' w_p$; N_q and N_c are the appropriate bearing capacity factors of a deep strip footing with width *t* in clay.

Installation with suction assistance

Since the permeability which controls the hydraulic gradient of clay is rather small, the influences of suction pressure to the flow of water through the soil can be neglected. The suction pressure just results in an additional pressure differential across the top plate of the caisson. Therefore, an extra vertical force which equals the suction pressure multiplied by the plan area of the top plate is applied. The vertical bearing capacity can be calculated as follows:

$$V_0 = \int_0^{w_p} \alpha_{out} s_u(z)(\pi D_{out})dz + \int_0^{w_p} \alpha_{ins} s_u(z)(\pi D_{ins}) + (cN_c + qN_q)(\pi Dt) - s\left(\frac{\pi D_{ins}^2}{4}\right) \quad (2.23)$$

where *s* is the suction pressure applied.

Limits to suction assisted penetration

During the process of suction application, the average vertical stress σ_1 at the tip level inside the caisson can be reduced. Meanwhile, vertical pressure σ_2 caused by the vertical load during the installation on the rim area of the caisson skirt can be constant. Therefore, there is a possibility that, with a small enough value of σ_1 and a big enough value of σ_2, the local failure which leads to the flow of the soil into the caisson can happen. Byrne and Houlsby (2004a) have considered this failure as the "reverse" bearing capacity problem and proposed a formulation, estimating the limit magnitude of the suction pressure applied at a certain depth as follows:

$$s_{ultimate} = N_c^* s_u(z) + \frac{\pi D_{ins} \alpha_{ins} \int_0^{w_p} s_u(z)dz}{\frac{\pi D_{ins}^2}{4}} - \frac{\pi D_{out} \alpha_{out} \int_0^{w_p} s_u(z)dz}{\frac{\pi \left(D_m^2 - D_{out}^2\right)}{4}} \tag{2.24}$$

where $s_u(z)$ is the shear strength at depth z; N_c^* is the bearing capacity factor of a circular flat footing with diameter D_{ins}.

Vertical bearing capacity at full penetration

At full penetration position, the caisson footing is treated as a circular flat footing buried at depth L (full length of caisson skirt) plus the adhesion on outside surface of the skirt. It should be noted that the suction is turned off when the caisson reaches to the full penetration depth.

$$V_0 = \int_0^L \alpha_{out} s_u(z)(\pi D_{out})dz + \left(cN_c + qN_q\right)\left(\frac{\pi D_{out}^2}{4}\right) \tag{2.25}$$

2.3.2.2 Installation of caisson footing on sand

In a similar way to the previous section, this section briefly reviews the work of Houlsby and Byrne (2005a) with extra explanation. Figure 2.12 shows the outline of the caisson and the notations for the following discussion.

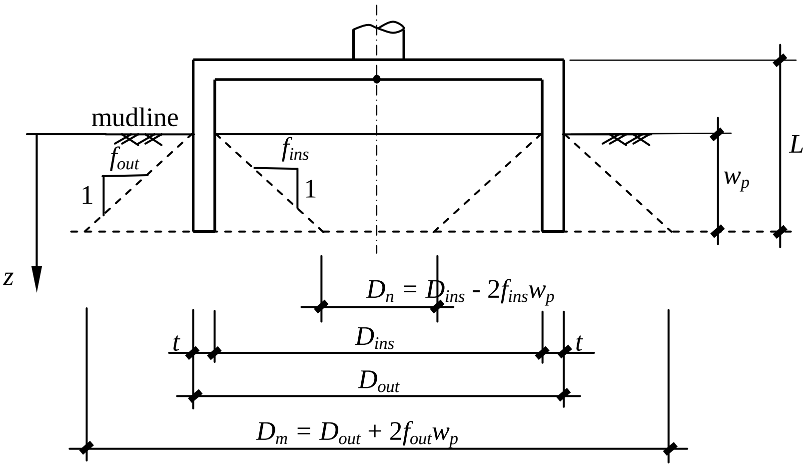

Figure 2.12 Outline of the caisson in sand

Purely vertical penetration

Vertical bearing capacity on sand can be calculated as:

$$V_0 = \int_0^{w_p} \tau_{out}(z)(\pi D_{out})dz + \int_0^{w_p} \tau_{ins}(z)(\pi D_{ins})dz + \left(\sigma'_{Vout} N_q + \gamma'\left(t - \frac{2x^2}{t}\right)N_\gamma\right)(\pi D t) \quad (2.26)$$

where $\tau_{out}(z) = (K\tan\delta)_{out}\sigma'_{Vout}(z)$ and $\tau_{ins}(z) = (K\tan\delta)_{ins}\sigma'_{Vins}(z)$ are friction stresses which depend on the vertical stress level $\sigma'_{Vout}(z)$ and $\sigma'_{Vins}(z)$ respectively on outside and inside surfaces of the skirt. $(K\tan\delta)_{out}$ and $(K\tan\delta)_{ins}$ are the combined friction factors on the outside and inside skirt surface. x is a factor depending on the ratio between σ'_{Vout} and σ'_{Vins} at the tip of caisson skirt. The detail calculation of $\sigma'_{Vout}(z)$, $\sigma'_{Vins}(z)$ and x can be found in Byrne and Houlsby (2004b).

Installation with suction

Based on the assumption that there is a uniform hydraulic gradient of water flow caused by suction pressure in the soil media, Houlsby and Byrne (2005a) suggest the formulation for vertical bearing capacity with suction assistance as:

$$\begin{aligned} V_0 = & \int_0^{w_p} \sigma'_{Vout}(z)dz(K\tan\delta)_{out}(\pi D_{out}) + \int_0^{w_p} \sigma'_{Vins}(z)dz(K\tan\delta)_{ins}(\pi D_{ins}) + \\ & + (\sigma'_{Vout}N_q + \gamma' t N_\gamma)(\pi D t) - s\left(\pi\frac{D_{ins}^2}{4}\right) \end{aligned} \tag{2.27}$$

in which the vertical effective stress $\sigma'_{Vout}(z)$ can be calculated with the replaced effective weight of sand $\gamma' + \frac{as}{w_p}$ instead of γ'; the stress $\sigma'_{Vins}(z)$ can be calculated with the replaced effective weight of sand $\gamma' - \frac{(1-a)}{w_p}s$ instead of γ'. The factor a is a pressure factor which represents the variation of excess pore pressure in the soil medium around the caisson.

Limits to suction assisted penetration

In the case of sand, the local failure is observed when the soil inside the caisson is totally liquefied. At that time, a major flow of water goes into the caisson without any further penetration. From these observations, Houlsby and Byrne (2005a) have proposed the mathematical explanation that the local failure occurs when $\sigma'_{Vins}(w_p) = 0$ i.e.:

$$s_{ultimate} = \frac{\gamma' w_p}{(1-a)} \tag{2.28}$$

where w_p is the depth of the tip of the caisson.

Vertical bearing capacity at full penetration

In a similar way to the expression of caisson on clay, the vertical bearing capacity of caisson on sand could be calculated by using Eq. (2.25). Figure 2.13 shows the typical shape of the vertical bearing capacity versus penetration depth of a caisson foundation.

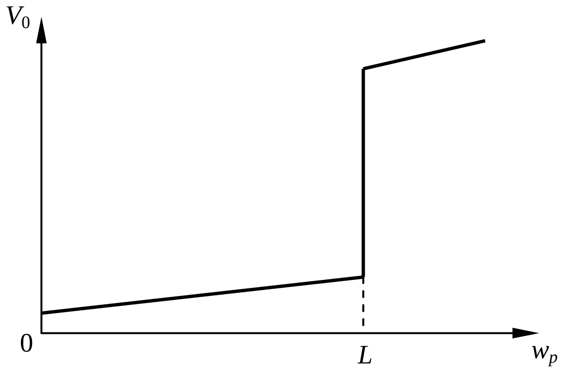

Figure 2.13 Typical calculation curve of vertical bearing capacity of caisson

2.4 Conventional plasticity models for shallow foundation for offshore structures

The idea of establishing a plasticity model in terms of the force resultants acting on the footings and the corresponding footing displacements have been first proposed by Roscoe and Schofield (1956). Based on experiments of rigid foundation subjected to combined loads, Butterfield and Ticof (1979) have expressed the foundation behaviour in the form of an interaction diagram (figure 2.10). This directs towards establishing the main components of plasticity models. Martin (1994) constructed a plasticity model using force resultant concept for circular footings based on a comprehensive series of tests of both shallow and deep foundations in Kaolin clay. Cassidy (1999) developed a complete plasticity model for spudcan footings on sand in a similar way to Martin’s work.

In general, the plasticity-based approach using force resultants concept has been regarded as a more powerful and consistent technique than the use of conventional bearing capacity methods with increasing number of empirical parameters (Gottardi *et al.*, 1999).

As this study will be started from the developments of Model B (Martin, 1992) and Model C (Cassidy, 1999), the following sections review the main ideas of these two models.

2.4.1 Plasticity model for circular shallow foundation on clay

In Martin (1994), the behaviour of spudcan footing on cohesive soil in three-dimensional load space has been conducted from test results and modelled in terms of a work hardening plasticity theory which was named Model B. The yield function of the model has been presented in Eq. (2.20).

In addition, non-associated plasticity has been considered through the change of volumetric strain component in Martin's solution (Model B). An empirical "association parameter", ζ , has been introduced in the flow rule for Model B:

$$\begin{Bmatrix} \delta w_p \\ \delta \theta_p \\ \delta u_p \end{Bmatrix} = \Lambda \begin{Bmatrix} \zeta \dfrac{\partial f}{\partial V} \\ \dfrac{\partial f}{\partial M} \\ \dfrac{\partial f}{\partial H} \end{Bmatrix} \tag{2.29}$$

Where Λ is a non-negative scalar determining the magnitude of the plastic increment; δw_p, $\delta \theta_p$ and δu_p are plastic increments of displacement corresponding to vertical, moment and horizontal load increments respectively.

2.4.2 Plasticity model for circular shallow foundation on sand

Based on a series of loading tests performed by Gottardi and Houlsby (1995), Cassidy (1999) has constructed a numerical model named Model C to simulate the behaviour of a spudcan footing on dense sand. He has proposed a yield function which has a similar form as that in Model B (Martin, 1994). In Model C, based on the observation results from experiments, a potential function which had the similar form with the yield function, but using different exponential factors, was given to treat the non-associated characteristic of the behaviour of sand:

$$g=\left(\frac{h'}{h_0}\right)^2+\left(\frac{m'}{m_0}\right)^2-2a\left(\frac{h'}{h_0}\right)\left(\frac{m'}{m_0}\right)-\alpha_V^2\beta_{34}\left(v'\right)^{2\beta_3}\left(1-v'\right)^{2\beta_4}=0 \qquad (2.30)$$

where

$\beta_{34}=\left(\frac{(\beta_3+\beta_4)^{(\beta_3+\beta_4)}}{(\beta_3)^{\beta_3}(\beta_4)^{\beta_4}}\right)^2$; α_V is an association parameter (associated flow is given by $\alpha_V=1.0$); $h'=H/V_0'$, $m'=M/2RV_0'$, $v'=V/V_0'$ and V_0' is a dummy parameter which gives the intersection of the plastic potential g with the V-axis; h_0 and m_0 are the ratios of *H/V* and *M/*2*RV* at the widest section of the yield surface.

As shown in Figure 2.14, the flow rule of plasticity in Model C is defined as:

$$\begin{Bmatrix}\delta w_p\\ \delta\theta_p\\ \delta u_p\end{Bmatrix}=\Lambda\begin{Bmatrix}\dfrac{\partial g}{\partial V}\\ \dfrac{\partial g}{\partial M}\\ \dfrac{\partial g}{\partial H}\end{Bmatrix} \qquad (2.31)$$

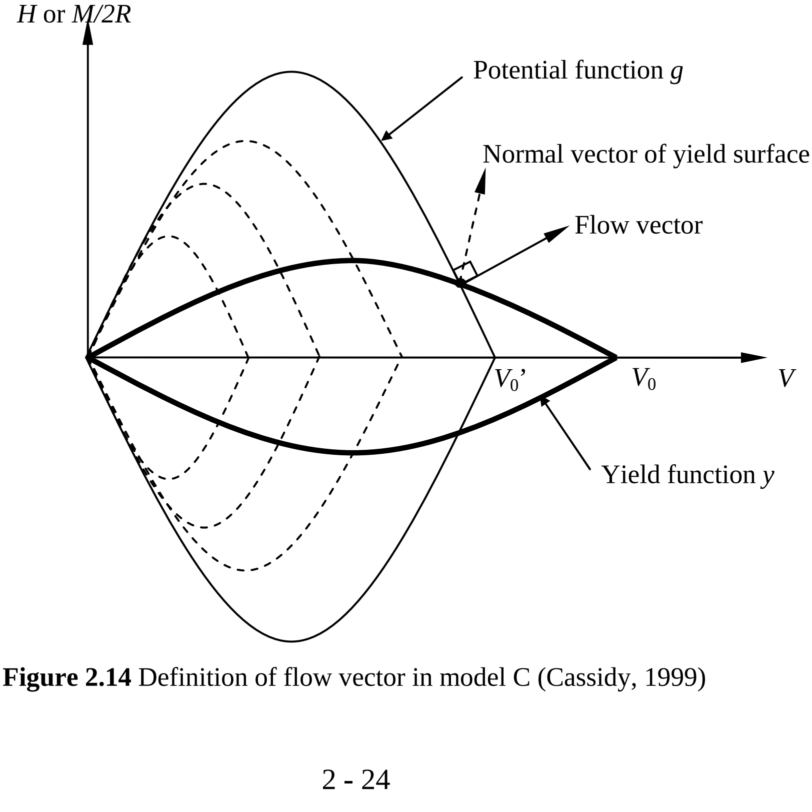

Figure 2.14 Definition of flow vector in model C (Cassidy, 1999)

However, both Model B and Model C, which are constructed based on classical expressions of plasticity theory, have not taken into account the cyclic nature of environmental loading. Moreover, the case of a caisson footing has not been considered in these models. Besides, a series of tests have been implemented by Byrne (2000), Byrne and Houlsby (2004), Houlsby *et al.* (2005a) and Villalobos *et al.* (2003a, 2003b, 2004a, 2004b) for both spudcan and caisson footing under cyclic loading. It is therefore necessary to develop a theoretical model which can explain logically special aspects of cyclic behaviour of foundation, especially for caisson footings. This is the motivation of this research.

2.5 Plasticity models based on a thermodynamic framework

One of the disadvantages of using conventional plasticity theory as in Model B and Model C is the lack of ability to capture the foundation behaviour under cyclic loadings. In order to overcome this difficulty, Houlsby and Puzrin (2000) and Puzrin and Houlsby (2001b) have set out a broad and rigorous framework of plasticity based on thermodynamic principles. The key feature of this approach is that the entire constitutive behaviour is fully described by two scalar functions, the free energy and dissipation functions. Consequently, the loading history which is representative of the cyclic loading is effectively captured through the use of internal variables. In addition, Puzrin and Houlsby (2001a) have modified this framework with the concept of infinite numbers of internal variables, which are so-called internal functions. This development provides ability to model realistic hardening effects and a smooth transition between elastic and plastic behaviour. Rate-dependent behaviour has been described in Houlsby and Puzrin (2002, 2003) to get a more accurate modelling for the behaviour of soils, and also to provide a proper way to avoid the numerical difficulties rising during the calculation process using rate-independent behaviour. This section briefly presents the theoretical framework.

This section reviews briefly the development of plasticity theory based on the thermodynamic framework of Houlsby and Puzrin (2000). Afterwards, the application of this theory to the force resultant model will be discussed.

2.5.1 Single-yield-surface hyperplasticity

2.5.1.1 Energy function and internal variables

In Houlsby and Puzrin (2000), the internal energy is derived from that of classical fluid thermodynamics, with a slight difference. To be applied to solid mechanics, the pressure and the specific volume are replaced by the stress tensor and the strain tensor respectively. In this research, the Gibbs free energy and its variables will be used. The tensor, α_{ij}, denotes internal state variables. The tensor, $\bar{\chi}_{ij}$, defines generalised stresses which depend on the change of energy with respect to the change of internal state variables.

Neglecting thermal effects (i.e. neglecting θ), Collins and Houlsby (1997) have shown that, by using a proper choice of the internal variables α_{ij}, the Gibbs free energy can be written in the form of a combination of a function of stresses, $g_1(\sigma_{ij})$, a function of internal variables, $g_2(\alpha_{ij})$, and a function of the cross effect between stresses and internal variables, $\alpha_{ij}\sigma_{ij}$, as follows:

$$g = g_1\left(\sigma_{ij}\right) + g_2\left(\alpha_{ij}\right) - \sigma_{ij}\alpha_{ij} \tag{2.32}$$

For a decoupled material in which the elastic response is independent of plastic deformation, this follows the relationship:

$$\varepsilon_{ij} = -\frac{\partial g}{\partial \sigma_{ij}} \tag{2.33}$$

$$\overline{\chi}_{ij} = -\frac{\partial g}{\partial \alpha_{ij}} \tag{2.34}$$

The internal variables, α_{ij}, play the same role as plastic strains in conventional plasticity theory.

2.5.1.2 Dissipation and yield function

Dissipation function

The main goal of the definition of the internal variables is to supply the tools for the study of the dissipation energy in materials. The concept of dissipation based on thermodynamic principles has been given in Ziegler (1977) and Collins and Houlsby (1997). Later, Houlsby and Puzrin (2000) have set out a slightly different approach, although consistent with the earlier works. In that paper, the dissipation function is defined as a function not only of the thermodynamic state of the material but also of the rate of change of state. In the case of using the Gibbs free energy function, the dissipation function is written as:

$$d = d\left(\sigma_{ij}, \alpha_{ij}, \dot{\alpha}_{ij}\right) \geq 0 \tag{2.35}$$

A concept of the dissipative generalised stress has been given: $\chi_{ij} = \frac{\partial d}{\partial \dot{\alpha}_{ij}}$. For a rate-independent material, the dissipation function must be a homogeneous first order function of the rate $\dot{\alpha}_{ij}$. This constraint will be different in the case of using a rate-dependent material and will be mentioned in section 2.5.1.3. The Euler's theorem for homogenous first order functions gives:

$$\frac{\partial d}{\partial \dot{\alpha}_{ij}} \dot{\alpha}_{ij} = \chi_{ij} \dot{\alpha}_{ij} = d \tag{2.36}$$

Following the approach of Houlsby and Puzrin (2000), the dissipation can be derived as follows:

$$d = \overline{\chi}_{ij} \dot{\alpha}_{ij} \tag{2.37}$$

Comparing with (2.36), it is straightforward to obtain that $\left(\overline{\chi}_{ij} - \chi_{ij}\right)\dot{\alpha}_{ij} = 0$. Ziegler (1977) has made a stronger condition which has been followed by Houlsby and Puzrin (2000):

$$\overline{\chi}_{ij} = \chi_{ij} \tag{2.39}$$

Yield function and flow rule

The yield function in this formulation is a degenerate special case of the Legendre transformation of the dissipation function. Since the dissipation is a homogeneous first order function, its Legendre transform is singular (see Collins and Houlsby, 1997) and defines a yield function:

$$\lambda y = \chi_{ij} \dot{\alpha}_{ij} - d = 0 \tag{2.40}$$

Where λ is an arbitrary non-negative multiplier and the flow rule is followed:

$$\dot{\alpha}_{ij} = \lambda \frac{\partial y}{\partial \chi_{ij}} \tag{2.41}$$

It can be seen that the yield function is derived directly and automatically from the dissipation function through the Legendre transformation. The explanation of the Legendre transformation that makes the conversion between the potentials proposed in this framework will not be described here but it can be found in Collins and Houlsby (1997). In addition, the rate of change of the internal variables, as shown in Eq. (2.52), is the differential of the yield function with respect to the generalised stress, unlike the conventional plasticity theory where the flow rule (in the case of associated plasticity) is the differential of the plastic potential with respect to the true stress. Besides, Collins and Houlsby (1997) have demonstrated that the non-associated plastic behaviour is obtained automatically if the yield function involves the true stresses. This result will be applied in this study. The yield function used in this research is based on that of Model B and Model C, but it will be discussed in terms of internal variables, true stress space and generalised stress space instead of purely true stress space as in conventional plasticity formulation.

2.5.1.3 Incremental response

The implementation of the constitutive relationship in numerical analysis usually requires an incremental form. This section firstly presents the derivation of a rate-independent solution, and then the rate-dependent solution is expressed, based on the formulation of rate-independent solution for brevity.

Rate-independent solution

In a rate-independent solution for a decoupled material, Puzrin and Houlsby (2001) have proposed a description similar to a conventional plasticity. When plasticity occurs, the incremental response is derived by invoking the consistency condition of the yield function: $y(\alpha_{ij}, \chi_{ij}, \sigma_{ij}) = 0$. Consequently, the incremental response can be expressed as follows:

$$\dot{\varepsilon}_{ij} = -\frac{\partial^2 g_1}{\partial \sigma_{ij} \partial \sigma_{kl}} \dot{\sigma}_{kl} + \lambda \frac{\partial y}{\partial \chi_{ij}} \tag{2.42}$$

where λ is a non-negative scalar multiplier. The details of the calculation of λ can be found in Houlsby and Puzrin (2001b).

Rate-dependent solution

The rate-dependent behaviour of materials is addressed by Lemaitre and Chaboche (1990) and Maugin (1990). From another approach, based on the thermodynamic framework, Houlsby and Puzrin (2002) have modified their framework to be able to apply for both rate-independent and rate-dependent material. They have emphasized strongly the specification of material behaviour entirely through two potential functions, free energy and dissipation energy. In this study, the works of Houlsby and Puzrin (2002) will be used to investigate the rate-dependent behaviour of soil. The Gibbs free energy does not change in the rate-dependent behaviour, but the dissipation function does not serve as a pure potential. Due to the fact that the dissipation function is no longer a homogeneous first order function, it is divided into two separate potentials called the force potential and flow potential.

The force potential $z = z\left(\sigma_{ij}, \alpha_{ij}, \dot{\alpha}_{ij}\right)$ serves as the potential of the dissipative generalised stress, χ_{ij}. It is, therefore, written as follows:

$$\chi_{ij} = \frac{\partial z}{\partial \dot{\alpha}_{ij}} \tag{2.43}$$

The dissipation function, *d*, can now be written in the form:

$$d = \left(\frac{\partial z}{\partial \dot{\alpha}_{ij}}\right)\dot{\alpha}_{ij} \tag{2.44}$$

It is noted that the force potential and the flow potential are linked by the Legendre transformation. Thus, the flow potential *w* can be defined as follows:

$$w\left(\sigma_{ij}, \alpha_{ij}, \chi_{ij}\right) = \chi_{ij}\,\dot{\alpha}_{ij} - z = d - z \tag{2.45}$$

Therefore: $\dot{\alpha}_{ij} = \frac{\partial w}{\partial \chi_{ij}}$.

The flow potential function *w*, which is analogous to the yield function *y* in the rate-independent case (see Houlsby and Puzrin, 2002) is not equal to zero due to the fact that *w* is not a homogeneous first order function of the rate of change of internal variables. If *d* is chosen as a homogeneous function of order *n* in the internal variable rates, the force potential can be chosen as *z = d/n* so that $\left(\frac{\partial z}{\partial \dot{\alpha}_{ij}}\right)\dot{\alpha}_{ij} = nz = d$. It is clear to see that when *n* = 1, the above relationship becomes that of rate-independent behaviour.

The incremental relationships are obtained from the above definitions:

$$\dot{\varepsilon}_{ij} = -\frac{\partial^2 g}{\partial \sigma_{ij}\partial \sigma_{kl}}\dot{\sigma}_{kl} - \frac{\partial^2 g}{\partial \sigma_{ij}\partial \alpha_{kl}}\dot{\alpha}_{kl} = -\frac{\partial^2 g}{\partial \sigma_{ij}\partial \sigma_{kl}}\dot{\sigma}_{kl} - \frac{\partial^2 g}{\partial \sigma_{ij}\partial \alpha_{kl}}\frac{\partial w}{\partial \chi_{kl}} \tag{2.46}$$

2.5.2 Multiple-yield-surface hyperplasticity and continuous hyperplasticity

2.5.2.1 Rate-independent solution

The main reasons for the introduction of multiple-yield-surface and continuous yield surface hyperplasticity are the simulation of the smooth transitions between elastic and plastic behaviour (see Puzrin and Houlsby, 2001) and the capture of the hysteretic response with a reasonable accuracy that cannot be obtained by using a single-yield-surface plasticity model. The internal variables α_{ij}, in this case, are replaced by $\alpha^{(n)}_{ij}$ (*n* = 1..*N*). Therefore, the energy and dissipation functions become:

$$g\left(\sigma_{ij}, \alpha_{ij}^{(1)}, ..., \alpha_{ij}^{(N)}\right) = g_1\left(\sigma_{ij}\right) - \sigma_{ij}\sum_{n=1}^{N}\alpha_{ij}^{(n)} + \sum_{n=1}^{N} g_2^{(n)}\left(\alpha_{ij}^{(n)}\right) \tag{2.47}$$

$$d\left(\sigma_{ij}, \alpha_{ij}^{(1)}, ..., \alpha_{ij}^{(N)}, \dot{\alpha}_{ij}^{(1)}, ..., \dot{\alpha}_{ij}^{(N)}\right) = \sum_{n=1}^{N} d^{(n)}\left(\sigma_{ij}, \alpha_{ij}^{(1)}, ..., \alpha_{ij}^{(N)}, \dot{\alpha}_{ij}^{(1)}, ..., \dot{\alpha}_{ij}^{(N)}\right) \tag{2.48}$$

By using the degenerate of the Legendre transformation for the dissipation function *d*, for each *n* = 1,…, *N*, the *n*th yield function is:

$$y^{(n)} = y^{(n)}\left(\sigma_{ij}, \alpha_{ij}^{(1)}, \dots, \alpha_{ij}^{(N)}, \chi_{ij}^{(n)}\right) = 0 \tag{2.49}$$

The dissipative generalised stress $\chi_{ij}^{(n)}$ corresponding to the *n*th yield function is defined as:

$$\chi_{ij}^{(n)} = \frac{\partial d^{(n)}\left(\sigma_{ij}, \alpha_{ij}^{(1)}, \dots, \alpha_{ij}^{(N)}, \overset{\bullet}{\alpha}{}_{ij}^{(1)}, \dots, \overset{\bullet}{\alpha}{}_{ij}^{(N)}\right)}{\partial \overset{\bullet}{\alpha}{}_{ij}^{(n)}} \tag{2.50}$$

The flow rule for the *n*th yield surface therefore becomes:

$$\overset{\bullet}{\alpha}{}_{ij}^{(n)} = \frac{\partial d^{(n)}\left(\sigma_{ij}, \alpha_{ij}^{(1)}, \dots, \alpha_{ij}^{(N)}, \overset{\bullet}{\alpha}{}_{ij}^{(1)}, \dots, \overset{\bullet}{\alpha}{}_{ij}^{(N)}\right)}{\partial \chi_{ij}^{(n)}} \tag{2.51}$$

By invoking the consistency condition for every single yield surface, $\overset{\bullet}{y}{}^{(n)} = 0$, the incremental response can be written as follows:

$$\overset{\bullet}{\varepsilon}_{ij} = -\frac{\partial^2 g_1}{\partial \sigma_{ij} \partial \sigma_{kl}} \overset{\bullet}{\sigma}_{kl} + \sum_{n=1}^{N} \lambda^{(n)} \frac{\partial y^{(n)}}{\partial \chi_{ij}^{(n)}} \tag{2.52}$$

where $\lambda^{(n)}$ is the non negative scalar multiplier corresponding to the *n*th yield function and is derived from the consistency condition similar to those of single-yield-surface model.

The continuous yield surface plasticity can be derived in a similar way. The internal variables, now, become the internal functions $\hat{\alpha}_{ij}(\eta)$ and their rates become $\overset{\bullet}{\hat{\alpha}}_{ij}(\eta)$. Following this, the free energy function and dissipation function become functionals:

$$g\left[\sigma_{ij}, \hat{\alpha}_{ij}\right] = g_1\left(\sigma_{ij}\right) - \sigma_{ij} \int_Y \hat{\alpha}_{ij}(\eta) d\eta + \int_Y \hat{g}_2\left(\hat{\alpha}_{ij}(\eta), \eta\right) d\eta \tag{2.53}$$

$$d\left[\sigma_{ij},\hat{\alpha}_{ij},\dot{\hat{\alpha}}_{ij}\right]=\int_Y \hat{d}\left(\sigma_{ij},\hat{\alpha}_{ij}(\eta),\dot{\hat{\alpha}}_{ij}(\eta),\eta\right)d\eta \tag{2.54}$$

Where Y is the domain of η.

The derivation from the above two functions can be seen in Puzrin and Houlsby (2001) and will not be presented here for brevity. As the final result of this process, the incremental response is expressed as follows:

$$\dot{\varepsilon}_{ij}=-\frac{\partial^2 g_1}{\partial\sigma_{ij}\partial\sigma_{kl}}\dot{\sigma}_{kl}+\int_Y \dot{\hat{\lambda}}(\eta)\frac{\partial\hat{y}}{\partial\hat{\chi}_{ij}}d\eta \tag{2.55}$$

2.5.2.2 Rate-dependent solution

As mentioned in section 2.5.2.1, in the case of using multiple-yield-surface model or continuous plasticity model, in order to calculate the multiplier $\lambda^{(n)}$ for each yield function $y^{(n)}$, the consistency conditions of all yield surfaces must be satisfied at the same time. For instance in the case of multiple-yield-surface model, this requirement could be expressed as a system of equations as:

$$\begin{cases}\dot{y}^{(1)}\left(\sigma_{ij},\alpha_{ij}^{(1)},\ldots,\alpha_{ij}^{(N)},\chi_{ij}^{(1)}\right)=0\\ \ldots\\ \dot{y}^{(n)}\left(\sigma_{ij},\alpha_{ij}^{(1)},\ldots,\alpha_{ij}^{(N)},\chi_{ij}^{(n)}\right)=0\\ \ldots\\ \dot{y}^{(N^*)}\left(\sigma_{ij},\alpha_{ij}^{(1)},\ldots,\alpha_{ij}^{(N)},\chi_{ij}^{(N^*)}\right)=0\end{cases} \tag{2.56}$$

where N^* is the number of the yield surfaces which have been activated.

This leads to a very complicated numerical procedure. In particular, in order to ensure that the load point always lie exactly on the intersection of the yield surfaces activated, the system of equations in Eq. (2.56) must be satisfied completely at every single load step. A numerical correction to satisfy this consistency condition must be implemented for all the yield surfaces activated instead of only for one yield surface as in single-yield-surface model. This work could require a very long calculation time and it may lead to unstable numerical results. These difficulties are not significant in the case of using single-yield-surface model but they become critical when the multiple-yield-surface or continuous plasticity model is applied.

The above obstacle can be overcome by using the rate-dependent solution. The consistency condition for the yield surface is no longer required therefore Eq. (2.56) can be neglected. The framework of rate-dependent solution has been reviewed in section 2.5.1.3 and can be found in Puzrin and Houlsby (2003) for more details.

The force potential *w* in the case of using multiple-yield-surface model becomes:

$$w = w\left(\sigma_{ij}, \alpha_{ij}^{(1)}, \ldots, \alpha_{ij}^{(N)}, \chi_{ij}^{(1)}, \ldots, \chi_{ij}^{(N)}\right) \qquad (2.57)$$

The incremental response is:

$$d\varepsilon_{ij} = -\frac{\partial^2 g}{\partial\sigma_{ij}\partial\sigma_{kl}} d\sigma_{kl} - \sum_{n=1}^{N} \frac{\partial^2 g}{\partial\sigma_{ij}\partial\alpha_{kl}^{(n)}} \frac{\partial w}{\partial\chi_{kl}^{(n)}} dt \qquad (2.58)$$

In the case of using continuous plasticity model, Puzrin and Houlsby (2003) have given the force potential as:

$$w\left[\sigma_{ij}, \hat{\alpha}_{ij}, \dot{\hat{\alpha}}_{ij}\right] = \int_Y \hat{w}\left(\sigma_{ij}, \hat{\alpha}_{ij}, \dot{\hat{\alpha}}_{ij}, \eta\right) d\eta \qquad (2.59)$$

Then the incremental response can be derived as follows:

$$d\varepsilon_{ij} = -\frac{\partial^2 \hat{g}}{\partial\sigma_{ij}\partial\sigma_{kl}} d\sigma_{kl} - \int_Y \frac{\partial^2 \hat{g}}{\partial\sigma_{ij}\partial\alpha_{kl}^{(n)}} \frac{\partial \hat{w}}{\partial\chi_{kl}^{(n)}} dt d\eta \qquad (2.60)$$

Using the rate-dependent solution, the load point can be accepted to lie outside the yield surfaces thus there will be different results obtained from the use of rate-dependent and rate-independent solution. However, if the rate effects which relate to the viscosity factor μ and the time increment *dt* are small enough, the rate-dependent solution can mimic the rate-independent solution. Houlsby and Puzrin (2002) have demonstrated this feature.

Although the rate-dependent solution is used mainly for computational convenience, almost all materials in nature reveal the rate-dependent behaviour and soil is not an exception. Therefore, the use of rate-dependent solution can be useful for more realistic models.

2.5.3 Application of the hyperplasticity theory to a force resultant model

In earlier papers (Collins and Houlsby, 1997; Houlsby and Puzrin, 2000), a plasticity theory, named hyperplasticity, which is based on thermodynamics has been described. Afterwards, this theory has been extended in two directions. Firstly, the concept of internal variables is extended to that of finite numbers of internal variables (for multiple-yield-surface plasticity) and infinite numbers of internal variables (for continuous plasticity). The purpose of this work is to describe the smooth transitions between elastic and elastic-plastic behaviour (Purzin and Houlsby, 2001a). Secondly, Houlsby and Puzrin (2002) have proposed the concept of rate-dependent behaviour to the thermodynamic framework. From this development of the hyperplasticity theory, which has also been reviewed briefly in sections 2.5.1 and 2.5.2, it can be found that a thermodynamic framework for modelling of constitutive behaviour of both rate-independent and rate-dependent plastic materials has been established in terms of stress and strain tensors.

In a similar way to the development of the hyperplasticity theory, a force resultant model can be established. In this case, the whole system of the foundation is treated in macroscopic terms and is expressed in terms of force resultants. Therefore, the plastic displacement components of the foundation, α_i, can be referred as the internal state variables instead of the plastic strain α_{ij}. The true stress space, which is described as σ_{ij} in the thermodynamic framework, can be represented by the load space σ_i. This means that the loads will play the role of true stresses in this model. The subscript i represents the six degree-of-freedom in three-dimensional space. The entropy s and the temperature θ are not considered in the foundation model. All the definitions of variables in a force resultant model are the same with those of hyperplasticity theory but in terms of vectors.

This strategy of the development of a force resultant model will be applied for the development of the ISIS model which is the main work of this study.

2.6 Summary

In this chapter, the fundamental literature has been presented briefly. The two main aspects that the author would like to mention as the goals of this research are the analysis of a novel type of footing, called caisson, and the new derivation of plasticity model, called hyperplasticity. The analyses of other types of circular shallow foundation such as circular flat and jack-up footing in the case of monotonic loading have been discussed in previous research.

The background for the development of the new model of shallow foundation for offshore wind turbine has been presented in this chapter. There are three main steps that have been considered in order for a plasticity model to be established:

- The elastic solution applied for the elastic response of the model (section 2.2).
- The bearing capacity formulations that are keys to determining the yield function for plastic behaviour (section 2.3).
- The new expression of the plasticity theory that is the base to derive the plastic response for the new model (section 2.5).

The two first steps above have been well-established and will be used as the starting point to this study. This research will be continued with the developing of the new plasticity model, which is the so-called ISIS model using hyperplasticity theory.

CHAPTER 3

SINGLE-YIELD-SURFACE HYPERPLASTICITY MODEL

3.1 Introduction

This chapter presents the development of a single-yield-surface hyperplastic formulation for modelling of circular shallow foundations for offshore wind turbines. The three types of footing considered in this chapter are circular flat footing, spudcan and caisson. Although spudcan is not relevant to the wind turbine case, it is analysed in this study to illustrate the model capacity. Four main tasks are completed in this chapter:

(a) A numerical model called ISIS is established for the six-degree-of-freedom problem with the six general components of external forces. Based on the experimentally determined yield functions of both Model B (for clay) and Model C (for sand), a modified yield function is suggested for a caisson footing. The explicit incremental response for the rate-independent case is established by using the yield function instead of the dissipation function.

(b) The rate-dependent solution is introduced. This approach extends the work on rate-independent materials to give an alternative solution. The dissipation function is no longer first-order homogeneous. It is divided into two separate potentials: force potential and flow potential. The incremental response is established by using the flow potential involving the yield function of the work (a).

(c) The application of the vertical bearing capacity of caissons in the ISIS model is presented. A mathematical treatment used to adjust the theoretical evaluation of vertical bearing capacity of caisson is discussed. In addition, the principle of the application of suction in the model is described.

(d) Some numerical examples are performed to demonstrate the capabilities of the single-yield-surface hyperplasticity model (ISIS) in reproducing the behaviours of Model B and Model C. This work also shows the single-yield-surface ISIS model as the starting point for the modelling of shallow foundations under cyclic loading.

There are several parameters and experimental factors which are introduced in this chapter. The values chosen for the numerical examples are preliminary. A detailed discussion about the choice of these values and their relationships is not given in this chapter but is presented later in chapter 5 – Parametric study.

3.2 Conventions of foundation

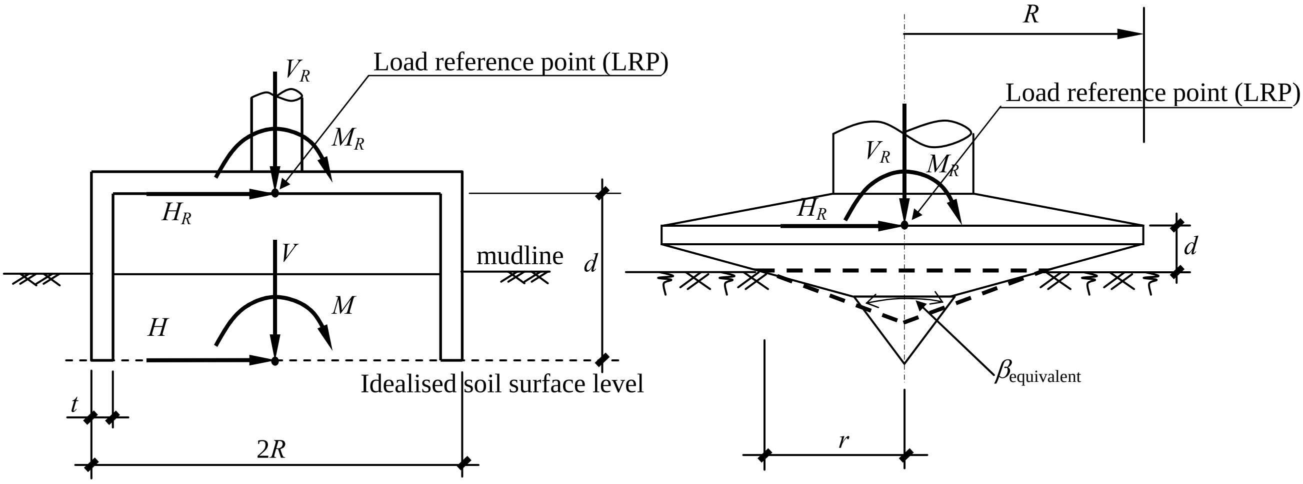

(a) Caisson footing

(b) Spudcan footing

Figure 3.1 Foundation geometry

Initially, it is necessary to introduce the geometry of footing and the convention system for forces and corresponding displacements. The geometries of circular flat footings and spudcans have been described in Martin (1994) and many other previous studies.

Therefore, this section just focuses on the description of the conventions of force directions and displacement systems. In the case of caisson footing, there are essentially two parts: a circular top plate and a perimeter skirt. Figure 3.1a shows the geometry of caisson in which d is the distance between the load reference point (LRP) and an idealised soil surface at the depth of the skirt's tip. In both foundations, the position of the LRP is arbitrary and depends on the preference of the analyst. However, for convenience, the position of the LRP can be taken at the joint between the caisson and the support structure as shown in Figure 3.1a. Meanwhile, in the case of a spudcan footing, the LRP can be located as shown in Figure 3.1b. Obviously, in the case of a circular flat footing, the LRP can always be at the idealised soil surface level and therefore $d = 0$.

The displacement vector at soil surface level is $\varepsilon_i = (w, u_2, u_3, \omega, \theta_2, \theta_3)$ as shown in Figure 3.2. The components w, u_2, and u_3 are the vertical displacement, horizontal displacement in 2-axis and horizontal displacement in 3-axis respectively. The components ω, θ_2, and θ_3 are the rotational displacement about 1-axis, 2-axis and 3-axis respectively. The corresponding displacements at the LRP are given as follows:

$$\begin{aligned} w &= w_R \\ u_2 &= u_{2R} + d\theta_{3R} \\ u_3 &= u_{3R} - d\theta_{2R} \\ \omega &= \omega_R \\ \theta_2 &= \theta_{2R} \\ \theta_3 &= \theta_{3R} \end{aligned} \tag{3.1}$$

Figure 3.3 shows the convention for the force system. The forces V_R, H_{2R}, H_{3R}, Q_R, M_{2R}, M_{3R} are applied at the LRP. However, in the analysis, it is convenient to use the force vector $\sigma_i = (V, H_2, H_3, Q, M_2, M_3)$ at the soil surface level. The radius r of the footing at the soil surface level depends on the type of footing considered. In the case of a flat footing or a caisson, r is equal to R. Otherwise, in the case of a spudcan, r is smaller than R if $d > 0$ and r is equal to R when $d = 0$.

The relationship between the two force systems is described as follows:

$$\begin{aligned} V &= V_R \\ H_2 &= H_{2R} \\ H_3 &= H_{3R} \\ Q &= Q_R \\ M_2 &= M_{2R} + dH_{3R} \\ M_3 &= M_{3R} - dH_{2R} \end{aligned} \tag{3.2}$$

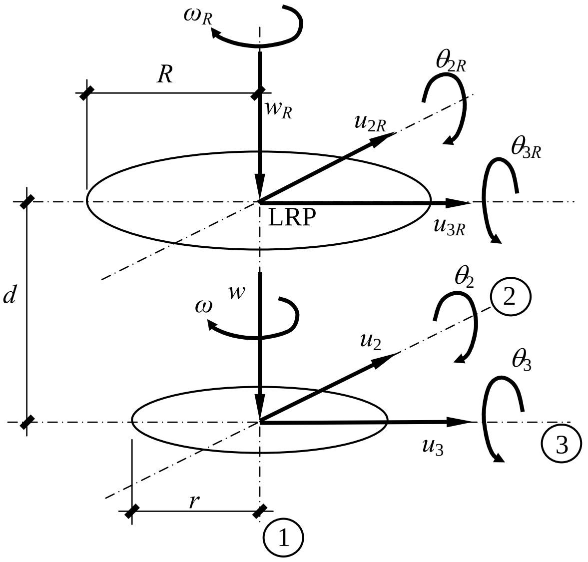

Figure 3.2 Convention for displacement system

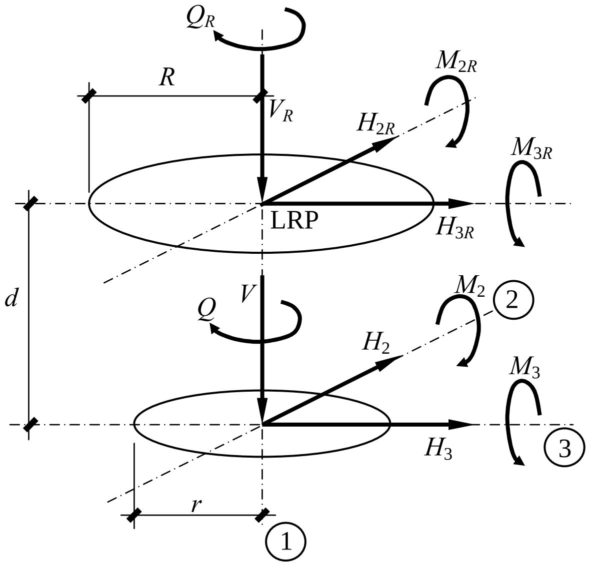

Figure 3.3 Convention for force system

From now on, by using the relationships in Eq. (3.1) and Eq. (3.2), force results or displacement results can be obtained through the load reference point. Thus, the forces or the displacements used in the following sections are at the load reference point. For simplicity, the subscript R is taken out of the force and the displacement variables.

3.3 Single-yield surface hyperplasticity model using rate-independent behaviour

Based on the hyperplasticity framework (Houlsby and Puzrin, 2000), a mechanical model can be derived from two scalar functions: the Gibbs free energy g, and either the dissipation function d or the yield function y. In this study, the yield function y is used.

3.3.1 Free energy function and definitions of internal state variables for the foundation using the macro element concept

This section discusses the application of the internal variables and the choice of the Gibbs free energy function in the case of a circular foundation under a six-degree-of-freedom combined loading. As mentioned in section 2.5.3, the internal state variables, α_i, represent the plastic displacements of the foundation. The true stress space is replaced by the load space σ_i.

There are six components of plastic displacement corresponding to six degrees of freedom in three-dimensional analysis. These components are $\alpha_i = (\alpha_V, \alpha_{H2}, \alpha_{H3}, \alpha_Q, \alpha_{M2}, \alpha_{M3})$ and represent the vertical, horizontal and rotational displacements in the chosen orthogonal coordinate system. The subscripts of these variables define the force components and the axes that they refer to.

The Gibbs free energy still has the original style as in Houlsby and Puzrin (2000b). For a model without elastic-plastic coupling, it can be rewritten as:

$$g = g_1(V, H_2, H_3, Q, M_2, M_3) - V\alpha_V - H_2\alpha_{H2} - H_3\alpha_{H3} - Q\alpha_Q - M_2\alpha_{M2} - M_3\alpha_{M3} + g_2(\alpha_i) \tag{3.3}$$

The first term g_1 represents elastic response of the foundation under the combined loading. This response is based on the elastic solution of Bell (1991) or Ngo-Tran (1996) or Doherty (2004) and has been extended to a six-degree-of-freedom solution as mentioned in section 2.2.1. Based on the matrix form of the elastic solution in Eq. (2.4), the general formulation of g_1 in three-dimensional analysis can be expressed as follows:

$$g_1 = -\frac{V^2}{2K_1} - \frac{K_2H_2^2}{2D} - \frac{K_2H_3^2}{2D} - \frac{Q^2}{2K_5} - \frac{K_3M_2^2}{2D} - \frac{K_3M_3^2}{2D} + \frac{K_4H_3M_2}{D} - \frac{K_4H_2M_3}{D} \quad (3.4)$$

in which the definitions of the elastic stiffness factors K_1, K_2, K_3, K_4 and K_5 are similar to those in Eq. (2.3) and Eq. (2.6), except that they are modified by the effects of the distance d between the LRP and the soil surface level as follows:

$$K_1 = 2GRk_1 \quad (3.5)$$

$$K_2 = GR^3k_2 - 8GR^2k_4d + 2GRd^2k_3 \quad (3.6)$$

$$K_3 = 2GRk_3 \quad (3.7)$$

$$K_4 = 4GR^2k_4 - 2GRk_3d \quad (3.8)$$

$$K_5 = 8GR^3k_5 \quad (3.9)$$

$$D = K_2K_3 - K_4^2 \quad (3.10)$$

where G is the shear modulus of the soil; k_1, k_2, k_3, k_4 and k_5 are the dimensionless stiffness coefficients obtained from the elastic solutions of different kinds of footings. Ngo-Tran (1996) has proposed the values of these elastic coefficients for spudcan and flat footing. Doherty *et al.* (2004) have given an elastic solution for caisson foundation in which the relation between the elastic stiffness of the caisson itself and the soil has been taken into account.

The term $g_2(\alpha_i)$, which is a function of plastic displacements, defines the type of kinematic hardening of the plastic response. In this research, there are two types of hardening that will be used: isotropic hardening and mixed kinematic-isotropic hardening. The isotropic hardening is discussed firstly in a single-yield-surface model which is presented in this section. The mixed isotropic-kinematic hardening will be described in the next chapter for the multiple-yield-surface model. Therefore, in what follows, it is suitable simply to take $g_2 = 0$ since the single-yield-surface model does not undergo kinematic hardening.

In the thermodynamic framework (Houlsby and Puzrin, 2000), the elastic response, g_1, is completely independent of the internal variables. In this study, however, g_1 cannot be considered independently of the plastic displacements, which play the role of internal variables. Indeed, as shown in Eq. (3.4), the g_1 term includes the elastic stiffness factors $K_i \left(i = 1 \rightarrow 5\right)$. These factors, as defined in Eq. (3.5) to Eq. (3.9), involve the radius R, the shear modulus G and the elastic stiffness coefficients $k_i \left(i = 1 \rightarrow 5\right)$. The radius R and the G value concerning the elastic stiffness of soil depend on the depth, which is representative of the vertical plastic displacement α_V of the foundation. The elastic stiffness coefficients k_i are also calculated from the depth of footing (see Ngo-Tran, 1996 or Doherty et al., 2004). All these factors are combined in the K_i factors, leading to the dependence of the g_1 term on the displacement α_V. In addition, from the definitions of thermodynamic framework which has been explained by Houlsby and Purzin (2000), the orthogonality leads to $\chi_i = \overline{\chi}_i$. Therefore, the generalised dissipative forces $\chi_i = \left(\chi_V, \chi_{H2}, \chi_{H3}, \chi_Q, \chi_{M2}, \chi_{M3}\right)$ can be defined as follows:

$$\chi_V = \overline{\chi}_V = -\frac{\partial g}{\partial \alpha_V} = -\frac{\partial g_1}{\partial \alpha_V} + V \tag{3.11}$$

$$\chi_{H2} = \overline{\chi}_{H2} = -\frac{\partial g}{\partial \alpha_{H2}} = H_2 \tag{3.12}$$

$$\chi_{H3} = \overline{\chi}_{H3} = -\frac{\partial g}{\partial \alpha_{H3}} = H_3 \tag{3.13}$$

$$\chi_Q = \overline{\chi}_Q = -\frac{\partial g}{\partial \alpha_Q} = Q \tag{3.14}$$

$$\chi_{M2} = \overline{\chi}_{M2} = -\frac{\partial g}{\partial \alpha_{M2}} = M_2 \tag{3.15}$$

$$\chi_{M3} = \overline{\chi}_{M3} = -\frac{\partial g}{\partial \alpha_{M3}} = M_3 \tag{3.16}$$

The back forces $\rho_i = (\rho_V, \rho_{H2}, \rho_{H3}, \rho_{M2}, \rho_{M3}, \rho_Q)$ which are the differences between true forces σ_i and corresponding generalised forces χ_i are in turn expressed as functions of the internal variables α_i as follows:

$$\rho_V = V - \overline{\chi}_V = V + \frac{\partial g}{\partial \alpha_V} \tag{3.17}$$

$$\rho_{H2} = H_2 - \overline{\chi}_{H2} = H_2 + \frac{\partial g}{\partial \alpha_{H2}} \tag{3.18}$$

$$\rho_{H3} = H_3 - \overline{\chi}_{H3} = H_3 + \frac{\partial g}{\partial \alpha_{H3}} \tag{3.19}$$

$$\rho_Q = Q - \overline{\chi}_Q = Q + \frac{\partial g}{\partial \alpha_Q} \tag{3.20}$$

$$\rho_{M2} = M_2 - \overline{\chi}_{M2} = M_2 + \frac{\partial g}{\partial \alpha_{M2}} \tag{3.21}$$

$$\rho_{M3} = M_3 - \overline{\chi}_{M3} = M_3 + \frac{\partial g}{\partial \alpha_{M3}} \tag{3.22}$$

Nevertheless, for the time being, the isotropic hardening is applied, which means that there is no translation of the yield surface in the force space. Therefore, in the case of using isotropic hardening, the back forces ρ_i are zero except the vertical component ρ_V because of the dependence of the elastic response on the depth of footing as expressed in Eq. (3.11).

3.3.2 Yield function

In the conventional approach to plasticity, the plastic behaviour of a material depends on three main items: the yield function, the flow rule and the hardening rule. The yield function defines of the boundary of the zone in which an elastic response exists. The flow rule represents the incremental response of the plastic behaviour. The hardening rule expresses the expansion or the contraction of the yield surface. This section presents the discussion about the first item: yield function.

In the hyperplasticity framework (Houlsby and Puzrin, 2000), for a rate-independent material, the yield function is the singular Legendre transform of the dissipation function, which is a function of the rate of change of the internal state variables $\dot{\alpha}_{ij}$ (corresponding to $\dot{\alpha}_i$ in this study). Thus, by using the macro-element idea, the yield function can be expressed as a function of the generalised dissipative forces χ_i. Furthermore, Collins and Houlsby (1997) have demonstrated that the appearance of true force components in the yield function leads to a non-associated flow rule known as the appropriate flow rule for the foundation behaviour. From the definition of the non-associated flow rule, there are differences between the partial differentials of the yield function with respect to the true force space and those with respect to the generalised force space. In other words, the flow vectors and the normal vectors of the yield surface do not coincide. The differences between these vectors depend on the relationship between the true and the generalised forces in the yield functions. Consequently, it is necessary to introduce new factors to conduct the interpolation between these two force spaces in the yield function. These factors called association factors give the ability to adjust the non-associated characteristics of the model to be more realistic.

Therefore, to establish the yield functions for circular flat footing, spudcan and caisson, there are two main stages implemented. Firstly, based on the yield functions which have been used in Model B (Martin, 1994) and Model C (Cassidy, 1999), a new expression of the yield function for circular flat footings and spudcans is proposed to include the non-associated flow rule and also to be available for six-degree-of-freedom problems. Secondly, from this result, the yield function for caisson is derived with certain modifications to include the special aspects of caissons.

3.3.2.1 Yield function for circular flat footing and spudcan

In Model B and Model C for the analysis of spudcan and circular flat footing either on clay or on sand, Martin (1994) and Cassidy (1999) have proposed the same forms for the yield function as in Eq. (2.20). In order to describe the non-associated flow rule, these two models have to use an additional assumption such as the association parameter ζ for the volumetric term as in Eq. (2.29) (Model B) or the potential function g as in Eq. (2.30) (Model C). In this study, by using hyperplasticity theory, these further assumptions are no longer necessary. The appearance of both true and generalised dissipative forces and their relationship can be used to derive the non-associated flow rules within only one yield function. Certainly, there are many options for the relationship between σ_i and χ_i. However, for simplicity, the linear relationship is chosen in this research.

The experimental yield function of either Model B or Model C in true force space, $y(\sigma_i, w_p)$, now becomes the yield function in both true and generalised dissipative force space, $y(\chi_i, \sigma_i, w_p)$. The Eq. (2.20) can be rewritten as follows:

$$y(\chi_i, \sigma_i, w_p) = \sqrt{h^2 + m^2 - 2ehm} - S\beta_{12} |v_1|^{\beta_1} |1 - v_2|^{\beta_2} = 0 \qquad (3.23)$$

in which:

$$S = \mathrm{sgn}\left[v_1\left(1 - v_2\right)\right];\ \beta_{12} = \frac{\left(\beta_1 + \beta_2\right)^{\left(\beta_1 + \beta_2\right)}}{(\beta_1)^{\beta_1}(\beta_2)^{\beta_2}};\ e = e_1 + e_2\left(\frac{V}{V_0}\right)\left(\frac{V}{V_0} - 1\right)$$

and

$$v_1 = \frac{a_{V1}\chi_V + (1 - a_{V1})V}{V_0} \tag{3.24}$$

$$v_2 = \frac{a_{V2}\chi_V + (1 - a_{V2})V}{V_0} \tag{3.25}$$

$$m = \frac{a_M\chi_m + (1 - a_M)M}{2Rm_0V_0} \tag{3.26}$$

$$h = \frac{a_H\chi_H + (1 - a_H)H}{h_0V_0} \tag{3.27}$$

V_0 is the bearing capacity of the foundation at the penetration depth considered. The six parameter values obtained from experimental data (see Martin and Houlsby, 2001) are still used for clay: $h_0 = 0.127$, $m_0 = 0.083$, $e_1 = 0.518$, $e_2 = -1.180$, $\beta_1 = 0.764$ and $\beta_2 = 0.882$. For sand, these parameters can be: $h_0 = 0.116$, $m_0 = 0.086$, $e_1 = -0.2$, $e_2 = 0.0$, $\beta_1 = 0.9$ and $\beta_2 = 0.99$ (see Cassidy, 1999). The factors a_{V1}, a_{V2}, a_M and a_H are the association factors which play the role of the interpolation between the true forces *V*, *M*, *H* and the generalised dissipative forces χ_V, χ_M, χ_H. The values of these association factors should be chosen from 0 to 1 so that the equations from Eq. (3.23) to Eq. (3.27) represent an interpolation between the true and generalised forces. The projections of the yield surface presented by Eq. (3.23) in plane (*V*:*H*) and (*V*:*M*) are shown in Figure 3.4, in which the factor α which determines the position of the largest cross section of the yield surface can be calculated as: $\alpha = \dfrac{\beta_1}{\beta_1 + \beta_2}$. Figure 3.4 shows the projection of the yield function expressed in Eq. (3.23) in true force space.

Eq. (3.23) shows the yield function using the hyperplasticity expression for the cases of circular flat footing and spudcan under planar combined loading either on clay or on sand. In fact, if the association factors a_{V1}, a_{V2}, a_M and a_H are all equal to zero, the yield function in Eq. (3.23) will be back to the form of that in Model B and Model C as in Eq. (2.20). In another extreme condition, if these association factors are all equal to one, the yield function becomes purely dependent on the generalised dissipative forces and reveals the associated plasticity behaviour. This matter has been explained in the hyperplasticity framework (see Houlsby and Puzrin, 2000).

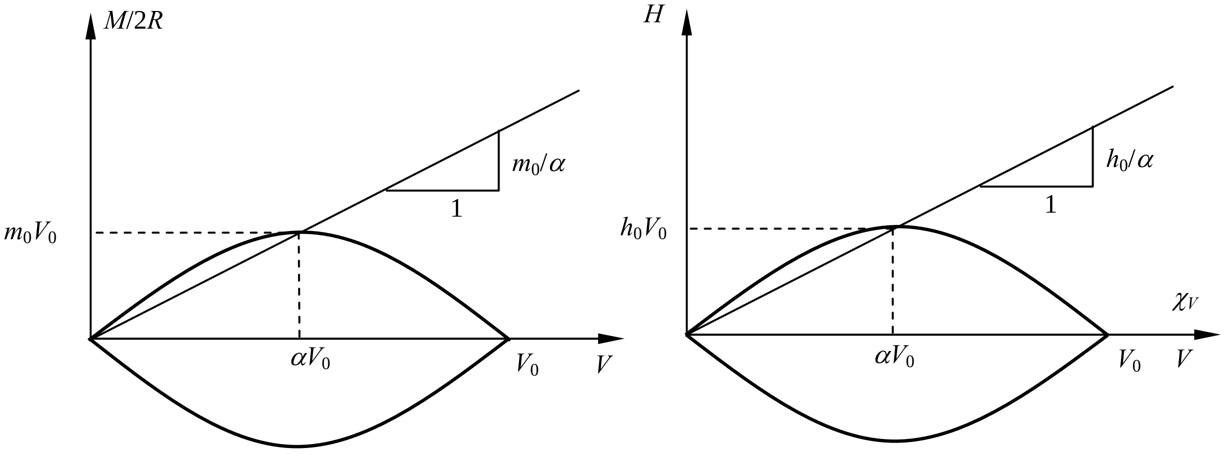

(a) Yield function in (V:M)

(b) Yield function in (V:H)

Figure 3.4 Projections of the yield function in true force space

Besides, comparing with the Eq. (2.20), there are some modifications introduced in the Eq. (3.23): the appearance of the square root term, the absolute value forms and the changes in the definitions of v_1, v_2, h and m.

Firstly, the purpose of changing the form of the yield function as in the Eq. (3.23) is to ensure that the numerical value of the yield function is always negative inside the yield surface, positive outside the yield surface and zero on the yield surface. By using the form of the yield function as in Eq. (2.20) these conditions could not be satisfied because of the non-integer values of the exponents β_1 and β_2.

Secondly, the definitions of v_1, v_2, h and m as from Eq. (3.24) to Eq. (3.27) allow the appearance of both the generalised forces χ_i and the true forces σ_i in the yield function. The non-associated flow rule can therefore be derived from this form of the yield function.

In order to extend to the six-degree-of-freedom problem, the yield function as in Eq. (3.23) is modified and can be written as follows:

$$y(\chi_i, \sigma_i, w_p) = t - S\beta_{12}|v_1|^{\beta_1}|1-v_2|^{\beta_2} = 0 \tag{3.28}$$

in which:

$$S = \mathrm{sgn}[v_1(1-v_2)];\ \beta_{12} = \frac{(\beta_1+\beta_2)^{(\beta_1+\beta_2)}}{(\beta_1)^{\beta_1}(\beta_2)^{\beta_2}};$$

and

$$t = \sqrt{h_2^2 + h_3^2 + m_2^2 + m_3^2 + q^2 - 2e(h_2 m_3 - h_3 m_2)} \tag{3.29}$$

Further definitions are expressed as follows:

$$v_1 = \frac{a_{V1}\chi_V + (1-a_{V1})(V-\rho_V)}{V_0} \tag{3.30}$$

$$v_2 = \frac{a_{V2}\chi_V + (1-a_{V2})(V-\rho_V)}{V_0} \tag{3.31}$$

$$h_2 = \frac{a_H\chi_{H2} + (1-a_H)H_2}{h_0 V_0} \tag{3.32}$$

$$h_3 = \frac{a_H\chi_{H3} + (1-a_H)H_3}{h_0 V_0} \tag{3.33}$$

$$m_2 = \frac{a_M(\chi_{M2} + d\chi_{H3}) + (1-a_M)(M_2 + dH_3)}{2Rm_0 V_0} \tag{3.34}$$

$$m_3 = \frac{a_M\left(\chi_{M3} - d\chi_{H2}\right) + \left(1 - a_M\right)\left(M_3 - dH_2\right)}{2Rm_0V_0} \tag{3.35}$$

$$q = \frac{a_Q\chi_Q + (1 - a_Q)Q}{2Rm_0V_0} \tag{3.36}$$

In which the parameters a_{V1}, a_{V2}, a_H, a_M and a_Q are again the associate factors which have values inside [0.0, 1.0]; the parameters h_0, m_0 which determine the sizes of the yield surface in horizontal and moment directions can take the values as in Model B (for clay) or Model C (for sand); the additional parameter q_0 which determines the size of the yield surface in the torsion direction can be temporarily chosen as 0.1; the shape parameters e_1, e_2, β_1 and β_2 which determine the shape of the yield surface in the cross section and the smooth peaks in the vertical direction can also take the values as in either Model B or Model C;

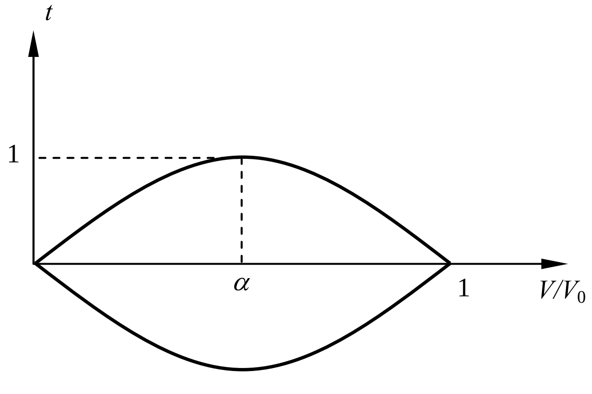

Figure 3.5 Yield function in six-degree-of-freedom problem for circular and spudcan footing

In the definitions of m_2 and m_3 as in Eq. (3.34) and Eq. (3.35), d is the distance between the point used to apply the loads for the model analysis and the LRP used to apply the internal forces transferred from the superstructure. The additional effects in moment loadings coming from the products of horizontal loads and this distance, as has been expressed in Eq. (3.2), are taken into account in Eq. (3.34) and Eq. (3.35).

The yield function in six-degree-of-freedom problem can be roughly shown in Figure 3.5. In which *t* is the square root term in Eq. (3.28).

3.3.2.2 Yield function for caisson footing

In the case of a caisson footing, in serviceability conditions, the interaction between the perimeter skirt and the soil results in a tensile bearing capacity. This is a difference compared with either a circular flat footing or spudcan. Particularly, in the case of the leeward leg of a multi-caisson foundation, the vertical load *V* can tend to zero or become negative, but the whole structure is still stable. It is therefore necessary to explore a new yield function to be able to reflect this tensile bearing capacity of the caisson foundation.

Based on the yield function for a circular footing and spudcan as in Eq. (3.28), a modified version of this function is proposed incorporating a tensile capacity factor t_0 to take into account the tensile bearing capacity V_t. Essentially, this tensile capacity factor can be defined in term of a ratio between tensile bearing capacity V_t and the compression bearing capacity V_0. Thus, the proposed yield function can be rewritten as follows:

$$y = t - \beta_{12} S \left| v_1 + t_0 \right|^{\beta_1} \left| 1 - v_2 \right|^{\beta_2} = 0 \tag{3.37}$$

in which: $S = \operatorname{sgn}\left[(v_1 + t_0)(1 - v_2) \right]$; $\beta_{12} = \dfrac{\left(\dfrac{\beta_1 + \beta_2}{1 + t_0} \right)^{\beta_1 + \beta_2}}{(\beta_1)^{\beta_1} (\beta_2)^{\beta_2}}$;

Further definitions follow below:

$$t = \sqrt{h_2^2 + h_3^2 + m_2^2 + m_3^2 + q^2 + 2e(h_2 m_3 - h_3 m_2)} \tag{3.29bis}$$

$$t_0 = \frac{V_t}{V_0} \tag{3.38}$$

The definitions of v_1, v_2, h_2, h_3, m_2, m_3 and q in Eq. (3.36) and Eq. (3.29bis) are the same as from Eq. (3.30) to Eq. (3.36). It is convenient to note that the vertical load at which the maximum dimension of the yield surface is achieved is:

$$\frac{V}{V_0} = \alpha = \frac{\beta_1 - \beta_2 t_0}{\beta_1 + \beta_2} \tag{3.39}$$

This leads to an equation for the parameters β_1 and β_2:

$$\frac{\beta_1}{\beta_2} = \frac{t_0 + \alpha}{1 - \alpha} \tag{3.40}$$

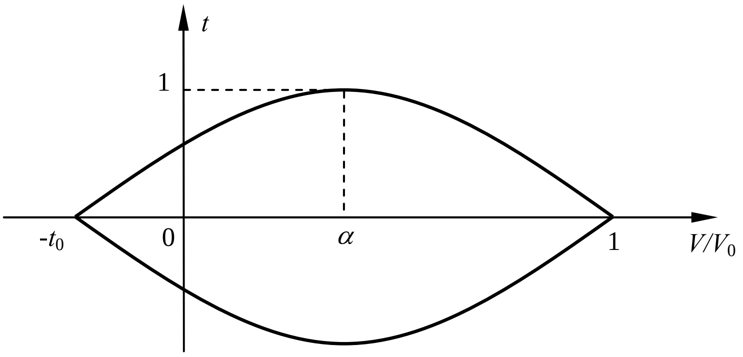

Figure 3.6 Yield function in six-degree-of-freedom problem for caisson footing

The yield surface using Eq. (3.36) is shown in Fig. (3.6). There is an extension of the yield surface to the negative part of the horizontal axis corresponding to the tensile capacity of the caisson. The parameters h_0, m_0 and q_0 still are the shape factors which determine the size of the yield surface in the moment, horizontal and torsion directions. They are all experimental factors coming from a series of tests for caisson implemented at Oxford University (Villalobos, personal communication), Villalobos *et al.* (2004c) and Villalobos *et al.* (2005). Particularly, the typical values of h_0, m_0 and q_0 for a caisson with (L/R = 1) are 0.15, 0.337 and 0.1 respectively.

The calculation procedure of the tensile bearing capacity V_t can be based on that of the vertical bearing (compression) capacity V_0. As mentioned in section 2.3.2, the vertical bearing capacity of the caisson foundation includes three components which are the vertical bearing capacity of the top flat plate, the friction forces along the surface of the perimeter skirt and the vertical end bearing capacity of the rim of the skirt. In the case of tensile loading (negative vertical load), the vertical bearing capacity of the top flat plate and of the rim of skirt will vanish and the only remaining force resultant is the friction on the skirt. Therefore, it could be simple to take the friction force on the skirt as the tensile capacity of the caisson footing. However, from the Oxford University test results, the tensile capacity V_t is not completely the same as the friction force calculated by using the procedure in Byrne and Houlsby (2004a, 2004b). From experiments, Kelly *et al.* (2004, 2005) have pointed out that there is a complicated variation of V_t with α_V. This matter needs more investigation but this is beyond the scope of this study. For the time being, the tensile capacity V_t is accepted as a fraction taken from V_0. Therefore it could be simple to take t_0 as a constant. From the test observations (personal information from Fellipe Villalobos, Oxford University), the value of t_0 can be chosen roughly from 0.06 to 0.1088 for a typical caisson with $L/D = 0.5$.

It is clear that the yield function in Eq. (3.37) can be applied easily for both caisson and spudcan footing as well as for circular flat footing. In fact, when t_0 is equal to zero, the yield function in Eq. (3.37) goes back to the form of that in Eq. (3.28). Thus, from this time, the yield function in Eq. (3.37) will be used as the general form for the analysis.

3.3.3 Flow rule

Following the introduction of the yield surface, the next item which should be discussed for a plasticity model is the flow rule. The main role of the flow rule is to present ratios between plastic displacement increments. Based on the hyperplasticity theory, the core of the calculation of the flow rule for rate-independent materials is the product of differentials of the yield function with respect to the generalised dissipative forces χ_i and a positive scalar multiplier λ (see Puzrin and Houlsby, 2001). The general expression of the flow rule is:

$$\dot{\alpha}_i = \lambda \frac{\partial y}{\partial \chi_i} \tag{3.41}$$

where $\dot{\alpha}_i$ is the rate of change of the plastic displacements.

This is the difference between the conventional plasticity theory and hyperplasticity theory. In conventional plasticity theory, $\dot{\alpha}_i$ is calculated from the differentials of a potential function which is often different from the yield function. Therefore, it is necessary to propose an additional potential function, and sometimes this function may imply that the model violates the thermodynamic principles. Meanwhile, by using the hyperplasticity concept, there is no need to propose a further potential function. The yield function is in fact the singular Legender transformation of the dissipation function. Therefore, the thermodynamic principles are satisfied, provided that the rate of the dissipative energy $d \geq 0$, which transforms to $\chi_i \frac{\partial y}{\partial \chi_i} \geq 0$. This is always satisfied if (1) y is convex and (2) it contains the origin in χ_i space.

Differentials of the yield surface in generalised stress space will be (after removing the zero terms):

$$\frac{\partial y}{\partial \chi_V} = \frac{\partial y}{\partial v_1}\frac{\partial v_1}{\partial \chi_V} + \frac{\partial y}{\partial v_2}\frac{\partial v_2}{\partial \chi_V} \tag{3.42}$$

$$\frac{\partial y}{\partial \chi_{H2}} = \frac{\partial y}{\partial t}\left(\frac{\partial t}{\partial h_2}\frac{\partial h_2}{\partial \chi_{H2}} + \frac{\partial t}{\partial m_3}\frac{\partial m_3}{\partial \chi_{H2}}\right) \tag{3.43}$$

$$\frac{\partial y}{\partial \chi_{H3}} = \frac{\partial y}{\partial t}\left(\frac{\partial t}{\partial h_3}\frac{\partial h_3}{\partial \chi_{H3}} + \frac{\partial t}{\partial m_2}\frac{\partial m_2}{\partial \chi_{H3}}\right) \tag{3.44}$$

$$\frac{\partial y}{\partial \chi_Q} = \frac{\partial y}{\partial t}\frac{\partial t}{\partial q}\frac{\partial q}{\partial \chi_Q} \tag{3.45}$$

$$\frac{\partial y}{\partial \chi_{M2}} = \frac{\partial y}{\partial t}\frac{\partial t}{\partial m_2}\frac{\partial m_2}{\partial \chi_{M2}} \tag{3.46}$$

$$\frac{\partial y}{\partial \chi_{M3}} = \frac{\partial y}{\partial t}\frac{\partial t}{\partial m_3}\frac{\partial m_3}{\partial \chi_{M3}} \tag{3.47}$$

In this case, since the isotropic hardening is used, the “back forces” ρ_i are all equal to zero. Thus, the partial differentials in the formulations from Eqs. (3.42) to (3.47) can be expressed as follows:

$$\frac{\partial y}{\partial v_1} = -\beta_1 \frac{\left(\dfrac{\beta_1+\beta_2}{1+t_0}\right)^{(\beta_1+\beta_2)}}{(\beta_1)^{\beta_1}(\beta_2)^{\beta_2}}\left[(v_1+t_0)^2\right]^{\left(\frac{\beta_1}{2}-0.5\right)}(1-v_2)\left[(1-v_2)^2\right]^{\left(\frac{\beta_2}{2}-0.5\right)} \tag{3.48}$$

$$\frac{\partial y}{\partial v_2} = \beta_2 \frac{\left(\dfrac{\beta_1+\beta_2}{1+t_0}\right)^{(\beta_1+\beta_2)}}{(\beta_1)^{\beta_1}(\beta_2)^{\beta_2}}(v_1+t_0)\left[(v_1+t_0)^2\right]^{\left(\frac{\beta_1}{2}-0.5\right)}\left[(1-v_2)^2\right]^{\left(\frac{\beta_2}{2}-0.5\right)} \tag{3.49}$$

$$\frac{\partial v_1}{\partial \chi_V} = \frac{a_{V1}}{V_0} \tag{3.50}$$

$$\frac{\partial v_2}{\partial \chi_V} = \frac{a_{V2}}{V_0} \tag{3.51}$$

$$\frac{\partial h_2}{\partial \chi_{H2}} = \frac{a_H}{h_0 V_0} \tag{3.52}$$

$$\frac{\partial h_3}{\partial \chi_{H3}} = \frac{a_H}{h_0 V_0} \tag{3.53}$$

$$\frac{\partial q}{\partial \chi_Q} = \frac{a_Q}{2Rq_0V_0} \tag{3.54}$$

$$\frac{\partial m_2}{\partial \chi_{M2}} = \frac{a_M}{2Rm_0V_0} \tag{3.55}$$

$$\frac{\partial m_2}{\partial \chi_{H3}} = \frac{a_M d}{2Rm_0V_0} \tag{3.56}$$

$$\frac{\partial m_3}{\partial \chi_{M3}} = \frac{a_M}{2Rm_0V_0} \tag{3.57}$$

$$\frac{\partial m_3}{\partial \chi_{H2}} = \frac{-a_M d}{2Rm_0V_0} \tag{3.58}$$

$$\frac{\partial y}{\partial t} = 1.0 \tag{3.59}$$

$$\frac{\partial t}{\partial h_2} = \frac{h_2 + em_3}{t},\ \frac{\partial t}{\partial h_3} = \frac{h_3 - em_2}{t},\ \frac{\partial t}{\partial q} = \frac{q}{t},\ \frac{\partial t}{\partial m_2} = \frac{m_2 - eh_3}{t},\ \frac{\partial t}{\partial m_3} = \frac{m_3 + eh_2}{t} \tag{3.60}$$

3.3.4 Incremental stress-strain response

In the incremental response of the single-yield-surface plasticity model, in a similar way to conventional plasticity models, there are two possibilities. The first is that, when the loading point is still inside the yield surface, the response of the model is purely elastic. It also means that the value of the yield function is negative ($y < 0$) and the multiplier $\lambda = 0$. The second possibility is that the loading point lies on the yield surface. Therefore, the plastic behaviour occurs and leads to the conditions: $y = 0$ and $\lambda \geq 0$.

In general, based on the thermodynamic framework (Houlsby and Puzrin, 2000), the incremental stress-strain relationship can be defined as follows:

$$\dot{\varepsilon}_i = -\frac{\partial^2 g}{\partial \sigma_i \partial \sigma_j}\dot{\sigma}_j - \frac{\partial^2 g}{\partial \sigma_i \partial \alpha_j}\dot{\alpha}_j \tag{3.61}$$

The dot notations express that the variables are presented in terms of their rates of changes within a time step *dt* i.e.:

$$\overset{\bullet}{x} = \frac{dx}{dt} \tag{3.62}$$

In the thermodynamic framework (Houlsby and Puzrin, 2000), the Gibbs free energy function for a decoupled material includes three terms, $g_1(\sigma_i)$, $g_2(\alpha_i)$ and the coupling term $-\sigma_i\alpha_i$. In which g_1 is a function of stresses σ_i and represents the elastic energy. The incremental response is therefore expressed as follows:

$$\overset{\bullet}{\varepsilon}_i = -\frac{\partial^2 g_1}{\partial\sigma_i\partial\sigma_j}\overset{\bullet}{\sigma}_j + \overset{\bullet}{\alpha}_i \tag{3.63}$$

For a coupled material, g_1 is not purely a function of stress, it includes the existence of the state variables α_i i.e. $g_1 = g_1(\sigma_i, \alpha_i)$. Particularly, in this study, the elastic behaviour involves the vertical plastic displacement, α_V. Therefore, it should be necessary to consider the case of coupled material in this problem. Converting to the matrix form using macro element concept, the incremental response can be:

$$\overset{\bullet}{\varepsilon}_i = -\frac{\partial^2 g_1}{\partial\sigma_i\partial\sigma_j}\overset{\bullet}{\sigma}_j - \frac{\partial^2 g_1}{\partial\sigma_i\partial\alpha_j}\overset{\bullet}{\alpha}_j + \overset{\bullet}{\alpha}_i \tag{3.64}$$

where $\varepsilon_i = (w, u_2, u_3, \omega, \theta_2, \theta_3)$ is the displacement vector.

3.3.4.1 Elastic response

The incremental elastic response can be expressed in the following formulation:

$$\overset{\bullet}{\varepsilon}{}_i^{e} = -\frac{\partial^2 g_1}{\partial\sigma_i\partial\sigma_j}\overset{\bullet}{\sigma}_j \tag{3.65}$$

In which the notations *e* represent the elastic case.

In the case of clay, the shear modulus G is independent of the vertical load V. The elastic response as in Eq. (3.65), after removing the zero terms, can be described in more detail as follows:

$$\delta w^e = -\frac{\partial}{\partial V}\left(\frac{\partial g_1}{\partial V}\right)\delta V \tag{3.66}$$

$$\delta u_2^e = -\frac{\partial}{\partial H_2}\left(\frac{\partial g_1}{\partial H_2}\right)\delta H_2 - \frac{\partial}{\partial H_2}\left(\frac{\partial g_1}{\partial M_3}\right)\delta M_3 \tag{3.67}$$

$$\delta u_3^e = -\frac{\partial}{\partial H_3}\left(\frac{\partial g_1}{\partial H_3}\right)\delta H_3 - \frac{\partial}{\partial H_3}\left(\frac{\partial g_1}{\partial M_2}\right)\delta M_2 \tag{3.68}$$

$$\delta \omega^e = -\frac{\partial}{\partial Q}\left(\frac{\partial g_1}{\partial Q}\right)\delta Q \tag{3.69}$$

$$\delta \theta_2^e = -\frac{\partial}{\partial M_2}\left(\frac{\partial g_1}{\partial H_3}\right)\delta H_3 - \frac{\partial}{\partial M_2}\left(\frac{\partial g_1}{\partial M_2}\right)\delta M_2 \tag{3.70}$$

$$\delta \theta_3^e = -\frac{\partial}{\partial M_3}\left(\frac{\partial g_1}{\partial H_2}\right)\delta H_2 - \frac{\partial}{\partial M_3}\left(\frac{\partial g_1}{\partial M_3}\right)\delta M_3 \tag{3.71}$$

In the case of sand, the shear modulus G of soil depends on the vertical load V (see Cassidy, 1999). Thus, the expressions for the elastic response become more complicated:

$$\begin{aligned}\delta w^e = &-\frac{\partial}{\partial V}\left(\frac{\partial g_1}{\partial V} + \sum_{i=1}^{5}\frac{\partial g_1}{\partial K_i}\frac{\partial K_i}{\partial G}\frac{\partial G}{\partial V}\right)\delta V - \frac{\partial}{\partial V}\left(\frac{\partial g_1}{\partial H_2}\right)\delta H_2 - \frac{\partial}{\partial V}\left(\frac{\partial g_1}{\partial H_3}\right)\delta H_3 \\ &-\frac{\partial}{\partial V}\left(\frac{\partial g_1}{\partial Q}\right)\delta Q - \frac{\partial}{\partial V}\left(\frac{\partial g_1}{\partial M_2}\right)\delta M_2 - \frac{\partial}{\partial V}\left(\frac{\partial g_1}{\partial M_3}\right)\delta M_3\end{aligned} \tag{3.72}$$

$$\delta u_2^e = -\frac{\partial}{\partial H_2}\left(\frac{\partial g_1}{\partial V} + \sum_{i=1}^{5}\frac{\partial g_1}{\partial K_i}\frac{\partial K_i}{\partial G}\frac{\partial G}{\partial V}\right)\delta V - \frac{\partial}{\partial H_2}\left(\frac{\partial g_1}{\partial H_2}\right)\delta H_2 - \frac{\partial}{\partial H_2}\left(\frac{\partial g_1}{\partial M_3}\right)\delta M_3 \tag{3.73}$$

$$\delta u_3^e = -\frac{\partial}{\partial H_3}\left(\frac{\partial g_1}{\partial V} + \sum_{i=1}^{5}\frac{\partial g_1}{\partial K_i}\frac{\partial K_i}{\partial G}\frac{\partial G}{\partial V}\right)\delta V - \frac{\partial}{\partial H_3}\left(\frac{\partial g_1}{\partial H_3}\right)\delta H_3 - \frac{\partial}{\partial H_3}\left(\frac{\partial g_1}{\partial M_2}\right)\delta M_2 \tag{3.74}$$

$$\delta \omega^e = -\frac{\partial}{\partial Q}\left(\frac{\partial g_1}{\partial V} + \sum_{i=1}^{5}\frac{\partial g_1}{\partial K_i}\frac{\partial K_i}{\partial G}\frac{\partial G}{\partial V}\right)\delta V - \frac{\partial}{\partial Q}\left(\frac{\partial g_1}{\partial Q}\right)\delta Q \tag{3.75}$$

$$\delta\theta_2^e = -\frac{\partial}{\partial M_2}\left(\frac{\partial g_1}{\partial V} + \sum_{i=1}^{5}\frac{\partial g_1}{\partial K_i}\frac{\partial K_i}{\partial G}\frac{\partial G}{\partial V}\right)\delta V - \frac{\partial}{\partial M_2}\left(\frac{\partial g_1}{\partial H_3}\right)\delta H_3 - \frac{\partial}{\partial M_2}\left(\frac{\partial g_1}{\partial M_2}\right)\delta M_2 \quad (3.76)$$

$$\delta\theta_3^e = -\frac{\partial}{\partial M_3}\left(\frac{\partial g_1}{\partial V} + \sum_{i=1}^{5}\frac{\partial g_1}{\partial K_i}\frac{\partial K_i}{\partial G}\frac{\partial G}{\partial V}\right)\delta V - \frac{\partial}{\partial M_3}\left(\frac{\partial g_1}{\partial H_2}\right)\delta H_2 - \frac{\partial}{\partial M_3}\left(\frac{\partial g_1}{\partial M_3}\right)\delta M_3 \quad (3.77)$$

The above calculations are straightforward but quite lengthy. Therefore, it is inappropriate to describe the full details in this chapter.

3.3.4.2 Plastic response

Once the yield surface is activated, the incremental expression of y can be written as follows:

$$\dot{y} = \frac{\partial y}{\partial \alpha_i}\dot{\alpha}_i + \frac{\partial y}{\partial \chi_j}\dot{\chi}_j + \frac{\partial y}{\partial \sigma_k}\dot{\sigma}_k = 0 \quad (3.78)$$

By using the isotropic hardening with $g_2 = 0$, the generalised dissipative force can be expressed as follows:

$$\chi_j = -\frac{\partial g}{\partial \alpha_j} = -\frac{\partial g_1}{\partial \alpha_j} + \sigma_j \quad (3.79)$$

Thus, the rate of change of the generalised dissipative forces is:

$$\dot{\chi}_j = -\frac{\partial^2 g_1}{\partial \alpha_j \partial \sigma_l}\dot{\sigma}_l - \frac{\partial^2 g_1}{\partial \alpha_j \partial \alpha_l}\dot{\alpha}_l + \dot{\sigma}_j \quad (3.80)$$

The incremental change of plastic displacement is defined as:

$$\dot{\alpha}_l = \lambda \frac{\partial y}{\partial \chi_l} \quad (3.81)$$

Substituting (3.80) and (3.81) into (3.78):

$$\frac{\partial y}{\partial \alpha_i}\left(\lambda \frac{\partial y}{\partial \chi_i}\right) + \frac{\partial y}{\partial \chi_j}\left(-\frac{\partial^2 g_1}{\partial \alpha_j \partial \sigma_l}\dot{\sigma}_l - \frac{\partial^2 g_1}{\partial \alpha_j \partial \alpha_l}\left(\lambda \frac{\partial y}{\partial \chi_l}\right) + \dot{\sigma}_j\right) + \frac{\partial y}{\partial \sigma_k}\dot{\sigma}_k = 0 \quad (3.82)$$

By converting the Eq. (3.82), the scalar multiplier λ is calculated as follows:

$$\lambda = \frac{\dfrac{\partial y}{\partial \chi_j}\dot{\sigma}_j + \dfrac{\partial y}{\partial \sigma_k}\dot{\sigma}_k - \dfrac{\partial y}{\partial \chi_j}\dfrac{\partial^2 g_1}{\partial \alpha_j \partial \sigma_l}\dot{\sigma}_l}{\dfrac{\partial y}{\partial \chi_j}\dfrac{\partial^2 g_1}{\partial \alpha_j \partial \alpha_l}\dfrac{\partial y}{\partial \chi_l} - \dfrac{\partial y}{\partial \alpha_i}\dfrac{\partial y}{\partial \chi_i}} \tag{3.83}$$

Therefore, the plastic response can be expressed as follows:

$$\dot{\alpha}_m = \frac{\dfrac{\partial y}{\partial \chi_j}\dot{\sigma}_j + \dfrac{\partial y}{\partial \sigma_k}\dot{\sigma}_k - \dfrac{\partial y}{\partial \chi_j}\dfrac{\partial^2 g_1}{\partial \alpha_j \partial \sigma_l}\dot{\sigma}_l}{\dfrac{\partial y}{\partial \chi_j}\dfrac{\partial^2 g_1}{\partial \alpha_j \partial \alpha_l}\dfrac{\partial y}{\partial \chi_l} - \dfrac{\partial y}{\partial \alpha_i}\dfrac{\partial y}{\partial \chi_i}}\frac{\partial y}{\partial \chi_m} \tag{3.84}$$

In more details, the scalar multiplier λ in Eq. (3.83) after removing the zero terms is:

$$\lambda = \lambda_V \delta V + \lambda_{H2}\delta H_2 + \lambda_{H3}\delta H_3 + \lambda_Q \delta Q + \lambda_{M2}\delta M_2 + \lambda_{M3}\delta M_3 \tag{3.85}$$

In which:

$$\lambda_V = \frac{\left(\begin{array}{l} \dfrac{\partial y}{\partial V} + \dfrac{\partial y}{\partial \chi_V} - \dfrac{\partial y}{\partial \chi_V}\dfrac{\partial^2 g_1}{\partial V \partial \alpha_V} - \dfrac{\partial y}{\partial \chi_{H2}}\dfrac{\partial^2 g_1}{\partial H_2 \partial \alpha_V} - \dfrac{\partial y}{\partial \chi_{H3}}\dfrac{\partial^2 g_1}{\partial H_3 \partial \alpha_V} \\ - \dfrac{\partial y}{\partial \chi_Q}\dfrac{\partial^2 g_1}{\partial Q \partial \alpha_V} - \dfrac{\partial y}{\partial \chi_{M2}}\dfrac{\partial^2 g_1}{\partial M_2 \partial \alpha_V} - \dfrac{\partial y}{\partial \chi_{M3}}\dfrac{\partial^2 g_1}{\partial M_3 \partial \alpha_V} \end{array}\right)}{\dfrac{\partial y}{\partial \chi_V}\dfrac{\partial^2 g_1}{\partial \alpha_V^2}\dfrac{\partial y}{\partial \chi_V} - \left(\dfrac{\partial y}{\partial V_0}\dfrac{\partial V_0}{\partial \alpha_V} + \dfrac{\partial y}{\partial r}\dfrac{\partial r}{\partial \alpha_V}\right)\dfrac{\partial y}{\partial \chi_V}} \tag{3.86}$$

$$\lambda_{H2} = \frac{\dfrac{\partial y}{\partial H_2} + \dfrac{\partial y}{\partial \chi_{H2}}}{\dfrac{\partial y}{\partial \chi_V}\dfrac{\partial^2 g_1}{\partial \alpha_V^2}\dfrac{\partial y}{\partial \chi_V} - \left(\dfrac{\partial y}{\partial V_0}\dfrac{\partial V_0}{\partial \alpha_V} + \dfrac{\partial y}{\partial r}\dfrac{\partial r}{\partial \alpha_V}\right)\dfrac{\partial y}{\partial \chi_V}} \tag{3.87}$$

$$\lambda_{H3} = \frac{\dfrac{\partial y}{\partial H_3} + \dfrac{\partial y}{\partial \chi_{H3}}}{\dfrac{\partial y}{\partial \chi_V}\dfrac{\partial^2 g_1}{\partial \alpha_V^2}\dfrac{\partial y}{\partial \chi_V} - \left(\dfrac{\partial y}{\partial V_0}\dfrac{\partial V_0}{\partial \alpha_V} + \dfrac{\partial y}{\partial r}\dfrac{\partial r}{\partial \alpha_V}\right)\dfrac{\partial y}{\partial \chi_V}} \tag{3.88}$$

$$\lambda_Q = \frac{\dfrac{\partial y}{\partial Q} + \dfrac{\partial y}{\partial \chi_Q}}{\dfrac{\partial y}{\partial \chi_V}\dfrac{\partial^2 g_1}{\partial \alpha_V^2}\dfrac{\partial y}{\partial \chi_V} - \left(\dfrac{\partial y}{\partial V_0}\dfrac{\partial V_0}{\partial \alpha_V} + \dfrac{\partial y}{\partial r}\dfrac{\partial r}{\partial \alpha_V}\right)\dfrac{\partial y}{\partial \chi_V}} \tag{3.89}$$

$$\lambda_{M2} = \frac{\dfrac{\partial y}{\partial M_2} + \dfrac{\partial y}{\partial \chi_{M2}}}{\dfrac{\partial y}{\partial \chi_V}\dfrac{\partial^2 g_1}{\partial \alpha_V^2}\dfrac{\partial y}{\partial \chi_V} - \left(\dfrac{\partial y}{\partial V_0}\dfrac{\partial V_0}{\partial \alpha_V} + \dfrac{\partial y}{\partial r}\dfrac{\partial r}{\partial \alpha_V}\right)\dfrac{\partial y}{\partial \chi_V}} \tag{3.90}$$

$$\lambda_{M3} = \frac{\dfrac{\partial y}{\partial M_3} + \dfrac{\partial y}{\partial \chi_{M3}}}{\dfrac{\partial y}{\partial \chi_V}\dfrac{\partial^2 g_1}{\partial \alpha_V^2}\dfrac{\partial y}{\partial \chi_V} - \left(\dfrac{\partial y}{\partial V_0}\dfrac{\partial V_0}{\partial \alpha_V} + \dfrac{\partial y}{\partial r}\dfrac{\partial r}{\partial \alpha_V}\right)\dfrac{\partial y}{\partial \chi_V}} \tag{3.91}$$

where *r*, the radius of the footing at the mudline, is applied for the spudcan only. In cases of circular flat footing and caisson, the terms which involve *r* vanish since the radius of these footings are constant.

Again, in the above formulations from Eq. (3.66) to Eq. (3.91), both in elastic and plastic responses, all the partial differentials can be evaluated numerically or by closed forms which are derived from the Gibbs free energy function and the yield function. These processes are straightforward but quite lengthy so it is not necessary to describe them here.

Finally, the incremental response for a rate-independent solution is written as follows:

$$\delta\varepsilon_i = -\frac{\partial^2 g_1}{\partial\sigma_i \partial\sigma_j}\delta\sigma_j - \frac{\partial^2 g_1}{\partial\sigma_i \partial\alpha_j}\delta\alpha_j + \lambda\frac{\partial y}{\partial \chi_i} \tag{3.92}$$

In which λ can be calculated by using Eq. (3.83) with the variations $\delta\sigma_i$ instead of using $\dot{\sigma}_i$.

3.4 Single-yield surface hyperplasticity model using rate-dependent behaviour

Houlsby and Puzrin (2001) have introduced the rate-dependent solution using the hyperplasticity theory. There are two main differences compared with those of the rate-independent solution: the form of dissipation function and the consequent incremental response. This section presents the particular application of the rate-dependent behaviour to the ISIS model.

3.4.1 Flow potential function

In the rate-dependent solution, the dissipation function is no longer first-order homogeneous. It can be separated into two functions which are the force potential z and the dissipation potential w (see Houlsby and Puzrin, 2001) as follows:

$$d = z(\sigma_i, \alpha_i, \dot{\alpha}_i) + w(\sigma_i, \alpha_i, \chi_i) \tag{3.93}$$

If the dissipation function d can also be written as:

$$d = \left(\frac{\partial z(\sigma_i, \alpha_i, \dot{\alpha}_i)}{\partial \dot{\alpha}_i} \right) \dot{\alpha}_i \tag{3.94}$$

Then a Legendre-Fenchel transformation can give:

$$w(\sigma_i, \alpha_i, \chi_i) = d - z(\sigma_i, \alpha_i, \dot{\alpha}_i) = \chi_i \dot{\alpha}_i - z(\sigma_i, \alpha_i, \dot{\alpha}_i) \tag{3.95}$$

In which the definitions of the generalised dissipative forces χ_i and the rates of change of the state variables α_i can be expressed as follows:

$$\chi_i = \frac{\partial z}{\partial \dot{\alpha}_i} \tag{3.96}$$

$$\dot{\alpha}_i = \frac{\partial w}{\partial \chi_i} \tag{3.97}$$

Therefore, the flow potential function w is analogous with the expression of the yield function y in case of using rate-independent solution which is described as $y(\sigma_i, \alpha_i, \chi_i) = \chi_i \dot{\alpha}_i - d$. However, since z is not a homogeneous first-order function of $\dot{\alpha}_i$, the flow potential function could not be zero during the calculation. Houlsby and Puzrin (2001) have proposed several theories to give the form of w such as linear viscosity, nonlinear viscosity and rate process theory. In this study, the linear viscosity form is used for *w* as the starting point.

For brevity, the derivation of the rate-dependent solution presented in this section is just implemented with the linear viscosity formulation of *w* which is defined as:

$$w = \frac{\langle y \rangle^2}{2\mu} \tag{3.98}$$

where μ is the viscosity factor; *y* is the yield function as in Eq. (3.37) of the rate-independent solution; $\langle \ \rangle$ are the Macaulay brackets which operate as $\langle x \rangle = x$ if $x > 0$ and $\langle x \rangle = 0$ if $x \le 0$. Other theories can be derived using the same framework.

3.4.2 Incremental stress-strain response

As proved in Houlsby and Puzrin (2001) and extended in Puzrin and Houlsby (2003), the incremental response of the rate-dependent behaviour can still be expressed by using Eq. (3.63). The definitions of the generalised dissipation forces χ_i and the rate of change of plastic displacements $\dot{\alpha}_i$ are expressed in Eq. (3.96) and Eq. (3.97). Furthermore, the time increment *dt* described in Eqs. (3.62) now has real physical meaning instead of an artificial value as in the rate-independent solution.

By substituting Eq. (3.98) into Eq. (3.97) and then applying to Eq. (3.63), the incremental stress-strain response using rate-dependent behaviour can be written as:

$$\dot{\varepsilon}_i = -\frac{\partial^2 g_1}{\partial \sigma_i \partial \sigma_j}\dot{\sigma}_j - \frac{\partial^2 g_1}{\partial \sigma_i \partial \alpha_j}\frac{\langle y \rangle}{\mu}\frac{\partial y}{\partial \chi_j} + \frac{\langle y \rangle}{\mu}\frac{\partial y}{\partial \chi_i} \tag{3.99}$$

Converting Eq. (3.99) to the variational form, it becomes:

$$\delta\varepsilon_i = -\frac{\partial^2 g_1}{\partial\sigma_i\partial\sigma_j}\delta\sigma_j - \frac{\partial^2 g_1}{\partial\sigma_i\partial\alpha_j}\frac{\langle y\rangle}{\mu}\frac{\partial y}{\partial\chi_j}dt + \frac{\langle y\rangle}{\mu}\frac{\partial y}{\partial\chi_i}dt \tag{3.100}$$

In which the functions g_1 and y are still used as in Eq. (3.4) and Eq. (3.37). The definitions of the partial differentials in Eq. (3.100) are exactly the same as those of the rate-independent solution.

There are two factors that have strong effects on the rate-dependent solution: the viscosity factor μ and time increment *dt*. Houlsby and Puzrin (2001) have demonstrated that by choosing suitable values for the viscosity and the time increment, the rate-dependent solution can simulate well the results of the rate-independent solution. Otherwise, inappropriate values of μ and *dt* can lead to either instability or inaccuracy of the numerical calculation. Unfortunately, there is no explicit mathematical expression for the relationship between μ and *dt* to give a correct answer to this problem. However, some empirical remarks can be useful for the analyst to choose appropriate values for these factors. The details will be presented in the parametric study (Section 6.6).

3.5 Application of the vertical bearing capacity of caisson in ISIS model

3.5.1 Modification of the vertical bearing capacity of caisson foundation

In section 2.3.2, the calculation procedure for the vertical bearing capacity of caisson foundation has been reviewed. However, in this calculation, the heave caused by the inward movement of soil during the installation process has not been taken into account. Particularly, at the end of the installation, this volume of soil is roughly equivalent to one half of the volume occupied by the perimeter skirt in the soil medium. In addition, the changes of relative density of the soil inside the caisson during the suction process also have not been considered. Indeed, from experimental observations (Villalobos *et al.*, 2003a), the full penetration can be determined as the position at which the vertical bearing capacity curve changes its direction dramatically. After finishing the installation process, the depth at the full penetration position is always smaller than the length of the skirt of caisson. Figure 3.7 shows the V_0 curves versus w_p obtained from the tests and from the calculation using the concept of Houlsby and Byrne (2004a and 2004b) in which L^* represents the full penetration depth in experiments and L is the length of the skirt. From now, for simplicity, V_0 which is the calculation result from the concept of Houlsby and Byrne (2004a and 2004b) is called $V_{0-ideal}$. Therefore, this section presents a procedure used to modify the $V_{0-ideal}$ curve to capture the real V_0 curve versus penetration with a reasonable precision.

In principle, the calculation of the vertical bearing capacity is based on the conventional limit analysis solutions and some further assumptions. Furthermore, this procedure can be implemented separately from the model analysis. Therefore, it is possible to evaluate both the $V_{0\text{-}ideal}$ curve and V_0 curve as the set of points corresponding to the positions of the caisson during the installation process. Then, during the analysis, the vertical bearing capacity used at a certain depth is interpolated from these pre-calculated points. Based on this principle, the modification process is implemented to convert the set of points of the $V_{0-ideal}$ curve to those of the V_0 curve.

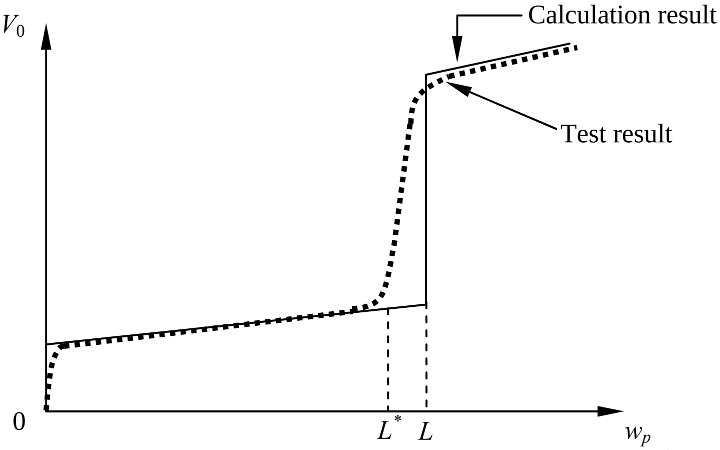

Figure 3.7 Comparison between the calculation result and test observation of V_0 curves versus w_p

The core of the modification is the introduction a bell-shaped smoothing function. Each point on the V_0 curve is the result from the adjustment of the corresponding point on the $V_{0-ideal}$ curve. There are two steps in this process. Firstly, a segment, in which the considered point is the central point, is picked from the $V_{0-ideal}$ curve. Then, the bell-shaped function is applied to this segment as the weight function. Consequently, the values of the other points within one segment will affect the value of V_0 at the considered point as shown in Figure 3.8.

In this study, there are two forms of bell-shaped function used: the Gauss form and the quadratic form. The Gauss form can be expressed as follows:

$$f_{bell}(x_i) = e^{\left(-\frac{x_i^2}{2}\right)} \tag{3.101}$$

where x_i is the local coordinate of the point i considered on the segment and has the value in the range [-4.0, 4.0]. Figure 3.9 shows the graph of the Gauss function. The limitation of x values from –4.0 to 4.0 means that outside this boundary, the influence of other points to the central point which is being corrected can be neglected.

As shown in Figure 3.8a, the bell width w_{bell}, which is also the length of the segment, can determine the influence range of the adjacent points to the central point considered and therefore affect the shape of the ($V_0 : w_p$) curve. At an adjacent point i at the depth w_{pi}, the corresponding value of x can be calculated as follows:

$$x_i = 4.0\frac{w_{pi} - w_{p-central}}{\frac{w_{bell}}{2}} \tag{3.102}$$

where $w_{p-central}$ is the depth of the central point which is being adjusted.

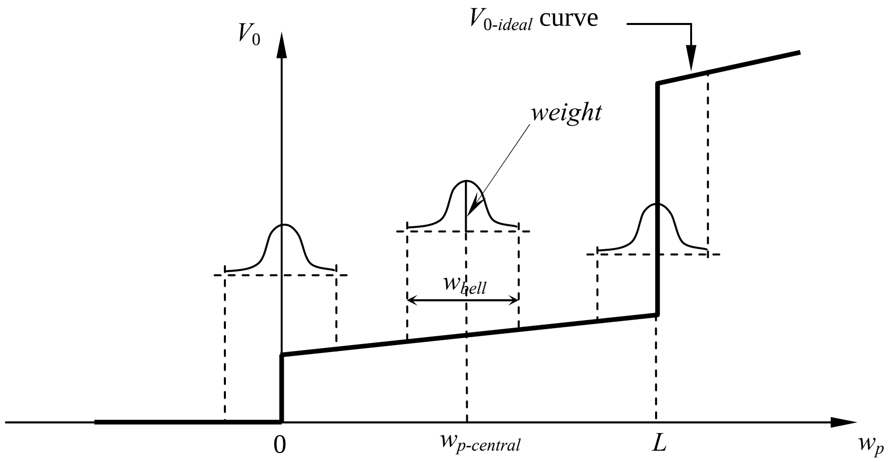

(a) Application of the bell-shaped weight function to the $V_{0\text{-}ideal}$ curve

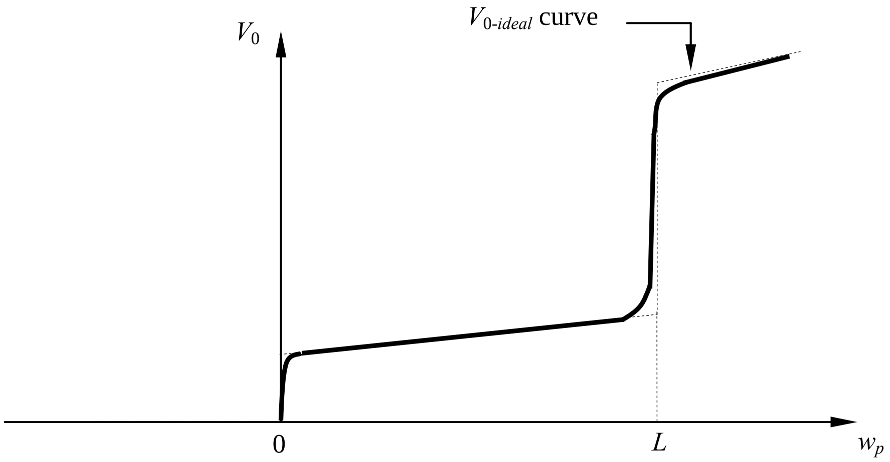

(b) V_0-w_p curve after the correction

Figure 3.8 Modification of the V_0 curve versus penetration w_p

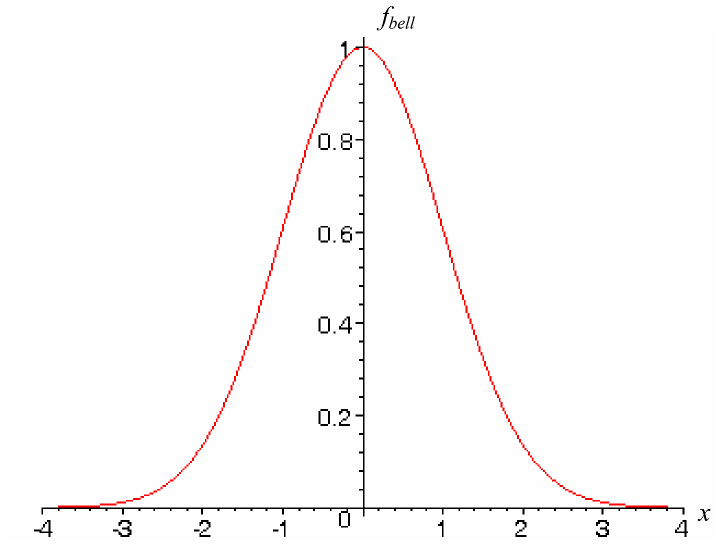

Figure 3.9 Gauss function

The correction using the quadratic form of the bell-shape function is similar to that using the Gauss form. The quadratic form can be written as:

$$f_{bell}(x_i) = \left(1 - \left(\frac{x_i}{2}\right)^2\right)^2 \tag{3.103}$$

In which x_i is in [-2.0, 2.0] as shown in Figure 3.10. The calculation of x_i can be:

$$x_i = 2.0\frac{w_{pi} - w_{p-central}}{\frac{w_{bell}}{2}} \tag{3.104}$$

Finally the value of V_0 can be calculated as follows:

$$V_0(w_{p-central}) = \frac{\sum_{i=1}^{n} f_{bell}(x_i) V_{0-ideal}(w_{pi})}{\sum_{i=1}^{n} f_{bell}(x_i)} \tag{3.105}$$

where n is the number of points taken into account in a segment;

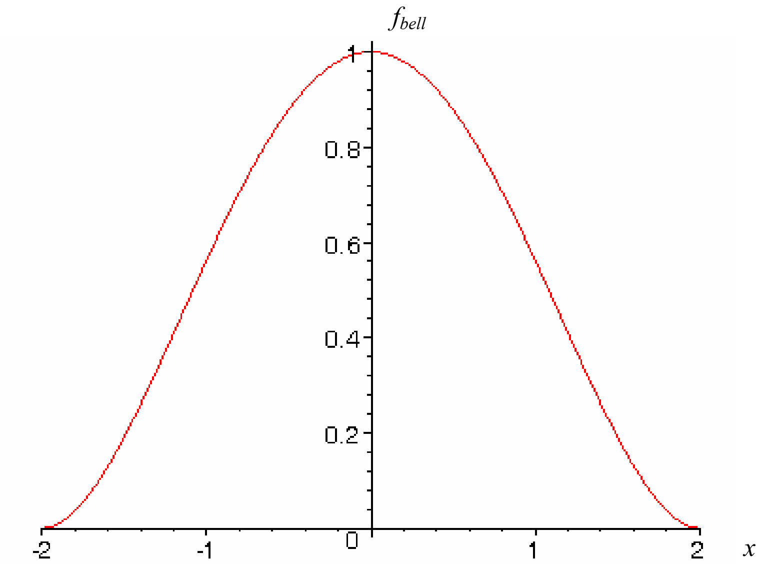

Figure 3.10 Quadratic form of the bell-shape function

It is clear that the heave inside the caisson at the full penetration position involves the factors of skirt length L, skirt thickness t, suction pressures s during the installation and the relative density D_r of the soil. Therefore, the bell width w_{bell} which is the core parameter to simulate the heave should be a function of these factors. However, in order to explore this function, it is necessary to implement an investigation in the soil structures under the effects of suction pressure which is beyond the range of this study. Therefore, the magnitudes of the bell width used in this research basically come from laboratory observations.

3.5.2 Analysis of the suction assisted penetration in ISIS model

In the installation of caisson foundations, the suction technique is used to reduce the vertical force needed to push the caisson into the seabed. There are two main effects from the application of suction pressure to the soil medium during the installation process. The first effect is that the suction pressure causes the difference between the vertical pressure inside and outside the caisson as the additional vertical forces. The second effect is the influence of water flow caused by the suction pressure on the pore pressures at the tip of the caisson's skirt. This means that the bearing capacity of the soil is reduced while the suction occurs. Therefore, the vertical bearing capacity of the caisson, V_0, becomes a function of depth w_p and suction pressure s instead of a function of depth only.

The main idea of the suction assisted penetration is that firstly the caisson can be pushed into the seabed to a certain initial depth by its own weight. Then, the suction pressure is applied and the vertical force is still equal to the self-weight of the caisson during this process.

Figure 3.11a shows the outline of the development of the yield surface during the installation with suction assistance. V_{0s} is the vertical bearing capacity of the foundation during the suction process. Essentially, V_{0s} is evaluated by using the calculation procedure of V_0, which is now treated as a function of both w_p and s. Figure 3.11b shows the outline of the calculation procedure of V_{0s}. Each dashed line represents a (V_{0s}: w_p) curve corresponding to a value of the suction pressure. When the suction increases from the pressure $s^{(i)}$ to $s^{(i+2)}$, the V_{0s} value does not change but the penetration depth w_p is increased from $w_p^{(i)}$ to $w_p^{(i+2)}$.

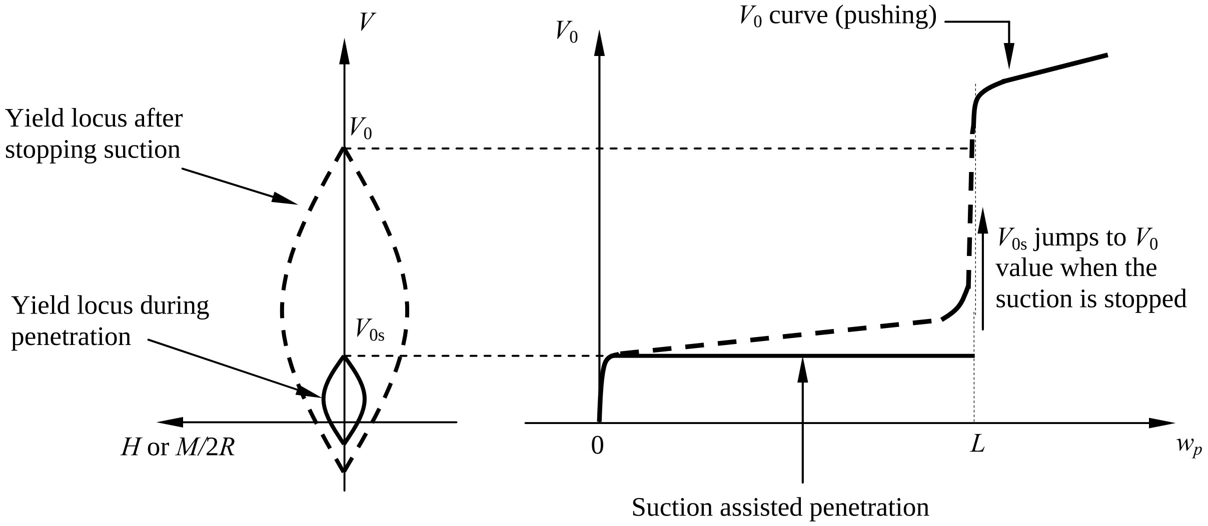

(a) Developments of the yield surface during the suction assisted penetration

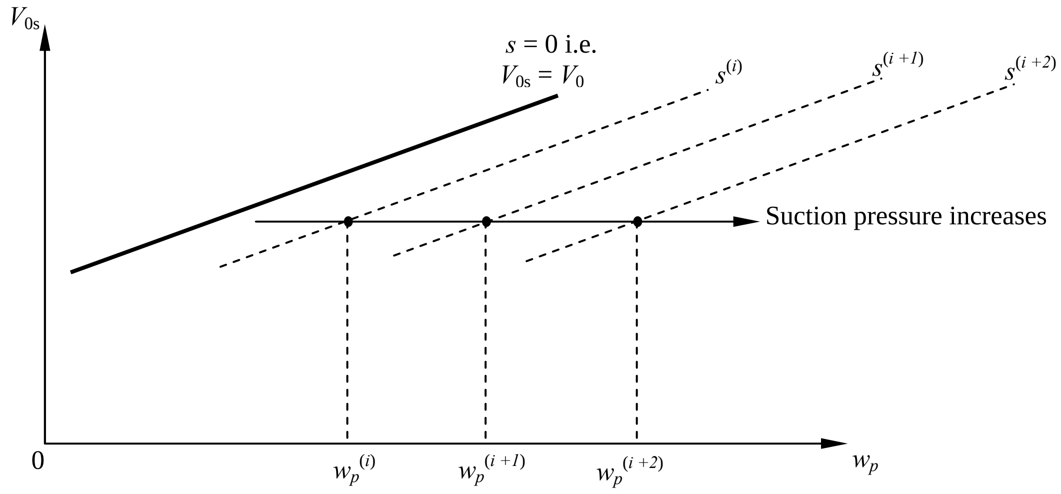

(b) Outline of the calculation procedure of V_{0s} as a function of the depth w_p and suction pressure s

Figure 3.11 Outline of the installation using suction assistance

During the suction process, V_{0s} plays the role of V_0 in the yield function. Since the suction pressure causes disturbance of the soil, it leads to a decrease in the vertical bearing capacity V_{0s}. Thus, the size of the yield surface dominated by V_{0s} does not increase with depth as in pushing installation (the dashed line in Figure 3.11a).

After completing the installation, the suction is terminated. Therefore, the soil can recover the original bearing capacity, V_0, which is again a function of depth only. This is the application principle of the suction installation in ISIS model.

3.6 Numerical illustrations

This section presents a series of numerical examples of circular flat footing, spudcan and caisson on both clay and sand using single-yield-surface ISIS model. There are three main aspects that can be validated through these examples.

The first aspect is the validation of the ISIS model in the analyses of a circular flat footing and spudcan. The comparisons will be made between the solution using conventional plasticity theory (Model B or Model C) and that using the rate-independent hyperplasticity (ISIS model). This work aims at proving that the ISIS model reproduces completely the solutions of Model B and Model C which have been achieved and verified in Martin (1994) and Cassidy (1999).

The second aspect is the illustration of the simulation of suction assisted penetration in the ISIS model of which the principle has been discussed in section 3.5.2. A numerical analysis of the installation process using both suction and vertical loading of caisson foundation is introduced. This work is used to demonstrate the ability of the ISIS model in describing the caisson footing behaviour using the rate-independent solution.

Lastly, the rate-dependent solution is implemented in an example of caisson footing and compared with the results of rate-independent solution. The purpose of this work is to show the potential of the rate-dependent solution in the application to the next development of the ISIS model, multiple-yield-surface model.

3.6.1 Simulations of the behaviours of circular flat footing and spudcan on both clay and sand using rate-independent hyperplasticity

In this section, there are four examples implemented: circular flat footing on clay, circular flat footing on sand, spudcan on clay and spudcan on sand.

Example 1: Circular flat footing on clay

This example describes the response of a circular flat footing under combined loading. The input data file which include geometry, loads, hardening rule and soil type are listed in Table 3.1.

Table 3.1 Input data of Example 1

<table>
<tr><th colspan="7">Soil properties and geometry</th></tr>
<tr><td colspan="3">Type of soil</td><td colspan="4">Clay</td></tr>
<tr><td colspan="3">Hardening</td><td colspan="4">Isotropic</td></tr>
<tr><td colspan="3">Number of loading stages</td><td colspan="4">3</td></tr>
<tr><td colspan="3">Radius (m)</td><td colspan="4">15.0</td></tr>
<tr><td colspan="3">Initial V_0 (kN)</td><td colspan="4">10^3</td></tr>
<tr><td colspan="3">Undrained shear strength (at mudline) (kN/m^2)</td><td colspan="4">20.0</td></tr>
<tr><td colspan="3">Effective unit weight (kN/m^3)</td><td colspan="4">10.0</td></tr>
<tr><td colspan="3">Mode of shear strength variation</td><td colspan="4">Linear</td></tr>
<tr><td colspan="3">Poisson’s ratio ν</td><td colspan="4">0.5</td></tr>
<tr><td colspan="3">ρ (kPa/m)</td><td colspan="4">2.0</td></tr>
<tr><td colspan="3">$I_r = G/s_u$</td><td colspan="4">400</td></tr>
<tr><th colspan="7">Model parameters (for ISIS model)</th></tr>
<tr><td colspan="2" rowspan="2">Association factors</td><td>a_{V1}</td><td>a_{V2}</td><td>a_H</td><td>a_M</td><td>a_Q</td></tr>
<tr><td>0.58</td><td>0.58</td><td>1.0</td><td>1.0</td><td>1.0</td></tr>
<tr><td colspan="2" rowspan="8">Shape factors of yield surface</td><td colspan="2">e_1</td><td colspan="3">0.518</td></tr>
<tr><td colspan="2">e_2</td><td colspan="3">-1.18</td></tr>
<tr><td colspan="2">t_0</td><td colspan="3">0.0</td></tr>
<tr><td colspan="2">m_0</td><td colspan="3">0.083</td></tr>
<tr><td colspan="2">h_0</td><td colspan="3">0.127</td></tr>
<tr><td colspan="2">q_0</td><td colspan="3">0.1</td></tr>
<tr><td colspan="2">β_1</td><td colspan="3">0.764</td></tr>
<tr><td colspan="2">β_2</td><td colspan="3">0.882</td></tr>
<tr><th colspan="7">Loading process</th></tr>
<tr><td>Load stage</td><td>V (kN)</td><td>H_2(kN)</td><td>H_3(kN)</td><td>Q(kNm)</td><td>M_2(kNm)</td><td>M_3(kNm)</td></tr>
<tr><td>1</td><td>0.0 to 9000</td><td>0.0</td><td>0.0</td><td>0.0</td><td>0.0</td><td>0.0</td></tr>
<tr><td>2</td><td>9000 to11000</td><td>0.0 to 1000</td><td>0.0 to 1000</td><td>0.0</td><td>0.0</td><td>0.0 to -17000</td></tr>
<tr><td>3</td><td>11000</td><td>1000 to 1500</td><td>1000</td><td>0.0</td><td>0.0 to -17000</td><td>-17000</td></tr>
</table>

The numerical results compared with those of the Model B are shown in Figure 3.12, Figure 3.13 and Figure 3.14. Model B is implemented in the same code of ISIS program but using the conventional plasticity theory.

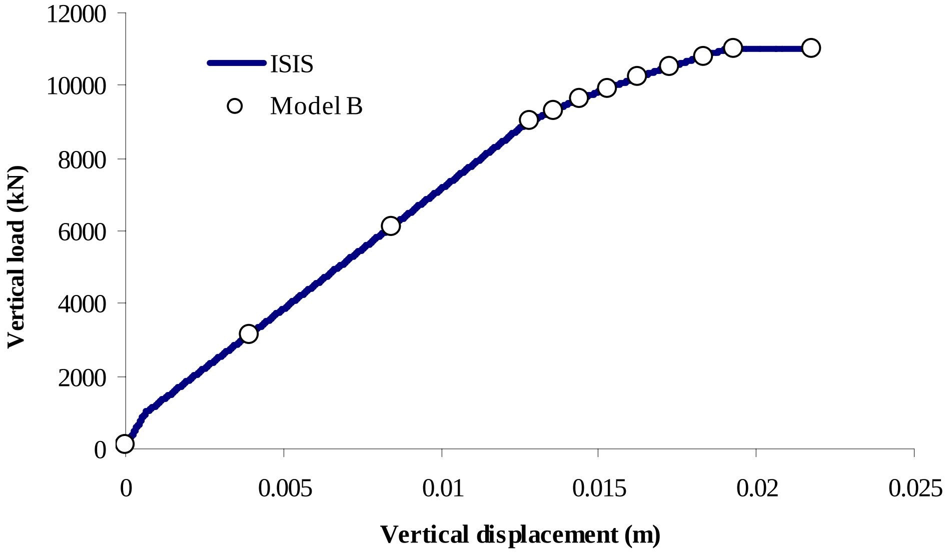

Figure 3.12 Comparison between ISIS and Model B in vertical response

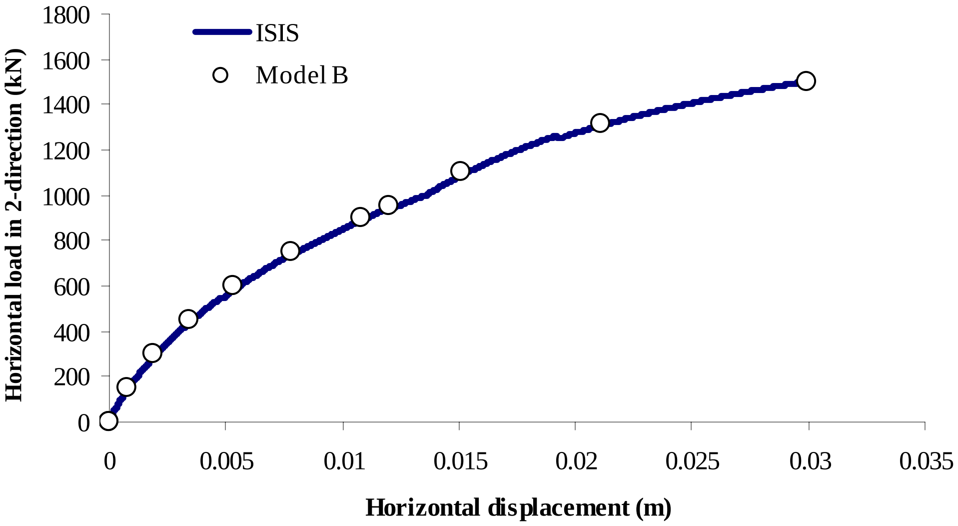

Figure 3.13 Comparison between ISIS and Model B in horizontal response

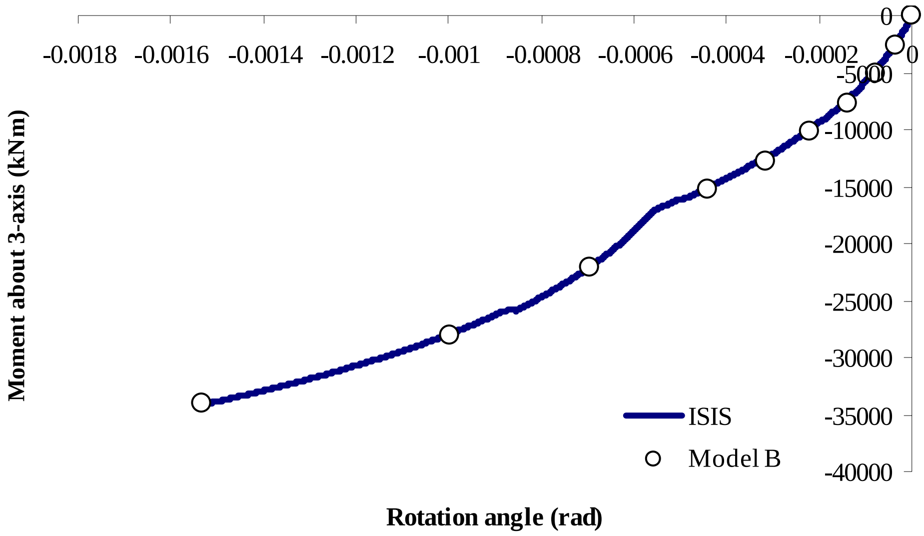

Figure 3.14 Comparison between ISIS and Model B in rotational response

It should be noted that the shape factors of the yield function are the same as those of the yield function used in Model B. Besides, the association factors are chosen to be able to reproduce the flow rule of Model B and the explanation of these options will be presented in section 6.3.

Example 2: Circular flat footing on sand

In this example, a circular flat footing working under combined loadings on sand is analysed. In a similar way to the first example, the details of the input data file are described in Table 3.2. The shape factors of the yield function used in this example are taken from those of the yield function of Model C. Using the same strategy as in Example 1, the association factors are the results of the attempt to reproduce the flow rule of Model C with the use of the yield function of the ISIS model. The numerical results are compared with that of the conventional plasticity model (Model C).

Figures 3.15, 3.16 and 3.17 show the response of the foundation in vertical, horizontal (3-axis) and rotational (about 3-axis) directions respectively.

Table 3.2 Input data of Example 2

Soil properties and geometry	
Type of soil	Sand
Hardening	Isotropic
Number of loading stages	4
Radius (m)	10.0
Initial V_0 (kN)	71600.0
Shear modulus G (initial value) (MN/m^2)	80.0
Effective unit weight (kN/m^3)	10.0
Angle of friction	45^o
Poisson's ratio ν	0.2

Model parameters (for ISIS model)					
Association factors	a_{V1}	a_{V2}	a_H	a_M	a_Q
	0.55	1.0	0.6	0.95	0.4

Shape factors of yield surface		
	e_1	-0.2
	e_2	0.0
	t_0	0.0
	m_0	0.086
	h_0	0.116
	q_0	0.1
	β_1	0.9
	β_2	0.99

Loading process						
Load stage	V (kN)	H_2(kN)	H_3(kN)	Q(kNm)	M_2(kNm)	M_3(kNm)
1	0.0 to 140000.0	0.0	0.0	0.0	0.0	0.0
2	140000.0 down to 70000.0	0.0 to 1000.0	0.0	0.0	0.0	0.0
3	70000.0 to 85000.0	0.0 to 7500.0	0.0	0.0	0.0	0.0 to 150000.0
4	85000.0 to 100000.0	7500.0 to 13995.0	0.0 to 3750.0	0.0	0.0 to -75000.0	150000.0 to 279900.0

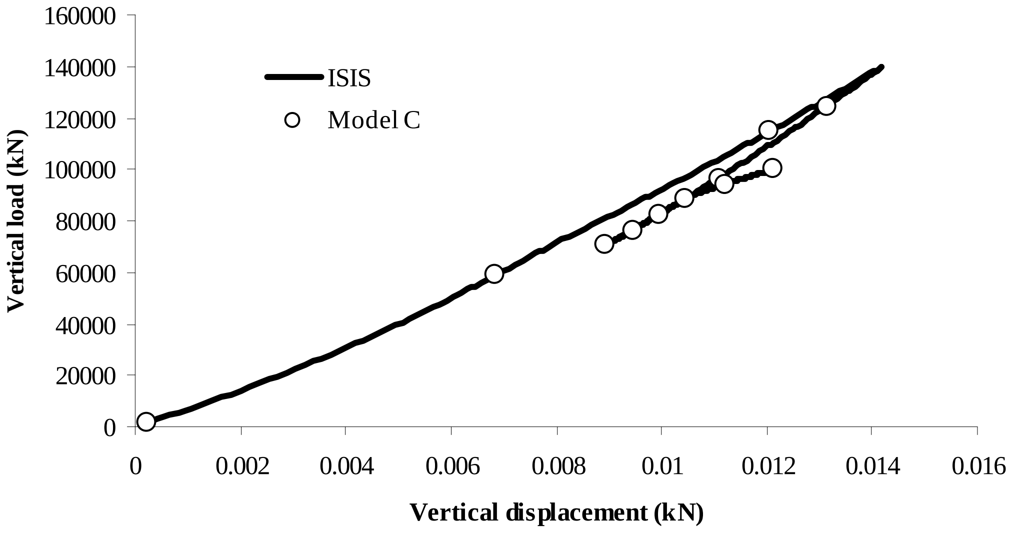

Figure 3.15 Vertical response of the circular flat footing on sand

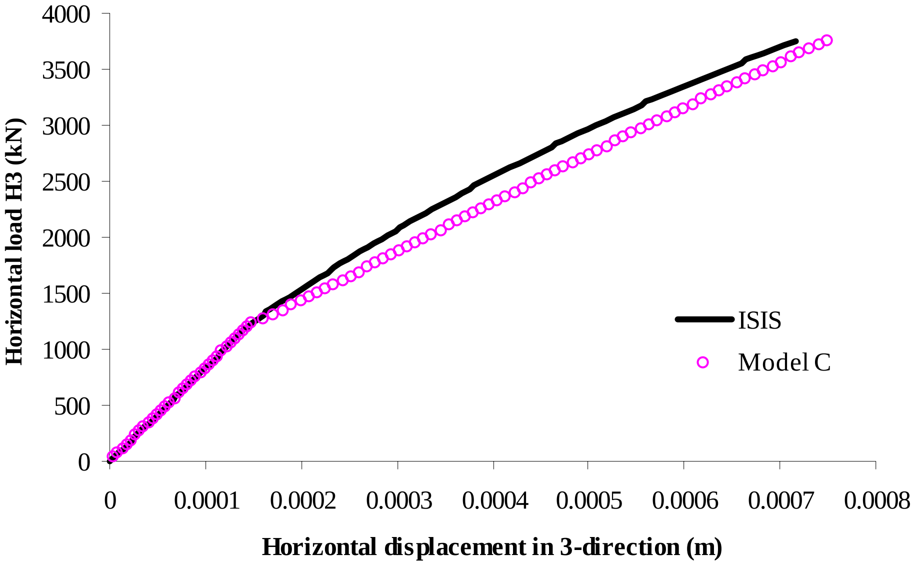

Figure 3.16 Horizontal response of the circular flat footing on sand

As shown in Figure 3.15, there is a loading-unloading process of vertical load applied in this example. This load path leads to the fact that the load point moves firstly to the peak of the yield surface and therefore increases the size of this surface (first loading stage). Afterward, it goes back nearly half way coming inside the yield surface (unloading stage). Therefore, in this stage, the foundation exhibits an elastic response. Later on, in the last two loading stages, since the horizontal and moment loads are applied with big enough magnitudes, the load point touches the yield surface again. The footing behaviour therefore becomes plastic as shown in the curvature parts of the responses shown in Figure 3.16 and 3.17.

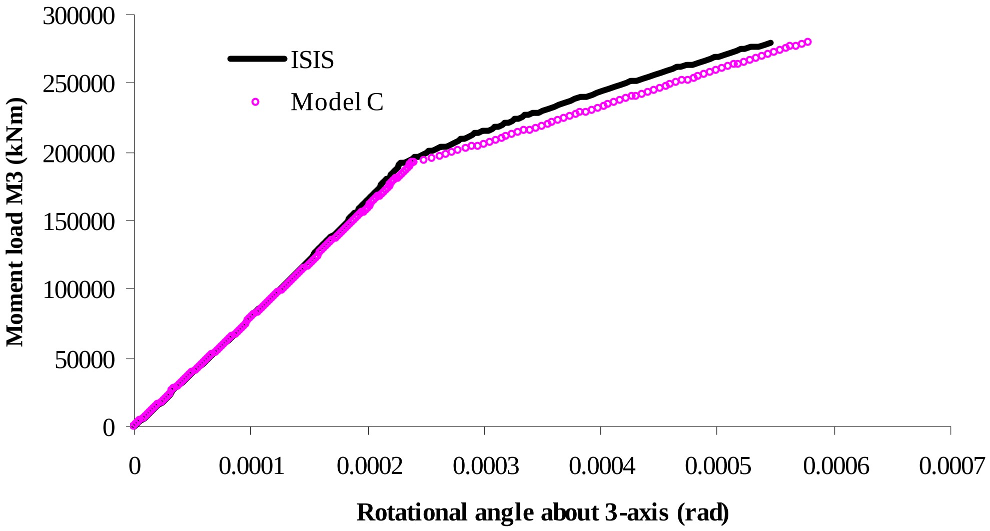

Figure 3.17 Rotational response of the circular flat footing on sand

As shown in Figures 3.16, 3.17, there are some minor differences between the ISIS and Model C in horizontal and moment responses. There are two main reasons which come from the formulation of the potential function and the expressions of the association factors in Model C. Firstly, in the formulation of the potential function of Model C, there is a factor $V_0^{'}$ which is determined by an empirical formulation. This value essentially determines the longitudinal size of a potential surface at a certain point on the yield surface. In the ISIS model, there is no point which involves this expression of $V_0^{'}$. In other words, the ISIS model and Model C are not mathematically identical. Secondly, the expressions of the association factors in Model C are the functions of the plastic displacements in the forms of the ratios $\frac{u_p}{w_p}$ and $\frac{2R\theta_p}{w_p}$ in which u_p and θ_p are the horizontal and rotational plastic displacements. The association factors in the ISIS model are not functions of these ratios. However, it could be expected that by using the multiple-yield-surface model in which the yield surfaces are activated with respect to the level of plastic displacements, the flow rule could be changed correspondingly. The plastic response can therefore give a result closer to that of Model C.

Example 3: Spudcan on clay

This example presents the analysis of a spudcan footing under combined loadings on clay.

The geometric sketch of this footing is shown in Figure 3.18. The soil properties, loading process and the model parameters are presented in Table 3.3. The numerical results compared with those of Model C are shown in Figure 3.19 and 3.20 for vertical and horizontal component respectively. The rotational response has the same form as that of horizontal response; therefore it is omitted for brevity.

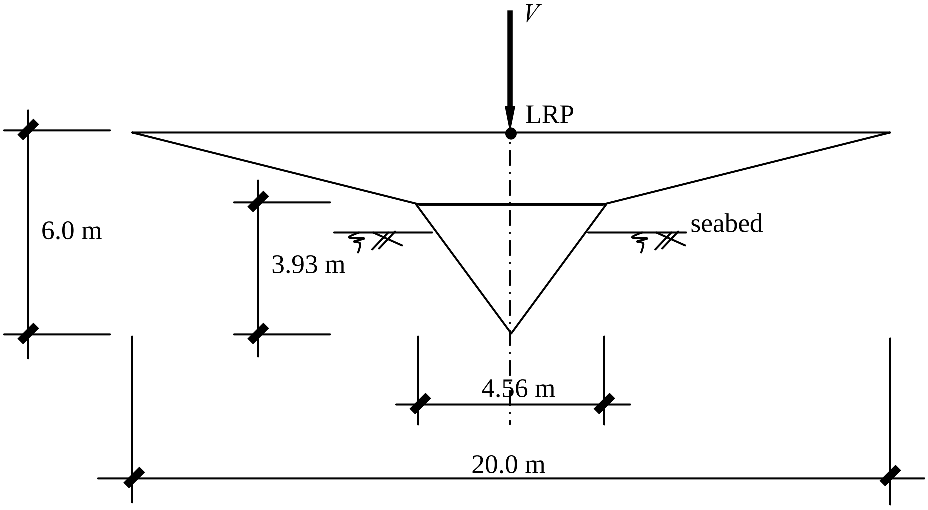

Figure 3.18 Geometry of the spudcan footing considered in Example 3

As shown in Figure 3.19, there is an initial penetration of spudcan. This is made by the self-weight of the spudcan in the first touch on the seabed before the loading process occurs and results in an initial size for the yield surface. Consequently, it leads to elastic behaviour in the first stage of loading as can be seen in the very first part of the curve in Figure 3.19.

Table 3.3 Input data of Example 3

<table>
<tr><th colspan="7">Soil properties and geometry</th></tr>
<tr><td colspan="4">Type of soil</td><td colspan="3">Clay</td></tr>
<tr><td colspan="4">Hardening</td><td colspan="3">Isotropic</td></tr>
<tr><td colspan="4">Number of loading stages</td><td colspan="3">3</td></tr>
<tr><td colspan="4">Initial V_0 (kN)</td><td colspan="3">10^3</td></tr>
<tr><td colspan="4">Undrained shear strength (at mudline) (kN/m^2)</td><td colspan="3">150.0</td></tr>
<tr><td colspan="4">Effective unit weight (kN/m^3)</td><td colspan="3">10.0</td></tr>
<tr><td colspan="4">Mode of shear strength variation</td><td colspan="3">Constant</td></tr>
<tr><td colspan="4">Poisson’s ratio ν</td><td colspan="3">0.5</td></tr>
<tr><td colspan="4">$I_r = G/s_u$</td><td colspan="3">400</td></tr>
<tr><th colspan="7">Model parameters (for ISIS model)</th></tr>
<tr><td colspan="2" rowspan="2">Association factors</td><td>a_{V1}</td><td>a_{V2}</td><td>a_H</td><td>a_M</td><td>a_Q</td></tr>
<tr><td>0.58</td><td>0.58</td><td>1.0</td><td>1.0</td><td>1.0</td></tr>
<tr><td colspan="2" rowspan="8">Shape factors of yield surface</td><td colspan="2">e_1</td><td colspan="3">0.518</td></tr>
<tr><td colspan="2">e_2</td><td colspan="3">-1.18</td></tr>
<tr><td colspan="2">t_0</td><td colspan="3">0.0</td></tr>
<tr><td colspan="2">m_0</td><td colspan="3">0.083</td></tr>
<tr><td colspan="2">h_0</td><td colspan="3">0.127</td></tr>
<tr><td colspan="2">q_0</td><td colspan="3">0.1</td></tr>
<tr><td colspan="2">β_1</td><td colspan="3">0.764</td></tr>
<tr><td colspan="2">β_2</td><td colspan="3">0.882</td></tr>
<tr><th colspan="7">Loading process</th></tr>
<tr><td>Load stage</td><td>V (kN)</td><td>H_2(kN)</td><td>H_3(kN)</td><td>Q(kNm)</td><td>M_2(kNm)</td><td>M_3(kNm)</td></tr>
<tr><td>1</td><td>0.0 to 11000</td><td>0.0</td><td>0.0</td><td>0.0</td><td>0.0</td><td>0.0</td></tr>
<tr><td>2</td><td>11000 down to 9000</td><td>0.0</td><td>0.0</td><td>0.0</td><td>0.0</td><td>0.0</td></tr>
<tr><td>3</td><td>9000</td><td>0.0 to 500</td><td>0.0 to 500</td><td>0.0</td><td>0.0</td><td>0.0 to -900</td></tr>
</table>

In a similar way to Example 1, there is also an unloading of the vertical load. However, the decrease of vertical load is rather small. This means that the load point is still near the peak point V_0 of the yield surface before the horizontal and moment loads are applied. Then, the horizontal and moment loads are applied with the constant vertical load. Figure 3.20 shows an almost horizontal line for the plastic behaviour of the footing. This is because of the fact that the influence of the hardening in this case is very small.

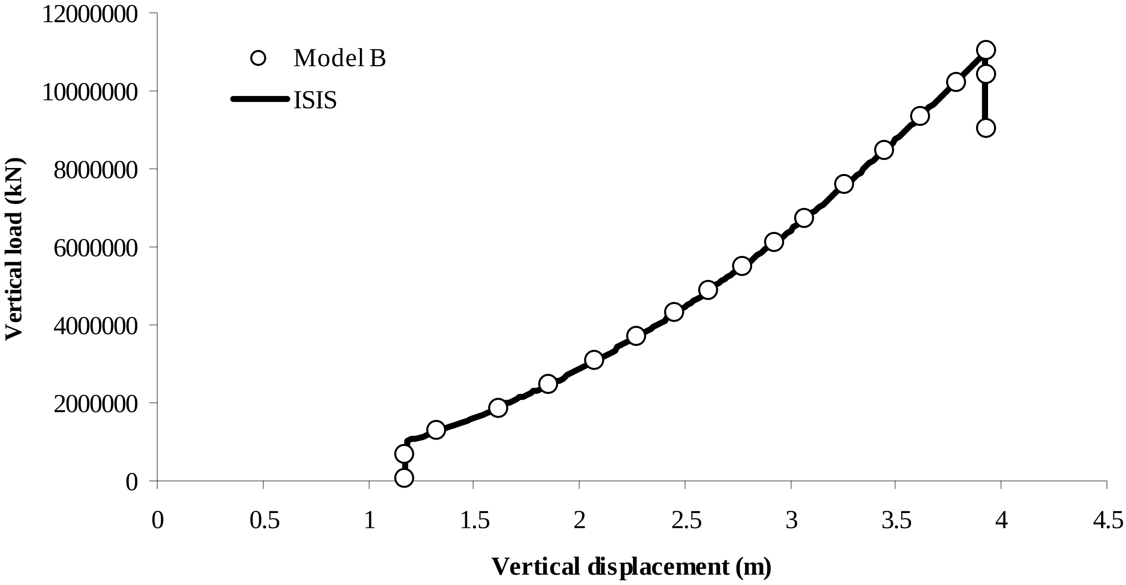

Figure 3.19 Vertical response of spudcan footing on clay

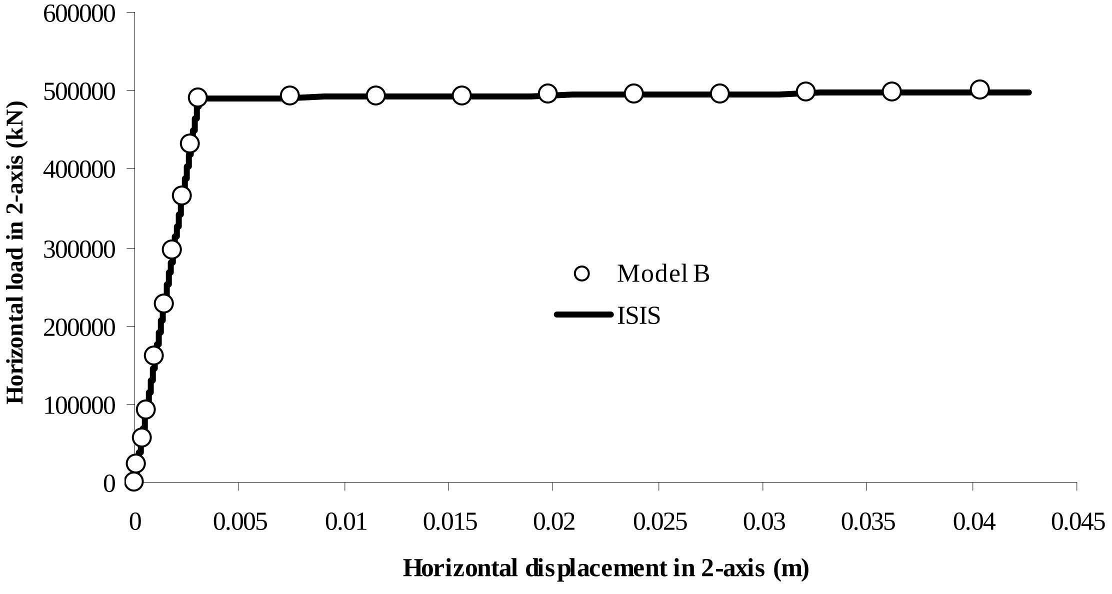

Figure 3.20 Horizontal response of spudcan footing on clay

Example 4: Spudcan on sand

In this example, the spudcan as shown in Example 3 is used. The details of the input data file are shown in Table 3.4. The numerical results of vertical response, horizontal response in 3-axis and rotational response about 3-axis are shown in Figures 3.21, 3.22 and 3.23 respectively.

Table 3.4 Input data of Example 4

Soil properties and geometry	
Type of soil	Sand
Hardening	Isotropic
Number of loading stages	4
Radius (m)	10.0
Initial V_0 (kN)	6820.0
Shear modulus G (initial value) (MN/m^2)	25.0
Effective unit weight (kN/m^3)	10.0
Angle of friction	35^{o}
Poisson's ratio ν	0.2

Model parameters (for ISIS model)					
Association factors	a_{V1}	a_{V2}	a_H	a_M	a_Q
	0.1	1.0	0.4	0.4	0.1

Shape factors of yield surface		
	e_1	-0.2
	e_2	0.0
	t_0	0.0
	m_0	0.086
	h_0	0.116
	q_0	0.1
	β_1	0.9
	β_2	0.99

Loading process						
Load stage	V (kN)	H_2(kN)	H_3(kN)	Q(kNm)	M_2(kNm)	M_3(kNm)
1	0.0 to 140000.0	0.0	0.0	0.0	0.0	0.0
2	140000.0 down to 70000.0	0.0 to 1000.0	0.0	0.0	0.0	0.0
3	70000.0 to 85000.0	0.0 to 7500.0	0.0	0.0	0.0	0.0 to 150000.0
4	85000.0 to 100000.0	7500 to 14000.0	0.0 to 3750.0	0.0	0.0 to -75000.0	150000.0 to 279900.0

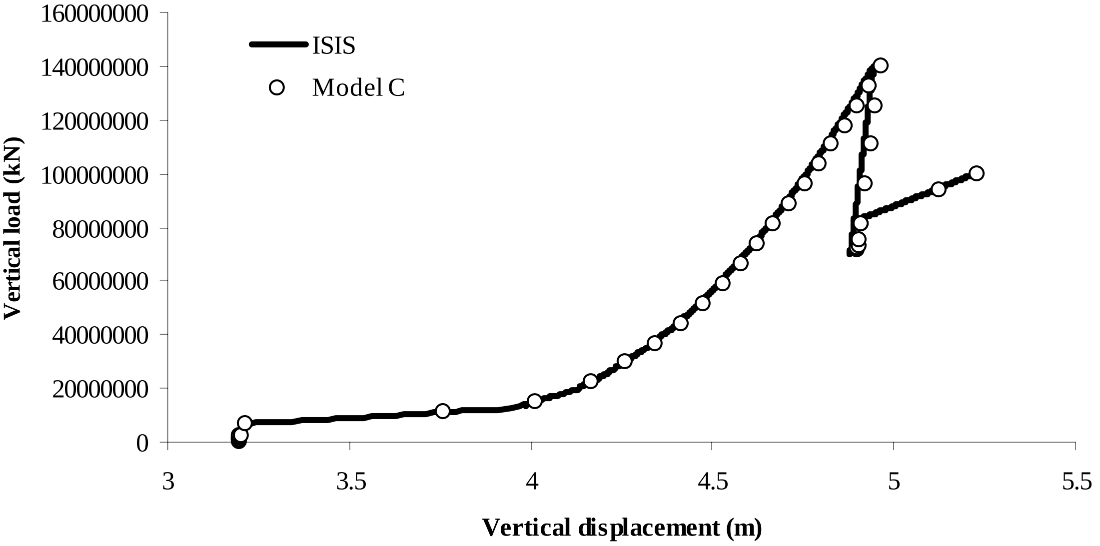

Figure 3.21 Vertical response of the spudcan on sand in Example 4

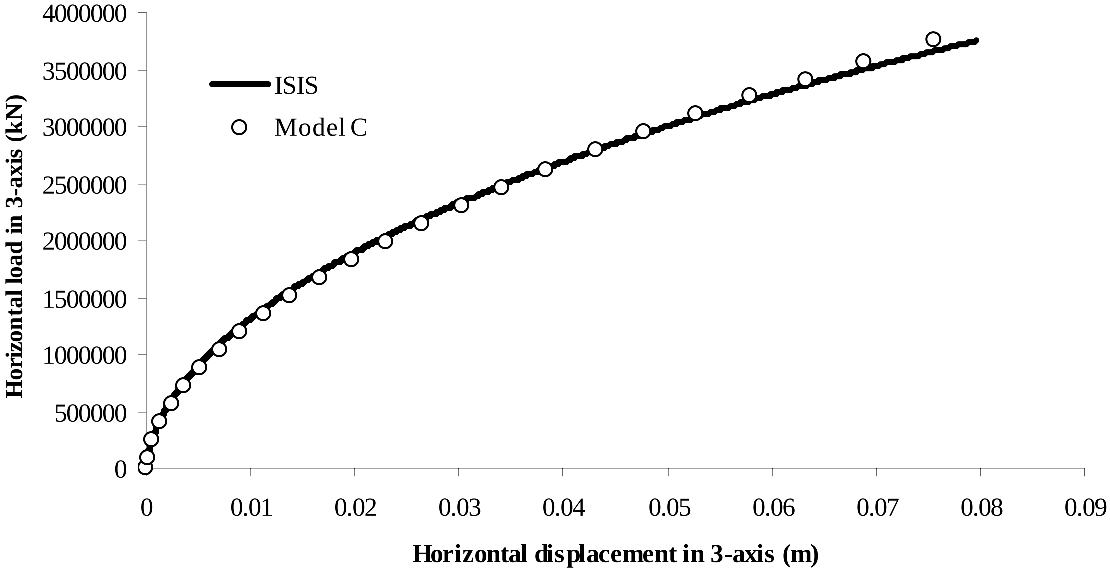

Figure 3.22 Horizontal response of the spudcan on sand in Example 4

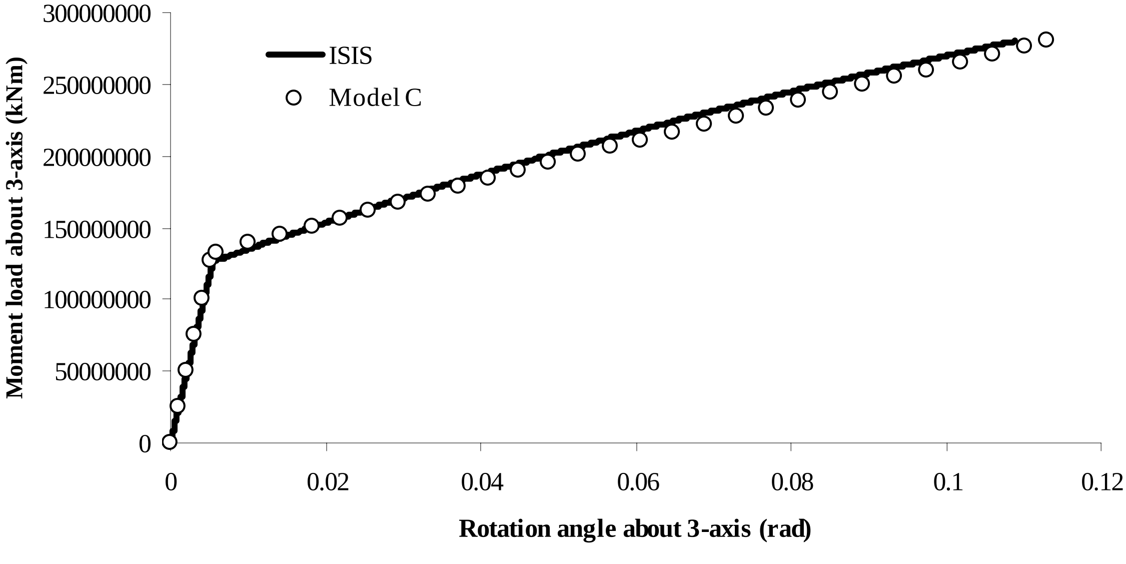

Figure 3.23 Rotational response of the spudcan on sand in Example 4

Again, the numerical results given by the ISIS model capture rather well those of Model C. The ability of ISIS in reproducing the results of Model C can be confirmed.

3.6.2 Installation of caisson with and without suction assistance

In this section, a numerical simulation of the installation process of a caisson using suction is presented. In order to demonstrate the effect of the suction technique, an analysis of the installation of this caisson without suction is also implemented. The outline of the caisson is shown in Figure 3.24. The details of the soil properties, vertical loads and suction process are described in Table 3.5.

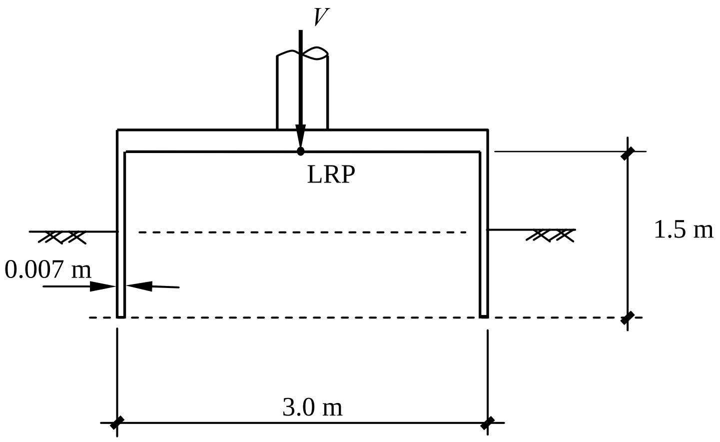

Figure 3.24 Outline of the caisson

There are five stages of loading implemented in this example. The first two stages are implemented without suction to describe the initial penetration of the caisson into the seabed by its own weight. In the third, fourth and fifth loading stages, the suction pressure is applied and increase gradually. The more the caisson is penetrated the bigger the suction pressure should be applied. The whole process represents a typical installation of caisson footing in practice.

Table 3.5 Input data of the installation of caisson using suction assistance

<table>
<tr><th colspan="8">Soil properties and geometry</th></tr>
<tr><td colspan="4">Type of soil</td><td colspan="4">Clay</td></tr>
<tr><td colspan="4">Hardening</td><td colspan="4">Isotropic</td></tr>
<tr><td colspan="4">Number of loading stages</td><td colspan="4">5</td></tr>
<tr><td colspan="4">Initial V_0 (kN)</td><td colspan="4">3.0</td></tr>
<tr><td colspan="4">Undrained shear strength (at mudline) (kN/m^2)</td><td colspan="4">10.54</td></tr>
<tr><td colspan="4">Effective unit weight (kN/m^3)</td><td colspan="4">10.0</td></tr>
<tr><td colspan="4">Mode of shear strength variation</td><td colspan="4">linear</td></tr>
<tr><td colspan="4">Friction angle</td><td colspan="4">35^o</td></tr>
<tr><td colspan="4">Poisson's ratio ν</td><td colspan="4">0.5</td></tr>
<tr><td colspan="4">$I_r = G/s_u$</td><td colspan="4">200</td></tr>
<tr><td colspan="4">ρ</td><td colspan="4">1.96</td></tr>
<tr><th colspan="8">Model parameters (for ISIS model)</th></tr>
<tr><td colspan="3" rowspan="2">Association factors</td><td>a_{V1}</td><td>a_{V2}</td><td>a_H</td><td>a_M</td><td>a_Q</td></tr>
<tr><td>0.297</td><td>0.297</td><td>0.7</td><td>0.7</td><td>0.7</td></tr>
<tr><td colspan="3" rowspan="8">Shape facors of yield surface</td><td colspan="2">e_1</td><td colspan="3">-0.2</td></tr>
<tr><td colspan="2">e_2</td><td colspan="3">0.0</td></tr>
<tr><td colspan="2">t_0</td><td colspan="3">0.1088</td></tr>
<tr><td colspan="2">m_0</td><td colspan="3">0.15</td></tr>
<tr><td colspan="2">h_0</td><td colspan="3">0.337</td></tr>
<tr><td colspan="2">q_0</td><td colspan="3">0.2</td></tr>
<tr><td colspan="2">β_1</td><td colspan="3">0.99</td></tr>
<tr><td colspan="2">β_2</td><td colspan="3">0.99</td></tr>
<tr><td colspan="3">Bell width (w_{bell}) (m)</td><td colspan="5">0.15</td></tr>
<tr><th colspan="8">Loading process</th></tr>
<tr><td>Load stage</td><td>Suction (kN/m^2)</td><td>V (kN)</td><td>H_2(kN)</td><td>H_3(kN)</td><td>Q(kNm)</td><td>M_2(kNm)</td><td>M_3(kNm)</td></tr>
<tr><td>1</td><td>Off</td><td>0.0 to 20.0</td><td>0.0</td><td>0.0</td><td>0.0</td><td>0.0</td><td>0.0</td></tr>
<tr><td>2</td><td>Off</td><td>20.0 to 21.0</td><td>0.0</td><td>0.0</td><td>0.0</td><td>0.0</td><td>0.0</td></tr>
<tr><td>3</td><td>0.0 to 0.8</td><td>21.0</td><td>0.0</td><td>0.0</td><td>0.0</td><td>0.0</td><td>0.0</td></tr>
<tr><td>4</td><td>0.8 to 2.3</td><td>21.0 to 23.0</td><td>0.0</td><td>0.0</td><td>0.0</td><td>0.0</td><td>0.0</td></tr>
<tr><td>5</td><td>2.3 to 22.3</td><td>23.0</td><td>0.0</td><td>0.0</td><td>0.0</td><td>0.0</td><td>0.0</td></tr>
</table>

Figure 3.25 shows the comparison of the two installation methods. If using the installation without suction, the need to apply a very big vertical load can be an obstacle to the installation in practice. Furthermore, this work may be very costly. Otherwise, it is clear that with the suction assistance the magnitude of the vertical load needed to push the caisson to the full penetration position is much smaller than without suction. This is the most important advantage of the suction method.

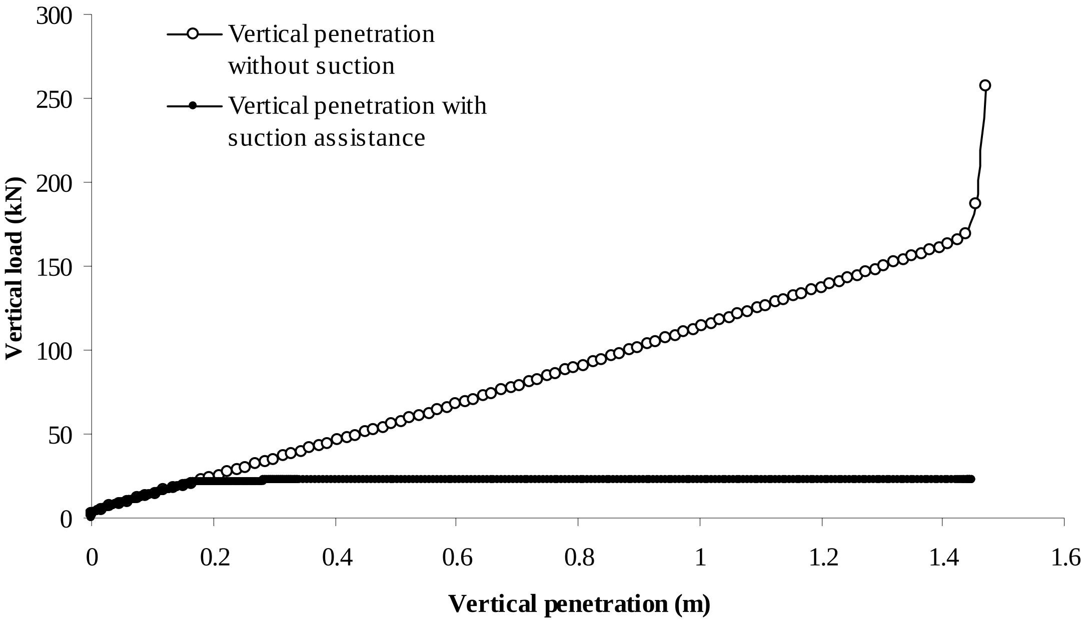

Figure 3.25 Installation of caisson with and without suction assistance

3.6.3 Rate-dependent solution

This section presents a numerical example implemented for a full scale caisson. This footing is installed by pure vertical load (without suction assistance). The numerical results using the rate-dependent solution are compared with those of the rate-independent solution. The purpose of this work is to show that, by using suitable values of viscosity and time increments, the results of rate-independent solution can be reproduced completely by the rate-dependent solution in the ISIS model. The geometry of the caisson in this example is shown in Figure 3.26. The details of the input data file are presented in Table 3.6.

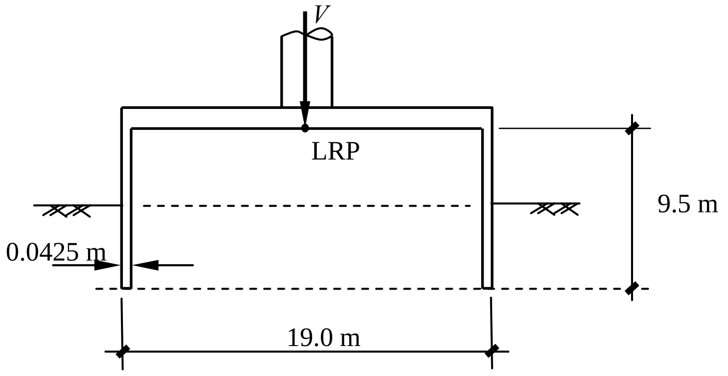

Figure 3.26 Outline of the caisson

Table 3.6 Input data of the installation of caisson without suction assistance

<table>
<tr><th colspan="8">Soil properties and geometry</th></tr>
<tr><td colspan="4">Type of soil</td><td colspan="4">Sand</td></tr>
<tr><td colspan="4">Hardening</td><td colspan="4">Isotropic</td></tr>
<tr><td colspan="4">Number of loading stages</td><td colspan="4">3</td></tr>
<tr><td colspan="4">Initial V_0 (kN)</td><td colspan="4">20.0</td></tr>
<tr><td colspan="4">Shear modulus G (initial value) (MN/m^2)</td><td colspan="4">25.0</td></tr>
<tr><td colspan="4">Effective unit weight (kN/m^3)</td><td colspan="4">10.0</td></tr>
<tr><td colspan="4">Angle of friction</td><td colspan="4">35°</td></tr>
<tr><td colspan="4">Poisson's ratio ν</td><td colspan="4">0.2</td></tr>
<tr><th colspan="8">Model parameters (for ISIS model)</th></tr>
<tr><td rowspan="2" colspan="2">Association factors</td><td>a_{V1}</td><td>a_{V2}</td><td>a_H</td><td>a_M</td><td colspan="2">a_Q</td></tr>
<tr><td>0.297</td><td>1.0</td><td>0.7</td><td>0.7</td><td colspan="2">0.7</td></tr>
<tr><td rowspan="8" colspan="2">Shape factors of yield surface</td><td colspan="2">e_1</td><td colspan="4">-0.2</td></tr>
<tr><td colspan="2">e_2</td><td colspan="4">0.0</td></tr>
<tr><td colspan="2">t_0</td><td colspan="4">0.1088</td></tr>
<tr><td colspan="2">m_0</td><td colspan="4">0.15</td></tr>
<tr><td colspan="2">h_0</td><td colspan="4">0.337</td></tr>
<tr><td colspan="2">q_0</td><td colspan="4">0.2</td></tr>
<tr><td colspan="2">β_1</td><td colspan="4">0.99</td></tr>
<tr><td colspan="2">β_2</td><td colspan="4">0.99</td></tr>
<tr><td colspan="2">Viscosity factor μ</td><td colspan="6">0.002</td></tr>
<tr><td colspan="2">Bell width (w_{bell}) (m)</td><td colspan="6">0.7</td></tr>
<tr><th colspan="8">Loading process</th></tr>
<tr><td>Load stage</td><td>V (kN)</td><td>H_2(kN)</td><td>H_3(kN)</td><td>Q(kNm)</td><td>M_2(kNm)</td><td>M_3(kNm)</td><td>Time increment</td></tr>
<tr><td>1</td><td>0.0 to 100.0</td><td>0.0</td><td>0.0</td><td>0.0</td><td>0.0</td><td>0.0</td><td>1000.0</td></tr>
<tr><td>2</td><td>100.0 to 8772.0</td><td>0.0</td><td>0.0</td><td>0.0</td><td>0.0</td><td>0.0</td><td>1000000.0</td></tr>
<tr><td>3</td><td>8772.0 to 81272.0</td><td>0.0</td><td>0.0</td><td>0.0</td><td>0.0</td><td>0.0</td><td>11000000.0</td></tr>
</table>

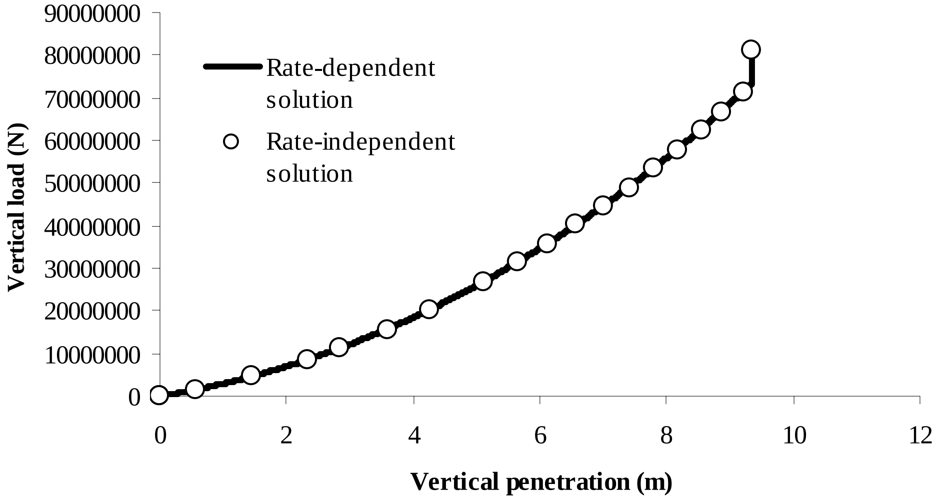

Figure 3.27 Installation of caisson using purely vertical loads

As shown in Figure 3.27, the results of the rate-dependent solution using the viscosity factor and the time increments as in Table 3.6 are almost the same as those of the rate-independent solution. This is a good starting point for the development of the ISIS model to the multiple-yield-surface version.

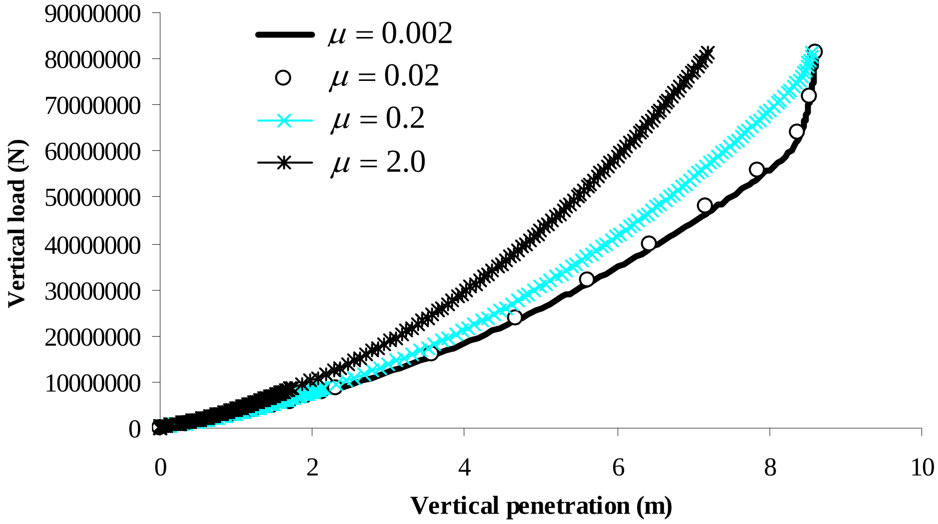

Figure 3.28 Rate-dependent solution with different values of the viscosity

Figure 3.28 shows the rate-dependent solution of the caisson given in Figure 3.26 and Table 3.6 but with various values of the viscosity factor. When the viscosity decreases, the result of the rate-dependent solution shows convergence to the rate-independent solution as shown by the plot of the rate-dependent solution corresponding to $\mu = 0.002$ (see Figure 3.27).

3.7 Discussion

In section 3.6, the numerical examples are mainly preformed under monotonic loadings. The analysis of footings under cyclic loading has not yet been performed. In principle, Model B, Model C and even the single-yield-surface ISIS model cannot reflect the behaviour of cyclic loadings correctly. In fact, since the unloading processes in these models are always elastic then the hysteresis which has been widely observed in experiments can not be simulated. This is also the motivation for the development of the multiple-yield-surface ISIS model. The main purpose of the numerical illustrations in this chapter is to validate the single-yield-surface ISIS model as the starting point for this development.

The yield surfaces used in the examples of section 3.6.1 essentially come from those of Model B (for clay) and Model C (for sand). Indeed, in true force space, the yield surfaces of the ISIS model and either Model C or Model B are exactly the same in the cases of circular flat footings and spudcans. Differences between ISIS and these conventional plasticity models are in the definitions of the flow rules, which are affected by the association factors. In the ISIS model, instead of using an additional potential function as in Model C or a modified yield function as in Model B, the flow rules are defined by the partial differentials of the yield function with respect to the generalised dissipative forces. In addition, the relations between true forces and generalised forces are controlled by the association factors. Therefore, it could be reasonable to predict that using appropriate values of the association factors, the ISIS Model cancapture entirely the results of either Model B or Model C.

Indeed, as presented in the examples for the circular flat footing and spudcan on clay (Examples 1 and 3) in section 3.6.1, by using the values of the association factors given in Table 3.1 and 3.3, the solution of Model B can be captured very well by the ISIS model. Furthermore, it is possible to establish the explicit relationship between the two models (Model B and ISIS) to determine the value of the association factors in ISIS. The details of this will be discussed in section 6.3.

In the analysis of caisson foundation, since the single-yield-surface model presented in this chapter is just the starting point of the ISIS model, the behaviour of caisson foundation cannot be reflected completely. Furthermore, the two previous models using conventional plasticity theory, Model B and Model C, also cannot simulate the behaviour of the caisson footing. Thus there is no theoretical solution that can be used to validate the new model. Consequently, no conclusion can be given for the comparison between the numerical results and the test results as well as for the consideration of the horizontal and moment loadings at this stage.

In section 3.6.2, a trial running of the ISIS model for the analysis of the penetration process of a caisson with and without suction assistance has been done to demonstrate the availability of the model. The idea about the application of the suction process in ISIS, which has been discussed in section 3.5.2, has been validated as shown in Figure 3.25. Besides, special features of the caisson foundation have been taken into account such as the vertical bearing capacity formulation and the shape factors of the yield surface of the caisson. These shape factors are observed experimentally from the series of tests in the Oxford University which can be found in Villalobos *et al.* (2004a) and Villalobos *et al.* (2004b).

3.8 Concluding remarks

The first version of an elasto-plastic model using hyperplasticity theory, named ISIS, has been achieved. This version is appropriate for the modelling of caisson foundation as well as circular flat footing and spudcan types. The main advantages of the ISIS model presented in this chapter include:

- Its formulation can express the plastic behaviour more rigorously and broadly by using the two functions without any further assumption. In addition, this derivation automatically obeys the thermodynamic principles.
- It can reproduce entirely the solutions of conventional plasticity models (Model B and Model C) in the analyses of circular flat footings and spudcans.
- By using the concept of association factor, the problems of associated plasticity and non-associated plasticity can be expressed in a general way.
- It gives the solution for the installation with and without suction assistance as well as the solution for the vertical loading for caisson foundation.
- It introduces the rate-dependent solution as the alternative solution as well as the starting point for the next developments to capture the foundation behaviour more realistically.

CHAPTER 4

CONTINUOUS HYPERPLASTICITY AND THE DISCRETIZATION FOR NUMERICAL ANALYSIS

4.1 Introduction

In the previous chapter, the single-yield-surface hyperplasticity model has been presented. Three kinds of analysis can be implemented in this model: elastic loading, elasto-plastic loading and elastic unloading. However, in geotechnics, the stiffness of soil depends not only on its properties but also on the stress level. This leads to the fact that, even in the unloading process, there are still changes of the soil stiffness that can be understood as elasto-plastic unloading processes causing so-called hysteresis. This response cannot be expressed by using the single-yield-surface model. This is therefore the main reason to develop an improved model, called continuous plasticity, in which internal variables in the form of continuous functions are introduced to allow the definition of the continuous yield surface. Consequently, the model can simulate the smooth transition between elastic and plastic behaviour in both loading and unloading processes, as well as predict with reasonable precision the hysteretic response of a foundation under cyclic loading.

This chapter presents firstly the establishment of the analytical expression of the continuous plasticity model. Secondly, the multiple-yield-surface model is derived by the discretization of the continuous plasticity formulation to serve the numerical analysis. Both rate-independent and rate-dependent solutions are considered in this model to show the theoretical basis. However, the numerical applications are implemented by using the rate-dependent solution only, because of its numerical advantages.

4.2 Continuous hyperplasticity formulation

In this model, the conventions for loads and displacements of the foundation are still used as those of the single-yield-surface model presented in chapter 3.

Based on the thermodynamic framework (Houlsby and Puzrin, 2000), there are two key functions defining a plasticity model: the free energy function and either the dissipation or the yield function. Thus, in order to establish the continuous hyperplasticity formulation, it is necessary to start with the free energy function and the yield function. The flow rule is followed to determine the incremental response. Then, the rate-dependent solution is introduced to provide another option for the numerical analysis.

4.2.1 Free energy functional and internal functions of the variables

Starting from the form of the Gibbs free energy function for a single-yield-surface model as in Eq. (3.3), further developments for the continuous hyperplasticity model are introduced. The internal variables now become functions of a dimensionless parameter η which varies from 0 to 1. The Gibbs free energy therefore becomes a functional as follows:

$$g = g_1 - \sigma_i \int_0^1 \hat{\alpha}_i(\eta) d\eta + g_2 \left[\hat{\alpha}_i \right] \tag{4.1}$$

In which the hat notation expresses that the variable is a function rather than a single value. The meaning of the dimensionless parameter η is that it represents the relative position of the variable in the yielding process. When η = 0, no plastic behaviour occurs. If η = 1, fully plastic behaviour occurs.

The term g_1 of the Gibbs function represents the elastic response and is still used as in Eq. (3.4). As mentioned in chapter 3, the elastic response of the foundation depends on the depth of the foundation, which is represented by the vertical plastic displacement α_V in the single-yield-surface model. Corresponding to this, in the continuous hyperplasticity model, the elastic response depends on the total vertical plastic displacement which is $\int_0^1 \hat{\alpha}_V(\eta)d\eta$ rather than the individual value of each $\hat{\alpha}_V(\eta)$. Therefore, there is no change in the mathematical expression for the elastic response in this version compared with that of the single-yield-surface version.

In order to establish the functional $g_2\left[\hat{\alpha}_i(\eta)\right]$, it is necessary to start from the expression of the function g_2 in Eq. (3.3). In the single-yield-surface model, using isotropic hardening, the function g_2 is taken as zero. However, considering kinematic hardening, this function requires more attention. Indeed, the term g_2 is the part of the work of plastic displacements that defines the kinematic hardening of the model. In order to choose the form for g_2, there are two issues that need to be involved: the dimension of the function and the relationship among plastic displacements. Firstly, g_2 is a part of the energy function that just includes the plastic displacements. Thus, it may be appropriate if g_2 is a function of squared terms of plastic displacements multiplied by factors which possess the dimensions of the stiffness factors to guarantee the dimension of energy. Secondly, the development of plastic displacements depends on the current deformations of the model which obviously involves the elastic parts. During the elastic stage, the relationship between the displacements is determined by the elastic stiffness factors as shown in function g_1. In the elasto-plastic stage, as discussed above, there are the factors having the dimensions of the stiffness factors in the function g_2. Therefore, it may be suitable and simple to use the relationship of elastic displacements in the g_1 term to apply the relationship of plastic displacements in the g_2 term. Of course, there could be many other ways to choose the form for g_2. However, in this study, the above expression seems to be one of the logical explanations. In the following section the details of g_2 are discussed.

The Gibbs free energy function of a single-yield-surface model can be rewritten with a slight modification for g_2 as follows:

$$g = g_1(V, H_2, H_3, Q, M_2, M_3) - V\alpha_V - H_2\alpha_{H2} - H_3\alpha_{H3} - Q\alpha_Q - M_2\alpha_{M2} - M_3\alpha_{M3} + g_2(\alpha_i^2) \quad (4.2)$$

In which the term g_1 is expressed in Eq. (3.4).

Based on the Thermodynamic framework in Houlsby and Puzrin (2000), the corresponding Helmholtz free energy function $f(\varepsilon_i, \alpha_i)$ coming from the Legendre transformation of Gibbs function $g(\sigma_i, \alpha_i)$ can be written as:

$$f = \frac{K_1 w^{e^2}}{2} + \frac{K_3 u_2^{e^2}}{2} + \frac{K_3 u_3^{e^2}}{2} + \frac{K_5 q^{e^2}}{2} + \frac{K_2 \theta_2^{e^2}}{2} + \frac{K_2 \theta_2^{e^2}}{2} + K_4 \theta_2^e u_3^e - K_4 \theta_3^e u_2^e - f_2(\alpha_i^2) \quad (4.3)$$

Where:

$$w^e = w - \alpha_V\, ;\; u_2^e = u_2 - \alpha_{H2}\, ;\; u_3^e = u_3 - \alpha_{H3}\, ;\; q^e = q - \alpha_Q\, ;\; \theta_2^e = \theta_2 - \alpha_{M2}\, ;\; \theta_3^e = \theta_3 - \alpha_{M3}$$

The components w^e, u_2^e, u_3^e, q^e, θ_2^e and θ_3^e are the elastic parts of the total displacements.

The expression of the Helmholtz energy function exhibits the relationship between the elastic displacement components in the model. As mentioned in the above paragraph, it is assumed that the g_2 term has the same style as the elastic part of the Helmholtz free energy. Therefore, the form of g_2 can be proposed as follows:

$$g_2 = \frac{H_1^* \alpha_V{}^2}{2} + \frac{H_3^* \alpha_{H2}{}^2}{2} + \frac{H_3^* \alpha_{H3}{}^2}{2} + \frac{H_5^* \alpha_Q{}^2}{2} + \frac{H_2^* \alpha_{M2}{}^2}{2} + \frac{H_2^* \alpha_{M3}{}^2}{2} + H_4^* \left(\alpha_{M2} \alpha_{H3} - \alpha_{M3} \alpha_{H2} \right) \tag{4.4}$$

Where H_1^*, H_2^*, H_3^*, H_4^* and H_5^* are the hardening parameters of α_V, α_{M2}, α_{M3}, α_{H2}, α_{H3} and α_Q as shown in Eq. (4.4). These hardening parameters can be chosen as functions of the stiffness factors K_1, K_2, K_3, K_4 and K_5 respectively and represent the kinematic haderning of the model.

Replacing the internal variables α_i in Eq. (4.4) by the internal functions $\hat{\alpha}_i(\eta)$, g_2 can be written as follows:

$$\begin{aligned} g_2 = & \int_0^1 \frac{\hat{H}_1^*(\eta) \hat{\alpha}_V^2(\eta)}{2} d\eta + \int_0^1 \frac{\hat{H}_3^*(\eta) \hat{\alpha}_{H2}^2(\eta)}{2} d\eta + \int_0^1 \frac{\hat{H}_3^*(\eta) \hat{\alpha}_{H3}^2(\eta)}{2} + \int_0^1 \frac{\hat{H}_5^*(\eta) \hat{\alpha}_Q^2(\eta)}{2} d\eta + \\ & + \int_0^1 \frac{\hat{H}_2^*(\eta) \hat{\alpha}_{M2}^2(\eta)}{2} d\eta + \int_0^1 \frac{\hat{H}_2^*(\eta) \hat{\alpha}_{M3}^2(\eta)}{2} d\eta + \int_0^1 \hat{H}_4^*(\eta) \left(\hat{\alpha}_{M2}(\eta) \hat{\alpha}_{H3}(\eta) - \hat{\alpha}_{M3}(\eta) \hat{\alpha}_{H2}(\eta) \right) d\eta \end{aligned} \tag{4.5}$$

In which the hardening parameters H_1^*, H_2^*, H_3^*, H_4^* and H_5^* also become the functions $\hat{H}_1^*(\eta)$, $\hat{H}_2^*(\eta)$, $\hat{H}_3^*(\eta)$, $\hat{H}_4^*(\eta)$ and $\hat{H}_5^*(\eta)$ respectively. These functions determine the shapes of force-displacement hardening curves. In this study, the hyperbolic shape will be used for the hardening curves. By using hyperbolae, the model is mathematically simple and capture the hardening observed from experiments. Thus, the hardening funtions can be defined as follows:

$$\hat{H}_i^{*}(\eta) = A_i K_i (b_i - \eta)^{n_i} \tag{4.5}$$

Where $i = \{1,\ldots,5\}$; A_i, b_i, n_i are parameters determining the shape of the hyperbolic curves. Discussions about the choice of hardening functions in continuum mechanics can be found in Puzrin and Houlsby (2001). In this study, they are extended to the general forms as in Eq. (4.5) to be able to capture the real curves obtained from tests of foundation behaviour.

The vertical generalised force can be defined as:

$$\hat{\chi}_V(\eta) = -\frac{\partial \hat{g}}{\partial \hat{\alpha}_V(\eta)} = -\frac{\partial \hat{g}_1}{\partial w_p}\frac{\partial w_p}{\partial \hat{\alpha}_V(\eta)} + \frac{\partial}{\partial \hat{\alpha}_V(\eta)}\left(V\int_0^1 \hat{\alpha}_V(\eta)\,d\eta\right) - \frac{\partial}{\partial \hat{\alpha}_V(\eta)}\left(\int_0^1 \hat{H}_1^{*}(\eta)\frac{\hat{\alpha}_V^{2}(\eta)}{2}\,d\eta\right) \tag{4.6}$$

where w_p is the total plastic displacement of the foundation and can be calculated as $w_p = \int_0^1 \hat{\alpha}_V(\eta)\,d\eta$. Therefore the vertical generalised force is:

$$\hat{\chi}_V = -\frac{\partial \hat{g}_1}{\partial w_p} + V - A_1 K_1 (b_1 - \eta)^{n_1}\,\hat{\alpha}_V(\eta) \tag{4.6bis}$$

The other generalised forces are defined as follows:

$$\hat{\chi}_{H2}(\eta) = -\frac{\partial \hat{g}}{\partial \hat{\alpha}_{H2}(\eta)} = \frac{\partial}{\partial \hat{\alpha}_{H2}(\eta)}\left(H_2\int_0^1 \hat{\alpha}_{H2}(\eta)\,d\eta\right) - \frac{\partial}{\partial \hat{\alpha}_{H2}(\eta)}\left(\int_0^1 \hat{H}_3^{*}(\eta)\frac{\hat{\alpha}_{H2}^{2}(\eta)}{2}\,d\eta\right)$$

$$-\frac{\partial}{\partial \hat{\alpha}_{H2}(\eta)}\left(\int_0^1 \hat{H}_4^*\left(\hat{\alpha}_{M2}(\eta)\hat{\alpha}_{H3}(\eta)-\hat{\alpha}_{M3}(\eta)\hat{\alpha}_{H2}(\eta)\right)d\eta\right)$$

$$= H_2 - A_3K_3(b_3-\eta)^{n_3}\,\hat{\alpha}_{H2}(\eta) + A_4K_4(b_4-\eta)^{n_4}\,\hat{\alpha}_{M3}(\eta) \tag{4.7}$$

$$\hat{\chi}_{H3}(\eta) = -\frac{\partial\hat{g}}{\partial\hat{\alpha}_{H3}(\eta)} = \frac{\partial}{\partial\hat{\alpha}_{H3}}\left(H_3\int_0^1\hat{\alpha}_{H3}(\eta)d\eta\right) - \frac{\partial}{\partial\hat{\alpha}_{H3}}\left(\int_0^1 \hat{H}_3^*(\eta)\frac{\hat{\alpha}_{H3}^2(\eta)}{2}d\eta\right)$$

$$-\frac{\partial}{\partial \hat{\alpha}_{H3}}\left(\int_0^1 \hat{H}_4^*\left(\hat{\alpha}_{M2}(\eta)\hat{\alpha}_{H3}(\eta)-\hat{\alpha}_{M3}(\eta)\hat{\alpha}_{H2}(\eta)\right)d\eta\right)$$

$$= H_3 - A_3K_3(b_3-\eta)^{n_3}\,\hat{\alpha}_{H3}(\eta) - A_4K_4(b_4-\eta)^{n_4}\,\hat{\alpha}_{M2}(\eta) \tag{4.8}$$

$$\hat{\chi}_{Q}(\eta) = -\frac{\partial\hat{g}}{\partial\hat{\alpha}_{Q}(\eta)} = \frac{\partial}{\partial\hat{\alpha}_{Q}(\eta)}\left(Q\int_0^1\hat{\alpha}_{Q}(\eta)d\eta\right) - \frac{\partial}{\partial\hat{\alpha}_{Q}^{(\eta_i)}}\left(\int_0^1 \hat{H}_5^*(\eta)\frac{\hat{\alpha}_{Q}^2(\eta)}{2}d\eta\right)$$

$$= Q - A_5K_5(b_5-\eta)^{n_5}\,\hat{\alpha}_{Q}(\eta) \tag{4.9}$$

$$\hat{\chi}_{M2}(\eta) = -\frac{\partial\hat{g}}{\partial\hat{\alpha}_{M2}(\eta)} = \frac{\partial}{\partial\hat{\alpha}_{M2}(\eta)}\left(M_2\int_0^1\hat{\alpha}_{M2}(\eta)d\eta\right) - \frac{\partial}{\partial\hat{\alpha}_{M2}(\eta)}\left(\int_0^1 \hat{H}_2^*(\eta)\frac{\hat{\alpha}_{M2}^2(\eta)}{2}d\eta\right)$$

$$-\frac{\partial}{\partial \hat{\alpha}_{M2}(\eta)}\left(\int_0^1 \hat{H}_4^*(\eta)\left(\hat{\alpha}_{M2}(\eta)\hat{\alpha}_{H3}(\eta)-\hat{\alpha}_{M3}(\eta)\hat{\alpha}_{H2}(\eta)\right)d\eta\right)$$

$$= M_2 - A_2K_2(b_2-\eta)^{n_2}\,\hat{\alpha}_{M2}(\eta) - A_4K_4(b_4-\eta)^{n_4}\,\hat{\alpha}_{H3}(\eta) \tag{4.10}$$

$$\hat{\chi}_{M3}(\eta) = -\frac{\partial\hat{g}}{\partial\hat{\alpha}_{M3}(\eta)} = \frac{\partial}{\partial\hat{\alpha}_{M3}(\eta)}\left(M_3\int_0^1\hat{\alpha}_{M3}(\eta)d\eta\right) - \frac{\partial}{\partial\hat{\alpha}_{M3}(\eta)}\left(\int_0^1 \hat{H}_2^*(\eta)\frac{\hat{\alpha}_{M3}^2(\eta)}{2}d\eta\right)$$

$$-\frac{\partial}{\partial \hat{\alpha}_{M3}(\eta)}\left(\int_0^1 \hat{H}_4^*(\eta)\left(\hat{\alpha}_{M2}(\eta)\hat{\alpha}_{H3}(\eta)-\hat{\alpha}_{M3}(\eta)\hat{\alpha}_{H2}(\eta)\right)d\eta\right)$$

$$= M_3 - A_2 K_2 (b_2 - \eta)^{n_2} \hat{\alpha}_{M3}(\eta) + A_4 K_4 (b_4 - \eta)^{n_4} \hat{\alpha}_{H2}(\eta) \tag{4.11}$$

Therefore, the coordinates of the centre of the yield surface at yielding level η in true force space can be defined as:

$$\hat{\rho}_V(\eta) = V - \hat{\bar{\chi}}_V(\eta) = A_1 K_1 (b_1 - \eta)^{n_1} \hat{\alpha}_V(\eta) \tag{4.12}$$

$$\hat{\rho}_{H2}(\eta) = H_2 - \hat{\bar{\chi}}_{H2}(\eta) = A_3 K_3 (b_3 - \eta)^{n_3} \hat{\alpha}_{H2}(\eta) - A_4 K_4 (b_4 - \eta)^{n_4} \hat{\alpha}_{M3}(\eta) \tag{4.13}$$

$$\hat{\rho}_{H3}(\eta) = H_3 - \hat{\bar{\chi}}_{H3}(\eta) = A_3 K_3 (b_3 - \eta)^{n_3} \hat{\alpha}_{H3}(\eta) + A_4 K_4 (b_4 - \eta)^{n_4} \hat{\alpha}_{M2}(\eta) \tag{4.14}$$

$$\hat{\rho}_Q(\eta) = Q - \hat{\bar{\chi}}_Q(\eta) = A_5 K_5 (b_5 - \eta)^{n_5} \hat{\alpha}_Q(\eta) \tag{4.15}$$

$$\hat{\rho}_{M2}(\eta) = M_2 - \hat{\bar{\chi}}_{M2}(\eta) = A_2 K_2 (b_2 - \eta)^{n_2} \hat{\alpha}_{M2}(\eta) + A_4 K_4 (b_4 - \eta)^{n_4} \hat{\alpha}_{H3}(\eta) \tag{4.16}$$

$$\hat{\rho}_{M3}(\eta) = M_3 - \hat{\bar{\chi}}_{M3}(\eta) = A_2 K_2 (b_2 - \eta)^{n_2} \hat{\alpha}_{M3}(\eta) - A_4 K_4 (b_4 - \eta)^{n_4} \hat{\alpha}_{H2}(\eta) \tag{4.17}$$

4.2.2 Yield functional

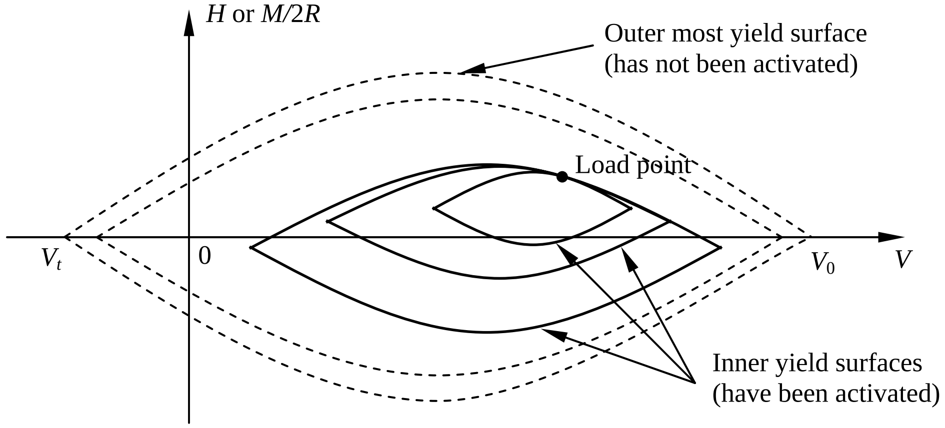

Figure 4.1 System of yield surfaces in continuous plasticity model

In the continuous-plasticity version of the ISIS model presented in this chapter, there is an infinite number of yield surfaces used in the analysis. The size of each inner yield surface is determined by a certain value of the internal parameter η as the scaled yield surface from the outermost yield surface (at $\eta = 1$). At a yielding level corresponding to a value of $0 < \eta^* < 1$, there is a set of yield surfaces which have been activated already corresponding to the values of $0 < \eta < \eta^*$. Therefore, every single incremental movement of the load point in the force space will be related to the translation and either expansion or contraction of that set of yield surfaces. Then, the plastic behaviour of the model at that time is determined by the combination of the plastic response caused by the yield surfaces activated. Figure 4.1 shows the system of yield surfaces in the continuous plasticity model.

At a certain value of η of a yield surface activated, the yield function can be described as follows:

$$\hat{y} = \hat{t} - \eta S \frac{\beta_{12}}{(t_0 + 1)^{(\beta_1 + \beta_2)}} \left(\left(\hat{v}_1 + t_0 \right)^2 \right)^{\frac{\beta_1}{2}} \times \left(\left(1 - \hat{v}_2 \right)^2 \right)^{\frac{\beta_2}{2}} = 0 \qquad (4.18)$$

Where

$$\hat{t} = \sqrt{\hat{h}_2^2 + \hat{h}_3^2 + \hat{m}_2^2 + \hat{m}_3^2 + \hat{q}^2 + 2e\left(\hat{h}_2 \hat{m}_3 - \hat{h}_3 \hat{m}_2 \right)} \qquad (4.19)$$

$$\hat{v}_1 = \frac{a_{V1} \hat{\chi}_V + (1 - a_{V1})\left(V - \hat{\rho}_V \right)}{\eta V_0} \qquad (4.20)$$

$$\hat{v}_2 = \frac{a_{V2} \hat{\chi}_V + (1 - a_{V2})\left(V - \hat{\rho}_V \right)}{\eta V_0} \qquad (4.21)$$

$$\hat{h}_2 = \frac{a_H \hat{\chi}_{H2} + (1 - a_H)\left(H_2 - \hat{\rho}_{H2} \right)}{h_0 V_0} \qquad (4.22)$$

$$\hat{h}_3 = \frac{a_H \hat{\chi}_{H3} + (1-a_H)\left(H_3 - \hat{\rho}_{H3}\right)}{h_0 V_0} \tag{4.23}$$

$$\hat{q} = \frac{a_Q \hat{\chi}_Q + (1-a_Q)\left(Q - \hat{\rho}_Q\right)}{2Rq_0 V_0} \tag{4.24}$$

$$\hat{m}_2 = \frac{a_M\left(\hat{\chi}_{M2} + d\,\hat{\chi}_{H3}\right) + (1-a_M)\left(M_2 + dH_3 - \left(\hat{\rho}_{M2} + d\,\hat{\rho}_{H3}\right)\right)}{2Rm_0 V_0} \tag{4.25}$$

$$\hat{m}_3 = \frac{a_M\left(\hat{\chi}_{M3} - d\,\hat{\chi}_{H2}\right) + (1-a_M)\left(M_3 - dH_2 - \left(\hat{\rho}_{M3} - d\,\hat{\rho}_{H2}\right)\right)}{2Rm_0 V_0} \tag{4.26}$$

The factors $S, \beta_{12}, \beta_1, \beta_2$, e and t_0 have similar definitions to those of the single-yield-surface model.

4.2.3 Flow rule and incremental response using rate-independent solution

The general expression of the flow rule may be written as:

$$\dot{\hat{\alpha}}_i = \hat{\lambda}\frac{\partial \hat{y}}{\partial \hat{\chi}_i} \tag{4.27}$$

where $\dot{\hat{\alpha}}_i$ is the rate of change of the plastic displacements at the yielding level η, and $\hat{\lambda}$ is the positive scalar multiplier of the η^{th} yield surface being considered.

In the same way as for the single-yield-surface model, the partial differentials of the yield surface in generalised dissipative force space will be (after removing the zero terms):

$$\frac{\partial \hat{y}}{\partial \hat{\chi}_V} = \frac{\partial \hat{y}}{\partial \hat{v}_1} \frac{\partial \hat{v}_1}{\partial \hat{\chi}_V} + \frac{\partial \hat{y}}{\partial \hat{v}_2} \frac{\partial \hat{v}_2}{\partial \hat{\chi}_V} \tag{4.28}$$

$$\frac{\partial \hat{y}}{\partial \hat{\chi}_{H2}} = \frac{\partial \hat{y}}{\partial \hat{t}} \left(\frac{\partial \hat{t}}{\partial \hat{h}_2} \frac{\partial \hat{h}_2}{\partial \hat{\chi}_{H2}} + \frac{\partial \hat{t}}{\partial \hat{m}_3} \frac{\partial \hat{m}_3}{\partial \hat{\chi}_{H2}} \right) \tag{4.29}$$

$$\frac{\partial \hat{y}}{\partial \hat{\chi}_{H3}} = \frac{\partial \hat{y}}{\partial \hat{t}} \left(\frac{\partial \hat{t}}{\partial \hat{h}_3} \frac{\partial \hat{h}_3}{\partial \hat{\chi}_{H3}} + \frac{\partial \hat{t}}{\partial \hat{m}_2} \frac{\partial \hat{m}_2}{\partial \hat{\chi}_{H3}} \right) \tag{4.30}$$

$$\frac{\partial \hat{y}}{\partial \hat{\chi}_Q} = \frac{\partial \hat{y}}{\partial \hat{t}} \frac{\partial \hat{t}}{\partial \hat{q}} \frac{\partial \hat{q}}{\partial \hat{\chi}_Q} \tag{4.31}$$

$$\frac{\partial \hat{y}}{\partial \hat{\chi}_{M2}} = \frac{\partial \hat{y}}{\partial \hat{t}} \frac{\partial \hat{t}}{\partial \hat{m}_2} \frac{\partial \hat{m}_2}{\partial \hat{\chi}_{M2}} \tag{4.32}$$

$$\frac{\partial \hat{y}}{\partial \hat{\chi}_{M3}} = \frac{\partial \hat{y}}{\partial \hat{t}} \frac{\partial \hat{t}}{\partial \hat{m}_3} \frac{\partial \hat{m}_3}{\partial \hat{\chi}_{M3}} \tag{4.33}$$

The partial differentials in Eqs. (4.28) to (4.33) can be expressed as follows:

$$\frac{\partial \hat{y}}{\partial \hat{v}_1} = -\eta\beta_1 \frac{\left(\dfrac{\beta_1 + \beta_2}{1 + t_0}\right)^{(\beta_1+\beta_2)}}{(\beta_1)^{\beta_1} (\beta_2)^{\beta_2}} \left[\left(\hat{v}_1 + t_0\right)^2\right]^{\left(\frac{\beta_1}{2} - 0.5\right)} \left(1 - \hat{v}_2\right) \left[\left(1 - \hat{v}_2\right)^2\right]^{\left(\frac{\beta_2}{2} - 0.5\right)} \tag{4.34}$$

$$\frac{\partial \hat{y}}{\partial \hat{v}_2} = \eta\beta_2 \frac{\left(\dfrac{\beta_1 + \beta_2}{1 + t_0}\right)^{(\beta_1+\beta_2)}}{(\beta_1)^{\beta_1} (\beta_2)^{\beta_2}} \left(\hat{v}_1 + t_0\right) \left[\left(\hat{v}_1 + t_0\right)^2\right]^{\left(\frac{\beta_1}{2} - 0.5\right)} \left[\left(1 - \hat{v}_2\right)^2\right]^{\left(\frac{\beta_2}{2} - 0.5\right)} \tag{4.35}$$

$$\frac{\partial \hat{v}_1}{\partial \hat{\chi}_V} = \frac{a_{V1}}{\eta V_0} \tag{4.36}$$

$$\frac{\partial \hat{v}_2}{\partial \hat{\chi}_V} = \frac{a_{V2}}{\eta V_0} \tag{4.37}$$

$$\frac{\partial \hat{h}_2}{\partial \hat{\chi}_{H2}} = \frac{a_H}{h_0 V_0} \tag{4.38}$$

$$\frac{\partial \hat{h}_3}{\partial \hat{\chi}_{H3}} = \frac{a_H}{h_0 V_0} \tag{4.39}$$

$$\frac{\partial \hat{q}}{\partial \hat{\chi}_Q} = \frac{a_Q}{2Rq_0 V_0} \tag{4.40}$$

$$\frac{\partial \hat{m}_2}{\partial \hat{\chi}_{M2}} = \frac{a_M}{2Rm_0 V_0} \tag{4.41}$$

$$\frac{\partial \hat{m}_2}{\partial \hat{\chi}_{H3}} = \frac{a_M d}{2Rm_0 V_0} \tag{4.42}$$

$$\frac{\partial \hat{m}_3}{\partial \hat{\chi}_{M3}} = \frac{a_M}{2Rm_0 V_0} \tag{4.43}$$

$$\frac{\partial \hat{m}_3}{\partial \hat{\chi}_{H2}} = \frac{-a_M d}{2Rm_0 V_0} \tag{4.44}$$

$$\frac{\partial \hat{y}}{\partial \hat{t}} = 1.0 \tag{4.45}$$

and

$$\frac{\partial \hat{t}}{\partial \hat{h}_2} = \frac{\hat{h}_2 + e\hat{m}_3}{\hat{t}} \tag{4.46}$$

$$\frac{\partial \hat{t}}{\partial \hat{h}_3} = \frac{\hat{h}_3 - e\hat{m}_2}{\hat{t}} \tag{4.47}$$

$$\frac{\partial \hat{t}}{\partial \hat{q}} = \frac{\hat{q}}{\hat{t}} \tag{4.48}$$

$$\frac{\partial \hat{t}}{\partial \hat{m}_2} = \frac{\hat{m}_2 - e\hat{h}_3}{\hat{t}} \tag{4.49}$$

$$\frac{\partial \hat{t}}{\partial \hat{m}_3} = \frac{\hat{m}_3 + e\hat{h}_2}{\hat{t}} \tag{4.50}$$

In the incremental response of a continuous-yield-surface hyperplasticity model, at a certain value of η, there are two possibilities. The first is that the loading point is still inside the η^{th} yield surface, and the response of the model is elasto-plastic from the beginning ($\eta = 0$) to η^* ($\eta^* < \eta$). The variable η^* represents the maximum value of η at which the yield surface has been activated. It also means that the value of the yield function is negative ($\hat{y}(\eta) < 0$) and the multiplier $\hat{\lambda}(\eta)$ equals zero for the range of $\eta^* < \eta < 1.0$. The second possibility is that the loading point lies on the η^{th} yield surface. Then, the plastic behaviour of the η^{th} yield surface is activated and leads to the conditions: $\hat{y}(\eta) = 0$ and $\hat{\lambda}(\eta) > 0$ for the range of $0.0 < \eta \le \eta^*$.

Once the η^{th} yield surface is activated, the incremental expression of $\hat{y}(\eta)$ can be written as follows:

$$\dot{\hat{y}} = \frac{\partial \hat{y}}{\partial \hat{\alpha}_i}\dot{\hat{\alpha}}_i + \frac{\partial \hat{y}}{\partial \hat{\chi}_j}\dot{\hat{\chi}}_j + \frac{\partial \hat{y}}{\partial \sigma_k}\dot{\sigma}_k = 0 \tag{4.51}$$

In general, the generalised dissipative forces can be expressed as follows:

$$\hat{\chi}_j = \hat{\bar{\chi}}_j = -\frac{\partial \hat{g}}{\partial \hat{\alpha}_j} = -\frac{\partial \hat{g}_1}{\partial \hat{\alpha}_j} + \sigma_j - \frac{\partial \hat{g}_2}{\partial \hat{\alpha}_j} \tag{4.52}$$

Then, the velocity of the generalised dissipative forces can be expressed as:

$$\dot{\hat{\chi}}_j = -\frac{\partial^2 \hat{g}_1}{\partial \hat{\alpha}_j \partial \sigma_l} \dot{\sigma}_l - \frac{\partial^2 \hat{g}_1}{\partial \hat{\alpha}_j \partial \hat{\alpha}_l} \dot{\hat{\alpha}}_l + \dot{\sigma}_j - \frac{\partial^2 \hat{g}_2}{\partial \hat{\alpha}_j \partial \hat{\alpha}_l} \dot{\hat{\alpha}}_l \tag{4.53}$$

The incremental change of plastic displacement is defined as:

$$\dot{\hat{\alpha}}_l = \hat{\lambda} \frac{\partial \hat{y}}{\partial \hat{\chi}_l} \tag{4.54}$$

By substituting Eq. (4.53) and Eq. (4.54), Eq. (4.51) becomes:

$$\frac{\partial \hat{y}}{\partial \hat{\alpha}_i} \left(\hat{\lambda} \frac{\partial \hat{y}}{\partial \hat{\chi}_i} \right) + \frac{\partial \hat{y}}{\partial \hat{\chi}_j} \left(\begin{array}{l} -\dfrac{\partial^2 \hat{g}_1}{\partial \hat{\alpha}_j \partial \sigma_l} \dot{\sigma}_l \\ -\dfrac{\partial^2 \hat{g}_1}{\partial \hat{\alpha}_j \partial \hat{\alpha}_l} \left(\hat{\lambda} \dfrac{\partial \hat{y}}{\partial \hat{\chi}_l} \right) + \dot{\sigma}_j \\ -\dfrac{\partial^2 \hat{g}_2}{\partial \hat{\alpha}_j \partial \hat{\alpha}_l} \left(\hat{\lambda} \dfrac{\partial \hat{y}}{\partial \hat{\chi}_l} \right) \end{array} \right) + \frac{\partial \hat{y}}{\partial \sigma_k} \dot{\sigma}_k = 0 \tag{4.55}$$

By converting Eq. (4.55), the scalar multiplier $\hat{\lambda}(\eta)$ can be calculated as follows:

$$\hat{\lambda} = \frac{\dfrac{\partial \hat{y}}{\partial \hat{\chi}_j} \dot{\sigma}_j + \dfrac{\partial \hat{y}}{\partial \sigma_k} \dot{\sigma}_k - \dfrac{\partial \hat{y}}{\partial \hat{\chi}_j} \dfrac{\partial^2 \hat{g}_1}{\partial \hat{\alpha}_j \partial \sigma_l} \dot{\sigma}_l}{\dfrac{\partial \hat{y}}{\partial \hat{\chi}_j} \left(\dfrac{\partial^2 \hat{g}_1}{\partial \hat{\alpha}_j \partial \hat{\alpha}_l} + \dfrac{\partial^2 \hat{g}_2}{\partial \hat{\alpha}_j \partial \hat{\alpha}_l} \right) \dfrac{\partial \hat{y}}{\partial \hat{\chi}_l} - \dfrac{\partial \hat{y}}{\partial \hat{\alpha}_i} \dfrac{\partial \hat{y}}{\partial \hat{\chi}_i}} \tag{4.56}$$

Therefore, the plastic response can be expressed as follows:

$$\dot{\hat{\alpha}}_m = \frac{\dfrac{\partial \hat{y}}{\partial \hat{\chi}_j}\dot{\sigma}_j + \dfrac{\partial \hat{y}}{\partial \sigma_k}\dot{\sigma}_k - \dfrac{\partial \hat{y}}{\partial \hat{\chi}_j}\dfrac{\partial^2 \hat{g}_1}{\partial \hat{\alpha}_j \partial \sigma_l}\dot{\sigma}_l}{\dfrac{\partial \hat{y}}{\partial \hat{\chi}_j}\left(\dfrac{\partial^2 \hat{g}_1}{\partial \hat{\alpha}_j \partial \hat{\alpha}_l} + \dfrac{\partial^2 \hat{g}_2}{\partial \hat{\alpha}_j \partial \hat{\alpha}_l}\right)\dfrac{\partial \hat{y}}{\partial \hat{\chi}_l} - \dfrac{\partial \hat{y}}{\partial \hat{\alpha}_i}\dfrac{\partial \hat{y}}{\partial \hat{\chi}_i}}\frac{\partial \hat{y}}{\partial \hat{\chi}_m} \qquad (4.57)$$

The full details of the partial differentials are straightforward and similar to those of the single-yield-surface model, but are lengthy. Therefore, it is considered inappropriate to present them here.

Finally, the incremental response for a rate-independent solution is written as follows:

$$\delta\varepsilon_i = -\frac{\partial^2 \hat{g}_1}{\partial \sigma_i \partial \sigma_j}\delta\sigma_j - \int_0^{\eta^*} \frac{\partial^2 \hat{g}_1}{\partial \sigma_i \partial \hat{\alpha}_j(\eta)}\hat{\lambda}(\eta)\frac{\partial \hat{y}(\eta)}{\partial \hat{\chi}_j(\eta)}d\eta + \int_0^{\eta^*} \hat{\lambda}(\eta)\frac{\partial \hat{y}(\eta)}{\partial \hat{\chi}_i(\eta)}d\eta \qquad (4.58)$$

In which $\hat{\lambda}(\eta)$ can be calculated by using Eq. (4.56) with the variations $\delta\sigma_i$ instead of using $\dot{\sigma}_i$; η^* is the maximum value of η at which the η^{th} yield surface has been activated.

4.2.4 Incremental response using rate-dependent solution

The rate-dependent solution has been proposed for the single-yield-surface hyperplasticity model in Houlsby and Puzrin (2001) and then rate-dependent hyperplasticity with internal functions has been developed in Puzrin and Houlsby (2003). By using this concept for the foundation problem in the ISIS model, the dissipation function now becomes a functional and can be separated into two functionals which are the force potential $z\left[\sigma_i,\hat{\alpha}_i,\dot{\hat{\alpha}}_i\right]$ and the dissipation potential $w\left[\sigma_i,\hat{\alpha}_i,\hat{\chi}_i\right]$.

$$d=\int_0^1 \hat{d}(\eta)d\eta = z\left[\sigma_i,\hat{\alpha}_i,\dot{\hat{\alpha}}_i\right]+w\left[\sigma_i,\hat{\alpha}_i,\hat{\chi}_i\right] \tag{4.59}$$

If the dissipation function $\hat{d}(\eta)$ can be written as:

$$\hat{d}(\eta)=\left(\frac{\partial \hat{z}\left(\sigma_i,\hat{\alpha}_i(\eta),\dot{\hat{\alpha}}_i(\eta)\right)}{\partial \dot{\hat{\alpha}}_i(\eta)}\right)\dot{\hat{\alpha}}_i(\eta) \tag{4.60}$$

Then a Legendre-Fenchel transformation can give:

$$\hat{w}\left(\sigma_i,\hat{\alpha}_i(\eta),\hat{\chi}_i(\eta)\right)=\hat{d}(\eta)-\hat{z}\left(\sigma_i,\hat{\alpha}_i(\eta),\dot{\hat{\alpha}}_i(\eta)\right)=\hat{\chi}_i(\eta)\dot{\hat{\alpha}}_i(\eta)-\hat{z}\left(\sigma_i,\hat{\alpha}_i(\eta),\dot{\hat{\alpha}}_i(\eta)\right) \tag{4.61}$$

In which the definitions of the generalised dissipative forces $\hat{\chi}_i(\eta)$ and the rates of change of the state variables $\hat{\alpha}_i(\eta)$ can be expressed as the internal functions as follows:

$$\hat{\chi}_i(\eta)=\frac{\partial \hat{z}}{\partial \dot{\hat{\alpha}}_i(\eta)} \tag{4.62}$$

$$\dot{\hat{\alpha}}_i(\eta)=\frac{\partial \hat{w}}{\partial \hat{\chi}_i(\eta)} \tag{4.63}$$

It can be seen that the use of the flow potential function at internal coordinate η, $\hat{w}(\eta)$, is analogous to that of the yield function $\hat{y}(\eta)$ in the case of using the rate-independent solution. However, since $\hat{z}(\eta)$ is not the homogeneous first-order function of $\dot{\hat{\alpha}}_i(\eta)$, the flow potential function cannot be required to be zero during the calculation (see Puzrin and Houlsby, 2003). As mentioned in chapter 2, in this study, the linear viscosity form is applied for $\hat{w}$ as follows:

$$\hat{w}(\eta) = \frac{\left\langle \hat{y}(\eta) \right\rangle^2}{2\mu} \tag{4.64}$$

where μ is the viscosity factor; $\hat{y}(\eta)$ is the yield function as in Eq. (4.18) of the rate-independent solution.

Developing the analysis as in the single-yield-surface model for rate-dependent solution, the incremental stress-strain response using rate-dependent behaviour can be written as:

$$\dot{\varepsilon}_i = -\frac{\partial^2 \hat{g}_1}{\partial\sigma_i \partial\sigma_j}\dot{\sigma}_j - \int_0^1 \frac{\partial^2 \hat{g}_1}{\partial\sigma_i \partial\hat{\alpha}_j(\eta)} \frac{\left\langle \hat{y}(\eta) \right\rangle}{\mu} \frac{\partial \hat{y}(\eta)}{\partial \hat{\chi}_j(\eta)} d\eta + \int_0^1 \frac{\left\langle \hat{y}(\eta) \right\rangle}{\mu} \frac{\partial \hat{y}(\eta)}{\partial \hat{\chi}_i(\eta)} d\eta \tag{4.65}$$

Converting Eq. (4.65) to the incremental form as:

$$\delta\varepsilon_i = -\frac{\partial^2 \hat{g}_1}{\partial\sigma_i \partial\sigma_j}\delta\sigma_j - dt\int_0^1 \frac{\partial^2 \hat{g}_1}{\partial\sigma_i \partial\hat{\alpha}_j(\eta)} \frac{\left\langle \hat{y}(\eta) \right\rangle}{\mu} \frac{\partial \hat{y}(\eta)}{\partial \hat{\chi}_j(\eta)} d\eta + dt\int_0^1 \frac{\left\langle \hat{y}(\eta) \right\rangle}{\mu} \frac{\partial \hat{y}(\eta)}{\partial \hat{\chi}_i(\eta)} d\eta \tag{4.66}$$

where μ and *dt* are the viscosity factor and the time increment respectively.

4.3 Discretization formulation – multiple-yield-surface model (ISIS)

In section 4.2, the formulation of the continuous-plasticity model has been presented and gives the possibility of capturing the cyclic behaviour. However, since this model is expressed in term of continuous functions, it is necessary to establish a discretization formulation based on the continuous formulation. This work needs some careful attention to ensure its consistency.

This section presents the discretization process from the continuous formulation to the multiple-yield-surface formulation for the ISIS model. The features of the continuous model will be rewritten in terms of the multiple-yield-surface model.

4.3.1 Discretization of the free energy functional and internal variable functions

From the section 4.2.1, the full expression of the Gibbs free energy function of the continuous plasticity model has been described. In this section, firstly, the integration terms will be changed to summation terms in the Gibbs function. Secondly, the definitions of variables will be established corresponding to the new expression of the Gibbs function.

By changing from integration to summation, the Gibbs free energy function of the continuous plasticity model now can be rewritten in terms of a multiple-yield-surface model as follows:

$$
\begin{aligned}
g = & -\frac{V^2}{2K_1} - \frac{K_2 H_2^2}{2D} - \frac{K_2 H_3^2}{2D} - \frac{Q^2}{2K_5} - \frac{K_3 M_2^2}{2D} - \frac{K_3 M_3^2}{2D} + \frac{K_4 H_3 M_2}{D} - \frac{K_4 H_2 M_3}{D} \\
& - \left(\begin{aligned} & V \sum_{i=1}^{N} \alpha_V{}^{(\eta_i)} d\eta_i + H_2 \sum_{i=1}^{N} \alpha_{H2}{}^{(\eta_i)} d\eta_i + H_3 \sum_{i=1}^{N} \alpha_{H3}{}^{(\eta_i)} d\eta_i + Q \sum_{i=1}^{N} \alpha_Q{}^{(\eta_i)} d\eta_i + \\ & + M_2 \sum_{i=1}^{N} \alpha_{M2}{}^{(\eta_i)} d\eta_i + M_3 \sum_{i=1}^{N} \alpha_{M3}{}^{(\eta_i)} d\eta_i \end{aligned} \right) + \\
& + \sum_{i=1}^{N} \frac{H_1^{*(\eta_i)} \alpha_V^{2(\eta_i)}}{2} d\eta_i + \sum_{i=1}^{N} \frac{H_3^{*(\eta_i)} \alpha_{H2}^{2\ (\eta_i)}}{2} d\eta_i + \sum_{i=1}^{N} \frac{H_3^{*(\eta_i)} \alpha_{H3}^{2\ (\eta_i)}}{2} d\eta_i + \sum_{i=1}^{N} \frac{H_5^{*(\eta_i)} \alpha_Q^{2(\eta_i)}}{2} d\eta_i + \\
& + \sum_{i=1}^{N} \frac{H_2^{*(\eta_i)} \alpha_{M2}^{2\ (\eta_i)}}{2} d\eta_i + \sum_{i=1}^{N} \frac{H_2^{*(\eta_i)} \alpha_{M3}^{2\ (\eta_i)}}{2} d\eta_i + \sum_{i=1}^{N} H_4^{*(\eta_i)} \left(\alpha_{M2}{}^{(\eta_i)} \alpha_{H3}{}^{(\eta_i)} - \alpha_{M3}{}^{(\eta_i)} \alpha_{H2}{}^{(\eta_i)} \right) d\eta_i
\end{aligned}
\tag{4.67}
$$

The hat notations are abandoned to show that the variables are no longer functions, they become a series of discretized values. *N* is the number of yield surfaces that are chosen to simulate the continuous yield surface. The factor η_i can be defined simply by the uniform distribution as $\eta_i = \frac{i}{N}$. Then, $d\eta_i = \frac{i}{N} - \frac{i-1}{N} = \frac{1}{N}$.

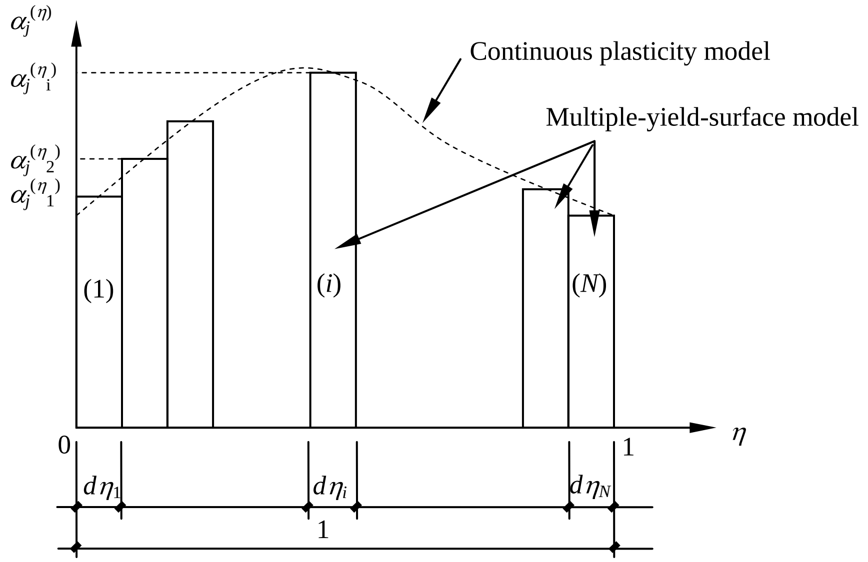

Figure 4.2 Discretization of internal function of state variables in internal coordinate η

A further simplification assumption here is that the *N* value chosen is big enough to make a small enough value for $d\eta_i$ in which the values of $\alpha_V{}^{(\eta_i)}$, $\alpha_{H2}{}^{(\eta_i)}$, $\alpha_{H3}{}^{(\eta_i)}$, $\alpha_Q{}^{(\eta_i)}$, $\alpha_{M2}{}^{(\eta_i)}$ and

$\alpha_{M3}^{(\eta_i)}$ can be treated approximately as constants. Figure 4.2 shows the concept of a uniform distribution of the internal variables $\alpha_j^{(\eta_i)}$ discretized from the internal function $\overset{\wedge}{\alpha}_j(\eta)$. The definitions in Eq. (4.5) now become:

$$H_1^{*(\eta_i)} = A_1 K_1 (b_1 - \eta_i)^{n_1} \tag{4.68}$$

$$H_2^{*(\eta_i)} = A_2 K_2 (b_2 - \eta_i)^{n_2} \tag{4.69}$$

$$H_3^{*(\eta_i)} = A_3 K_3 (b_3 - \eta_i)^{n_3} \tag{4.70}$$

$$H_4^{*(\eta_i)} = A_4 K_4 (b_4 - \eta_i)^{n_4} \tag{4.71}$$

$$H_5^{*(\eta_i)} = A_5 K_5 (b_5 - \eta_i)^{n_5} \tag{4.72}$$

The generalised forces can be defined as:

$$\begin{aligned}\overline{\chi}_V^{(\eta_i)} &= -N\frac{\partial g}{\partial \alpha_V^{(\eta_i)}} = -N\frac{\partial g_1}{\partial \alpha_V^{(\eta_i)}} + N\frac{\partial}{\partial \alpha_V^{(\eta_i)}}\left(V\sum_{i=1}^{N}\alpha_V^{(\eta_i)}d\eta_i\right) - N\frac{\partial}{\partial \alpha_V^{(\eta_i)}}\left(\sum_{i=1}^{N}A_1K_1(b_1-\eta_i)^{n_1}\frac{\alpha_V^{2(\eta_i)}}{2}d\eta_i\right)\\ &= -\frac{\partial g_1}{\partial w_p} + V - A_1K_1(b_1-\eta_i)^{n_1}\alpha_V^{(\eta_i)}\end{aligned} \tag{4.73}$$

$$\begin{aligned}\overline{\chi}_{H2}^{(\eta_i)} &= -N\frac{\partial g}{\partial \alpha_{H2}^{(\eta_i)}} = N\frac{\partial}{\partial \alpha_{H2}^{(\eta_i)}}\left(H_2\sum_{i=1}^{N}\alpha_{H2}^{(\eta_i)}d\eta_i\right) - N\frac{\partial}{\partial \alpha_{H2}^{(\eta_i)}}\left(\sum_{i=1}^{N}A_3K_3(b_3-\eta_i)^{n_3}\frac{\alpha_{H2}^{2\ (\eta_i)}}{2}d\eta_i\right)\\ &\quad - N\frac{\partial}{\partial \alpha_{H2}^{(\eta_i)}}\left(\sum_{i=1}^{N}A_4K_4(b_4-\eta_i)^{n_4}\left(\alpha_{M2}^{(\eta_i)}\alpha_{H3}^{(\eta_i)} - \alpha_{M3}^{(\eta_i)}\alpha_{H2}^{(\eta_i)}\right)d\eta_i\right)\\ &= H_2 - A_3K_3(b_3-\eta_i)^{n_3}\alpha_{H2}^{(\eta_i)} + A_4K_4(b_4-\eta_i)^{n_4}\alpha_{M3}^{(\eta_i)}\end{aligned} \tag{4.74}$$

$$\begin{aligned}\overline{\chi}_{H3}^{(\eta_i)} &= -N\frac{\partial g}{\partial \alpha_{H3}^{(\eta_i)}} = N\frac{\partial}{\partial \alpha_{H3}^{(\eta_i)}}\left(H_3\sum_{i=1}^{N}\alpha_{H3}^{(\eta_i)}d\eta_i\right) - N\frac{\partial}{\partial \alpha_{H3}^{(\eta_i)}}\left(\sum_{i=1}^{N}A_3K_3(b_3-\eta_i)^{n_3}\frac{\alpha_{H3}^{2\ (\eta_i)}}{2}d\eta_i\right)\\ &\quad - N\frac{\partial}{\partial \alpha_{H3}^{(\eta_i)}}\left(\sum_{i=1}^{N}A_4K_4(b_4-\eta_i)^{n_4}\left(\alpha_{M2}^{(\eta_i)}\alpha_{H3}^{(\eta_i)} - \alpha_{M3}^{(\eta_i)}\alpha_{H2}^{(\eta_i)}\right)d\eta_i\right)\end{aligned}$$

$$= H_3 - A_3 K_3 \left(b_3 - \eta_i\right)^{n_3} \alpha_{H3}^{(\eta_i)} - A_4 K_4 \left(b_4 - \eta_i\right)^{n_4} \alpha_{M2}^{(\eta_i)} \tag{4.75}$$

$$\overline{\chi}_{Q}^{(\eta_i)} = -N \frac{\partial g}{\partial \alpha_Q^{(\eta_i)}} = N \frac{\partial}{\partial \alpha_Q^{(\eta_i)}} \left(Q \sum_{i=1}^{N} \alpha_Q^{(\eta_i)} d\eta_i \right) - N \frac{\partial}{\partial \alpha_Q^{(\eta_i)}} \left(\sum_{i=1}^{N} A_5 K_5 \left(b_5 - \eta_i\right)^{n_5} \frac{\alpha_Q^{2(\eta_i)}}{2} d\eta_i \right)$$

$$= Q - A_5 K_5 \left(b_5 - \eta_i\right)^{n_5} \alpha_Q^{(\eta_i)} \tag{4.76}$$

$$\overline{\chi}_{M2}^{(\eta_i)} = -N \frac{\partial g}{\partial \alpha_{M2}^{(\eta_i)}} = N \frac{\partial}{\partial \alpha_{M2}^{(\eta_i)}} \left(M_2 \sum_{i=1}^{N} \alpha_{M2}^{(\eta_i)} d\eta_i \right) - N \frac{\partial}{\partial \alpha_{M2}^{(\eta_i)}} \left(\sum_{i=1}^{N} A_2 K_2 \left(b_2 - \eta_i\right)^{n_2} \frac{\alpha_{M2}^{2\ (\eta_i)}}{2} d\eta_i \right)$$

$$- N \frac{\partial}{\partial \alpha_{M2}^{(\eta_i)}} \left(\sum_{i=1}^{N} A_4 K_4 \left(b_4 - \eta_i\right)^{n_4} \left(\alpha_{M2}^{(\eta_i)} \alpha_{H3}^{(\eta_i)} - \alpha_{M3}^{(\eta_i)} \alpha_{H2}^{(\eta_i)} \right) d\eta_i \right)$$

$$= M_2 - A_2 K_2 \left(b_2 - \eta_i\right)^{n_2} \alpha_{M2}^{(\eta_i)} - A_4 K_4 \left(b_4 - \eta_i\right)^{n_4} \alpha_{H3}^{(\eta_i)} \tag{4.77}$$

$$\overline{\chi}_{M3}^{(\eta_i)} = -N \frac{\partial g}{\partial \alpha_{M3}^{(\eta_i)}} = N \frac{\partial}{\partial \alpha_{M3}^{(\eta_i)}} \left(M_3 \sum_{i=1}^{N} \alpha_{M3}^{(\eta_i)} d\eta_i \right) - N \frac{\partial}{\partial \alpha_{M3}^{(\eta_i)}} \left(\sum_{i=1}^{N} A_2 K_2 \left(b_2 - \eta_i\right)^{n_2} \frac{\alpha_{M3}^{2\ (\eta_i)}}{2} d\eta_i \right)$$

$$- N \frac{\partial}{\partial \alpha_{M3}^{(\eta_i)}} \left(\sum_{i=1}^{N} A_4 K_4 \left(b_4 - \eta_i\right)^{n_4} \left(\alpha_{M2}^{(\eta_i)} \alpha_{M2}^{(\eta_i)} - \alpha_{M3}^{(\eta_i)} \alpha_{H2}^{(\eta_i)} \right) d\eta_i \right)$$

$$= M_3 - A_2 K_2 \left(b_2 - \eta_i\right)^{n_2} \alpha_{M3}^{(\eta_i)} + A_4 K_4 \left(b_4 - \eta_i\right)^{n_4} \alpha_{H2}^{(\eta_i)} \tag{4.78}$$

Consequently, the coordinates of the centre of the i^{th} yield surface in true force space can be defined as follows:

$$\rho_V^{(\eta_i)} = V - \overline{\chi}_V^{(\eta_i)} - \frac{\partial g_1}{\partial w_p} = A_1 K_1 \left(b_1 - \eta_i\right)^{n_1} \alpha_V^{(\eta_i)} \tag{4.79}$$

$$\rho_{H2}^{(\eta_i)} = H_2 - \overline{\chi}_{H2}^{(\eta_i)} = A_3 K_3 \left(b_3 - \eta_i\right)^{n_3} \alpha_{H2}^{(\eta_i)} - A_4 K_4 \left(b_4 - \eta_i\right)^{n_4} \alpha_{M3}^{(\eta_i)} \tag{4.80}$$

$$\rho_{H3}^{(\eta_i)} = H_3 - \overline{\chi}_{H3}^{(\eta_i)} = A_3 K_3 \left(b_3 - \eta_i\right)^{n_3} \alpha_{H3}^{(\eta_i)} + A_4 K_4 \left(b_4 - \eta_i\right)^{n_4} \alpha_{M2}^{(\eta_i)} \tag{4.81}$$

$$\rho_Q^{(\eta_i)} = Q - \overline{\chi}_Q^{(\eta_i)} = A_5 K_5 \left(b_5 - \eta_i\right)^{n_5} \alpha_Q^{(\eta_i)} \tag{4.82}$$

$$\rho_{M2}^{(\eta_i)} = M_2 - \overline{\chi}_{M2}^{(\eta_i)} = A_2 K_2 \left(b_2 - \eta_i\right)^{n_2} \alpha_{M2}^{(\eta_i)} + A_4 K_4 \left(b_4 - \eta_i\right)^{n_4} \alpha_{H3}^{(\eta_i)} \tag{4.83}$$

$$\rho_{M3}^{(\eta_i)} = M_3 - \overline{\chi}_{M3}^{(\eta_i)} = A_2 K_2 \left(b_2 - \eta_i\right)^{n_2} \alpha_{M3}^{(\eta_i)} - A_4 K_4 \left(b_4 - \eta_i\right)^{n_4} \alpha_{H2}^{(\eta_i)} \tag{4.84}$$

4.3.2 Yield functions

By using the same style of yield function as in the continuous plasticity model, the *ith* yield surface has the following form:

$$y^{(i)} = t^{(\eta_i)} - \eta_i S^{(\eta_i)} \beta_{12} \left(\left(v_1^{(\eta_i)} + t_0\right)^2\right)^{\frac{\beta_1}{2}} \times \left(\left(1 - v_2^{(\eta_i)}\right)^2\right)^{\frac{\beta_2}{2}} \tag{4.85}$$

Where

$$t^{(\eta_i)} = \sqrt{h_2^{2(\eta_i)} + h_3^{2(\eta_i)} + m_2^{2(\eta_i)} + m_3^{2(\eta_i)} + q^{2(\eta_i)} + 2a\left(h_2^{(\eta_i)} m_3^{(\eta_i)} - h_3^{(\eta_i)} m_2^{(\eta_i)}\right)} \tag{4.86}$$

$$v_1^{(\eta_i)} = \frac{a_{V1} \chi_V^{(\eta_i)} + \left(1 - a_{V1}\right)\left(V - \rho_V^{(\eta_i)}\right)}{\eta_i V_0} \tag{4.87}$$

$$v_2^{(\eta_i)} = \frac{a_{V2} \chi_V^{(\eta_i)} + \left(1 - a_{V2}\right)\left(V - \rho_V^{(\eta_i)}\right)}{\eta_i V_0} \tag{4.88}$$

$$h_2^{(\eta_i)} = \frac{a_H \chi_{H2}^{(\eta_i)} + \left(1 - a_H\right)\left(H_2 - \rho_{H2}^{(\eta_i)}\right)}{h_0 V_0} \tag{4.89}$$

$$h_3^{(\eta_i)} = \frac{a_H \chi_{H3}^{(\eta_i)} + \left(1 - a_H\right)\left(H_3 - \rho_{H3}^{(\eta_i)}\right)}{h_0 V_0} \tag{4.90}$$

$$q^{(\eta_i)} = \frac{a_Q \chi_Q^{(\eta_i)} + \left(1 - a_Q\right)\left(Q - \rho_Q^{(\eta_i)}\right)}{2R q_0 V_0} \tag{4.91}$$

$$m_2^{(\eta_i)} = \frac{a_M \left(\chi_{M2}^{(\eta_i)} + d\chi_{H3}^{(\eta_i)}\right) + \left(1 - a_M\right)\left(M_2 + dH_3 - \left(\rho_{M2}^{(\eta_i)} + d\rho_{H3}^{(\eta_i)}\right)\right)}{2R m_0 V_0} \tag{4.92}$$

$$m_3^{(\eta_i)} = \frac{a_M \left(\chi_{M3}^{(\eta_i)} - d\chi_{H2}^{(\eta_i)}\right) + \left(1 - a_M\right)\left(M_3 - dH_2 - \left(\rho_{M3}^{(\eta_i)} - d\rho_{H2}^{(\eta_i)}\right)\right)}{2R m_0 V_0} \tag{4.93}$$

The factors, $\beta_{12}, \beta_1, \beta_2$ and t_0, have similar definitions to those in the single-yield-surface model. $S^{(\eta_i)}$ can be defined by using the formulation of S in single-yield-surafce model and replacing v_1 and v_2 by $v_1^{(\eta_i)}$ and $v_2^{(\eta_i)}$.

4.3.3 Modification of the yield functions

In the development of the continuous plasticity model as well as the discretization of the multiple-yield-surface model, the initial size of the first yield surface can be infinitesimal depending on the η or η_i values. In order to control this initial size in the vertical direction, modifications of the definitions of $v_1^{(\eta_i)}$ and $v_2^{(\eta_i)}$ are expressed as follows:

$$v_1^{(\eta_i)} = \frac{a_{V1}\chi_V^{(\eta_i)} + (1 - a_{V1})\left(V - \rho_V^{(\eta_i)}\right)}{\eta_{0i}V_0} \tag{4.87bis}$$

$$v_2^{(\eta_i)} = \frac{a_{V2}\chi_V^{(\eta_i)} + (1 - a_{V2})\left(V - \rho_V^{(\eta_i)}\right)}{\eta_{0i}V_0} \tag{4.88bis}$$

There is a new factor η_{0i} which is used in the denominators of $v_1^{(\eta_i)}$ and $v_2^{(\eta_i)}$, as in Eq. (4.87bis) and Eq. (4.88bis), instead of η_i as in Eq. (4.87) and Eq. (4.88). The purpose of the introduction of this new factor is to be able to control the longitudinal size of the yield surfaces and the longitudinal distribution of these yield surfaces in true force space corresponding to specific kinds of footing. The calculation of η_{0i} can be expressed as follows:

$$\eta_{0i} = \eta_0^{initial} + \left(1.0 - \eta_0^{initial}\right)\frac{i}{N} \tag{4.94}$$

where $\eta_0^{initial}$ is an initial parameter which can be chosen in the range [0,…,1]. The choice of this parameter depends on the kind of footing considered. It is clear that when $\eta_0^{initial} = 0$, the factor $\eta_{0i} = \dfrac{i}{N} = \eta_i$ and Eqs. (4.87bis) and (4.88bis) reduce to the forms of Eqs. (4.87) and (4.88). By using the expression in Eq. (4.94), the distribution of the yield surfaces in the longitudinal axis (*V*-axis) is uniform from $\eta_0^{initial} V_0$ to V_0 when η_i goes from 1 to *N*.

Figure 4.3 shows an illustration of a multiple-yield-surface model using five yield surfaces in a fully plastic behaviour under vertical loading. The longitudinal sizes of the yield surfaces are calculated by using the relationship in Eq. (4.94) and Eq. (4.85).

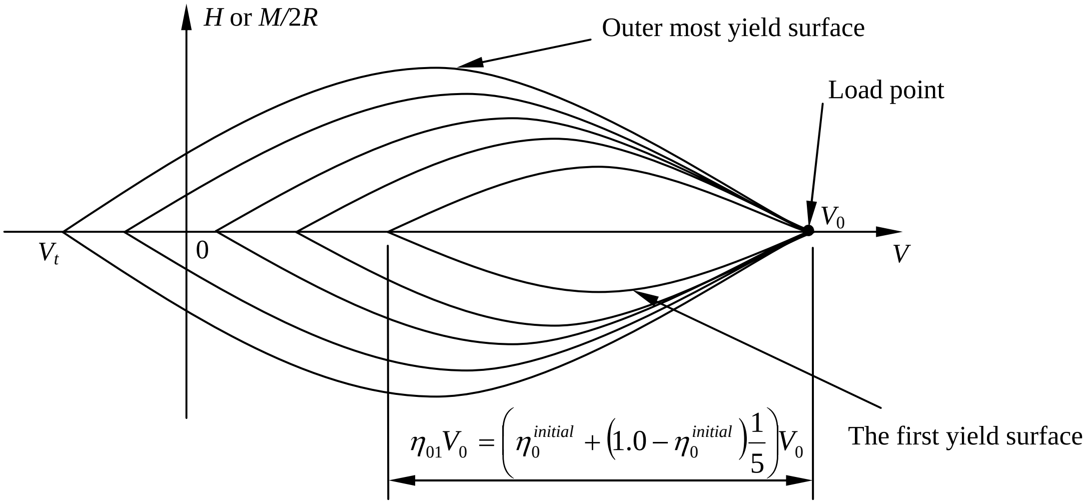

Figure 4.3 System of five yield surfaces in a full plastic vertical loading

The motivation of the introduction of the factor η_{0i} as well as the initial parameter $\eta_0^{initial}$ is to control the negative plastic displacements that occur during the unloading process especially in vertical unloading. There is a well-known phenomenon that during the vertical unloading process of the foundation, there always are some small negative plastic displacements. This phenomenon can be considered as the softening in plasticity models. It can produce a small decrease in the depth of the footing after the unloading process. By using the concept of the multiple-yield-surface model, the theoretical explanation for this is straightforward. However, quantitatively, by using the uniform distribution of the yield surfaces corresponding to the zero value of $\eta_0^{initial}$ in multiple-yield-surface model, the negative plastic displacements obtained after the unloading process can be overestimated. In fact, since the size of the first yield surface is too small, the first elastic unloading process will be terminated very early. It also means that the plastic behaviour that causes the negative plastic displacement increments will occur too early as well. This has effects not only in the flow rule resulting in negative increments but also in the decrease of the size of the whole yield surface system. Consequently, the vertical negative plastic displacement increases faster and faster in an unrealistic way. Therefore, it is necessary to control the developments of the negative plastic displacement increments and the introduction of $\eta_0^{initial}$ is an appropriate way to do this.

4.3.4 Flow rule and incremental response using rate-independent solution

In order to avoid any misunderstanding about the subscripts, the n^{th} yield surface is considered instead of the i^{th} yield surface as in the previous section. In the rate-independent solution, the flow rule of the n^{th} yield surface corresponding to the internal coordinate $\eta_n = \dfrac{n}{N}$ can be defined as follows:

$$\dot{\alpha}_l^{(\eta_n)} = \lambda^{(\eta_n)} \frac{\partial y^{(n)}}{\partial \chi_l^{(\eta_n)}} \tag{4.95}$$

where $\lambda^{(\eta_n)}$ is the non-negative scalar multiplier of the n^{th} yield function; the subscript l represents the notations V, H_2, H_3, Q, M_2 and M_3 respectively.

The establishment of $\lambda^{(\eta_n)}$, the detailed definitions of the flow rules and the incremental response are similar to those of the continuous plasticity model presented in section 4.2.3. The continuous values of η are replaced by the discretized value of η_n in the equations from Eq. (4.28) to Eq. (4.50). However, since there is a difference in the definition of the generalised force $\overline{\chi}_j^{(\eta_n)}$ in the multiple-yield-surface model compared with that of the continuous plasticity model, it is worth re-establishing some of these formulations with care.

When the n^{th} yield surface is activated, its incremental expression can be written as follows:

$$\overset{\bullet}{y}^{(\eta_n)}(\alpha_i,\chi_i,\sigma_i)=\frac{\partial y^{(n)}}{\partial\alpha_i^{(\eta_n)}}\overset{\bullet}{\alpha}_i^{(\eta_n)}+\frac{\partial y^{(n)}}{\partial\chi_j^{(\eta_n)}}\overset{\bullet}{\chi}_j^{(\eta_n)}+\frac{\partial y^{(n)}}{\partial\sigma_k^{(\eta_n)}}\overset{\bullet}{\sigma}_k=0 \tag{4.96}$$

where $\eta_n=\dfrac{n}{N}$.

Corresponding to the n^{th} yield surface, the generalised forces can be expressed as follows:

$$\chi_j^{(\eta_n)}=-N\frac{\partial g}{\partial\alpha_j^{(\eta_n)}}=-N\frac{\partial g_1}{\partial\alpha_j^{(\eta_n)}}+N\sigma_j-N\frac{\partial g_2}{\partial\alpha_j^{(\eta_n)}} \tag{4.97}$$

Thus, the velocity of the generalised forces is:

$$\overset{\bullet}{\chi}_j^{(\eta_n)}=\left(-\frac{\partial^2 g_1}{\partial\alpha_j^{(\eta_n)}\partial\sigma_l}\overset{\bullet}{\sigma}_l-\frac{\partial^2 g_1}{\partial\alpha_j^{(\eta_n)}\partial\alpha_l^{(\eta_n)}}\overset{\bullet}{\alpha}_l^{(\eta_n)}+\overset{\bullet}{\sigma}_j-\frac{\partial^2 g_2}{\partial\alpha_j^{(\eta_n)}\partial\alpha_l^{(\eta_n)}}\overset{\bullet}{\alpha}_l^{(\eta_n)}\right)N \tag{4.98}$$

The incremental changes of plastic displacements $\overset{\bullet}{\alpha}_l^{(\eta_i)}$ have been defined as in Eq. (9.45). Substituting Eq. (4.95) and Eq. (4.98) into Eq. (4.96), it becomes:

$$\frac{\partial y^{(n)}}{\partial \alpha_i^{(\eta_n)}}\left(\lambda^{(\eta_n)}\frac{\partial y^{(n)}}{\partial \chi_i^{(\eta_n)}}\right)+\frac{\partial y^{(n)}}{\partial \chi_j^{(\eta_n)}}N\begin{pmatrix} -\dfrac{\partial^2 g_1}{\partial \alpha_j^{(\eta_n)}\partial \sigma_l}\dot{\sigma}_l \\ -\dfrac{\partial^2 g_1}{\partial \alpha_j^{(\eta_n)}\partial \alpha_l^{(\eta_n)}}\left(\lambda^{(\eta_n)}\dfrac{\partial y^{(\eta_n)}}{\partial \chi_l^{(\eta_n)}}\right)+\dot{\sigma}_j \\ -\dfrac{\partial^2 g_2}{\partial \alpha_j^{(\eta_n)}\partial \alpha_l^{(\eta_n)}}\left(\lambda^{(\eta_n)}\dfrac{\partial y^{(n)}}{\partial \chi_l^{(\eta_n)}}\right)\end{pmatrix}+\frac{\partial y^{(n)}}{\partial \sigma_k}\dot{\sigma}_k=0 \quad (4.99)$$

The scalar multiplier $\lambda^{(\eta_n)}$ is therefore calculated by converting Eq. (4.99):

$$\lambda^{(\eta_n)}=\frac{N\dfrac{\partial y^{(n)}}{\partial \chi_j^{(\eta_n)}}\dot{\sigma}_j+\dfrac{\partial y^{(n)}}{\partial \sigma_k}\dot{\sigma}_k-N\dfrac{\partial y^{(n)}}{\partial \chi_j^{(\eta_n)}}\dfrac{\partial^2 g_1}{\partial \alpha_j^{(\eta_n)}\partial \sigma_l}\dot{\sigma}_l}{N\dfrac{\partial y^{(n)}}{\partial \chi_j^{(\eta_n)}}\left(\dfrac{\partial^2 g_1}{\partial \alpha_j^{(\eta_n)}\partial \alpha_l^{(\eta_n)}}+\dfrac{\partial^2 g_2}{\partial \alpha_j^{(\eta_n)}\partial \alpha_l^{(\eta_n)}}\right)\dfrac{\partial y^{(n)}}{\partial \chi_l^{(\eta_n)}}-\dfrac{\partial y^{(n)}}{\partial \alpha_i^{(\eta_n)}}\dfrac{\partial y^{(n)}}{\partial \chi_i^{(\eta_n)}}} \quad (4.100)$$

The incremental response, in general, is written as follows:

$$\dot{\varepsilon}_i=-\frac{\partial^2 g_1}{\partial \sigma_i \partial \sigma_j}\dot{\sigma}_j-\sum_{n=1}^{N}\frac{\partial^2 g_1}{\partial \sigma_i \partial \alpha_j^{(\eta_n)}}\dot{\alpha}_j^{(\eta_n)}+\sum_{n=1}^{N}\dot{\alpha}_j^{(\eta_n)} \quad (4.101)$$

For the rate-independent case, the detailed expression of the incremental response in Eq. (4.101) can be rewritten as:

$$\delta\varepsilon_i=-\frac{\partial^2 g_1}{\partial \sigma_i \partial \sigma_j}\delta\sigma_j-\sum_{n=1}^{N}\frac{\partial^2 g_1}{\partial \sigma_i \partial \alpha_j^{(\eta_n)}}\lambda^{(\eta_n)}\frac{\partial y^{(n)}}{\partial \chi_j^{(\eta_n)}}+\sum_{n=1}^{N}\lambda^{(\eta_n)}\frac{\partial y^{(n)}}{\partial \chi_j^{(\eta_n)}} \quad (4.102)$$

In which the multiplier $\lambda^{(\eta_n)}$ is calculated by using $\delta\sigma_j$, $\delta\sigma_k$ and $\delta\sigma_l$ instead of using the rate form $\dot{\sigma}_j$, $\dot{\sigma}_k$ and $\dot{\sigma}_l$ as in Eq. (4.100).

4.3.5 Flow rule and incremental response using rate-dependent solution

In the multiple-yield-surface model, the dissipation function d can be defined as a summation of N internal dissipation functions, $d^{(n)}$, as follows:

$$d = \sum_{n=1}^{N} d^{(n)} \tag{4.103}$$

By using the rate-dependent solution proposed in Houlsby and Puzrin (2001) and Puzrin and Houlsby (2003), each internal dissipation function, $d^{(n)}$, can be separated into two functions: the force potential function $z^{(n)}\left(\sigma_i, \alpha_i^{(\eta_n)}, \overset{\bullet}{\alpha}_i^{(\eta_n)}\right)$ and flow potential function $w^{(n)}\left(\sigma_i, \alpha_i^{(\eta_n)}, \chi_i^{(\eta_n)}\right)$. The relationship between $z^{(n)}$, $w^{(n)}$ and $d^{(n)}$ can be expressed as follows:

$$z^{(n)}\left(\sigma_i, \alpha_i^{(\eta_n)}, \overset{\bullet}{\alpha}_i^{(\eta_n)}\right) + w^{(n)}\left(\sigma_i, \alpha_i^{(\eta_n)}, \chi_i^{(\eta_n)}\right) = d^{(n)} = \chi_i^{(\eta_n)} \overset{\bullet}{\alpha}_i^{(\eta_n)} \tag{4.104}$$

Therefore, the definition of the rate of plastic displacements, $\overset{\bullet}{\alpha}_i^{(\eta_n)}$, is made by the Legendre transformation between $z^{(n)}$ and $w^{(n)}$ in which $\alpha_i^{(\eta_n)}$ and σ_i are passive variables:

$$\overset{\bullet}{\alpha}_i^{(\eta_n)} = \frac{\partial w^{(n)}}{\partial \chi_i^{(\eta_n)}} \tag{4.105}$$

By the use of linear viscosity as proposed in Houlsby and Puzrin (2001), the flow potential funtion $w^{(n)}$ can be defined as:

$$w^{(n)}\left(\sigma_i, \alpha_i^{(\eta_n)}, \chi_i^{(\eta_n)}\right) = \frac{\left\langle y^{(n)}\left(\sigma_i, \alpha_i^{(\eta_n)}, \chi_i^{(\eta_n)}\right)\right\rangle^2}{2\mu} \tag{4.106}$$

It should be noted that $w^{(n)}$ is often greater than zero in plastic behaviour and equals zero when the rates of plastic displacements, $\overset{\bullet}{\alpha}_i^{(\eta_n)}$ are all equal to zero, which means that the rate-independent condition is recovered for the elastic case.

By substituting Eq. (106) into Eq. (105), the plastic incremental response corresponding to the internal coordinate η_n is:

$$\overset{\bullet}{\alpha}_i^{(\eta_n)} = \frac{\partial w^{(n)}\left(\sigma_i, \alpha_i^{(\eta_n)}, \chi_i^{(\eta_i)}\right)}{\partial \chi_i^{(\eta_n)}} = \frac{\left\langle y^{(n)}\left(\sigma_i, \alpha_i^{(\eta_n)}, \chi_i^{(\eta_n)}\right)\right\rangle}{\mu} \frac{\partial y^{(n)}\left(\sigma_i, \alpha_i^{(\eta_n)}, \chi_i^{(\eta_n)}\right)}{\partial \chi_i^{(\eta_n)}} \tag{4.107}$$

The changes of the internal variables are now no longer independent from the time increment. Therefore the variation form of the plastic displacement increments can be written as follows:

$$\delta\alpha_i^{(\eta_n)} = \frac{\left\langle y^{(n)}\right\rangle}{\mu} \frac{\partial y^{(n)}}{\partial \chi_i^{(\eta_n)}} \delta t \tag{4.108}$$

Figure 4.4 shows an outline of the variation of plastic displacement under an incremental loading. The total value of the increase of the plastic displacement component is the area bounded by the dashed curves.

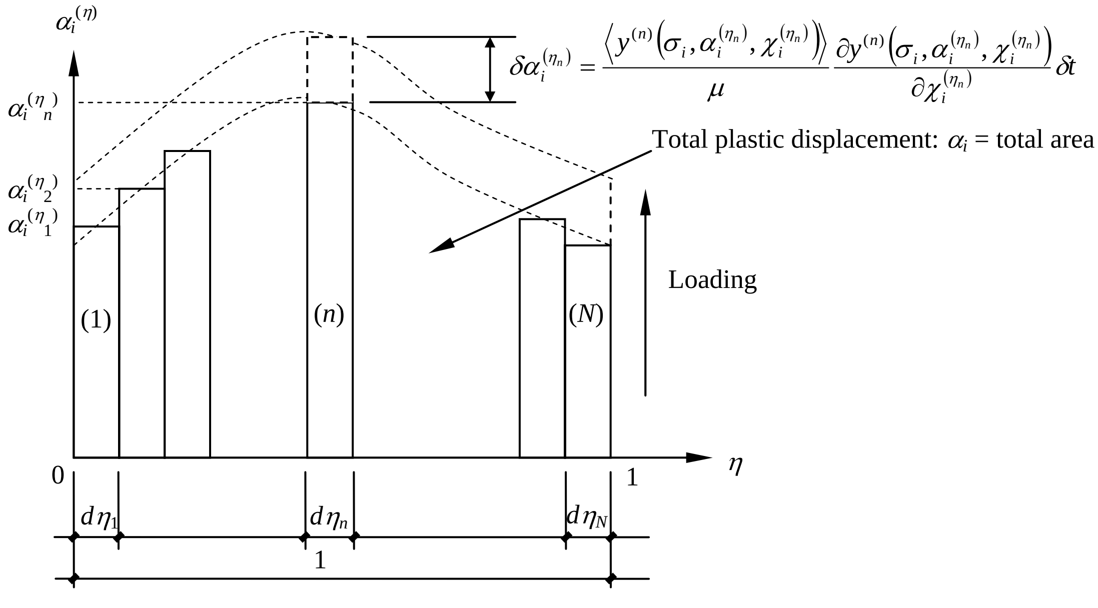

Figure 4.4 Illustration of an increment of a plastic displacement variable in the multiple-yield-surface model

By substituting Eq. (4.108) into the general relationship in Eq. (4.101), the incremental response of the multiple-yield-surface model using the rate-dependent solution can be expressed as follows:

$$\delta\varepsilon_i = -\frac{\partial^2 g_1}{\partial\sigma_i\partial\sigma_j}\delta\sigma_j - \sum_{n=1}^{N}\left(\frac{\partial^2 g_1}{\partial\sigma_i\partial\alpha_j^{(\eta_n)}} - 1\right)\frac{\left\langle y^{(n)}\left(\sigma_i,\alpha_i^{(\eta_n)},\chi_i^{(\eta_n)}\right)\right\rangle}{\mu}\frac{\partial y^{(n)}\left(\sigma_i,\alpha_i^{(\eta_n)},\chi_i^{(\eta_n)}\right)}{\partial\chi_j^{(\eta_n)}}d\eta_n\delta t \tag{4.109}$$

4.4 Application of hardening rules to the model

As mentioned in Collins and Houlsby (1997) and Houlsby and Puzrin (2000, 2002), by the use of the free energy function and either the dissipation function or the yield function, the elasto-plastic behaviour of the foundation can be fully described in the model, including the hardening. There are four options corresponding to four different hardening rules: elastic-perfectly plastic (no hardening), elastic-isotropic hardening plastic, elastic-kinematic hardening plastic and elastic-mixed isotropic-kinematic hardening plastic. The following discussion presents these cases and gives the reasons for the choice of the hardening rule applied in the model. The key functions proposed are based on those of the multiple-yield-surface ISIS model of this study. They are expressed in general forms for ease of discussion.

4.4.1 Possibilities of hardening rules

(1) *Elastic - Perfectly plastic*

In this behaviour, there is no hardening during the analysis. The Gibbs free energy function and either the yield function or the dissipation function can have the forms as follows:

$$g = g_1(\sigma_i) + \sigma_i\sum_{n=1}^{N}\alpha_i^{(\eta_n)}d\eta_n \tag{4.110}$$

$$y^{(n)} = y^{(n)}\left(\sigma_{0i}, \sigma_i, \chi_i^{(\eta_n)}\right) = 0 \text{ or } d^{(n)} = k_i^{(n)}\left(\sigma_{0i}, \sigma_i\right)\left|\overset{\bullet}{\alpha}_i^{(\eta_n)}\right| \qquad (4.111)$$

In which σ_{0i} are the forces defining the original sizes of the yield surface in force-axes; the term g_2, in this case, is zero. If σ_{0i} do not depend on the plastic displacements α_i then the functions $k_i^{(n)}\left(\sigma_{0i}, \sigma_i\right)$ do not involve the plastic displacements either. Thus, once the load point touches the yield surface, perfectly plastic behaviour occurs. Then the generalised forces are:

$$\chi_i^{(\eta_n)} = \frac{\partial d^{(n)}}{\partial \overset{\bullet}{\alpha}_i^{(\eta_n)}} = k_i^{(n)}\left(\sigma_{0i}, \sigma_i\right)\operatorname{sgn}\left(\overset{\bullet}{\alpha}_i^{(\eta_n)}\right) \qquad (4.112)$$

It can be found that at a certain force level, the plastic displacement increment is independent of the generalised force. Figure (4.5) shows the outline of this behaviour. Therefore, when yielding occurs, there is no change of the yield surface which means that perfectly plastic behaviour occurs.

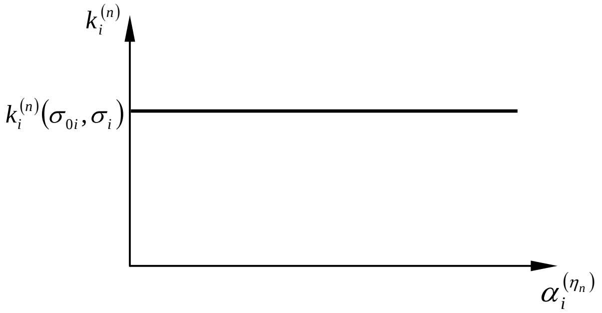

Figure 4.5 Perfectly plastic behaviour

(2) *Elastic – Isotropic hardening plastic*

Using isotropic hardening, the two main functions should be:

$$g = g_1\left(\sigma_i\right) + \sigma_i \sum_{n=1}^{N} \alpha_i^{(\eta_n)} d\eta_n \qquad (4.113)$$

$$y^{(n)} = y^{(n)}\left(\sigma_{0i}, \sigma_i, \alpha_i^{(\eta_n)}, \chi_i^{(\eta_n)}\right) = 0 \qquad (4.114)$$

Again, in this case, the term g_2 equals to zero. The existence of the plastic displacement variables in the yield function can lead to changes of the size of the yield surface during the yielding process. In fact, from the definition of the generalised forces, $\chi_i^{(\eta_n)} = \overline{\chi}_i^{(\eta_n)} = -N \dfrac{\partial g}{\partial \alpha_i^{(\eta_n)}}$, it can be found that $\rho_i^{(\eta_n)} = \sigma_i - \chi_i^{(\eta_n)} = 0$. This means that the centres of the yield surfaces in both true force space and generalised force space always coincide. This leads to the fact that there is no translation, but only expansion of the yield surfaces, and this type of hardening is defined as isotropic hardening.

(3) *Elastic – Kinematic hardening plastic*

By the use of the full expression of the Gibbs free energy function and the definitions of the yield functions which do not depend on plastic displacement variables, the hardening rule of the model can be demonstrated to involve kinematic hardening. The two functions, in this case, can be written as follows:

$$g = g_1(\sigma_i) + \sigma_i \sum_{n=1}^{N} \alpha_i^{(\eta_n)} d\eta_n + \sum_{n=1}^{N} g_2^{(n)}\left(\alpha_i^{(\eta_n)2}\right) \tag{4.115}$$

$$y^{(n)} = y^{(n)}\left(\sigma_{0i}, \sigma_i, \chi_i^{(\eta_n)}\right) = 0 \tag{4.116}$$

Since there is no plastic displacement variable in the yield function, the yield surfaces activated are therefore just move around in true force space without expansion. The details of the translations of the yield surfaces are defined by the definition of the "back forces" as:

$$\rho_i^{(\eta_n)} = \sigma_i - \chi_i^{(\eta_n)} = -\frac{\partial\left(\sum_{n=1}^{N} g_2^{(n)}\left(\alpha_i^{(\eta_n)2}\right)\right)}{\partial \alpha_i^{(\eta_n)}} \tag{4.117}$$

This means that the terms $g_2^{(n)}$ in the Gibbs free energy function govern the translation of the yield surfaces during the analysis. Note that the work caused by the plastic displacements is not dissipated completely but is partly stored. In this case, a part of this work is stored through the term $\sum_{n=1}^{N} g_2^{(n)}\left(\alpha_i^{(\eta_n)2}\right)$ in the Gibbs free energy function.

(4) *Elastic – Mixed isotropic-kinematic hardening plastic*

$$g = g_1(\sigma_i) + \sigma_i \sum_{n=1}^{N} \alpha_i^{(\eta_n)} d\eta_n + \sum_{n=1}^{N} g_2^{(n)}\left(\alpha_i^{(\eta_n)2}\right) \tag{4.118}$$

$$y^{(n)} = y^{(n)}\left(\sigma_{0i}, \sigma_i, \alpha_i^{(\eta_n)}, \chi_i^{(\eta_n)}\right) = 0 \tag{4.119}$$

By using the above forms of the Gibbs free energy function and the yield function, a mixed isotropic-kinematic hardening rule is achieved. In fact, referring to the previous two possibilities of hardening rules (isotropic and kinematic), the existence of the plastic displacement variables in the yield function can lead to the isotropic hardening. Meanwhile, the appearance of the term $\sum_{n=1}^{N} g_2^{(n)}\left(\alpha_i^{(\eta_n)2}\right)$ in the Gibbs free energy function represents the kinematic hardening. In this case, the yield surfaces activated will have both actions: expansion (or contraction) and translation in the true force space.

4.4.2 Discussion

In the above expressions, the four possibilities of the hardening rules that can be applied for the model have been presented. In the multiple-yield-surface ISIS model, the mixed isotropic-kinematic hardening rule has been used.

Firstly, as presented in the previous sections, all the yield functions that have been proposed in the single-yield-surface model, in the continuous plasticity model, and in the multiple-yield-surface model, have the form $y = y(V_0(w_p), \sigma_i, \chi_i) = 0$. In which the vertical bearing capacity, $V_0(w_p)$, plays the role of the force σ_{0i} and also is a function of the vertical plastic displacement w_p (or α_V). Therefore, by the use of $V_0(w_p)$ in the yield function, the ISIS model automatically obeys the isotropic hardening rule. The physical meaning of this aspect is that the vertical bearing capacity of the foundation not only depends on the soil properties but also depends on the depth represented by w_p. The deeper the footing is penetrated the larger the elastic range can be, essentially depending on $V_0(w_p)$. Furthermore, due to negative vertical forces (tensile forces) occurring in the leeward caisson of a multi-caisson, or applications of large moments or horizontal loads and small vertical loads, negative vertical displacements can occur. This leads to the possibility that the caisson is pulled out of the soil. During this process, the depth of the footing, w_p, decreases and the response of the foundation becomes weaker. By using isotropic hardening, this phenomenon can be explained clearly. Since the decrease of w_p leads to the decrease of $V_0(w_p)$, a contraction of the yield surface results, known as the softening phenomenon. In continuum mechanics using finite element analysis, solving the system of equations with softening can be a very complex process. However, fortunately, by using the macro element concept, there is no problem with the numerical solution. Modelling the softening phenomenon therefore also leads to the need to use the isotropic type of hardening in the model of this study.

Secondly, the appearance of the terms $\sum_{n=1}^{N} g_2^{(n)}\left(\alpha_i^{(\eta_n)2}\right)$ allows kinematic hardening represented by the concept of "back forces" $\rho_i^{(\eta_n)}$ in the equations from Eq. (4.79) to Eq. (4.84) playing the role of the coordinates of the centres of the yield surfaces in the true force space. As mentioned in the above expression of the kinematic hardening, the work caused by the plastic displacement is not completely dissipated. A part of this work is stored in the free energy function. The terms $\sum_{n=1}^{N} g_2^{(n)}\left(\alpha_i^{(\eta_n)2}\right)$ represent this work.

So far, there is still no way to estimate correctly the part of energy dissipated and the part of energy stored in the mechanisms proposed. Therefore, using the mixed isotropic-kinematic hardening rule and adjusting the energy functions to capture the real behaviour, one may obtain the appropriate solution.

4.5 Numerical illustrations

This section presents a number of numerical examples to validate the model. There are two main features that should be highlighted by the numerical results. Firstly, the numerical illustrations could be used to prove that the multiple-yield-surface model has some advantages compared with the single-yield-surface model. In the second feature, the availabilities of the model will be illustrated by the comparisons with test results to demonstrate that the model can capture the real behaviour with reasonable precision.

The functions of hardening determining the shapes of the force-displacement curves can be considered as the kernel functions of the model. As in formulations from Eq. (4.68) to Eq. (4.72), these kernel functions are now chosen with the specific expressions as follows.

$$H_1^{*(\eta_i)} = 1.0K_1(1.0-\eta_i)^{3.0} \tag{4.120}$$

$$H_2^{*(\eta_i)} = 0.5K_2(1.0-\eta_i)^{3.0} \tag{4.121}$$

$$H_3^{*(\eta_i)} = 0.5K_3(1.0-\eta_i)^{3.0} \tag{4.122}$$

$$H_4^{*(\eta_i)} = 0.5K_4(1.0-\eta_i)^{3.0} \tag{4.123}$$

$$H_5^{*(\eta_i)} = 0.5K_5(1.0-\eta_i)^{3.0} \tag{4.124}$$

Obviously, there could be many other options for the parameters, A_i, b_i and n_i, of the kernel functions. However, in this section, the above options are used as the preliminary choice to demonstrate the capabilities of the model. The effects of changing the values of these parameters in the kernel functions will be discussed in section 5.5.

4.5.1 Advantages of the multiple-yield-surface model compared with single-yield-surface model

As mentioned in the previous sections, the hysteretic phenomena and their effects on the foundation behaviour under cyclic loading cannot be described by the single-yield-surface model and are explained explicitly by the use of the multiple-yield concept. This section presents some numerical results of the multiple-yield-surface version of the ISIS model as well as comparisons with the single-yield-surface model.

Before discussing the numerical validation for the caisson footing, which is the main goal of this work, four numerical examples will be implemented for a circular flat footing and spudcan on both sand and clay. The purpose of this work is to prove the generality of the multiple-yield-surface model.

In addition, since the main goal of this research is to establish the numerical model for the caisson foundation, the comparison between theoretical model and experiments will be presented for the caisson only.

4.5.1.1 Numerical examples for circular flat footings

There are two examples presented in this section: a circular flat footing on sand and on clay. In each example, a variety of load paths are applied and their results described.

Example 1: Circular flat footing on sand

The soil properties, geometry and loading paths of the footing considered in this example are listed in Table 4.1.

The two load paths in Table 4.1 are shown in Figure 4.6. The purpose of load path 1 is to verify the model in the vertical direction. Load path 2 is used to check the model under cyclic horizontal forces and moments.

Table 4.1 Input data for circular flat footing on sand

<table>
<tr><th colspan="8">Soil properties and geometry</th></tr>
<tr><td colspan="4">Type of soil</td><td colspan="4">Sand</td></tr>
<tr><td colspan="4">Radius (m)</td><td colspan="4">10.0</td></tr>
<tr><td colspan="4">Shear modulus G (initial value) (MN/m^2)</td><td colspan="4">100.0</td></tr>
<tr><td colspan="4">Effective unit weight (kN/m^3)</td><td colspan="4">10.0</td></tr>
<tr><td colspan="4">Angle of friction</td><td colspan="4">35^o</td></tr>
<tr><td colspan="4">Poisson’s ratio ν</td><td colspan="4">0.2</td></tr>
<tr><th colspan="8">Model parameters (for ISIS model)</th></tr>
<tr><td colspan="3" rowspan="2">Association factors</td><td>a_{V1}</td><td>a_{V2}</td><td>a_H</td><td>a_M</td><td>a_Q</td></tr>
<tr><td>0.1</td><td>1.0</td><td>0.4</td><td>0.4</td><td>0.4</td></tr>
<tr><td colspan="2" rowspan="8">Shape factors of yield surface</td><td colspan="2">e_1</td><td colspan="4">-0.2</td></tr>
<tr><td colspan="2">e_2</td><td colspan="4">0.0</td></tr>
<tr><td colspan="2">t_0</td><td colspan="4">0.0</td></tr>
<tr><td colspan="2">m_0</td><td colspan="4">0.086</td></tr>
<tr><td colspan="2">h_0</td><td colspan="4">0.116</td></tr>
<tr><td colspan="2">q_0</td><td colspan="4">0.1</td></tr>
<tr><td colspan="2">β_1</td><td colspan="4">0.9</td></tr>
<tr><td colspan="2">β_2</td><td colspan="4">0.99</td></tr>
<tr><td colspan="2" rowspan="2">Parameters for the rate-dependent solution</td><td colspan="2">Viscosity μ</td><td colspan="4">60.0</td></tr>
<tr><td colspan="2">Time increment dt</td><td colspan="4">Changed with the load incerements</td></tr>
<tr><td colspan="2">Number of yield surfaces</td><td colspan="6">10 yield surfaces used</td></tr>
<tr><th colspan="8">Loading path 1</th></tr>
<tr><td>Load stage</td><td>V (MN)</td><td>H_2 (MN)</td><td>H_3 (MN)</td><td>Q (MNm)</td><td>M_2 (MNm)</td><td>M_3 (MNm)</td><td>Time increment dt</td></tr>
<tr><td>1</td><td>0.0 to 140.0</td><td>0.0</td><td>0.0</td><td>0.0</td><td>0.0</td><td>0.0</td><td>$3.0*10^7$</td></tr>
<tr><td>2</td><td>140.0 down to 0.0</td><td>0.0</td><td>0.0</td><td>0.0</td><td>0.0</td><td>0.0</td><td>10^8</td></tr>
<tr><td>3</td><td>0.0 to 200.0</td><td>0.0</td><td>0.0</td><td>0.0</td><td>0.0</td><td>0.0</td><td>$9.0*10^7$</td></tr>
<tr><th colspan="8">Loading path 2</th></tr>
<tr><td>1</td><td>0.0 to 140.0</td><td>0.0</td><td>0.0</td><td>0.0</td><td>0.0</td><td>0.0</td><td>$3.0*10^7$</td></tr>
<tr><td>2</td><td>140.0 down to 70.0</td><td>0.0</td><td>0.0</td><td>0.0</td><td>0.0</td><td>0.0</td><td>10^7</td></tr>
<tr><td>3</td><td>70.0</td><td>0.0 to 13.5</td><td>0.0</td><td>0.0</td><td>0.0</td><td>0.0 to -270.0</td><td>$3.0*10^9$</td></tr>
<tr><td>4</td><td>70.0</td><td>13.5 to -15.5</td><td>0.0</td><td>0.0</td><td>0.0</td><td>-270.0 to 310.0</td><td>$1.0*10^{10}$</td></tr>
<tr><td>5</td><td>70.0</td><td>-15.5 to 17.5</td><td>0.0</td><td>0.0</td><td>0.0</td><td>310.0 to -350.0</td><td>10^{10}</td></tr>
</table>

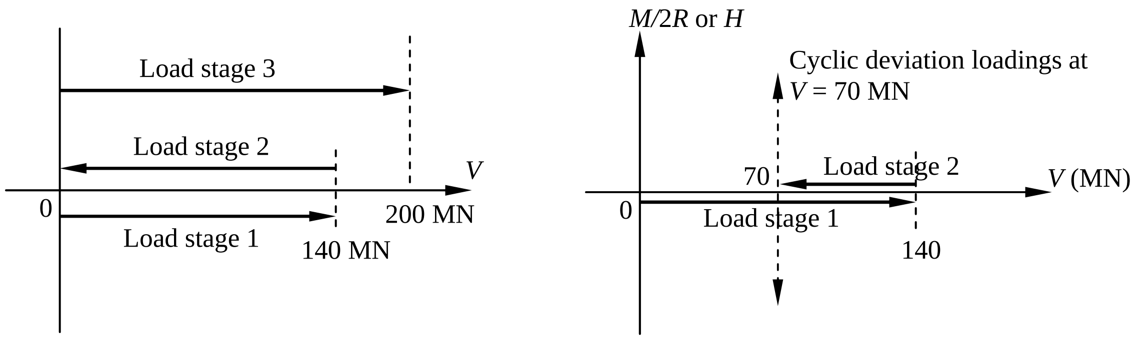

(a) Load path 1

(b) Load path 2

Figure 4.6 Load paths applied for example 1

The numerical results of each load path are compared with those of the solutions using the single-yield-surface model. The vertical response of the footing under load path 1 is shown in Figure 4.7a and 4.7b. In the result of the multiple-yield-surface model, there is a gap between the unloading and reloading curves. This is because the flow of the inner yield surface results in plastic response of the model. Meanwhile, the unloading and reloading curves in the single-yield-surface solution coincide completely. Figure 4.7b shows the variation of the plastic part of the vertical displacements. Obviously, in the unloading-reloading stage, there is no plastic displacement occurring in the solution using the single-yield-surface model.

In load path 2, instead of decreasing the vertical load down to zero, the unloading process is stopped at an intermediate value of V = 70 MN. Afterwards, the moments and horizontal forces are applied at that constant vertical load. Figure 4.8 and 4.9 show the responses of the footing in horizontal and rotational components. Figure 4.10 shows the relationship between rotational and vertical movements at such constant vertical load.

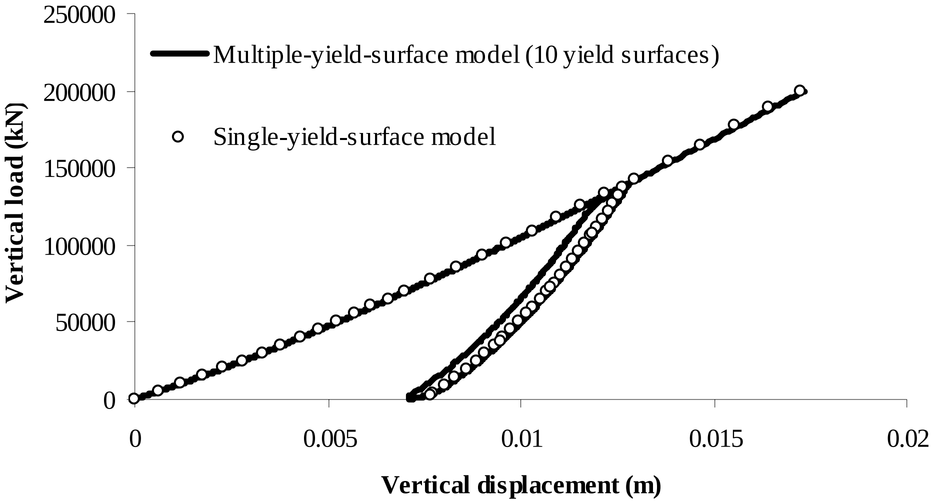

Figure 4.7a Vertical response of the circular flat footing in load path 1

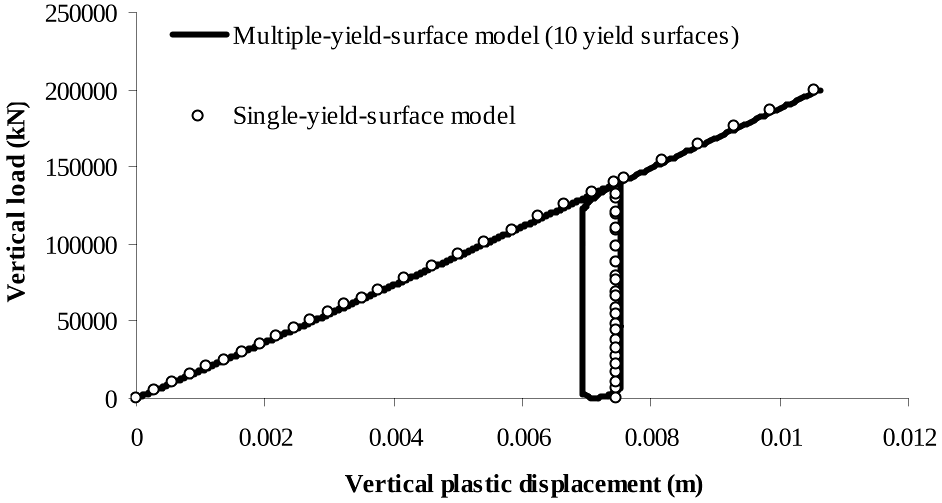

Figure 4.7b Vertical plastic response of the circular flat footing in load path 1

The main goal of running the example in load path 2 is to reveal the effects of inner yield surfaces in the behaviour of the multiple-yield-surface model. In fact, as shown in Figure 4.8, 4.9 and 4.10, since the vertical load is kept constant at half the value of the maximum vertical load, the horizontal and rotational loading processes start in the middle of the system of yield surfaces. Therefore, during the loading-unloading process, the inner yield surfaces are activated one by one. Consequently, the transitions between elastic and plastic response occur gradually. As shown in Figure 4.8 and 4.9, the horizontal and rotational responses of the multiple-yield-surface model show the much smoother transitions between elastic and elasto-plastic behaviour than those of the single-yield-surface model.

Furthermore, in the last loading stage of load path 2, all the yield surfaces of the model have been activated. Therefore, the elasto-plastic stiffness of the foundation at this time has a value which is similar to that of the single-yield-surface model. Consequently, it is clear that the two solutions of the multiple-yield-surface and the single-yield-surface models tend to coincide together at the end of the loading process.

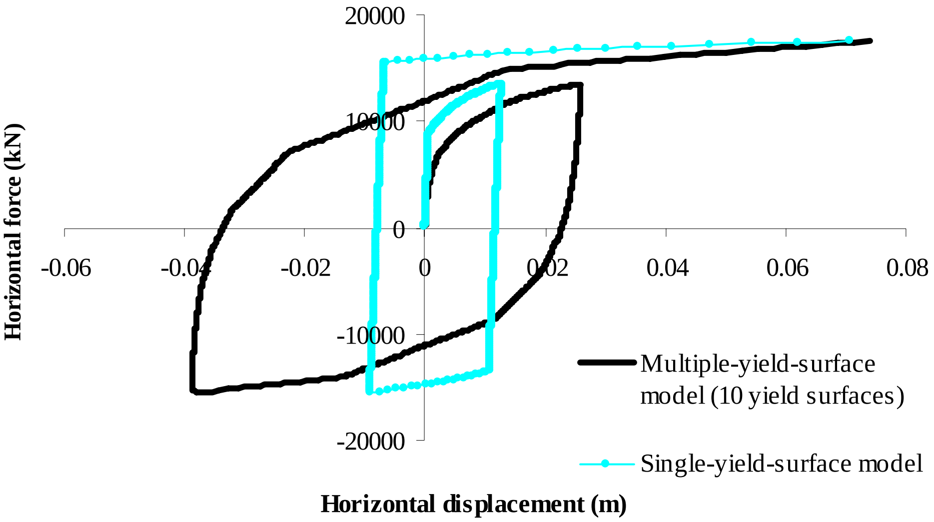

Figure 4.8 Horizontal response of the circular flat footing under load path 2

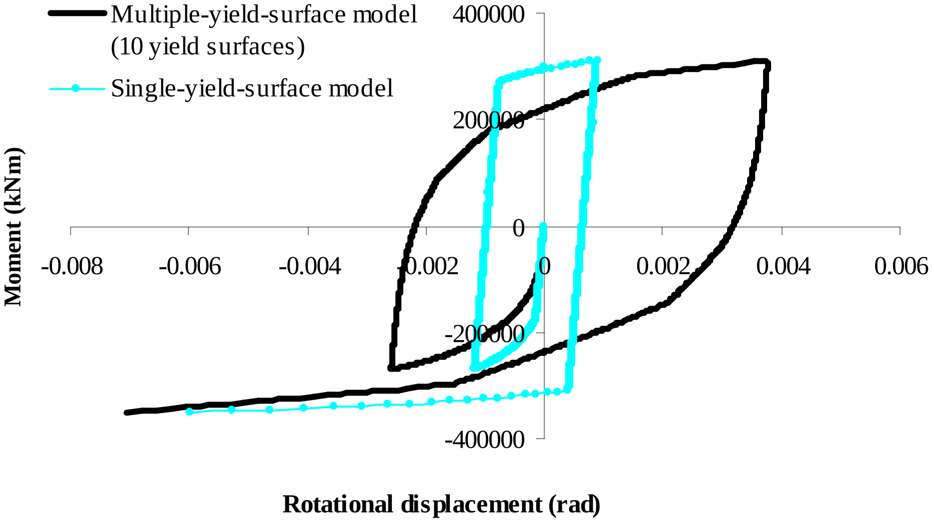

Figure 4.9 Rotational response of the circular flat footing under load path 2

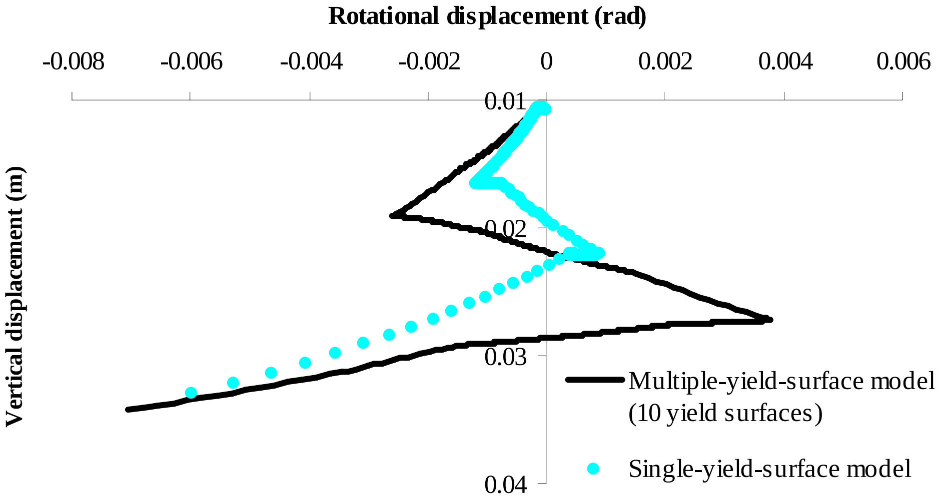

Figure 4.10 Vertical movements under load path 2

Figure 4.10 shows the vertical movement that occurs during the cyclic loading. In the partial plasticity stage, the vertical movement in the solution using the multiple-yield-surface model is larger than that using the single-yield-surface model. When the full plasticity occurs the two solutions tend to coincide, as for the horizontal and rotational responses.

Example 2: Circular flat footing on clay

This example is of a circular flat footing on clay. The soil properties, geometry, model parameters and loading process are given in Table 4.2. The horizontal response, rotational response and vertical movements during the cyclic loading are shown in Figure 4.11, 4.12 and 4.13 respectively.

In order to have a closer look at the actions of the inner yield surfaces, the cyclic horizontal forces and cyclic moments applied are chosen to be small enough to avoid the fully plastic behaviour occurring when all the ten yield surfaces are activated.

As shown in Figure 4.11 and 4.12, the full plasticity state has not been reached. This means that, in the case of using the single-yield-surface model, the loading point is still in the elastic zone and then the horizontal and rotational responses are still straight lines. Meanwhile, by the use of multiple-yield-surface model, the hysteresis has been revealed very significantly. This is because there are a number of inner yield surfaces activated and therefore a smooth transition between the elastic and plastic behaviours is made. As shown in Figure 4.13, it should be noted that, with the single-yield-surface model, the vertical movements during the small cyclic loading could not be simulated. However, upward or downward movements of the shallow foundation during cyclic loading are recorded in almost all test observations. Obviously, the multiple-yield-surface model can satisfy this requirement.

Table 4.2 Input data for circular flat footing on clay

<table>
<tr><th colspan="8">Soil properties and geometry</th></tr>
<tr><td colspan="4">Type of soil</td><td colspan="4">Clay</td></tr>
<tr><td colspan="4">Radius (m)</td><td colspan="4">15.0</td></tr>
<tr><td colspan="4">Undrained shear strength (at mudline) (kN/m^2)</td><td colspan="4">20.0</td></tr>
<tr><td colspan="4">Effective unit weight (kN/m^3)</td><td colspan="4">10.0</td></tr>
<tr><td colspan="4">Angle of friction</td><td colspan="4">35^o</td></tr>
<tr><td colspan="4">Poisson’s ratio ν</td><td colspan="4">0.5</td></tr>
<tr><td colspan="4">Mode of shear strength variation</td><td colspan="4">Linear</td></tr>
<tr><td colspan="4">ρ (kPa/m)</td><td colspan="4">2.0</td></tr>
<tr><td colspan="4">$I_r = G/s_u$</td><td colspan="4">400</td></tr>
<tr><th colspan="8">Model parameters (for ISIS model)</th></tr>
<tr><td colspan="2" rowspan="2">Association factors</td><td>a_{V1}</td><td>a_{V2}</td><td>a_H</td><td>a_M</td><td colspan="2">a_Q</td></tr>
<tr><td>0.58</td><td>0.58</td><td>1.0</td><td>1.0</td><td colspan="2">1.0</td></tr>
<tr><td colspan="2" rowspan="8">Shape factors of yield surface</td><td colspan="2">e_1</td><td colspan="4">0.518</td></tr>
<tr><td colspan="2">e_2</td><td colspan="4">-1.18</td></tr>
<tr><td colspan="2">t_0</td><td colspan="4">0.0</td></tr>
<tr><td colspan="2">m_0</td><td colspan="4">0.083</td></tr>
<tr><td colspan="2">h_0</td><td colspan="4">0.127</td></tr>
<tr><td colspan="2">q_0</td><td colspan="4">0.1</td></tr>
<tr><td colspan="2">β_1</td><td colspan="4">0.764</td></tr>
<tr><td colspan="2">β_2</td><td colspan="4">0.882</td></tr>
<tr><td colspan="2" rowspan="2">Parameters for the rate-dependent solution</td><td colspan="2">Viscosity μ</td><td colspan="4">60.0</td></tr>
<tr><td colspan="2">Time increment dt</td><td colspan="4">Changed with the load incerements</td></tr>
<tr><td colspan="2">Number of yield surfaces</td><td colspan="6">10 yield surfaces used</td></tr>
<tr><th colspan="8">Loading process</th></tr>
<tr><td>Load stage</td><td>V (MN)</td><td>H_2 (MN)</td><td>H_3 (MN)</td><td>Q (MNm)</td><td>M_2 (MNm)</td><td>M_3 (MNm)</td><td>Time increment dt</td></tr>
<tr><td>1</td><td>0.0 to 4.9</td><td>0.0</td><td>0.0</td><td>0.0</td><td>0.0</td><td>0.0</td><td>10^5</td></tr>
<tr><td>2</td><td>4.9 to 8.9</td><td>0.0</td><td>0.0</td><td>0.0</td><td>0.0</td><td>0.0</td><td>$5.0*10^6$</td></tr>
<tr><td>3</td><td>8.9 down to 4.9</td><td>0.0</td><td>0.0</td><td>0.0</td><td>0.0</td><td>0.0</td><td>10^6</td></tr>
<tr><td>4</td><td>4.9</td><td>0.0 to 0.5</td><td>0.0</td><td>0.0</td><td>0.0</td><td>0.0 to -8.5</td><td>10^8</td></tr>
<tr><td>5</td><td>4.9</td><td>0.5 to -0.7</td><td>0.0</td><td>0.0</td><td>0.0</td><td>-8.5 to 11.9</td><td>$2.0*10^8$</td></tr>
<tr><td>6</td><td>4.9</td><td>-0.7 to 0.7</td><td>0.0</td><td>0.0</td><td>0.0</td><td>11.9 to -11.9</td><td>$2.5*10^8$</td></tr>
</table>

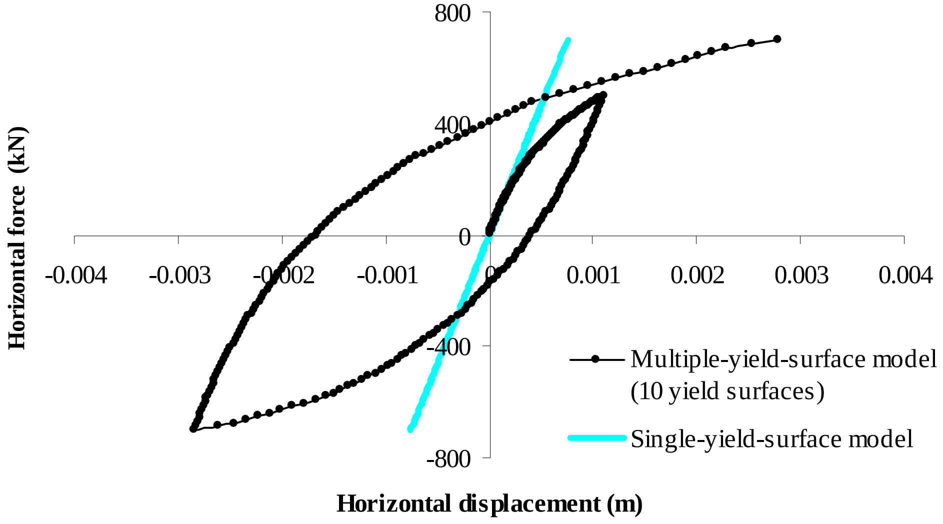

Figure 4.11 Horizontal response of circular flat footing on clay (Example 2)

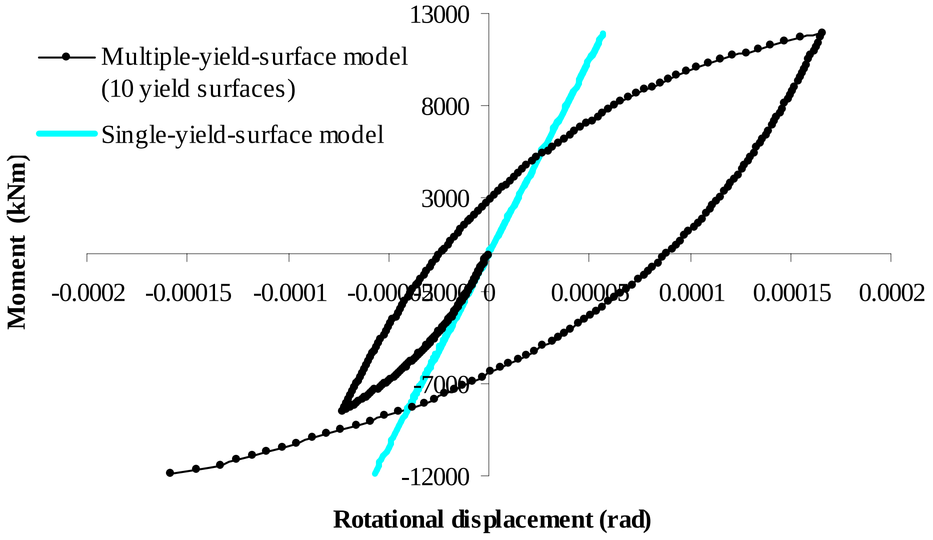

Figure 4.12 Rotational response of circular flat footing on clay (Example 2)

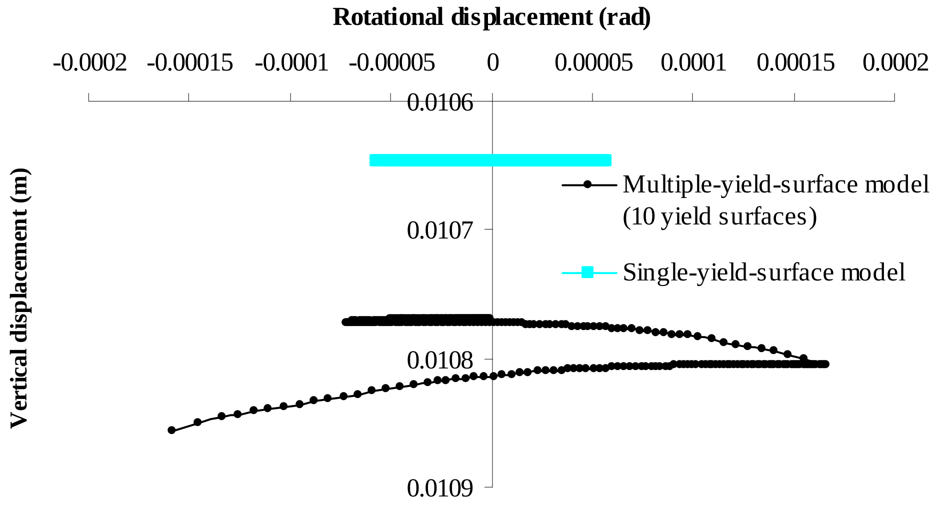

Figure 4.13 Vertical movements of circular flat footing under cyclic loading on clay (Example 2)

4.5.1.2 Numerical examples for spudcan footings

This section presents the numerical analyses of a spudcan in both cases of sand and clay. The outline of this footing is shown in Figure 4.14.

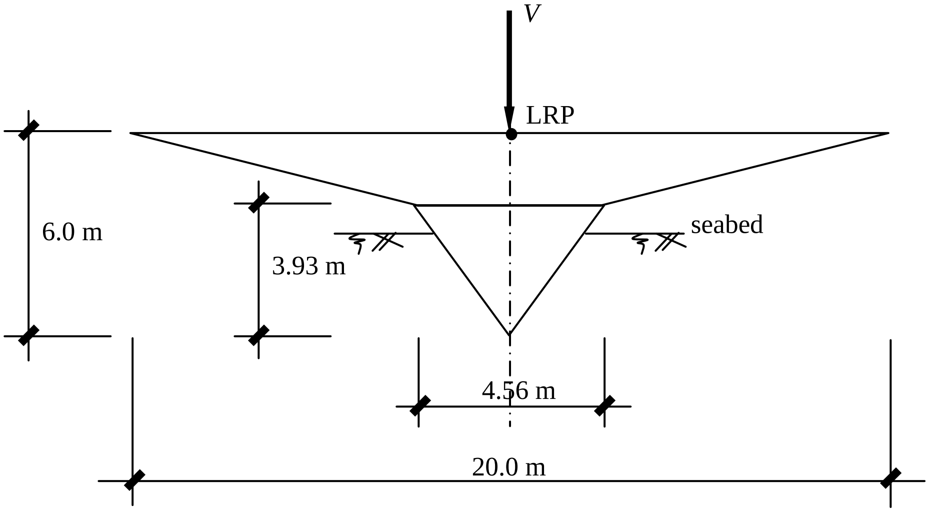

Figure 4.14 Geometric shape of the spudcan footing considered in section 4.5.1.2

Example 3: Spudcan on sand

Table 4.3 gives the input data for the analysis of the spudcan on sand. The installation process and one cycle of both horizontal and moment loading are taken into account. Since there is a variation of the effective footing diameter during the installation process, the rate of loading needs to be carefully controlled. Thus, there are six loading stages, from 1 to 6, applied to simulate the installation.

Figure 4.15 shows the vertical loading-unloading process. Again, the solutions of the single-yield-surface model and the multiple-yield-surface model are almost the same.

In addition, after the installation process, there is a small unloading stage (load stage 7). The purpose of this is to describe the behaviour of the model near the peak in *V*-direction of the yield surfaces. Figures 4.16, 4.17 and 4.18 show the horizontal and rotational responses and the vertical movements of the footing during the cyclic loading respectively. It is clear that the hysteresis is still modelled well compared with the results of the single-yield-surface model.

Table 4.3 Input data for spudcan footing on sand

Soil properties and geometry	
Type of soil	Sand
Radius (m)	10.0
Initial V_0 (kN)	1.0e3
Shear modulus G (initial value) (MN/m^2)	25.0
Effective unit weight (kN/m^3)	10.0
Angle of friction	35°
Poisson's ratio ν	0.2

Model parameters (for ISIS model)					
Association factors	a_{V1}	a_{V2}	a_H	a_M	a_Q
	0.1	1.0	0.4	0.4	0.1
Shape factors of yield surface	e_1	-0.2			
	e_2	0			
	t_0	0.0			
	m_0	0.086			
	h_0	0.116			
	q_0	0.1			
	β_1	0.9			
	β_2	0.99			
Parameters for the rate-dependent solution	Viscosity μ	60.0			
	Time increment dt	Changed with the load incerements			
Number of yield surfaces	10 yield surfaces used				

Loading process							
Load stage	V (MN)	H_2 (MN)	H_3 (MN)	Q (MNm)	M_2 (MNm)	M_3 (MNm)	Time increment dt
1	0.0 to 0.1	0.0	0.0	0.0	0.0	0.0	10^{9}
2	0.1 to 14.0	0.0	0.0	0.0	0.0	0.0	10^{11}
3	14.0 to 28.0	0.0	0.0	0.0	0.0	0.0	10^{12}
4	28.0 to 140.0	0.0	0.0	0.0	0.0	0.0	10^{13}
5	140.0 to 400.0	0.0	0.0	0.0	0.0	0.0	10^{15}
6	400.0 to 900.0	0.0	0.0	0.0	0.0	0.0	10^{15}
7	900.0 down to 850.0	0.0	0.0	0.0	0.0	0.0	10^{14}
8	8.50.0	0.0	0.0 to 10.0	0.0	0.0 to 200.0	0.0	$2.0*10^{14}$
9	850.0	0.0	10.0 to -14.0	0.0	200.0 to -280.0	0.0	$4.0*10^{14}$
10	850.0	0.0	-14.0 to 18.0	0.0	-280.0 to 360.0	0.0	$4.0*10^{14}$

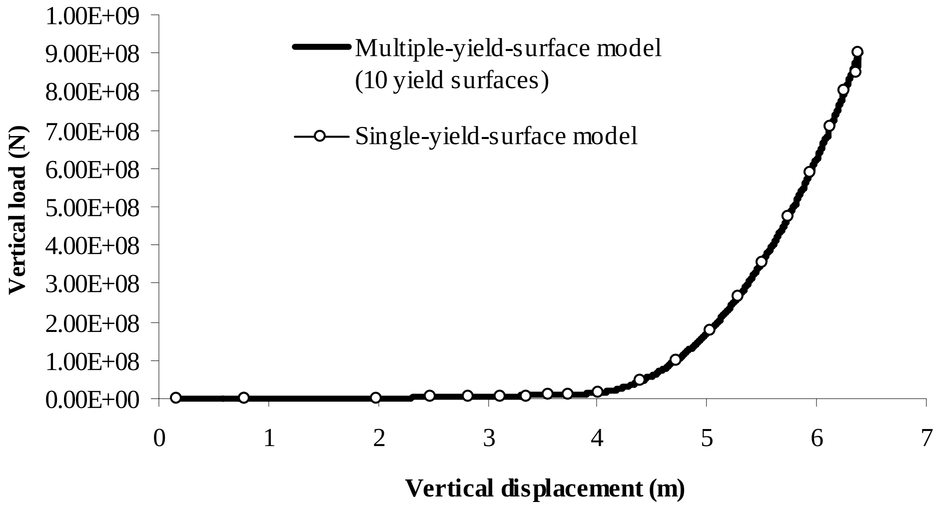

Figure 4.15 Installation of the spudcan on sand

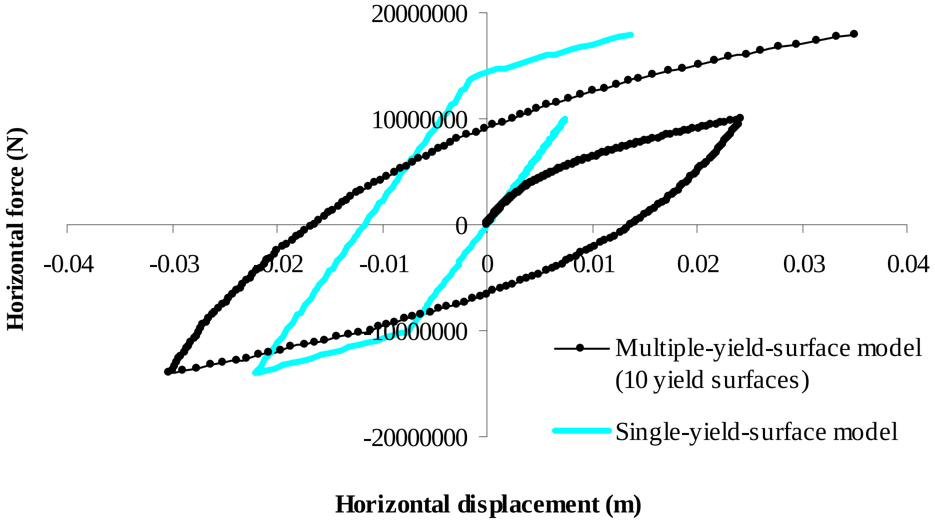

Figure 4.16 Horizontal response of the spudcan on sand

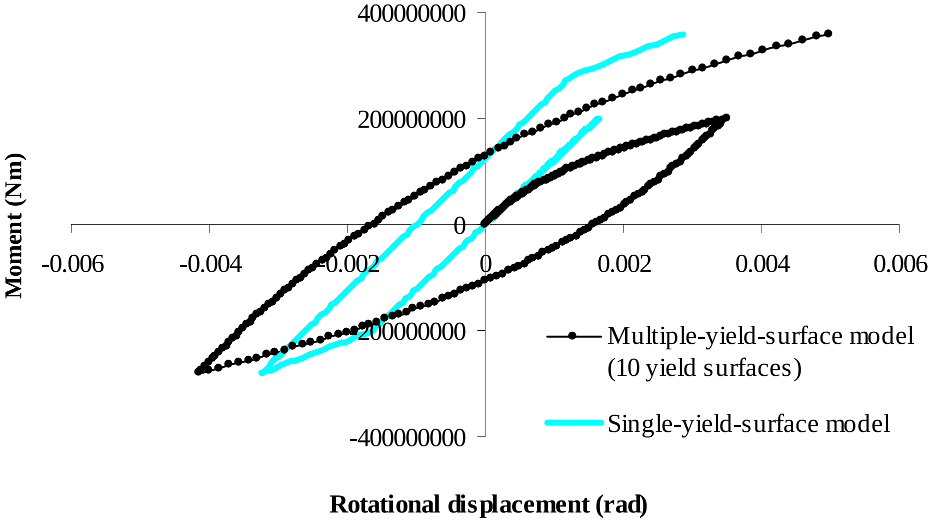

Figure 4.17 Rotational response of the spudcan on sand

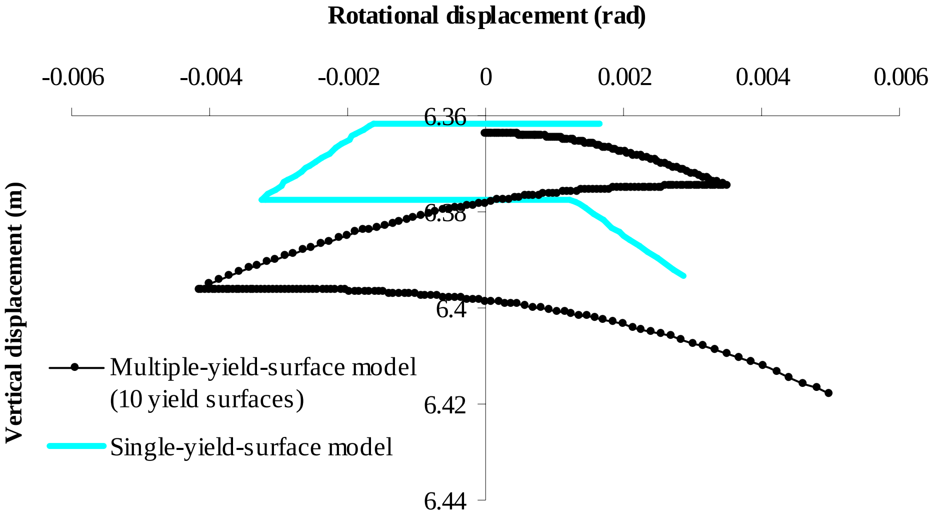

Figure 4.18 Vertical movements of the spudcan during cyclic loading on sand

Example 4: Spudcan on clay

Table 4.4 gives the information of the numerical example of the spudcan shown in Figure 4.14 on clay. The installation, the horizontal response, the rotational response and the vertical movements during cyclic loading are shown in Figure 4.19, 4.20, 4.21 and 4.22 respectively. In a similar way to the case of spudcan on sand, these responses reveal the differences between the results obtained by using the single-yield-surface model and the multiple-yield-surface model especially in the partial plasticity behaviour. Again, the outermost yield surface of multiple-yield-surface has not been activated. This corresponds to the fact that the yield surface of the single-yield-surface model has not been reached. In other words, the behaviour of the footing using the single-yield-surface model still is purely elastic.

In addition, it should be noted that, in the installation processes of both the circular flat footing and spudcan examples (from example 1 to example 4), there is almost no difference between the solutions of the multiple-yield-surface model and those of the single-yield-surface model. Meanwhile, there always are significant differences between them in the horizontal and rotational responses. The reason for this is that, in the installation process, the state of fully plastic behaviour, in which all the yield surfaces are activated, occurs after just a few loading steps. Therefore, the stiffness of the foundation in the multiple-yield-surface model becomes nearly the same as that in the single-yield-surface model. Consequently, the two results coincide during the installation.

Table 4.4 Input data for spudcan on clay

<table>
<tr><th colspan="8">Soil properties and geometry</th></tr>
<tr><td colspan="4">Type of soil</td><td colspan="4">clay</td></tr>
<tr><td colspan="4">Radius (m)</td><td colspan="4">10.0</td></tr>
<tr><td colspan="4">Initial V_0 (kN)</td><td colspan="4">1.0e3</td></tr>
<tr><td colspan="4">Undrain shear strength (at mudline) (kN/m^2)</td><td colspan="4">150.0</td></tr>
<tr><td colspan="4">Effective unit weight (kN/m^3)</td><td colspan="4">10.0</td></tr>
<tr><td colspan="4">Angle of friction</td><td colspan="4">35^o</td></tr>
<tr><td colspan="4">Poisson’s ratio ν</td><td colspan="4">0.5</td></tr>
<tr><td colspan="4">Mode of shear strength variation</td><td colspan="4">Constant</td></tr>
<tr><th colspan="8">Model parameters (for ISIS model)</th></tr>
<tr><td colspan="2" rowspan="2">Association factors</td><td colspan="2">a_{V1}</td><td>a_{V2}</td><td>a_H</td><td>a_M</td><td>a_Q</td></tr>
<tr><td colspan="2">0.645</td><td>0.645</td><td>1.0</td><td>1.0</td><td>1.0</td></tr>
<tr><td colspan="2" rowspan="8">Shape factors of yield surface</td><td colspan="2">e_1</td><td colspan="4">0.518</td></tr>
<tr><td colspan="2">e_2</td><td colspan="4">-1.18</td></tr>
<tr><td colspan="2">t_0</td><td colspan="4">0.0</td></tr>
<tr><td colspan="2">m_0</td><td colspan="4">0.083</td></tr>
<tr><td colspan="2">h_0</td><td colspan="4">0.127</td></tr>
<tr><td colspan="2">q_0</td><td colspan="4">0.1</td></tr>
<tr><td colspan="2">β_1</td><td colspan="4">0.764</td></tr>
<tr><td colspan="2">β_2</td><td colspan="4">0.882</td></tr>
<tr><td colspan="2" rowspan="2">Parameters for the rate-dependent solution</td><td colspan="2">Viscosity μ</td><td colspan="4">60.0</td></tr>
<tr><td colspan="2">Time increment <i>dt</i></td><td colspan="4">Changed with the load incerements</td></tr>
<tr><td colspan="2">Number of yield surfaces</td><td colspan="6">10 yield surfaces used</td></tr>
<tr><th colspan="8">Loading process</th></tr>
<tr><td>Load stage</td><td>V (MN)</td><td>H_2 (MN)</td><td>H_3 (MN)</td><td>Q (MNm)</td><td>M_2 (MNm)</td><td>M_3 (MNm)</td><td>Time increment <i>dt</i></td></tr>
<tr><td>1</td><td>0.0 to 0.5</td><td>0.0</td><td>0.0</td><td>0.0</td><td>0.0</td><td>0.0</td><td>1.0e9</td></tr>
<tr><td>2</td><td>0.5 to 9.0</td><td>0.0</td><td>0.0</td><td>0.0</td><td>0.0</td><td>0.0</td><td>1.0e11</td></tr>
<tr><td>3</td><td>9.0 to 49.0</td><td>0.0</td><td>0.0</td><td>0.0</td><td>0.0</td><td>0.0</td><td>1.0e13</td></tr>
<tr><td>4</td><td>49.0 to 255.0</td><td>0.0</td><td>0.0</td><td>0.0</td><td>0.0</td><td>0.0</td><td>1.2e15</td></tr>
<tr><td>5</td><td>255.0 down to 200.0</td><td>0.0</td><td>0.0</td><td>0.0</td><td>0.0</td><td>0.0</td><td>2.0e13</td></tr>
<tr><td>6</td><td>200.0</td><td>0.0</td><td>0.0 to 10.0</td><td>0.0</td><td>0.0 to 170.0</td><td>0.0</td><td>1.0e13</td></tr>
<tr><td>7</td><td>200.0</td><td>0.0</td><td>10.0 to -12.0</td><td>0.0</td><td>170.0 to -204.0</td><td>0.0</td><td>2.0e13</td></tr>
<tr><td>8</td><td>200.0</td><td>0.0</td><td>-12.0 to 14.0</td><td>0.0</td><td>-204.0 to 238.0</td><td>0.0</td><td>2.0e13</td></tr>
</table>

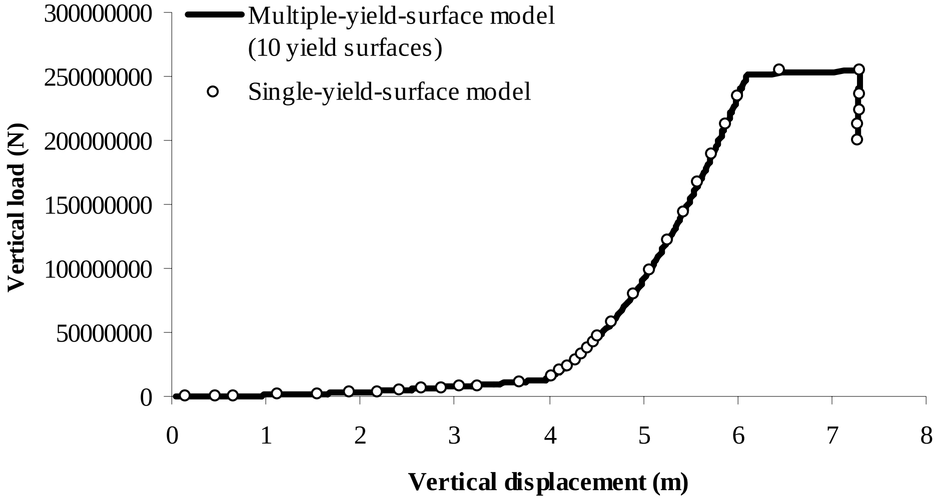

Figure 4.19 Installation of spudcan on clay

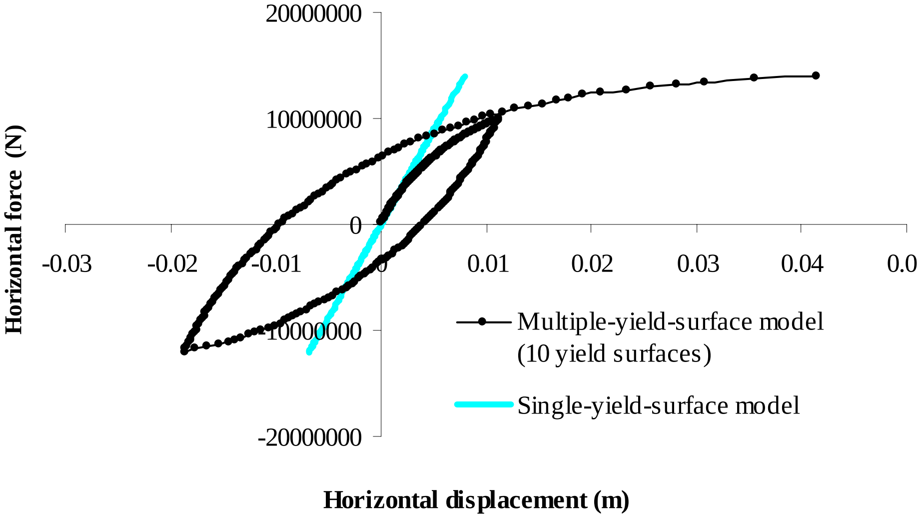

Figure 4.20 Horizontal response of spudcan on clay under cyclic loading

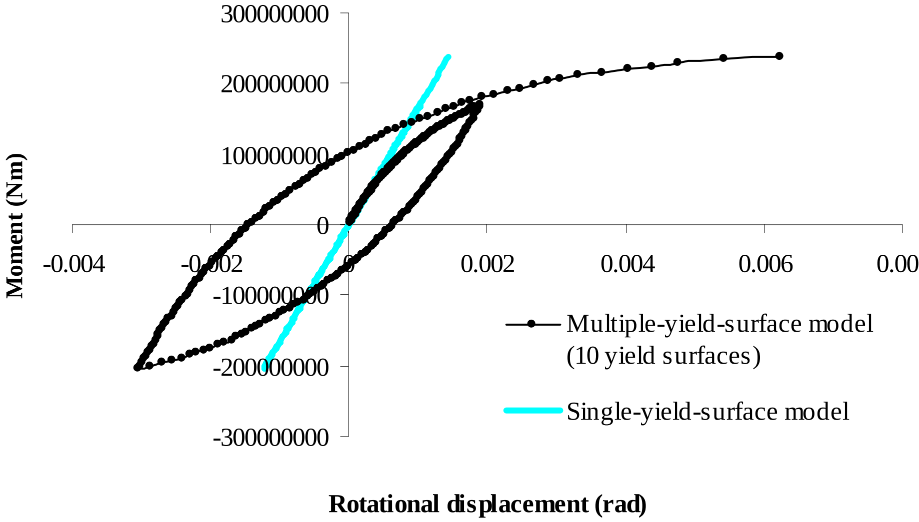

Figure 4.21 Rotational response of spudcan on clay under cyclic loading

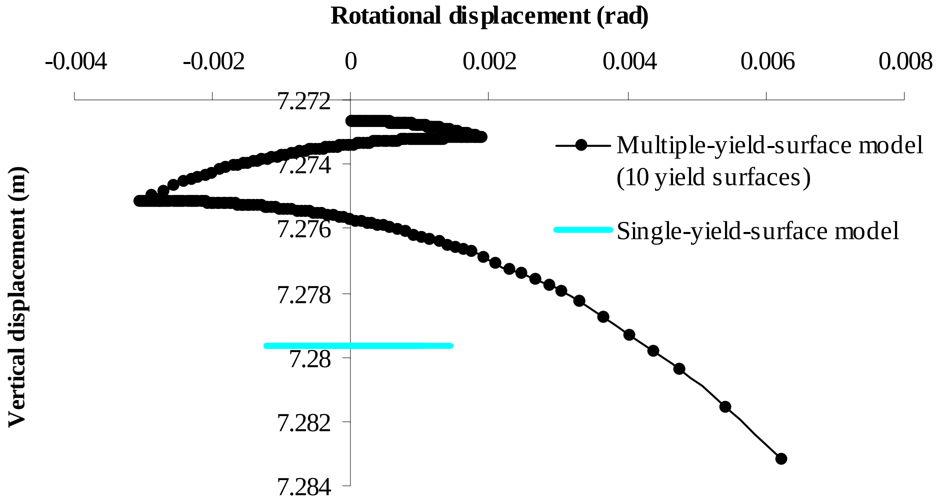

Figure 4.22 Vertical movements of spudcan on clay under cyclic loading

4.5.1.3 Numerical examples for caissons

As mentioned in the introduction, there are two main kinds of caisson footings suitable for offshore wind turbine structures: single caisson (monopod caisson) and multi-caisson (tripod or quadruped caisson). The serviceability conditions of these kinds of caisson are also different. During their lifetime, monopod caissons carry a compressive vertical load (downward) coming from the structure's own weight and from the dynamic effects from the blades, and cyclic horizontal forces and moments coming from the environmental conditions. On the other hand, multi-caissons withstand smaller horizontal forces and moments but the magnitude of vertical load varies more and occasionally there are some tensile vertical forces (upward). Therefore, this section presents two numerical examples for caissons. The first example simulates the behaviour of a monopod caisson in the installation process, with and without suction, and the responses under cyclic loading as in serviceability conditions. The second example describes the behaviour of a caisson under compression-tension vertical loading. The comparison between multiple-yield-surface and single-yield-surface solutions will be made to validate the abilities of the multiple-yield-surface model.

Example 5: Monopod caisson

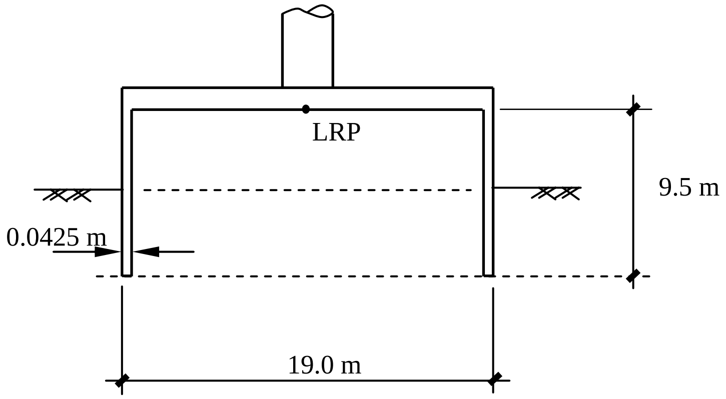

Figure 4.23 Outline of the monopod caisson

This example presents the behaviour of a single caisson as shown in Figure 4.23. Firstly, the installation using suction is implemented and compared with the installation using pure vertical force. Secondly, a cycle of the application of horizontal force and corresponding moment is calculated. The comparison between the solution of the multiple-yield-surface model and the single-yield-surface model will be made. The soil properties, the model parameters and the loading processes are described in Table 4.5.

The installations with and without suction assistance are shown in Figure 4.24. In the first period of the installation, when the suction is not yet applied, the caisson penetrates into the soil by self-weight. After the initial penetration, by turning the suction on and increasing the suction pressure gradually with the depth as shown in Figure 4.25, the caisson is installed continuously into the soil without any more vertical loading.

Table 4.5 Input data of the example 5 – monopod caisson

Soil properties	
Type of soil	Sand
Shear modulus *G* (initial value) (MN/m^2)	25.0
Effective unit weight (kN/m^3)	10.0
Angle of friction	35^o
Poisson's ratio ν	0.2

Model parameters (for ISIS model)					
Association factors	a_{V1}	a_{V2}	a_H	a_M	a_Q
	0.297	1.0	0.7	0.7	0.7
Shape factors of yield surface	e_1	-0.2			
	e_2	0.0			
	t_0	0.1088			
	m_0	0.15			
	h_0	0.337			
	q_0	0.2			
	β_1	0.99			
	β_2	0.99			
Parameters for the rate-dependent solution	Viscosity μ	0.002			
	Time increment *dt*	Changed with the load incerements			
Number of yield surfaces	20 yield surfaces used				
Bell width (w_{bell}) (m)	0.7				

Load stage	Suction pressure (kPa)	V (kN)	H_2 (kN)	H_3 (kN)	Q (kNm)	M_2 (kNm)	M_3 (kNm)	Time increment *dt*
Installation with suction assistance								
1	0.0	0.0 to 100.0	0.0	0.0	0.0	0.0	0.0	10^3
2	0.0	100.0 to 1000.0	0.0	0.0	0.0	0.0	0.0	10^6
3	0.0	1000.0 to 8772.0	0.0	0.0	0.0	0.0	0.0	10^8
4	0.0 to 20.0	8772.0	0.0	0.0	0.0	0.0	0.0	1.0e8
5	20.0 to 200.0	8772.0	0.0	0.0	0.0	0.0	0.0	1.0e8
Installation without suction assistance								
1	0.0	0.0 to 100.0	0.0	0.0	0.0	0.0	0.0	10^3
2	0.0	100.0 to 1000.0	0.0	0.0	0.0	0.0	0.0	10^6
3	0.0	1000.0 to 10000.0	0.0	0.0	0.0	0.0	0.0	10^8
4	0.0	10000.0 to 80000.0	0.0	0.0	0.0	0.0	0.0	$2.0*10^9$
5	0.0	80000.0 down to 8772.0	0.0	0.0	0.0	0.0	0.0	$2.0*10^9$
Application of 1 cycle of horizontal and moment loadings								
6	0.0	8772.0	0.0	0.0 to 400.0	0.0	0.0 to 12784.0	0.0	$4.0*10^7$
7	0.0	8772.0	0.0	400.0 to -800.0	0.0	12784 to -25568.0	0.0	$8.0*10^7$
8	0.0	8772.0	0.0	-800.0 to 1000.0	0.0	-25568.0 to 31960.0	0.0	$2.0*10^8$

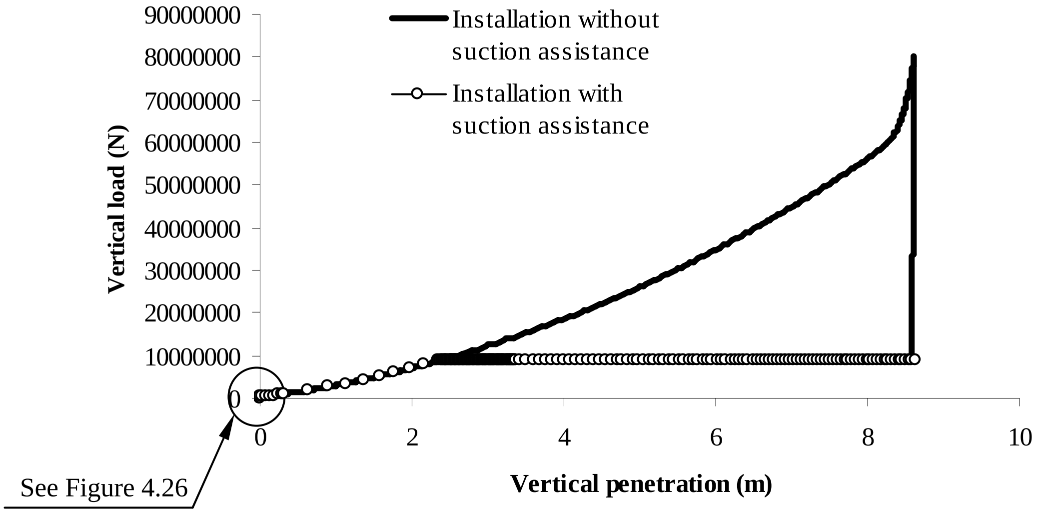

See Figure 4.26

Figure 4.24 Installation of the caisson with and without suction assistance

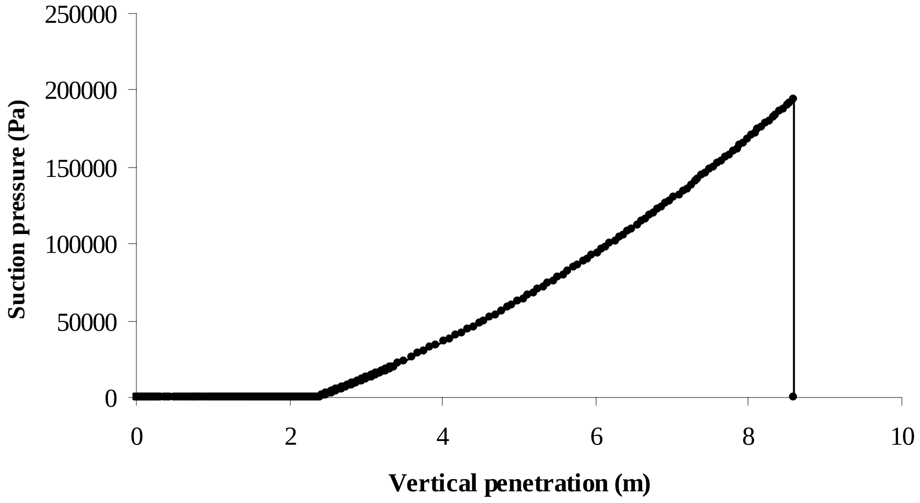

Figure 4.25 Suction pressure applied during the installation process

A comparison between the multiple-yield-surface solution and the single-yield-surface solution was carried out. However, since on the scale of the whole installation process the two solutions almost coincide, just the beginning of the vertical load-penetration curve in Figure 4.24 is chosen and shown in detail in Figure 4.26 to have a closer look at the differences. Again, in a similar way to the previous cases of circular flat footing and spudcan, the stiffness of the foundation analysis using the multiple-yield-surface model becomes the same as that of the single-yield-surface model when all its yield surfaces have been activated. In fact, Figure 4.26 shows a smooth transition from the elastic stiffness to the plastic stiffness in the case of using the multiple-yield-surface model instead of the sudden change from elastic to plastic stiffness as in the single-yield-surface model.

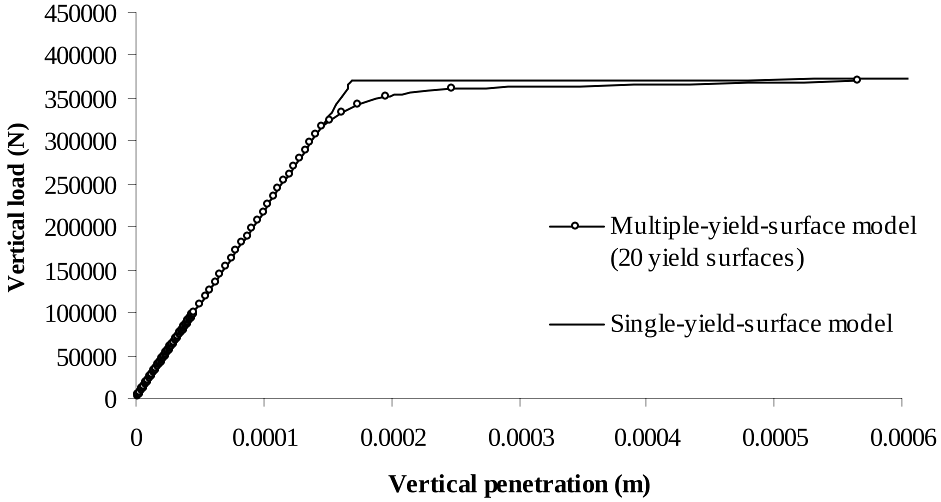

Figure 4.26 Vertical behaviour at the beginning of the installation

Figure 4.27, 4.28 and 4.29 show the horizontal, rotational and vertical responses respectively during the cyclic loading. It is found that there are similarities in horizontal and rotational responses as have been shown in the previous examples. However, in the vertical response, the differences are more important. Instead of downward movements as in the previous examples (from example 1 to 4), there are upward movements during the cyclic loading. Mathematically, this is caused by the negative values of the partial differential of the yield function with respect to the generalised vertical force, $\frac{\partial y^{(n)}}{\partial \chi_V^{(n)}}$, at the small ratio of $\frac{V}{V_0}$. In physical terms, this means that at a small vertical load, under cyclic horizontal loading, the footing can be pulled out of the seabed. The sign of the differential $\frac{\partial y^{(n)}}{\partial \chi_V^{(n)}}$ not only depends on the vertical load but also on the association factors a_{V1} and a_{V2} which will be discussed in section 5.3 in more detail.

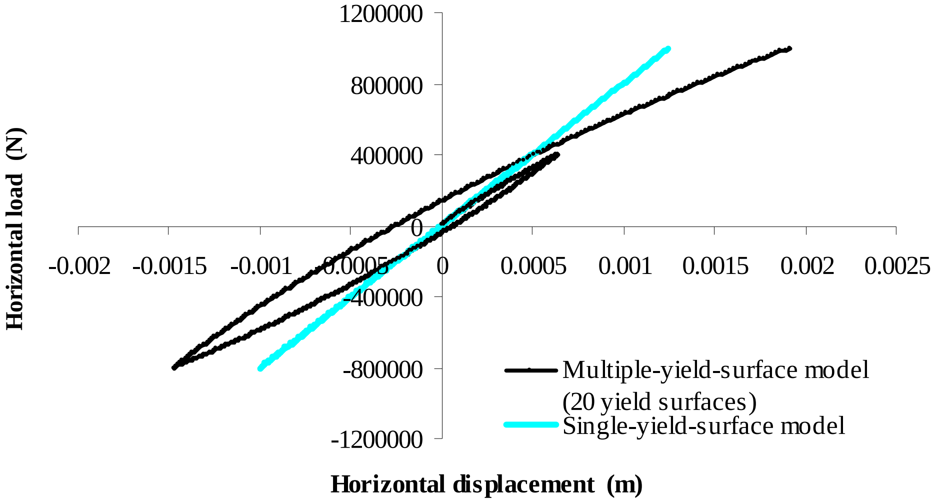

Figure 4.27 Horizontal response of the caisson

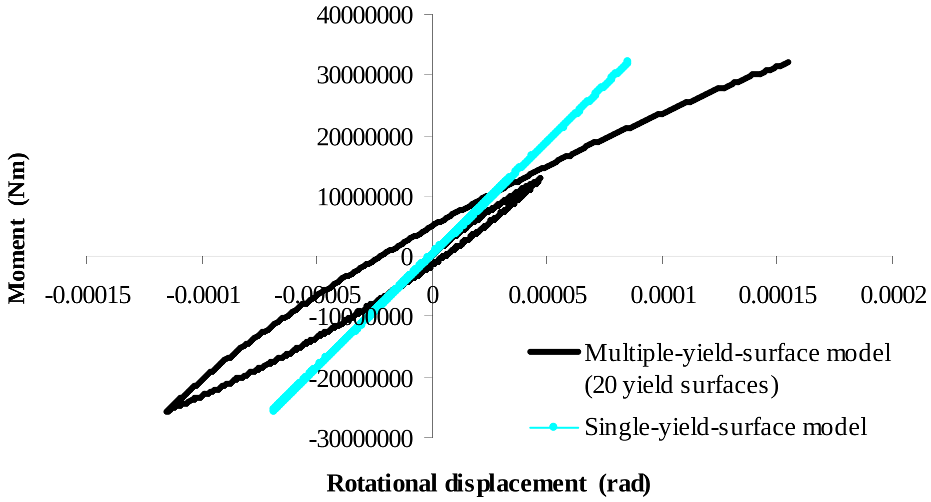

Figure 4.28 Rotational response of the caisson

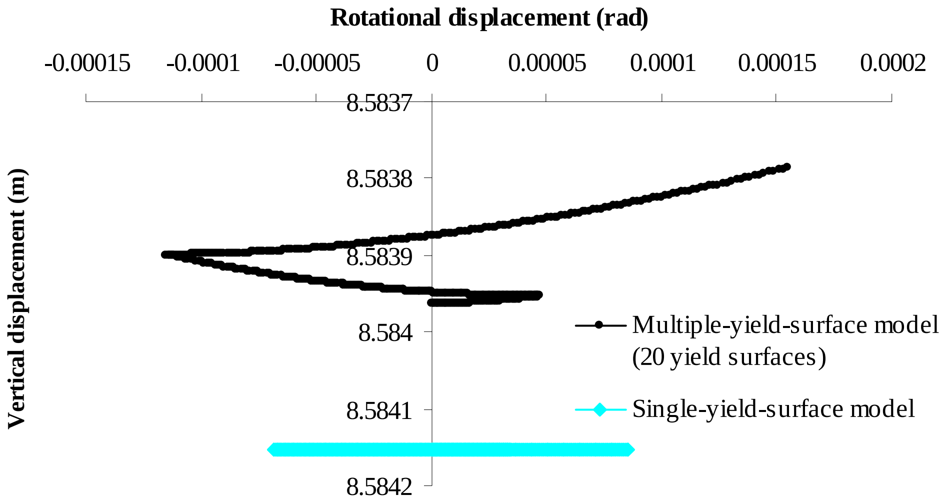

Figure 4.29 Vertical movements during the cyclic loading

Example 6: Caisson under vertical compression-tension forces

This example could have been implemented together with Example 5. However, since there are many issues to discuss, it is clearer to present the issue of compression-tension behaviour of the caisson in a separate example.

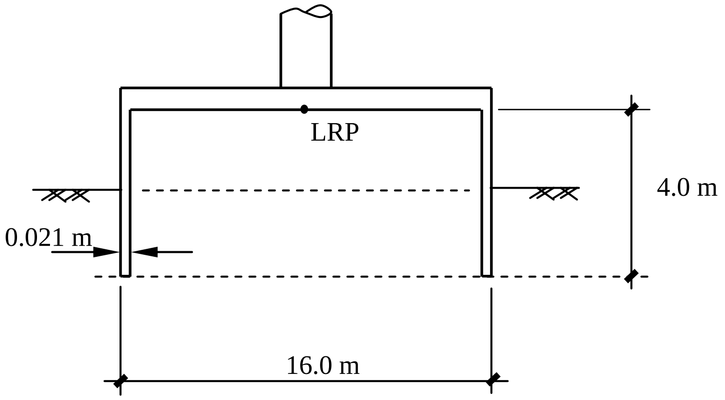

Figure 4.30 Outline of the caisson in Example 6

Figure 4.30 shows the outline of the caisson in this example. The soil properties and model parameters are exactly the same as those of example 5. The bell width w_{bell} is taken as 0.04. The loading process is described in Table 4.6.

Table 4.6 Loading process of the example 6

Loading process								
Load stage	Suction pressure (kPa)	*V* (kN)	H_2 (kN)	H_3 (kN)	*Q* (kNm)	M_2 (kNm)	M_3 (kNm)	Time increment *dt*
1	0.0	0.0 to 10.0	0.0	0.0	0.0	0.0	0.0	$2.0*10^2$
2	0.0	10.0 to 200.0	0.0	0.0	0.0	0.0	0.0	$3.5*10^3$
3	0.0	200.0 to 742.0	0.0	0.0	0.0	0.0	0.0	10^6
4	0.0	742.0 to 2742.0	0.0	0.0	0.0	0.0	0.0	$2.0*10^6$
5	0.0	2742.0 to 4742.0	0.0	0.0	0.0	0.0	0.0	$4.0*10^6$
6	0.0	4742.0 to 8742.0	0.0	0.0	0.0	0.0	0.0	$3.2*10^7$
7	0.0	8742.0 to 16742.0	0.0	0.0	0.0	0.0	0.0	$3.2*10^8$
8	0.0	16742.0 down to 1987.0	0.0	0.0	0.0	0.0	0.0	$2.0*10^9$
9	0.0	1987.0 to -1000.0	0.0	0.0	0.0	0.0	0.0	10^{10}
10	0.0	-1000 to 0.0	0.0	0.0	0.0	0.0	0.0	$2.0*10^3$
11	0.0	0.0 to 200.0	0.0	0.0	0.0	0.0	0.0	$2.0*10^6$
12	0.0	200.0 to 15000.0	0.0	0.0	0.0	0.0	0.0	$4.0*10^8$

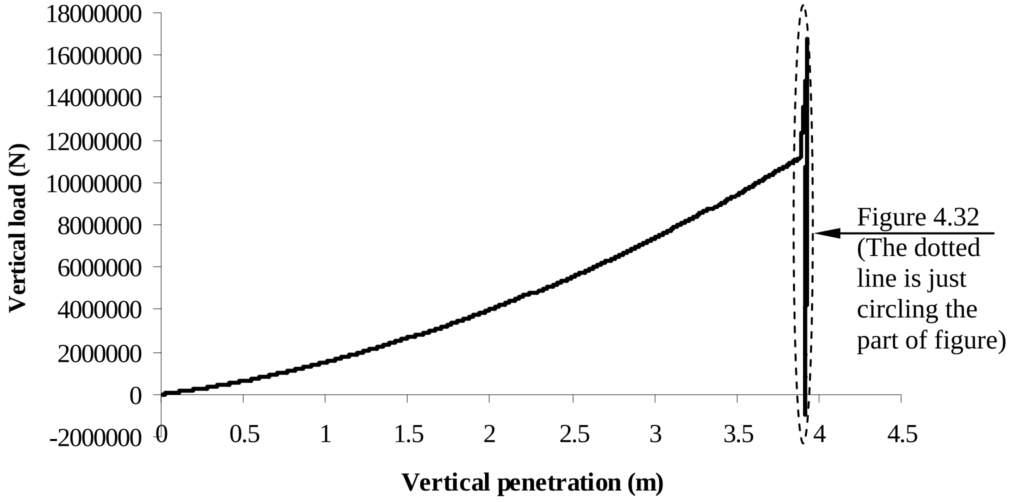

Figure 4.32
(The dotted line is just circling the part of figure)

Figure 4.31 Installation and compression-tension loading of the caisson in Example 6

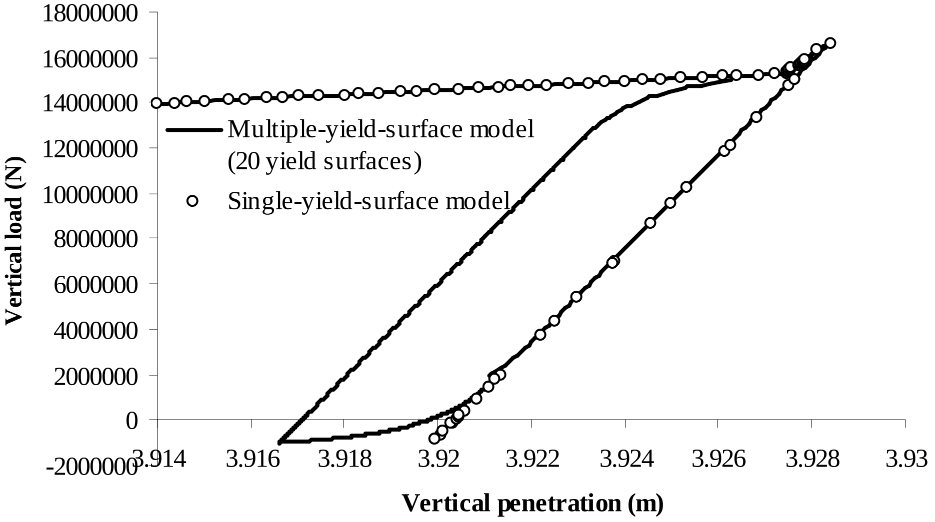

Figure 4.32 Closer look at the caisson behaviour under compression-tension loading

The vertical response of the caisson under the loading process in Table 4.6 is shown in Figure 4.31. The compression-tension part is scaled in Figure 4.32 and compared with the solution of the single-yield-surface model. Once again, the hysteresis loop occurs in the solution of multiple-yield-surface model but not in the single-yield-surface model.

4.5.1.4 Summary

In sections 4.5.1.1, 4.5.1.2 and 4.5.1.3, numerical examples for three kinds of shallow foundation of offshore structures, namely circular flat footing, spudcan and caisson, have been carried out. All these examples are implemented with comparisons between the two theoretical models: the multiple-yield-surface model and the single-yield-surface model. The most important feature highlighted is the potential of the multiple-yield-surface model to simulate the behaviour of shallow foundations under cyclic loadings. The results coming from the above six examples have satisfied this requirement. The hysteresis that usually occurs in cyclic behaviour of shallow foundations is modelled reasonably.

The remaining issue that must be addressed to validate the multiple-yield-surface model is to examine its ability to capture the real behaviour observed from experiments.

4.5.2 Capturing the real behaviour of caissons

This section presents the numerical illustrations using the multiple-yield-surface model to simulate the results observed from experiments of caisson models in sand. These tests have been carried out at Oxford University and reported in Villalobos *et al.* (2003a, 2003b, 2004a and 2004b). The installation without suction, and cyclic horizontal and rotational loadings at different constant vertical loads have been performed. Different kinds of caisson models have been used with different shape ratios, which is the ratio of the length of the skirt *L* over the diameter *D*. The results obtained have given a common shape of the installation curve. Thus, for simplicity, the numerical analysis will be implemented to capture the results of one of these tests. Particularly, the results of the test number T79-13-1 in Villalobos *et al.* (2004a) that has been done for cyclic moment loading are selected. The caisson model geometry is shown in Figure 4.33. The soil properties and model parameters are given in Table 4.7

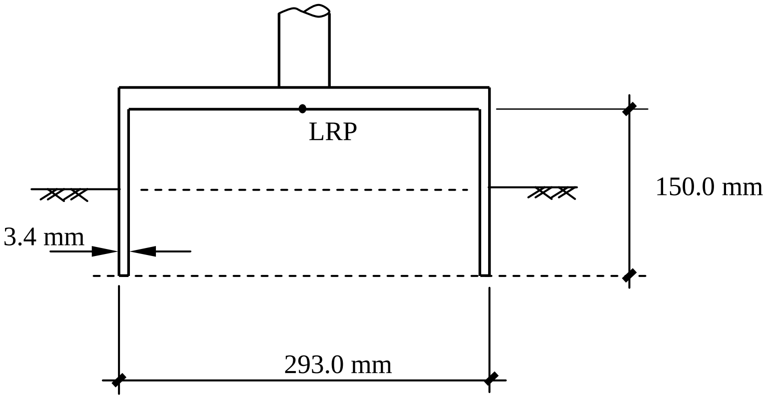

Figure 4.33 Outline of the caisson in laboratory tests
(After Villalobos *et al.*, 2004a)

There are two issues which should be focused on: (i) the installation process and (ii) the performance of caisson in serviceability conditions. Firstly, as shown in Figure 4.34, it is clear that the results of the theoretical solution for installation are rather close to the test results. Adjusting the bell width of the bell function and the parameters of the bearing capacity calculation procedure can change the gap between the two curves. However, since the tests for installation do not coincide, it is not necessary to adjust the theoretical solution to capture just one specific test. Furthermore, the theoretical curve also shows a very similar shape to that of the test in both installation and unloading process.

Secondly, in order to have a preliminary verification before moving on to the cyclic loading, a numerical analysis is implemented for the monotonic loading of horizontal force and corresponding moment at a constant vertical load, which is held from the end of the installation process (Figure 4.34). Figures 4.35 and 4.36 show the comparisons between the numerical results and test results during this loading. It is found that the two results are rather close.

Table 4.7 Input data of the caisson in test scale

Soil properties					
Type of soil	Sand				
Shear modulus *G* (initial value) (MN/m^2)	0.7				
Effective unit weight (kN/m^3)	10.0				
Angle of friction	35^o				
Poisson's ratio ν	0.2				
Model parameters (for ISIS model)					
Association factors	a_{V1}	a_{V2}	a_H	a_M	a_Q
	0.297	1.0	0.7	0.7	0.7
Shape factors of yield surface	e_1	-0.2			
	e_2	0.0			
	t_0	0.1088			
	m_0	0.15			
	h_0	0.337			
	q_0	0.2			
	β_1	0.99			
	β_2	0.99			
Parameters for the rate-dependent solution	Viscosity μ	0.002			
	Time increment *dt*	Changed with the load incerements			
Number of yield surfaces	20 yield surfaces used				
Bell width (w_{bell}) (m)	0.01				

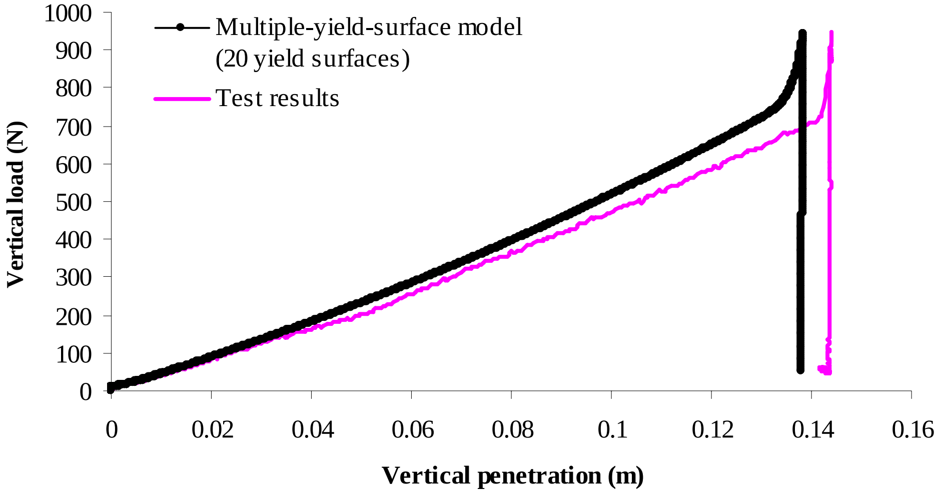

Figure 4.34 Installation of the caisson model

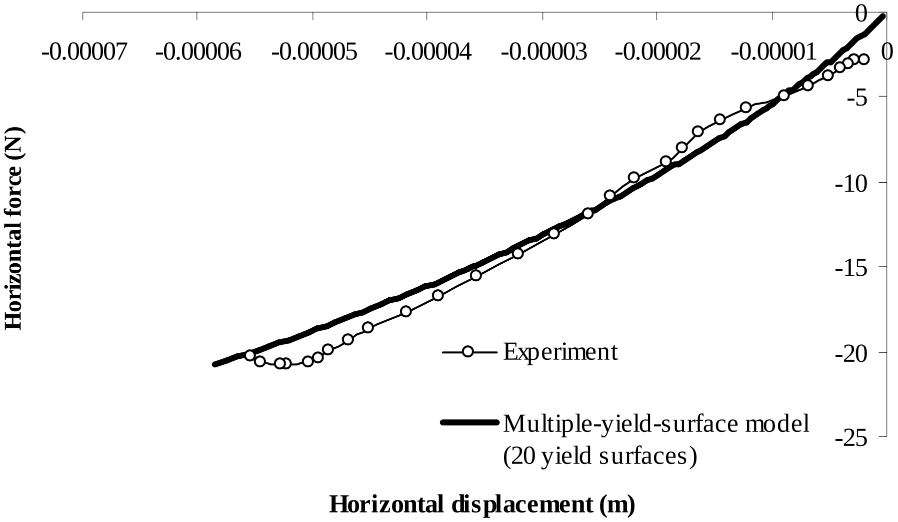

Figure 4.35 Horizontal response of the caisson model under monotonic loading

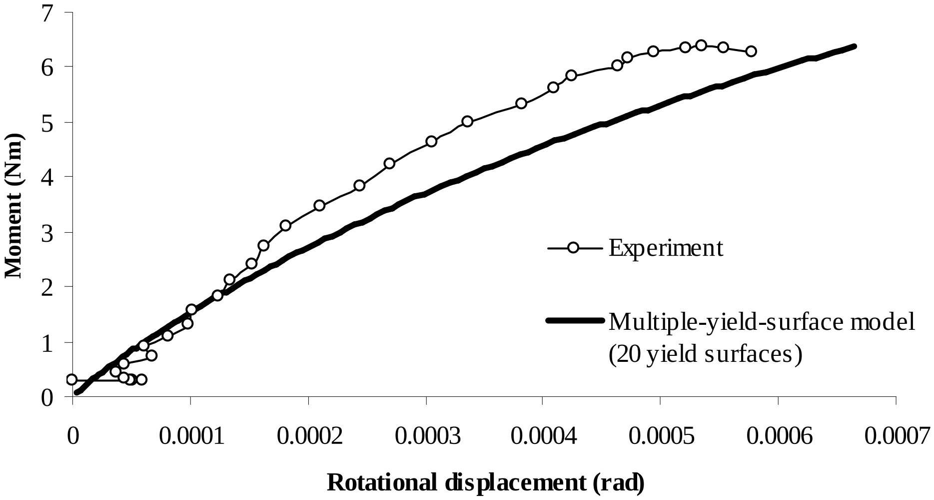

Figure 4.36 Rotational response of the caisson model under monotonic loading

Furthermore, the numerical analyses have been carried out with ten cycles of horizontal and corresponding rotational loading at constant vertical load (V = 50 N). Figures 4.37 and 4.38 show the results of the first four cycles. Figure 4.39 shows the vertical movements of the caisson during the cyclic loading which, in this case, are upward movements. In fact, in this case, the theoretical curves do not entirely capture the test. However, they show the correct trends, which look very similar to those of the test results, and the differences between the test and the theoretical curves are not too great. In addition, it should be noted that the comparisons presented in this example are made with the theoretical solution and a particular test, which can only be expected to provide the trend of the real behaviour and similar but not exact magnitudes. Besides, the theoretical solution uses preliminary choices for its model parameters and these parameters can be adjusted to get better results. Therefore, from the illustrations shown, it is reasonable to hope that the multiple-yield-surface model can be an applicable model to give reasonable predictions for the cyclic loading behaviour.

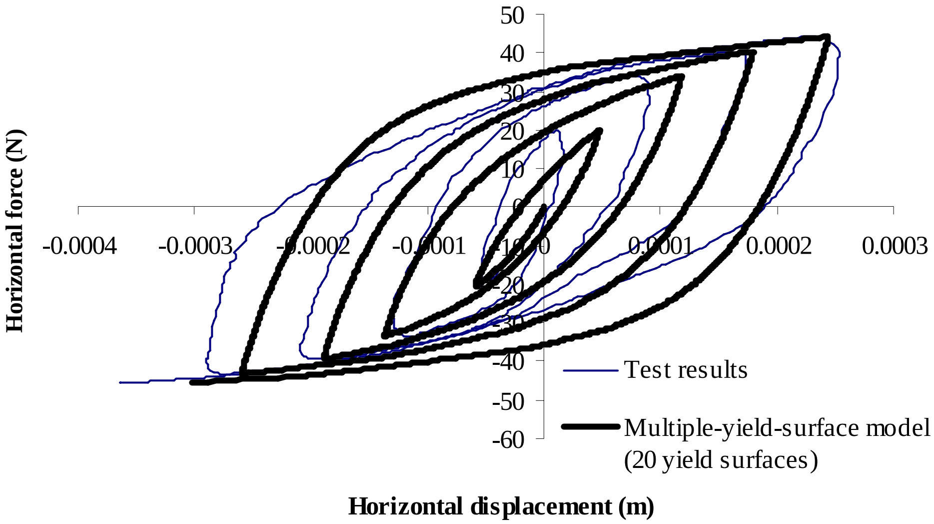

Figure 4.37 Horizontal response of the caisson model under cyclic loading

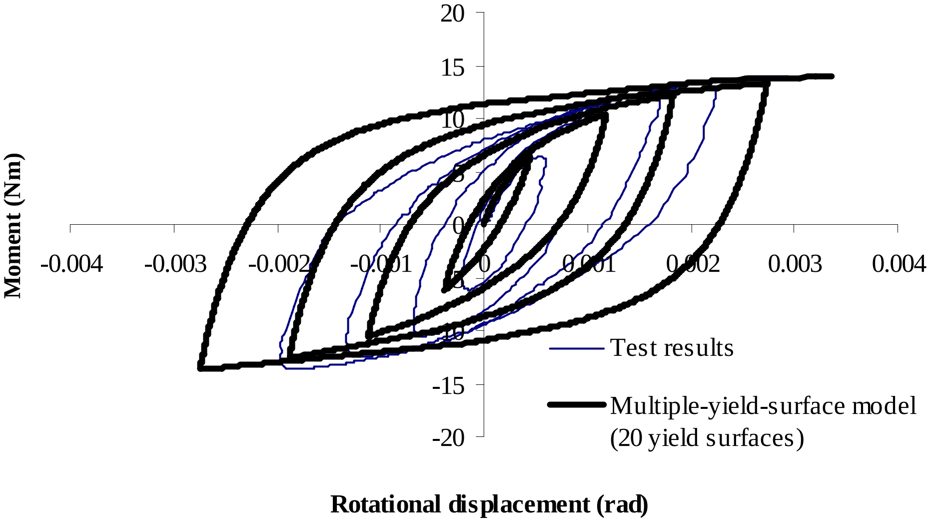

Figure 4.38 Rotational response of the caisson model under cyclic loading

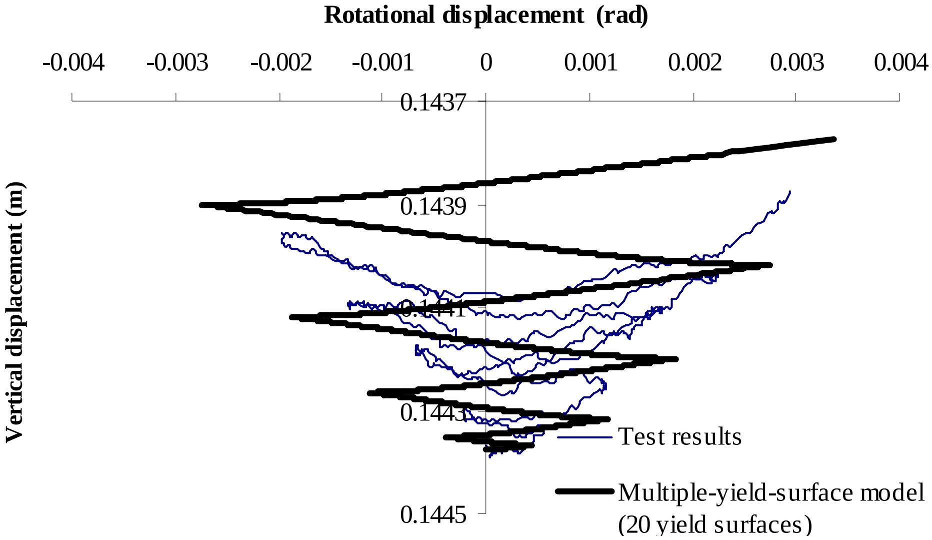

Figure 4.39 Vertical movements of the caisson model under cyclic loading

An alternative is to check the model by using the concept of “backbone” curve. Originally, Masing (1926) has given two statements for the behaviour of a pure kinematic hardening material, suggesting that the initial loading curve, so-called backbone curve, may be used to define the behaviour during all subsequent load reversals as follows:

(1) The tangent modulus at the start of each loading reversal assumes a value equal to the initial tangent modulus for the initial loading curve.

(2) The shape of the unloading or reloading curves is the same as that of the initial loading curve, except that the scales of both load and displacements axes are enlarged by a factor of 2

Then, Pyke (1979) has formally stated two additional rules, which are known as the extended Masing’s rules, as follows:

(3) The unloading and reloading curves should follow the initial loading curve (backbone curve) if the previous maximum shear strain is exceeded.

(4) If the current loading or unloading curve intersects the curve described by previous loading or unloading curve, the stress-strain relationship follows the previous curve.

Byrne and Houlsby (2004) state these rules and given some test results confirming the Masing behaviour for caisson foundations.

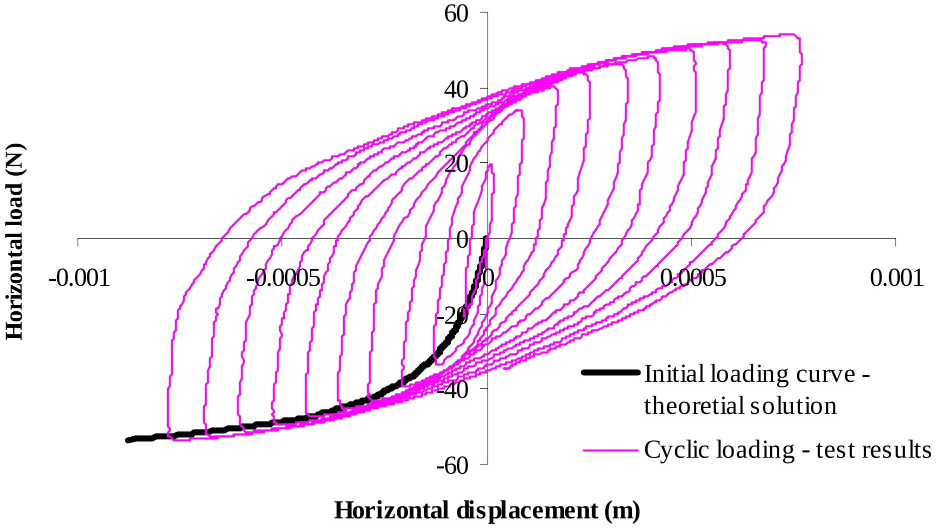

Figure 4.40 Theoretical horizontal backbone curve and the cyclic loading test

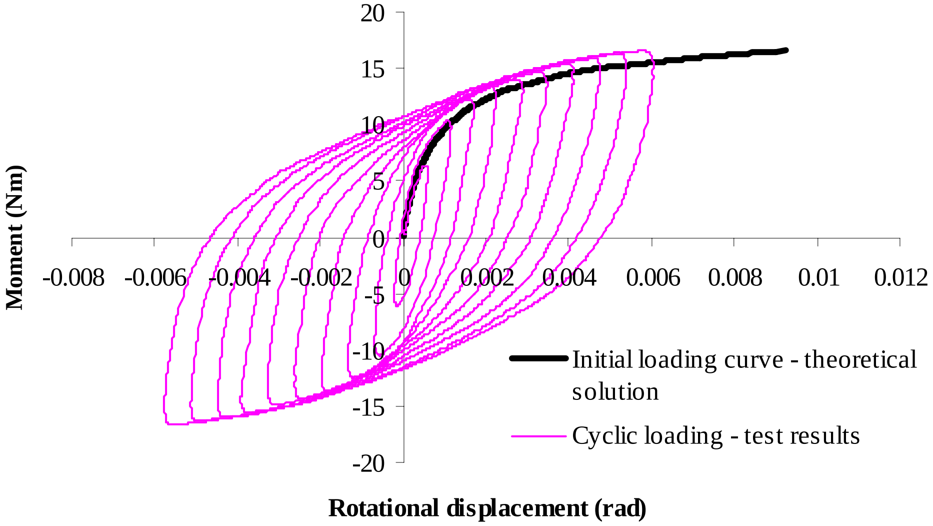

Figure 4.41 Theoretical moment backbone curve and the cyclic loading test

To examine whether the model of this study can obey the Masing behaviour and consequently confirm the ability to capture the cyclic behaviour, two steps are required. Firstly, a numerical calculation has been implemented to simulate the backbone curves of both horizontal loading and corresponding moment at the constant vertical load $V = 50$ N. Figures 4.40 and 4.41 show the results of this work compared with the total ten cycles of loading curves observed from the test T79-13-1 (Villalobos *et al.*, 2004a). It is clear that the theoretical backbone curves look very similar to the backbone of the test.

Secondly, by comparing the backbone curves of theoretical solution and test results at different constant vertical loads, the feature of Masing behaviour of the model can be confirmed. There are two numerical analyses undertaken with the caisson model in Figure 4.33. The model parameters are given in Table 4.8. The two tests, T1-1 with constant vertical load V = 50 N and T 31-4-1 with constant vertical load V = 100 N in Villalobos *et al.* (2004a), are used to validate the theoretical results.

Table 4.8 Model parameters of the caisson in test scale (Test T1-1 and T31-4-1)

Model parameters (for ISIS model)		
Shape factors of yield surface	e_1	-0.2
	e_2	0.0
	t_0	0.1088
	m_0	0.122
	h_0	0.229
	q_0	0.2
	β_1	0.99
	β_2	0.99

In the first analysis following the test number T1-1, the vertical load is kept constant at the value of 50 N, which is rather small compared with the maximum vertical load (V = 945 N). Therefore, the unloading causes some negative plastic vertical displacements (upward movements) and re-activates some of the yield surfaces. Particularly, in this case, the first five yield surfaces are re-activated during the unloading process as shown in Figure 4.42. Consequently, the horizontal and rotational responses start with the elasto-plastic stiffness of the first five yield surfaces contributing. Figures 4.43 and 4.44 show the results of these responses which are very close to the experimental observations.

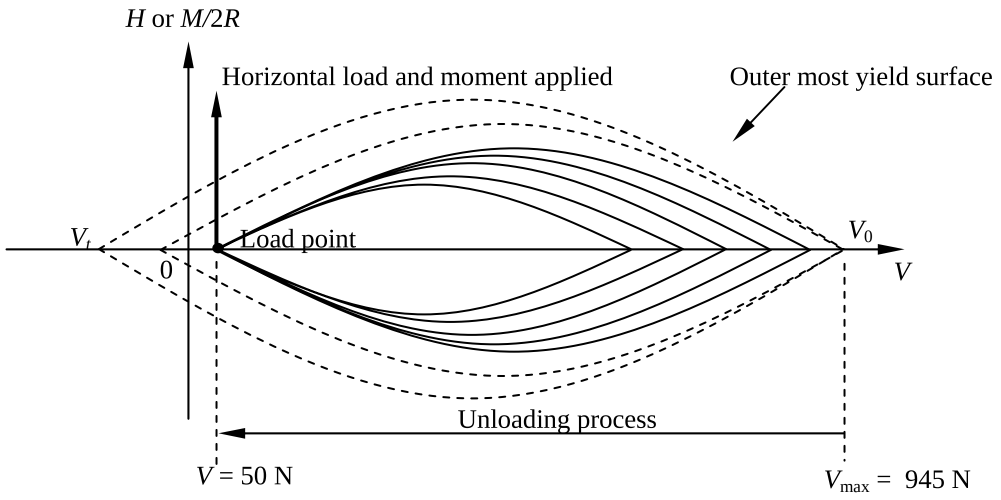

Figure 4.42 System of first five yield surfaces activated after unloading process (V = 50 N)

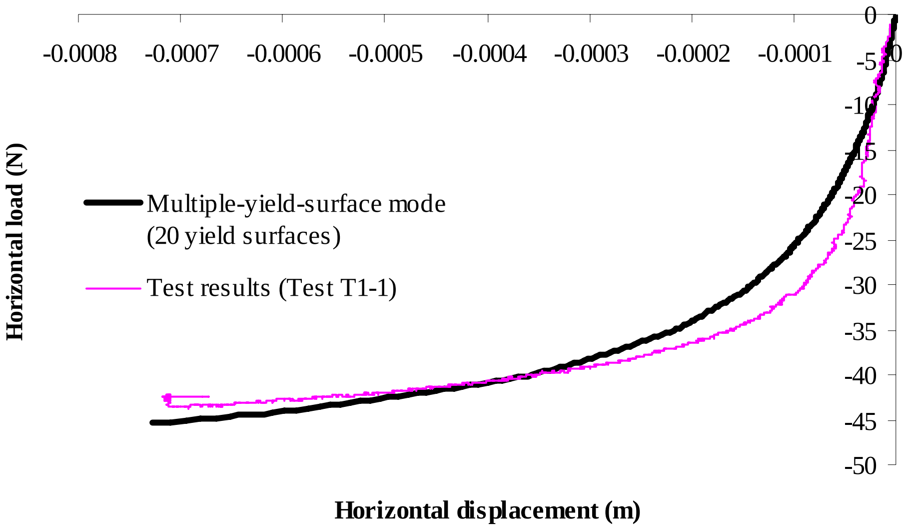

Figure 4.43 Initial horizontal loading (backbone) curve at constant vertical load V = 50 N

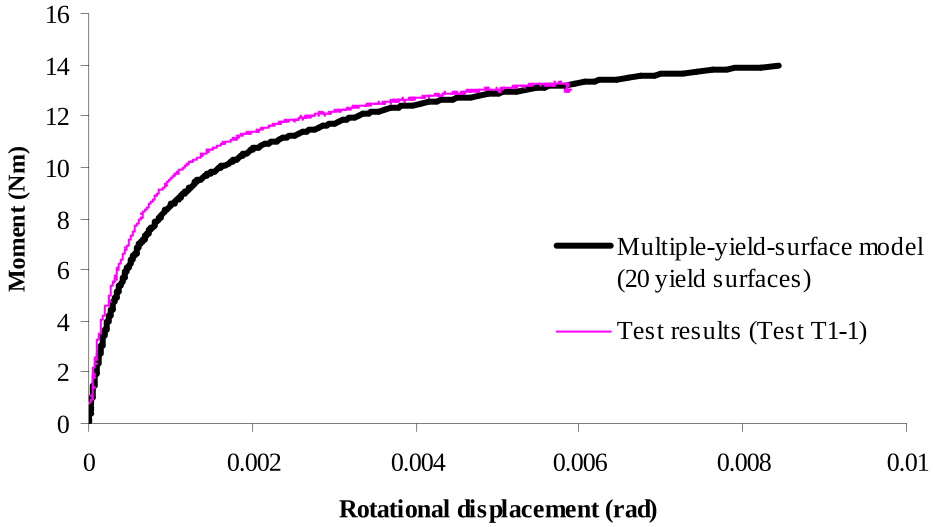

Figure 4.44 Initial rotational loading (backbone) curve at constant vertical load V = 50 N

In the second analysis compared with the test number T34-1-1, the constant vertical load is twice that in the previous analysis. Therefore, the unloading process reaching this value has not re-activated any yield surface. Consequently, the horizontal and rotational responses start with the purely elastic stiffness as shown in Figure 4.45. Figures 4.46 and 4.47 show the results of this work. Again, similarities between the theoretical solution and the test are clear.

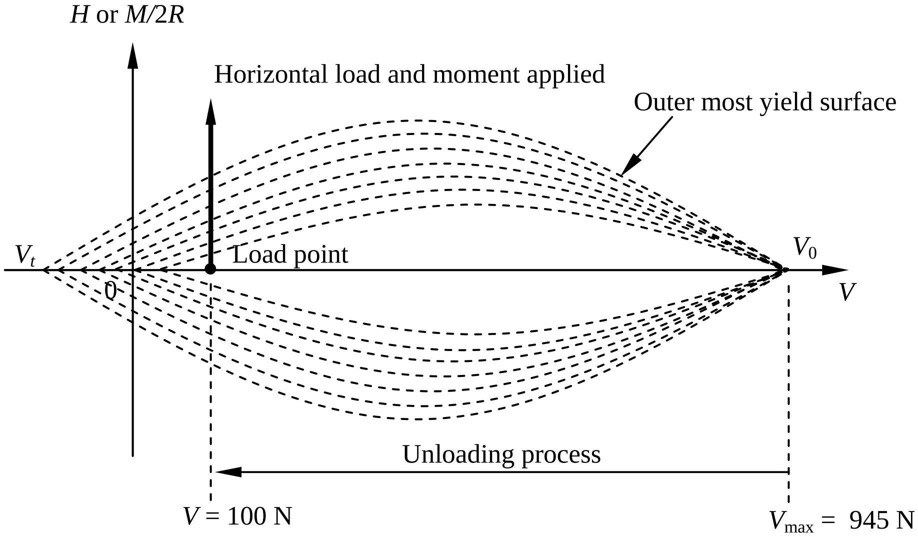

Figure 4.45 System of yield surfaces after unloading process (V = 100 N)

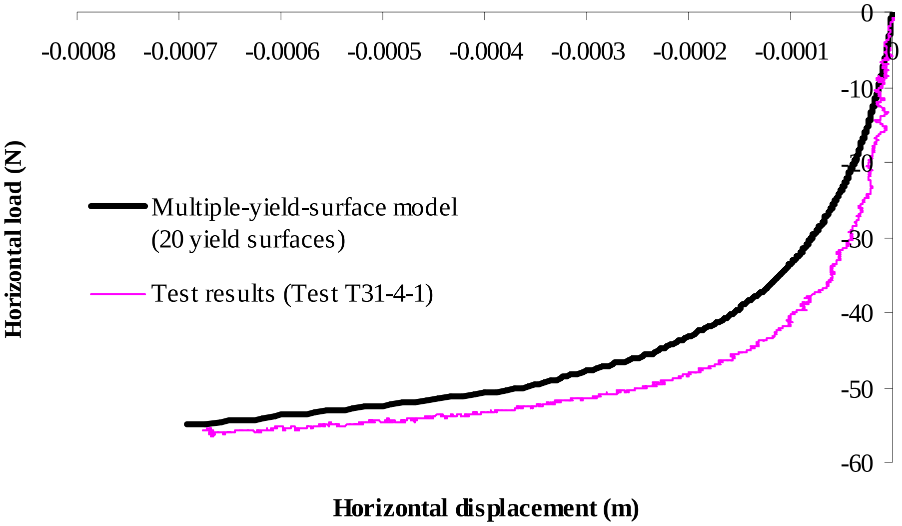

Figure 4.46 Initial horizontal (backbone) curve at constant vertical load V = 100 N

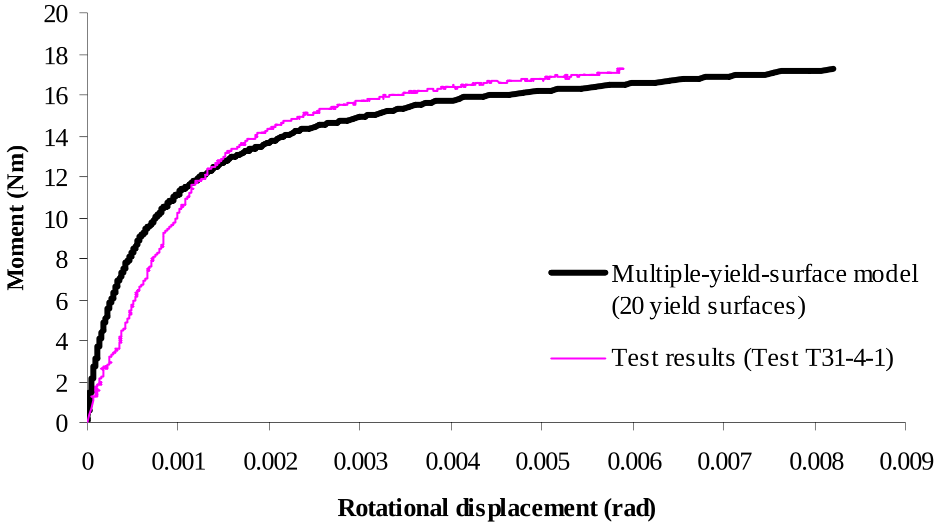

Figure 4.47 Initial rotational (backbone) curve at constant vertical load $V = 100$ N

Considering the vertical movements during the cyclic application of horizontal loads and moments at constant vertical loads, there is experimental evidence available (Villalobos *et al.*, 2004a and 2004b). This shows that the vertical movements depend on the ratio between the vertical load and the vertical bearing capacity of the foundation at the full penetration depth. In fact, the magnitudes of the vertical load during the installation without suction always approximate those of the corresponding vertical bearing capacities. As shown in Figure 4.48, Villalobos (2004d) has given evidence of this feature. In this figure, the U-shape curves show the trends of the vertical movement during the cyclic horizontal and moment loadings. Each point in a U-shape curve corresponds to a peak point of a cycle. A series of tests have been done with the caisson model as shown in Figure 4.33 on sand at different relative densities R_d. The maximum vertical load applied in these tests varies from 750 N up to 1100 N and then the constant vertical loads have been used as in Figure 4.33. From these tests, it can be found that once the vertical load applied is small the vertical movements during the cyclic loading tend to be upward. The magnitude of these movements decreases and even changes sign when the vertical load increases.

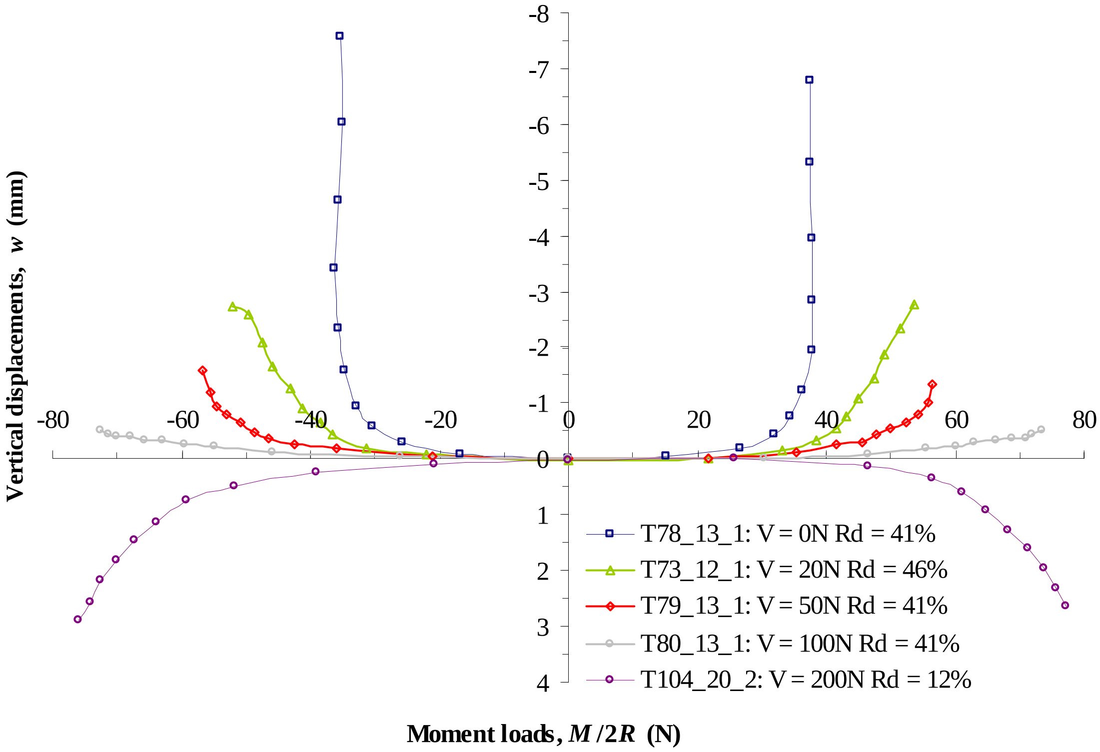

Figure 4.48 The peak points of moment responses, shown as the U-shape curves, represent the variations of the vertical movements which depend on the constant vertical load kept during the cyclic loading (after Villalobos, 2004d)

Using the multiple-yield-surface model (ISIS model) with the system of 20 yield surfaces for the caisson model in Figure 4.33, the results are shown in Figure 4.49. With the same maximum vertical load ($V_{\max}$ = 945 N), the model shows two different vertical behaviours at two different constant vertical loads, V = 200 N and V = 300 N. There is a difference between the experimental results and theory whereby, at the value of 200 N constant vertical load, the vertical movements in the test are downward while they are still upward in the theoretical results. However, in the tests, the magnitudes of maximum vertical loads as well as the soil specimen parameters cannot be exactly reproduced in theoretical analyses.

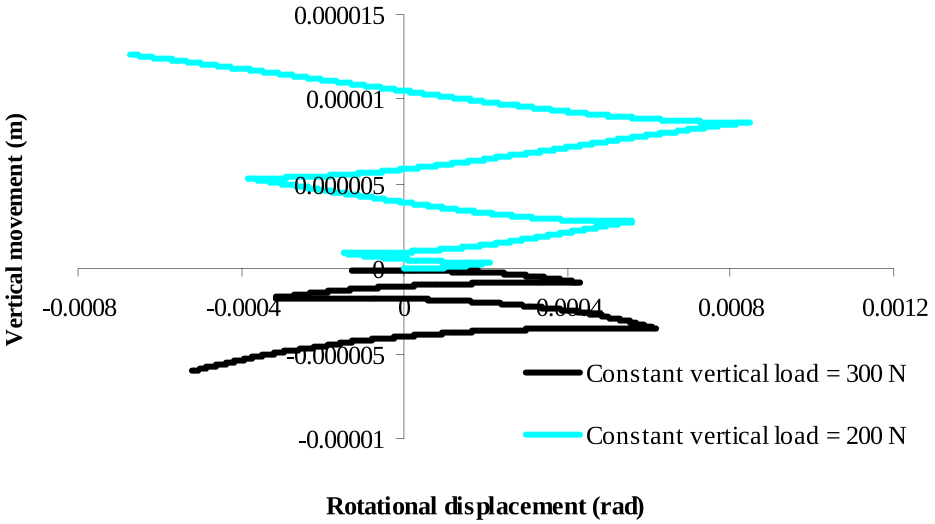

Figure 4.49 Vertical movements under cyclic loadings at different constant vertical loads (Theoretical solutions using multiple-yield-surface ISIS model with 20 yield surfaces)

Finally, in order to complete this section, it is necessary to mention the relationship between laboratory tests and field tests. There is a wide range of field tests that have been implemented and reported by Kelly *et al.* (2003, 2004) and Houlsby *et al.* (2005a, 2005b) for caisson foundations in both clay and sand. From the comparison between the laboratory test results and that of field trials, Kelly *et al.* (2005c) have pointed out that the quality of agreement between laboratory test results and the field trial results is highly satisfactory. This remark leads to more confidence not only for the scaling relationship between laboratory and field tests but also for the theoretical predictions presented in this study.

4.6 Discussion

In section 4.2, the analytical expression of a continuous hyperplasticity model for shallow foundations of offshore structures has been presented. Then, in sections 4.3 and 4.4, the discretization of this model which can be understood as the multiple-yield-surface model has been described to be suitable for numerical analyses. The mathematical difficulties coming from the consistency conditions for many yield surfaces at the same time in the rate-independent solution have led to the introduction of the rate-dependent solution. As discussed in chapter 3 and now confirmed in the numerical illustrations of this chapter, the rate-dependent solution with suitable values of its parameters can give very realistic results. However, using the rate-dependent solution to mimic the rate-independent solution, the values of the viscosity factor, time increments and number of steps in each load stage must be chosen with care, possibly after a few trials. The completion of this process depends on the experience of the analyst. This is a drawback of the rate-dependent solution of this model. This problem will be discussed in more detail in section 5.6.

In section 4.5, numerical validations have been performed with a series of numerical examples for circular flat footings, spudcans and caissons. The goal of introducing the numerical analyses for circular flat footings and spudcans is to prove that the hyperplasticity model can cover not only caisson footings but also other kinds of shallow foundations. In the main work of this research which is modelling for suction caisson, there are two main aspects which have been highlighted: the differences of the multiple-yield-surface model compared with the single-yield-surface model and the capability to capture the real behaviour observed from experiments.

In the first aspect, as discussed in section 4.5.1, there are significant differences between the solutions of the multiple-yield-surface model and the single-yield-surface model. The most impressive result obtained from the multiple-yield-surface model is that it can rigorously express the change of elastic stiffness depending on strain level by using the concept of the inner yield surfaces. This well-known phenomenon, which has been mentioned in Muir Wood (1991) or Atkinson (1993), cannot be simulated correctly by using either conventional single yield surface plasticity models or hyperplasticity single-yield-surface models.

In the second aspect, the process of capturing the experimental behaviour of a caisson has been presented. Firstly, the vertical response of the caisson during the installation is calculated and compared with that of the test. Secondly, the initial loading of horizontal and corresponding moment is simulated. Thirdly, the analysis of caisson behaviour under cyclic horizontal and moment loading is implemented. Afterwards, the verification of the model using the concepts of the Masing's rules have been made. Lastly, to confirm the similarities between the theoretical backbone curves (Masing curves) and the experimental backbone curves, two more calculation examples were undertaken for the caisson model under initial monotonic loading, as shown in Figures 4.43, 4.44, 4.46 and 4.47. In addition, a brief discussion about the connection between laboratory test results, theoretical results and field test results, has been presented. In general, throughout this work, similarities between theory and experiment were often observed or, at the worst, the model proposed has shown capabilities to be adjusted to capture the real behaviour.

4.7 Concluding remarks

The derivation for the multiple-yield-surface version of the ISIS model has been presented. This version possesses not only all the advantages of a model using hyperplasticity theory as mentioned in section 3.8 but also reveals some more important features as follows:

- It is flexible to adjust the two scalar functions, which are free energy function and either dissipation function or yield function, to describe as closely as possible the hardening rule.
- By using the concept of multiple-yield-surfaces, the model can simulate very well the smooth transition between the elastic and plastic stiffness. Consequently, hysteretic phenomena can be reproduced logically.
- As demonstrated in section 4.5, the model presented gives reliable predictions for the cyclic behaviour of caisson foundations under environmental loads.

The torsion component in the ISIS model has not been treated in detail. Essentially, the torsion response can be treated in the same way as the moment. Furthermore, the caisson response for many load cases is not sensitive to the torsion component. Since there is currently little available experimental data, the model parameters involving the torsion component are merely given as starting points. They can be adjusted to be more suitable for the model in the future works after collecting enough experimental data.

CHAPTER 5

PARAMETER SELECTION AND PARAMETRIC STUDY

5.1 Introduction

In the development of the model, a number of parameters are employed to make the model more flexible in capturing real foundation behaviour. There are four main groups of parameters in the model which control the numerical solution. These parameters are related to the yield function (m_0, h_0, t_0), the flow rule ($a_{V1}, a_{V2}, a_M, a_H, a_Q$), the distribution of the yield functions ($\eta_0^{initial}$) and the hardening rule (A_i, b_i, n_i). In addition, the requirement to mimic the rate-independent behaviour of the rate-dependent solution leads to an extra relationship between the viscosity factor μ, the time increment, the elastic stiffness factors and the number of either load increments or displacement increments in each stage of the analysis.

In previous chapters, from the first version of the model using a single yield surface to the current version using the multiple-yield surface concept, preliminary choices of values of the model parameters have merely been given without explaining their basis. This chapter presents details about the methods for choosing suitable values for the model parameters and discussion regarding the various values. In some cases, it may be impossible to give either explicit mathematical expressions or purely theoretical explanations for the values chosen. However, with empirical results and test observations, appropriate ranges for these parameters can be proposed.

5.2 Shape of the yield surface

5.2.1 Variations of the shape parameters corresponding to the ratios of *L/D*

In the theoretical models using macro-element concept such as model B (Martin, 1992), model C (Cassidy, 1999) as well as the current ISIS model for caisson foundations, the peak values on longitudinal axis of the yield surfaces have been determined from the vertical bearing capacity V_0. For other axes, they are calculated by multiplying V_0 by the factors h_0 and m_0 for the horizontal and moment force axes respectively.

The circular flat footing can essentially be considered as a special case of a caisson foundation with the ratio *L*/*D* = 0.0. In the case of a circular flat footing on sand, Cassidy (1999) has proposed the magnitudes for h_0 and m_0 as shown in Table 5.1. Villalobos (private correspondence, 2003) has observed the parameters corresponding to the shape ratios (*L*/*D*) of 0.5 and 1.0 which are also given in Table 5.1.

Table 5.1 Shape parameters for the yield surface (LRP at the base of the caisson)

L/*D*	h_0	m_0	t_0	Eccentricity factor *e*
0.0	0.116	0.086	0.0	-0.2
0.5	0.299	0.122	0.088	-0.75
1.0	0.21	0.172	0.115	-0.89

The values of h_0 and m_0 are the intersections of the yield surface with the horizontal force axis, $\frac{H}{V_0}$, and moment axis, $\frac{M}{2RV_0}$, respectively at its largest cross section. By using the Load

Reference Point (LRP) at the base of caisson as shown in Figure 5.1a, the cross section of the yield surface can be drawn as shown in Figure 5.1c.

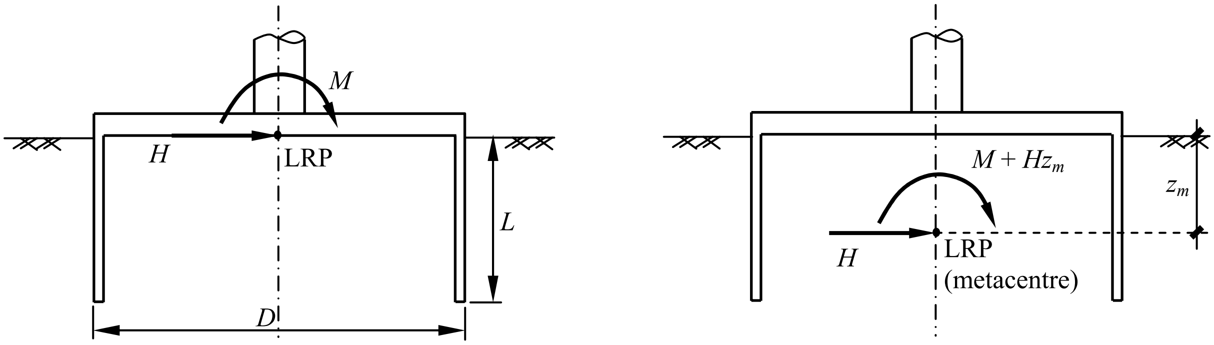

Figure 5.1a Load Reference Point at the base of the caisson **Figure 5.1b** Load Reference Point at metacentre

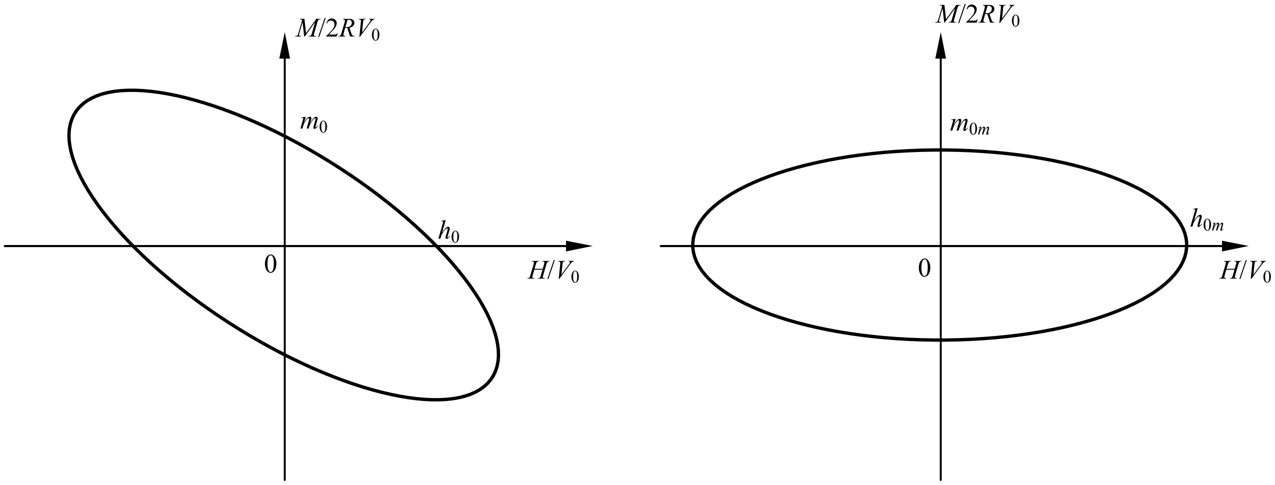

Figure 5.1c Biggest cross section of the yield surface corresponding to the LRP at the base

Figure 5.1d Biggest cross section of the yield surface corresponding to the LRP at metacentre

Figure 5.1 Cross section of the yield surface corresponding to the LRP viewpoint

In this case, the values of h_0 and m_0 are different from those of the corresponding peak points of the yield surface. Consequently, there could be some confusion and it might be difficult to determine the changes of h_0 and m_0 when the ratio $\frac{L}{D}$ of the caisson is changed. It is therefore convenient to look for a position of the LRP at which the yield surface does not have any the eccentricity in cross sections in the $\left(\frac{H}{V_0}:\frac{M}{2RV_0}\right)$ plane. The position of this new LRP can be called the *metacentre*. The position originally proposed by Bell (1991) for the elastic solution of offshore foundations and the cross section of the yield surface viewed at this position are shown in Figure 5.1b and 5.1d.

In addition, it should be emphasized that the two cross section shapes, shown in Figures 5.1c and 5.1d, are just alternative presentations of a unique yield surface. The different shapes are because the yield surface has been projected from different Load Reference Points. Therefore, it can be suggested that the yield functions when using the LRP at the metacentre has the form as follows:

$$y = t_m - \beta_{12} S \left| v_1 + t_0 \right|^{\beta_1} \left| 1 - v_2 \right|^{\beta_2} = 0 \tag{5.1}$$

In which, the subscript m is used to represent the term related to the metacentre.

Considering the yield surface in true force space and simplifying it for a 2-D analysis in (V: H_3: M_2) space, the relation between the two forms of the yield function, as in Eq. (3.36) and Eq. (5.1), must result in the following equation:

$$t = t_m \tag{5.2}$$

where t and t_m now can be expressed as:

$$t = \sqrt{h_3^2 + m_2^2 - 2e h_3 m_2} \tag{5.3}$$

$$t_m = \sqrt{h_{3m}^2 + m_{2m}^2} \tag{5.4}$$

Since the yield surface from the reference of the metacentre point is such that there is no eccentricity, the coupling of horizontal and moment components therefore vanishes from t_m. From Eq. (5.2), it follows:

$$\left(\frac{H_3}{h_0V_0}\right)^2+\left(\frac{M_2}{2Rm_0V_0}\right)^2-2e\left(\frac{H_3}{h_0V_0}\right)\left(\frac{M_2}{2Rm_0V_0}\right)=\left(\frac{H_3}{h_{0m}V_0}\right)^2+\left(\frac{M_2+z_mH_3}{2Rm_{0m}V_0}\right)^2 \tag{5.5}$$

It should be noted that since the yield surface is unique, Eq (5.5) must be satisfied at every point on the yield surface. Therefore Eq. (5.5) must be equivalent to the following system of equations derived from the equalities of the terms including H_3^2, M_2^2 and H_3M_2 respectively.

$$\left(\frac{H_3}{h_0V_0}\right)^2=\left(\left(\frac{1}{h_{0m}V_0}\right)^2+\left(\frac{z_m}{2Rm_{0m}V_0}\right)^2\right)H_3^2 \tag{5.6}$$

$$\left(\frac{M_2}{2Rm_0V_0}\right)^2=\left(\frac{M_2}{2Rm_{0m}V_0}\right)^2 \tag{5.7}$$

$$-2e\left(\frac{1}{h_0V_0}\right)\left(\frac{1}{2Rm_0V_0}\right)H_3M_2=\left(\frac{2z_m}{\left(2Rm_{0m}V_0\right)^2}\right)H_3M_2 \tag{5.8}$$

From the above equalities, the relations between h_0, m_0, e and h_{0m}, m_{0m}, z_m can be derived as follows:

$$h_{0m}=\frac{h_0}{\sqrt{1-e^2}} \tag{5.9}$$

$$m_{0m}=m_0 \tag{5.10}$$

$$\frac{z_m}{D}=-e\frac{m_0}{h_0} \tag{5.11}$$

The reverse relations also can be expressed as:

$$h_0=h_{0m}\sqrt{1-e^2} \tag{5.12}$$

$$m_0=m_{0m} \tag{5.13}$$

$$e = -\frac{\left(\frac{z_m}{D}\right)^2\left(\frac{h_{0m}}{m_{0m}}\right)^2}{\sqrt{1+\left(\frac{z_m}{D}\right)^2\left(\frac{h_{0m}}{m_{0m}}\right)^2}} \tag{5.14}$$

From Eq. (5.9) to (5.14), it can be found that there is a mapping between the shape factors of the yield surface using the LRP at the base of the caisson (h_0, m_0 and e) and that of the yield surface using the LRP at the metacentre (h_{0m}, m_{0m} and z_m). Table 5.2 shows the values of h_{0m}, m_{0m} and z_m corresponding to the values of h_0, m_0 and e shown in Table 5.1.

Table 5.2 Shape parameters of the yield surface (LRP at the metacentre)

L/D	h_{0m}	m_{0m}	z_m/D
0.0	0.118	0.086	0.148
0.5	0.45	0.122	0.3
1.0	0.46	0.172	0.729

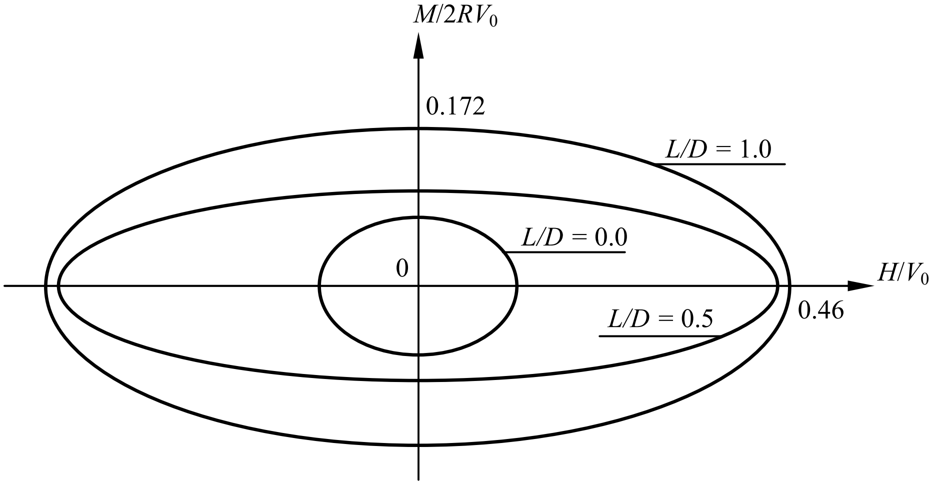

Figure 5.2 Variation of the biggest cross section of the yield surface corresponding to different ratios of *L/D* (LRP at the metacentre)

Figure 5.2 shows the changes of the cross section of the yield surface corresponding to the change of the ratio *L*/*D*. The physical meaning of the metacentre is that at that point, if there is purely horizontal load applied ($M = 0$), there will be no rotational displacements. The caisson is therefore just moving horizontally. By using the concept of a metacentre, it is easier to observe the variation of the peak values h_{0m} and m_{0m} and therefore easier to interpolate these values corresponding to any ratio of *L*/*D*. Furthermore, as mentioned above, from the values of h_{0m}, m_{0m} and z_m, it is possible to derive the values of h_0, m_0 and e at a certain ratio of *L*/*D*. An approach could thus be taken where the variations of h_{0m}, m_{0m} and z_m are interpolated before determining the values of h_0, m_0 and e.

However, since the experimental data observed so far are not sufficient to confirm the details of these curves, we can merely discuss expected trends. Firstly, the variations of the vertical bearing capacity V_0 and the passive pressures along the skirt of the caisson are assumed to be almost linear. This leads to the fact that the horizontal and rotational capacities of the caisson ($h_0 V_0$ and $m_0 2RV_0$) increase with the square of depth, meanwhile V_0 increases linearly with depth. The variations of h_{0m} and m_{0m} are therefore expected to be almost linear. Secondly, the ratio $\frac{z_m}{D}$, which represents the position of the metacentre, is expected to increase gradually with the length of caisson. The exact form of this variation has not been proposed yet but it could be varied to give steady values of the ratio $\frac{z_m}{L}$ in the range from 0.6 to 0.75 (in case of a long caisson or short pile, see Bell, 1991). Lastly, the value of t_0 can be determined from the ratio of total friction force along the skirt over the vertical bearing capacity V_0. It can be therefore calculated directly from the calculation procedure of V_0 and then adjusted by referring to the test results. Figures 5.3, 5.4, 5.5 and 5.6 show the common trends of the variations of h_{0m}, m_{0m}, $\frac{z_m}{D}$ and t_0.

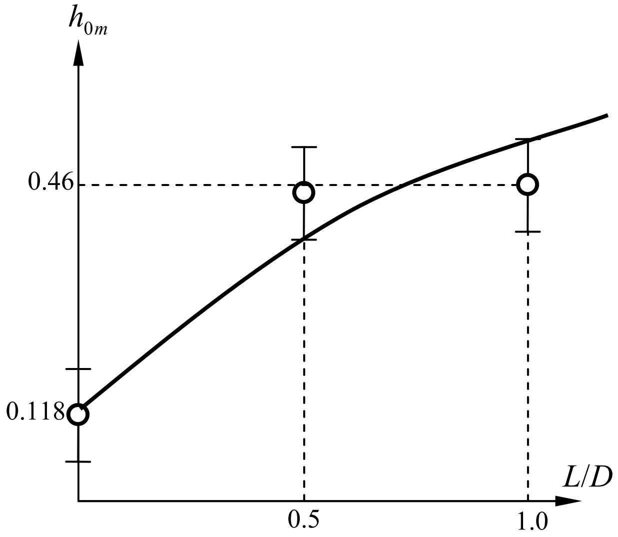

Figure 5.3 Variation of h_{0m} with respect to L/D

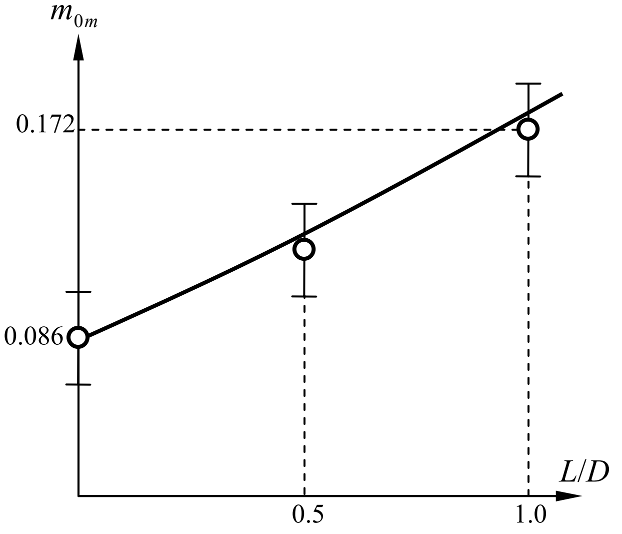

Figure 5.4 Variation of m_{0m} with respect to L/D

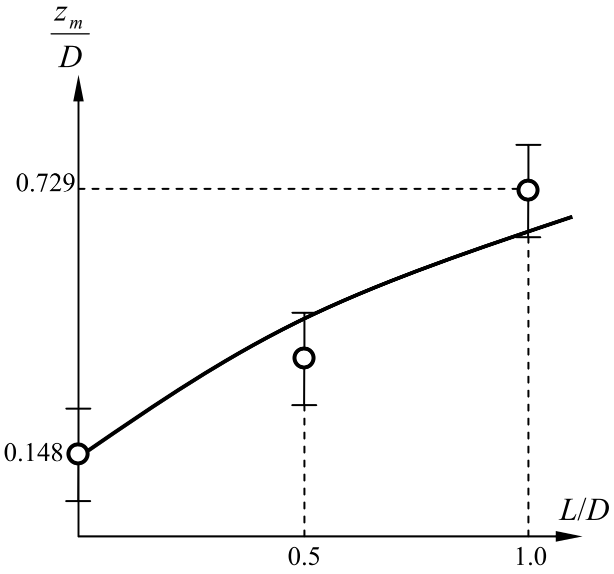

Figure 5.5 Variation of $\frac{z_m}{D}$ with respect to L/D

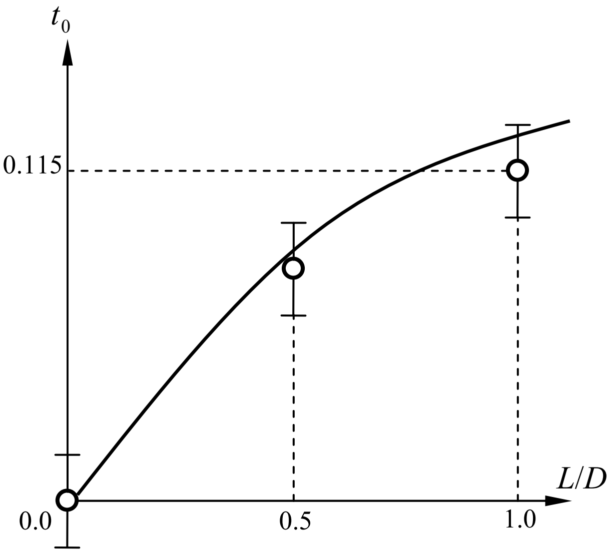

Figure 5.6 Variation of t_0 with respect to L/D

5.2.2 Discussion

In section 5.2.1, the procedure for determining the variations of the shape parameters of the single-yield-surface model for caisson footings in the serviceability condition (after finishing the installation process) with different ratios of the length *L* over the diameter *D* has been proposed. The key feature of this procedure is that it is based on a unique yield surface. The position of the metacentre therefore depends on this condition and consequently depends on the yielding process.

In the single-yield-surface model, as there is only one yield surface considered, the correlations from Eq. (5.9) to Eq. (5.14) can not be changed during the yielding process. The situation is much more complicated when considering the multiple-yield-surface model. The shapes of the inner yield surfaces are not the same. They are changed depending on the level of plasticity which implies the number of yield surfaces activated. The correlations from Eq. (5.9) to Eq. (5.14) are thus no longer applicable. Fortunately, the procedure for determining the system of yield surfaces based on the metacentre is not necessary. This is because the yield surface considered in the single-yield-surface model now plays the role as the outermost yield surface and it will be activated when full plasticity occurs. In addition, the shape of the inner yield surfaces can be flexibly chosen. In this study, the initial distribution of inner yield surfaces in the multiple-yield-surface model is based on the outer most yield surface which is the yield surface considered in the single-yield-surface model. Therefore, in the multiple-yield-surface model, the correlations from Eq. (5.9) to Eq. (5.14) are used to determine the outermost yield surface first and then the inner yield surfaces can be defined automatically.

For clay, since only very limited experimental data are available at present, there is no definitive expression for the yield function in clay. However, a similar approach to that proposed for a caisson in sand could be used. Furthermore, from the results obtained from Martin (1992) for spudcan footings on clay and Cassidy (2000) for spudcans on sand, it can be recognised that the behaviours of shallow foundation on clay and on sand in the case of undrained loading are not too different. Thus, it could be expected that there will not be many important changes in the relations established between clay and sand in the analysis described in this thesis.

5.3 Association factors

The association factors $(a_{V1}, a_{V2}, a_M, a_H, a_Q)$ are used to express the non-associated flow rule in which the flow vectors do not coincide with the normal vectors of the yield surface. In model B and model C, this feature has been described by using an extra function called the potential function. The flow vectors are then derived from the partial differentials of this function with respect to the corresponding true forces. In the ISIS model, the flow vectors are defined as the partial differentials of the yield function with respect to the corresponding generalised forces directly, and without further assumptions about the potential function as in model B or model C. The association factors are used to manage the interpolation between the true forces and the generalised forces in the yield function. Essentially, they play the role of adjustments in the directions of the flow vectors which can be observed from tests. The concept of association factors can allow the ISIS model to replicate flexibly the experimental observations as closely as possible. Therefore, it can be expected that by using suitable values of the association factors, in the case of circular footings and spudcans, the ISIS model can repeat the results of model B and model C. This aspect has been illustrated in section 3.6. In this section, the fundamental basis for choosing the suitable values for the association factors is presented.

5.3.1 Association factors for circular flat footings and spudcans in single-yield-surface model

For simplicity, the full three-dimensional yield surface will be simplified to a two-dimensional yield curve in the (*V*: *H*) plane to consider firstly three association factors a_H, a_{V1} and a_{V2}. Afterwards, this work will be repeated with the factors a_M and a_Q.

It is essential at the outset to point out the constraints due to the role of the "parallel point" in the models mentioned. A parallel point is a point on the yield curve at which the flow vector is parallel to the *H*-axis. It is analogous to the "critical state" in soil models, and was initially defined by Tan (1990). In the case of clay, the point at the top of yield curve in the *H*-direction, as shown in Figure 5.7a, is the parallel point in model B (Martin, 1994). In case of sand in model C (Cassidy, 1999), the position of the parallel point has to lie on the part to the left of the top of the yield curve. This means that the vertical load corresponding to this parallel point, V_p, must be smaller than αV_0. Figure 5.7b shows the position of the parallel point and its flow vector in the case of sand, for which, the factor α has been defined in section 3.3.2.1.

Secondly, in case of clay, Martin and Houlsby (2001) have recognised that the direction of the trigonometric angles between incremental plastic displacement vectors and normal vectors of the yield curve are changed when V is greater than the value of αV_0. For instance, as shown in Figure 5.8a, in the part of positive values of H, the incremental plastic displacement vectors are rotated clockwise from the normal vector when V is smaller than αV_0. Once V is greater than αV_0 this direction must be anti-clock-wise. In the case of sand, the experimental results, as shown by Cassidy (1999), give a different result. The flow vectors, which are incremental plastic displacement vectors, are always rotated clockwise from the normal vectors as shown in Figure 5.8(b).

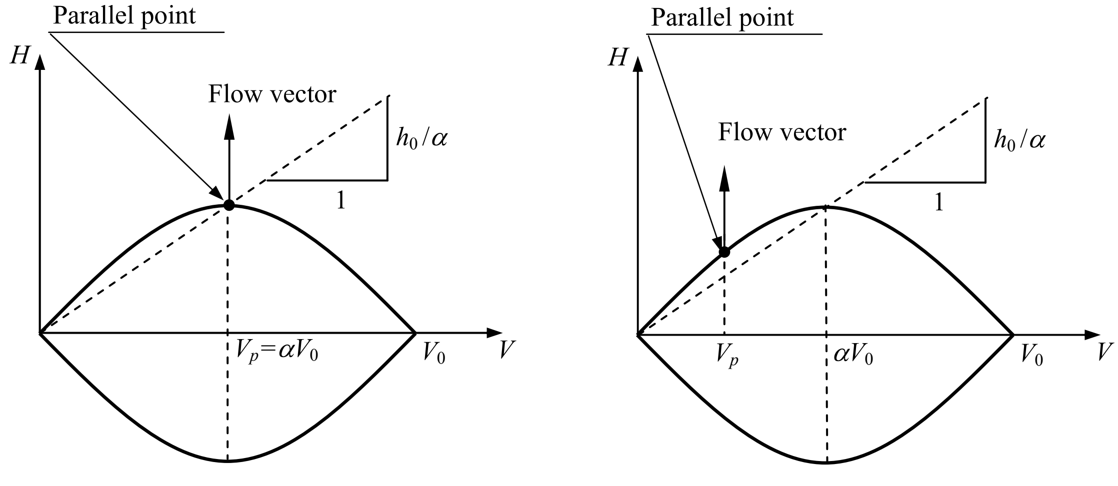

(a) Clay (b) Sand

Figure 5.7 Position of parallel point on the yield curve

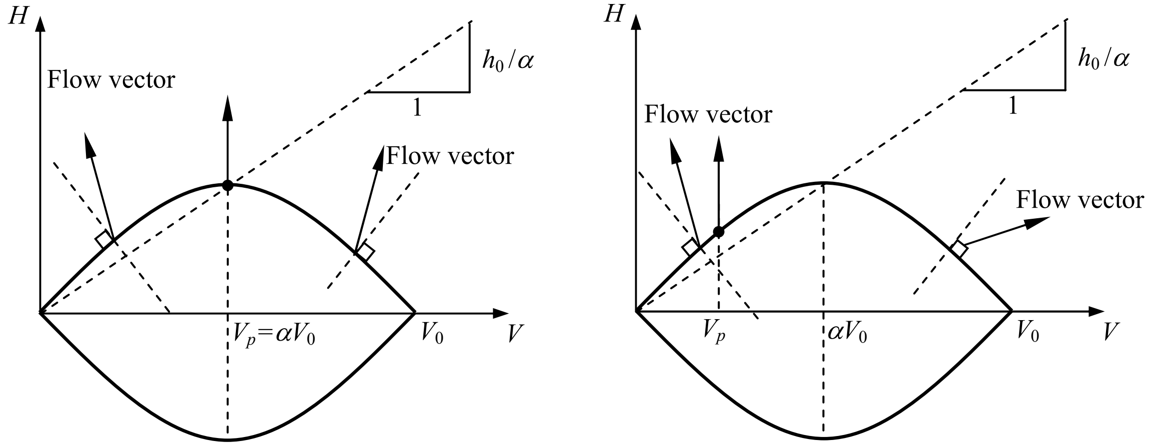

(a) Clay (b) Sand

Figure 5.8 Direction of plastic flow vectors on the yield curve

Based on the remarks above, there are some constraints that must be satisfied about the characteristics of flow vectors in each case. They are described in the following paragraphs.

The formulation of tanφ, tanφ_{normal} in both the case of clay and sand can be defined using the yield function in Eq. (3.17) as follows:

$$\overset{\bullet}{\alpha}_H = \lambda \frac{\partial y}{\partial \chi_H} = 2\lambda \frac{a_H}{h_0 V_0}\left[\frac{H}{h_0 V_0}\right] = 2\lambda a_H \frac{\beta_{12}\left(\frac{V}{V_0}\right)^{\beta_1}\left(1-\frac{V}{V_0}\right)^{\beta_2}}{h_0 V_0} \tag{5.15}$$

$$\overset{\bullet}{\alpha}_V = \lambda \frac{\partial y}{\partial \chi_V} = 2\lambda S \beta_{12}^2 \left(\frac{V}{V_0}\right)^{2\beta_1}\left(1-\frac{V}{V_0}\right)^{2\beta_2}\left[-\frac{a_{V1}\beta_1}{V} + \frac{a_{V2}\beta_2}{V_0\left(1-\frac{V}{V_0}\right)}\right] \tag{5.16}$$

$$\tan\varphi = \frac{\overset{\bullet}{\alpha}_H}{\overset{\bullet}{\alpha}_V} = \frac{a_H}{S\beta_{12} h_0 V_0}\left(\frac{V}{V_0}\right)^{-\beta_1}\left(1-\frac{V}{V_0}\right)^{-\beta_2}\left[-\frac{a_{V1}\beta_1}{V} + \frac{a_{V2}\beta_2}{V_0\left(1-\frac{V}{V_0}\right)}\right]^{-1} \tag{5.17}$$

$$\tan\varphi_{normal} = \left(\frac{\frac{\partial y}{\partial H}}{\frac{\partial y}{\partial V}}\right) = \frac{1}{\beta_{12} h_0 V_0}\left(\frac{V}{V_0}\right)^{-\beta_1}\left(1-\frac{V}{V_0}\right)^{-\beta_2}\left[-\frac{\beta_1}{V} + \frac{\beta_2}{V_0\left(1-\frac{V}{V_0}\right)}\right]^{-1} \tag{5.18}$$

where φ is the angle between flow vector and V-axis; φ_{normal} is the angle between the normal vector and the V-axis.

In the case of clay:

a. $\overset{\bullet}{\alpha}_V = \lambda \frac{\partial y}{\partial \chi_V} = 0$ when $V = V_p = \alpha V_0$ with $\alpha = 0.4 \approx 0.5$ (see Martin, 1994)

b. tan$\varphi \leq$ tan$\varphi_{normal} \leq 0$ when $V \leq \alpha V_0$.

c. $\tan\varphi \geq \tan\varphi_{normal} \geq 0$ when $V \geq \alpha V_0$.

In the case of sand:

a. $\dot{\alpha}_V = \lambda \dfrac{\partial y}{\partial \chi_V} = 0$ when $V = V_p \leq \alpha V_0$ with $\alpha = 0.33 \approx 0.4$ (see Cassidy and Houlsby, 2002)

b. $\tan\varphi \leq \tan\varphi_{normal} \leq 0$ when $V \leq V_p$.

c. $0 \leq \tan\varphi$ when $V_p \leq V \leq \alpha V_0$.

d. $\tan\varphi \leq \tan\varphi_{normal}$ when $V \geq \alpha V_0$.

where V_p is the value of vertical load at the parallel point.

Evaluating the above inequalities, the relationships between a_H, a_{V1}, a_{V2} can be defined.

- For clay: $a_H = 1$, $a_{V1} = a_{V2}$ (= 0.645 or 0.58) corresponding to model B (see Martin, 1994).

- For sand: $a_{V1} \leq a_H \leq a_{V2}$ corresponding to model C.

For the association factors a_M and a_Q, a similar procedure can be applied. It is straightforward and then not necessary to present in detail.

In general, the relationship of association factors in three-dimensional analysis may have the form as follows:

- For clay: $a_H = a_M = a_Q = 1$, $a_{V1} = a_{V2} = 0.645$

- For sand: $a_{V1} \approx 0.5 \leq a_H, a_M, a_Q \leq a_{V2} = 1$

The approximate value of 0.5 proposed for a_{V1} comes from empirical results obtained during attempts to capture the solution of model C.

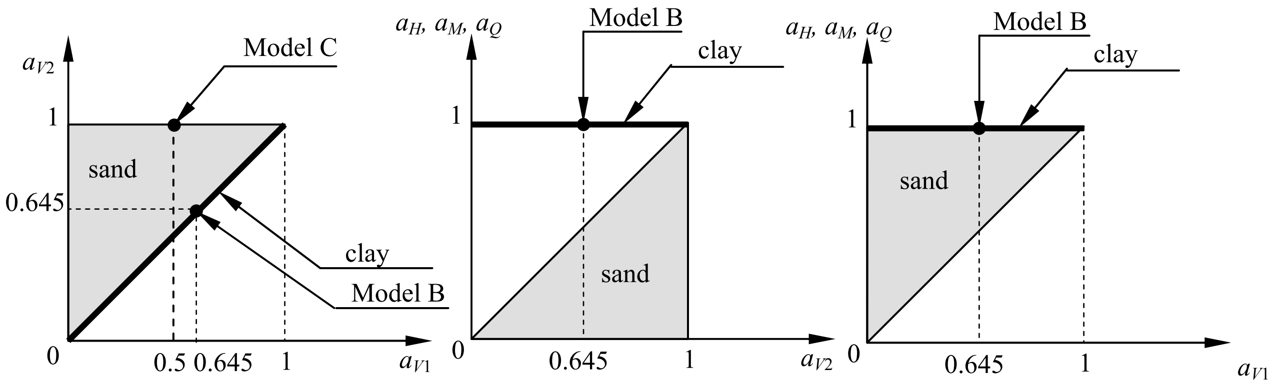

Figure 5.9 The ranges of values of association factors

Figure 5.9 shows the ranges of values of association factors which are appropriate for a circular flat footing or spudcan on either clay or sand. The grey areas in this figure represent the available ranges of values of the association factors.

5.3.2 Association factors for a caisson footing in single-yield-surface model

In this section, the association factors a_{V1} and a_{V2} which are related to the vertical plastic displacement increments are considered; first by using the concept of the parallel point. Secondly, there are some discussions about suitable values of a_M , a_H and a_Q which can be chosen empirically.

As presented in section 5.3.1, at the parallel point, the partial differential of the yield function with respect to χ_V must be zero. By using the yield function defined in Eq. (3.36) and the definition of the parallel point, the following equation can be derived:

$$\frac{\partial y}{\partial \chi_V} = -\frac{1}{V_0}\beta_{12} S \left|v_1 + t_0\right|^{\beta_1} \left|1 - v_2\right|^{\beta_2} \left(\frac{\beta_1 a_{V1}}{v_1 + t_0} - \frac{\beta_2 a_{V2}}{1 - v_2}\right) = 0 \tag{5.19}$$

In which v_1 and v_2 can still be defined as in Eq. (3.23) and Eq. (3.24) respectively. Then, from Eq. (5.19), the relationship between a_{V1} and a_{V2} can be expressed as follows:

$$a_{V1} = \frac{\beta_2}{\beta_1} \frac{v_1 + t_0}{1 - v_2} a_{V2} \tag{5.20}$$

In Eq. (5.20), v_1 and v_2 can be regards as values in true force space. This means that, referring to the true force space, they have the same magnitude and can be calculated as:

$$v_1 = v_2 = \frac{V}{V_0} \tag{5.21}$$

From the test results observed by Villalobos *et al.* (2004d), during cyclic horizontal loading there is almost no vertical movement when the constant vertical load applied is approximately 0.15 of the maximum vertical load applied in the installation process (without suction). Furthermore, the shape factors β_1 and β_2 can be taken as about the same with the value of 0.99. For a caisson with the ratio of *L*/*D* = 0.5, the value of t_0 is approximately 0.1. In addition, the association factor a_{V2} can be taken as 1.0 for simplicity. Therefore, in this particular case of a caisson footing, the value of a_{V1} would be approximately 0.3. This result can be used not only for the single-yield-surface model but also for the multiple-yield-surface model since the single yield surface essentially plays the role of the outermost yield surface in the multiple-yield version. For different caissons (different ratios of *L*/*D*), in order to calculate the value of a_{V1}, the tensile factor t_0 can be changed depending on the frictional resistance along the skirt of the caisson. In addition, the position of the parallel point can be changed.

These features require more experimental results, which are not yet available, to determine their rules. However, it would be straightforward using the procedure as expressed above.

In order to determine the factors a_M, a_H and a_Q, it would be necessary to collect the experimental data about the flow vector. Unfortunately, this information is not available yet. However, the ranges of values for the association factors as shown in Figure 5.9 for a circular flat footing and spudcan on sand are likely to be suitable for a caisson in sand. The evidence for this note is that, in the whole numerical examples shown in section 4.5, the association factors have been chosen using these ranges. As a result, the test curves have been captured quite well.

5.3.3 Effects of the association factors on the solutions using multiple-yield-surface model

This section presents effects of a_{V1}, a_{V2}, a_M and a_H on the model response.

Firstly, it is necessary to consider the trend of the vertical response of the model during cyclic loading analysis. So far, in the use of the multiple-yield-surface model, each association factor has a chosen value used for all the yield surfaces. This can lead to the result that, during cyclic horizontal or moment loading at a constant vertical load, the plastic response can produce vertical plastic displacement increments with different signs whenever an extra yield surface is activated. In the multiple-yield-surface model, the shapes of inner yield surfaces are different from each other, thus the relative locations of the parallel points of the yield surface system on the *V*-axis are different. In other words, the position of the parallel point of each yield surface depends not only on the magnitudes of the factors a_{V1} and a_{V2} for that surface but also on the shape of the yield surface. In addition, the parallel point plays the role of the threshold point between negative and positive zones of vertical displacement increments. Therefore, with a constant vertical load, the plastic response can give a positive vertical plastic displacement increment for the current yield surface but a negative increment for the next yield surface. Using the rate-dependent solution, the vertical displacement increments of each yield surface in multiple-yield-surface model can be written as follows:

$$\delta\alpha_V^{(\eta_n)} = \frac{\left\langle y^{(n)} \right\rangle}{\mu} \frac{\partial y^{(n)}}{\partial \chi_V^{(\eta_n)}} \delta t \tag{5.22}$$

In which the directions of the vertical movements depend on the sign of the term $\dfrac{\partial y^{(n)}}{\partial \chi_V^{(\eta_n)}}$ which can be derived as:

$$\frac{\partial y^{(n)}}{\partial \chi_V^{(\eta_n)}} = -\frac{1}{V_0} \beta_{12} S^{(\eta_n)} \left| v_1^{(\eta_n)} + t_0 \right|^{\beta_1} \left| 1 - v_2^{(\eta_n)} \right|^{\beta_2} \left(\frac{\beta_1 a_{V1}}{v_1^{(\eta_n)} + t_0} - \frac{\beta_2 a_{V2}}{1 - v_2^{(\eta_n)}} \right) \tag{5.23}$$

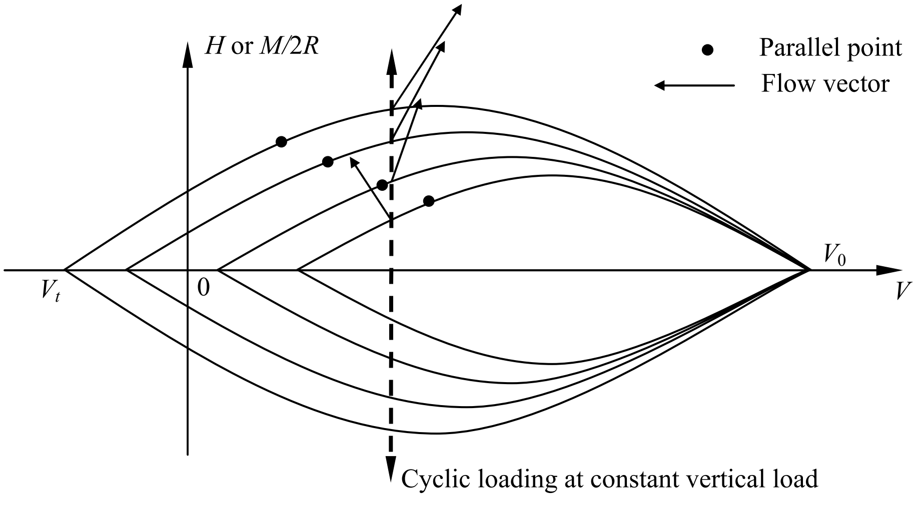

Figure 5.10 System of yield surfaces, their parallel points and their flow vectors during cyclic loading at constant vertical load

It is clear that the direction of vertical increment depends on a_{V1} and a_{V2} as shown in Eq. (5.23). When either these factors or the magnitudes of $v_1^{(\eta_n)}$ and $v_2^{(\eta_n)}$ are changed, the position of the parallel point is changed.

Furthermore, as shown in Figure 5.10, because of the different sizes of the yield surfaces, the parallel points of the yield surfaces can not be in a straight line which is perpendicular to the *V*-axis of the yield surface in true force space. Thus, the flow vector of the first yield surface shows a negative vertical displacement increment but the flow vectors of the other yield surfaces show positive vertical displacement increments. Consequently, during cyclic loading at constant vertical load, there might be upward movements at the beginning and downward movements when the horizontal loads and moments become bigger or vice versa. This feature can be seen in the test results of Villalobos *et al.* (2004a).

Obviously, there are many ways to arrange the positions of parallel points by using suitable formulations of a_{V1} and a_{V2} to change their values when going from the inner-most to the outer-most yield surface. However, it seems that a complex variation of these factors is not necessary. In fact, as shown in the numerical illustrations (section 4.5), by using the set of constant association factors ($a_{V1} = 0.297$, $a_{V2} = 1.0$, $a_M = 0.7$, $a_H = 0.7$, $a_Q = 0.7$), there are reasonably good solutions obtained for the caisson with the ratio *L*/*D* = 0.5. For other ratios of *L*/*D*, there is a need for more experimental results to give suitable values for the association factors but it could be reasonable to use constant values for them.

In order to show the effects of a_M, a_H and a_Q (mainly a_M and a_H), there are three examples implemented. In these examples, the test-scale model of the caisson and the soil properties as shown in section 4.5.2 are used.

In the first analysis, instead of using values for a_M, a_H and a_Q of 0.7, they now have the value of 1.0. The vertical association factors, a_{V1} and a_{V2}, are still 0.297 and 1.0 respectively. This work is to show how the changes of a_M, a_H and a_Q affect the model response. The numerical analysis is implemented for cyclic loading within 2 cycles under the constant vertical load of 50 N. The maximum vertical load used to install the caisson to the full penetration is 945 N. Thus, the ratio of V/V_{max} is 0.053. The results are compared with those using the constant factor of 0.7 for a_M, a_H and a_Q. Figures 5.11 and 5.12 show these comparisons.

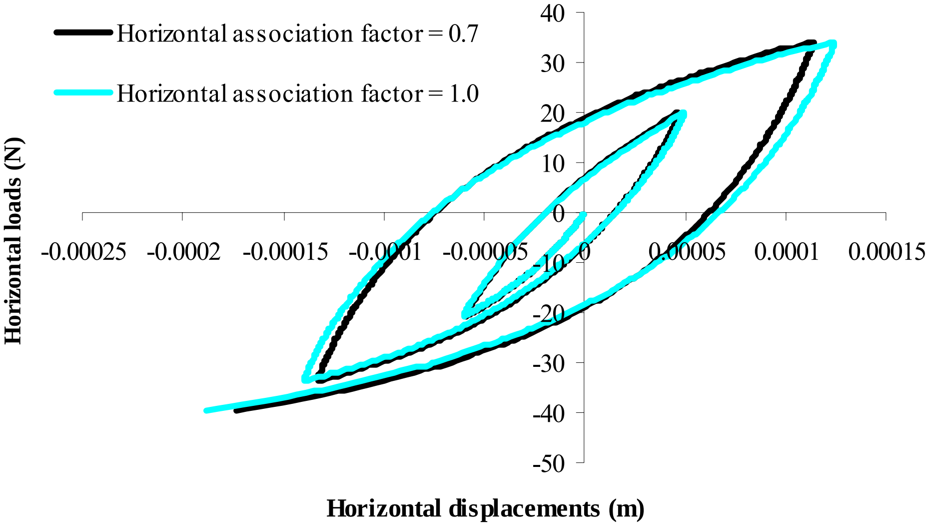

Figure 5.11 Horizontal response of caisson model during cyclic loading on sand (Constant vertical load $V/V_{max} = 0.053$, $a_{V1} = 0.297$, $a_{V2} = 1.0$)

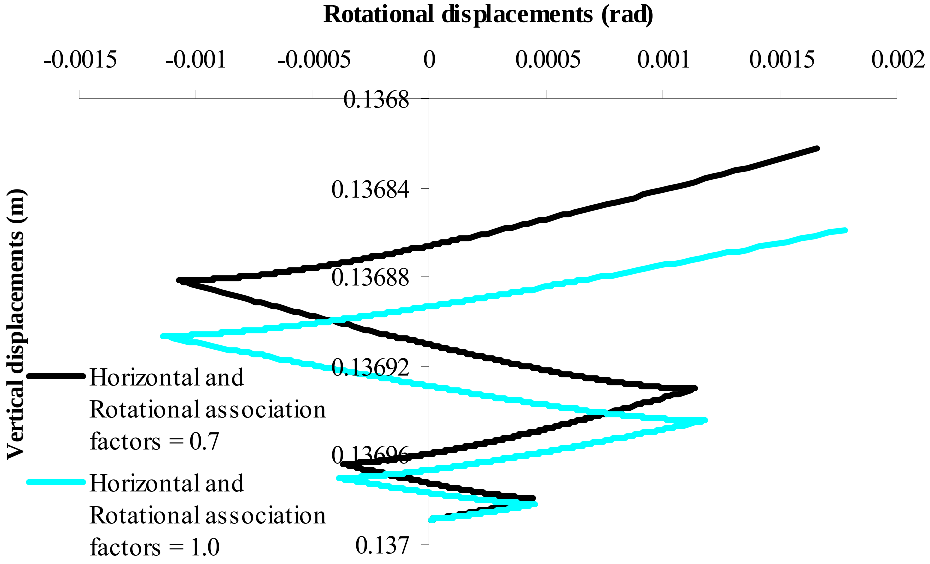

Figure 5.12 Vertical movements of caisson model during cyclic loading on sand (Constant vertical load $V/V_{max} = 0.053$; $a_{V1} = 0.297$, $a_{V2} = 1.0$)

In the second analysis, the vertical association factors are the same as in the first example ($a_{V1} = 0.297$ and $a_{V2} = 1.0$) but the other association factors are changed to vary linearly from 1.0 to 0.7 through the system of yield surfaces. This means that, at the first yield surface (inner-most yield surface), the factors a_M, a_H and a_Q are 1.0; at the last yield surface (outer-most yield surface) these factors are 0.7; at the i^{th} yield surface, the value of these factors will be: $a_M = a_H = a_Q = 1.0 - \frac{(i-1)}{(N-1)}(1.0 - 0.7)$, in which N is the number of yield surfaces used in the model. The results are also compared with the case using constant values of 0.7 for the association factors of horizontal, rotational and torsion components. Figures 5.13 and 5.14 show the plots of this work.

In the above two analyses, the horizontal and rotational displacements increase slightly. The most affected component is the vertical movement during the cyclic loading. Furthermore, since the cyclic loading is applied at the small ratio of $V/V_{\max,}$ the vertical movements are upward.

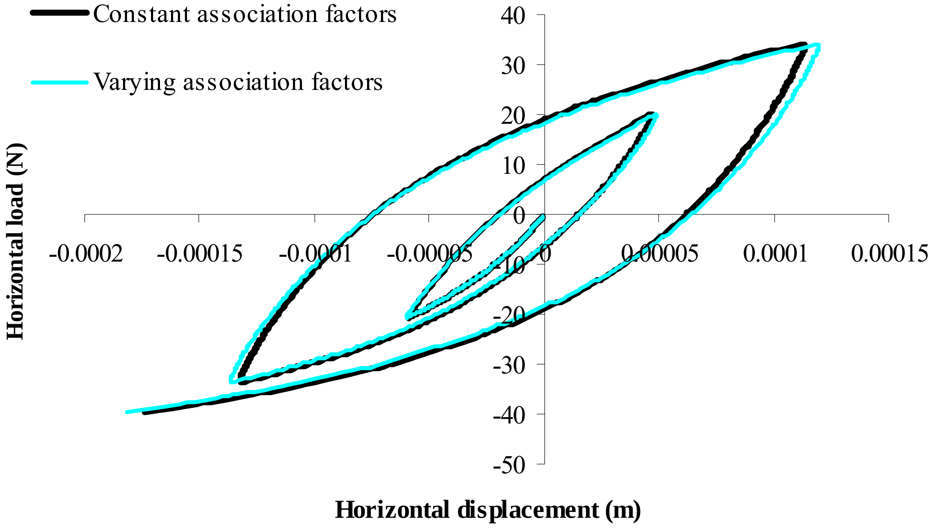

Figure 5.13 Horizontal response of caisson model during cyclic loading on sand (Constant vertical load $V/V_{max} = 0.053$; $a_{V1} = 0.297$; $a_{V2} = 1.0$)

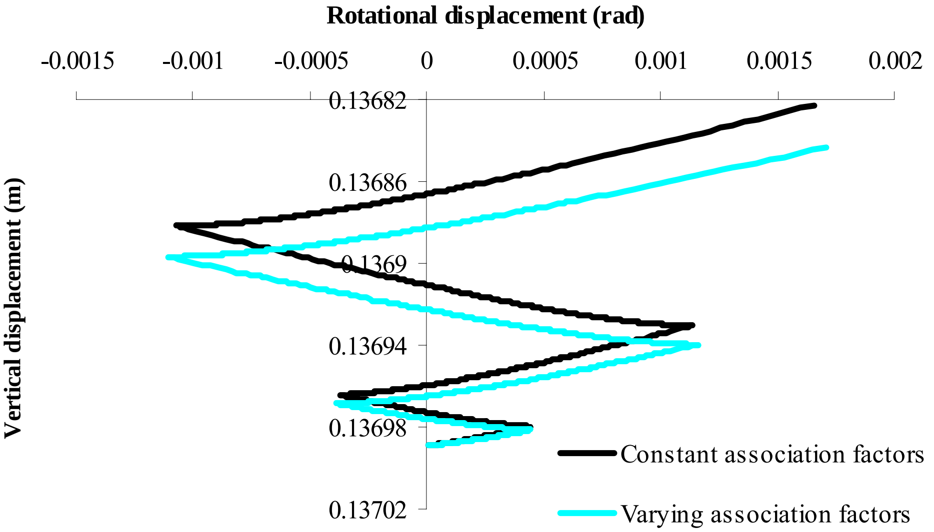

Figure 5.14 Vertical movements of caisson model during cyclic loading on sand (Constant vertical load $V/V_{max} = 0.053$; $a_{V1} = 0.297$; $a_{V2} = 1.0$)

The third analysis is implemented with a larger ratio of $V/V_{\max}$ of 0.423. By using this ratio, which is higher than the ratio of the parallel point of the outer most yield surface ($V_{\text{parallel}}/V_{\max} = 0.15$ as mentioned in section 5.3.2), the vertical movements during cyclic loadings are downward. The association factors a_M, a_H and a_Q are chosen to vary linearly from 1.0 to 0.7 in a similar fashion to the second example. Figures 5.15 and 5.16 show the comparisons between the results of this analysis and that of the case using a_M, a_H and a_Q with a constant value of 0.7. Again, there is still a gap between the two solutions of vertical movements and almost no difference obtained in horizontal and rotational responses.

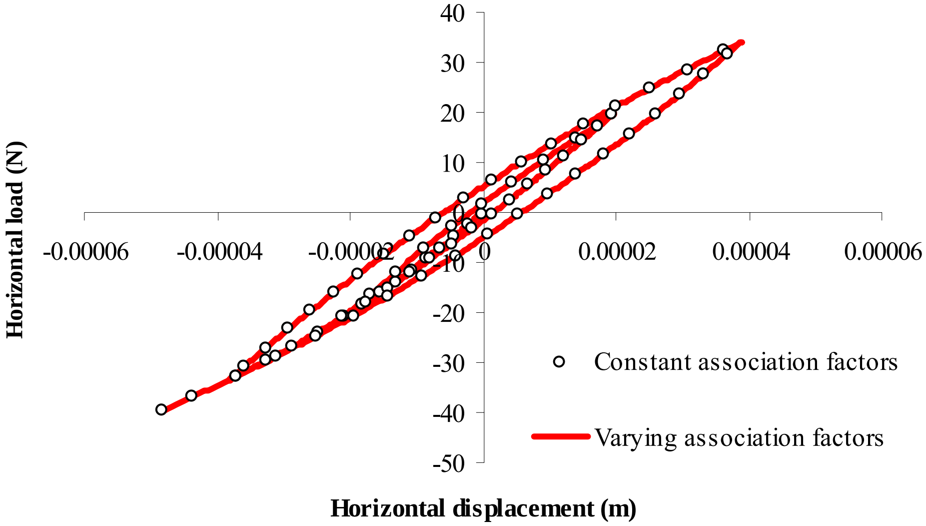

Figure 5.15 Horizontal response of caisson model during cyclic loading on sand (Constant vertical load $V/V_{max} = 0.423$; $a_{V1} = 0.297$; $a_{V2} = 1.0$)

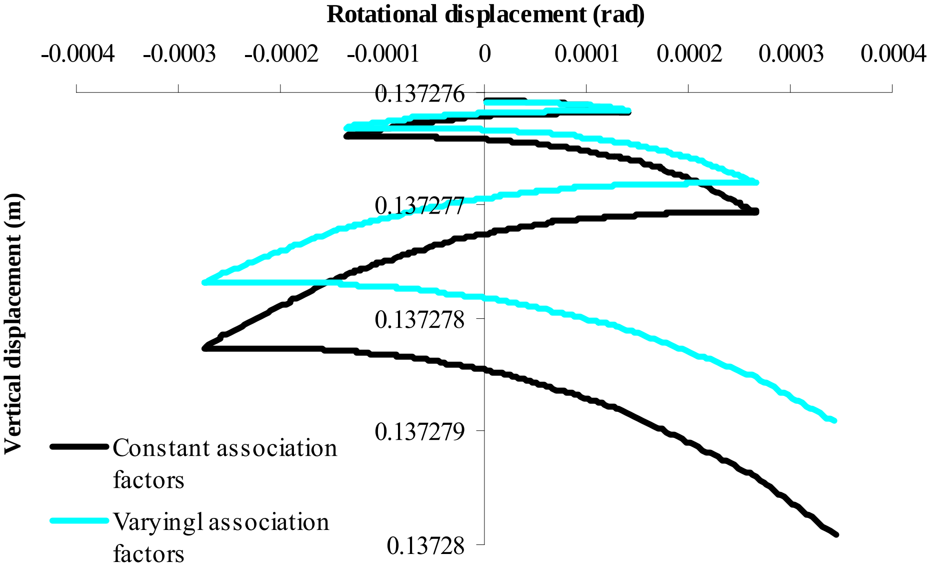

Figure 5.16 Vertical movements of caisson model during cyclic loading on sand (Constant vertical load $V/V_{max} = 0.423$; $a_{V1} = 0.297$; $a_{V2} = 1.0$)

It is clear that, in the case where association factors are all equal to 0.7 (except a_{V1} and a_{V2} which are kept at the values of 0.297 and 1.0 respectively), the vertical movements obtained are the largest. In the case of using linear variation for a_H, a_M and a_Q from 1.0 to 0.7, the vertical movements decrease. The smallest vertical movements are obtained when a_H, a_M and a_Q are all 1.0.

It should also be noted that the changes of a_H, a_M and a_Q do not significantly affect the horizontal and rotational response; especially in the case when the vertical load is applied constantly at small ratio of $V/V_{\max}$. This is in fact the usual serviceability condition for offshore wind turbine foundations.

Consequently, from the above verifications and with the numerical illustrations in section 4.5, there are three remarks which can be made about the choice of the association factors for the theoretical analysis for shallow foundation on sand using the multiple-yield-surface ISIS model.

(a) A suitable order for the magnitudes of the association factors is: $0 < a_{V1} \leq a_H$, a_M, $a_Q \leq a_{V2} = 1$.

(b) The values of a_{V1} and a_{V2} depend on the position of the parallel point, which depends on the shape of the footings and should be determined from tests. For simplicity, a_{V2} can take the value of 1.0.

(c) In order to adjust the numerical solutions to simulate cyclic responses, it should be noted that when the factors a_H and a_M increase, the vertical movements during cyclic loading will decrease and vice versa. The horizontal and rotational responses, however, are not changed significantly with the changes of a_H and a_M .

5.4 Initial distribution of the yield surfaces

In the use of the multiple-yield-surface model, the initial distribution of the yield surfaces can be defined in a variety of ways. In this study, the simplest option, including an initial size of the innermost yield surface, and a uniform distribution of the other surfaces in the remaining space between the first (inner-most) yield surface and the last (outer-most) yield surface has been used. By changing the initial size of the first yield surface, the plastic response of the model is changed significantly, not only in the vertical component but also in both the horizontal or rotational components. In section 4.3.2, there is a brief explanation of the effect of the initial parameter $\eta_0^{initial}$ which is the key factor in determining the initial size of the first yield surface in the vertical installation-unloading process.

In this section, the effect of $\eta_0^{initial}$ on vertical response is discussed in more detail. The changes of horizontal and rotational responses as a result of this are explained.

Firstly, it is necessary to discuss the mechanism of the yielding during the installation and unloading processes. Two possibilities can happen depending on the initial size of the first yield surface or, in other words, on the initial parameter $\eta_0^{initial}$.

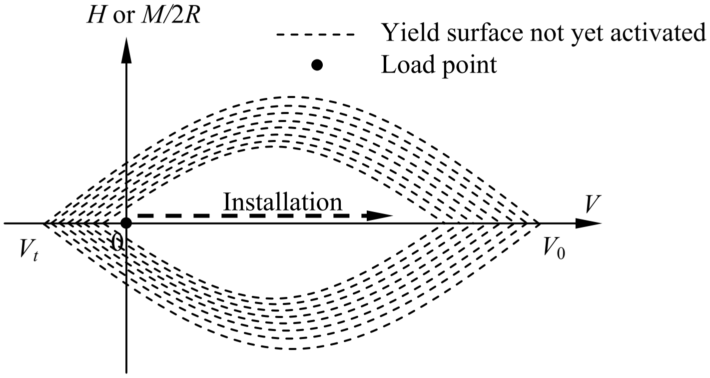

(a) Initial yield surface system

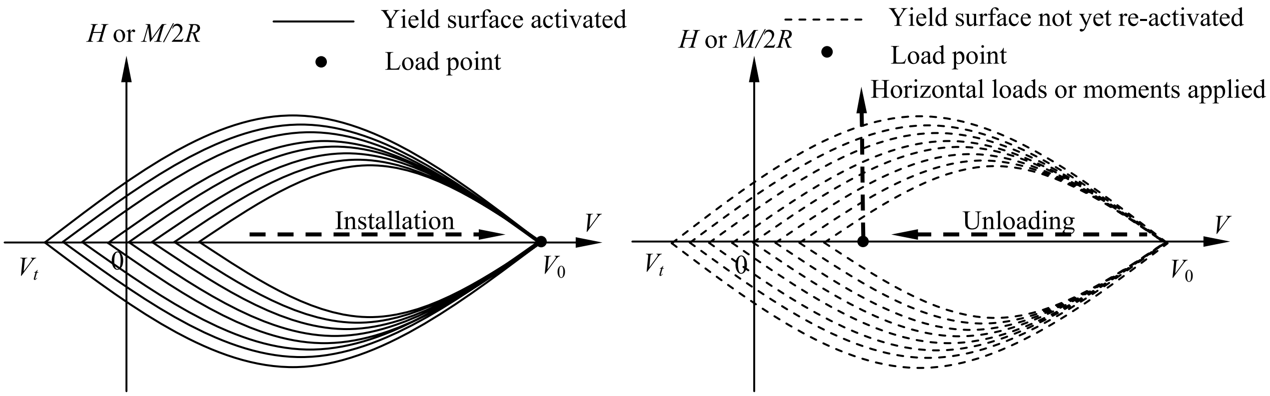

(b) Installation (vertical loading)

(c) Vertical unloading to the serviceability condition

Figure 5.17 Installation and purely elastic vertical unloading process to the serviceability condition

In the first possibility, shown in Figure 5.17, the installation process starts with purely elastic behaviour and quickly reaches the fully plastic state which means that all the yield surfaces have been activated (Figure 5.17b). After finishing the installation, the unloading process follows back to the vertical load of the serviceability condition at which the environmental horizontal forces and moments start to be applied. In this case, the size of the first yield surface is big enough so that the load point after the unloading process is still inside the first yield surface without any re-activated yield surface. The unloading process is therefore purely elastic (Figure 5.17c).

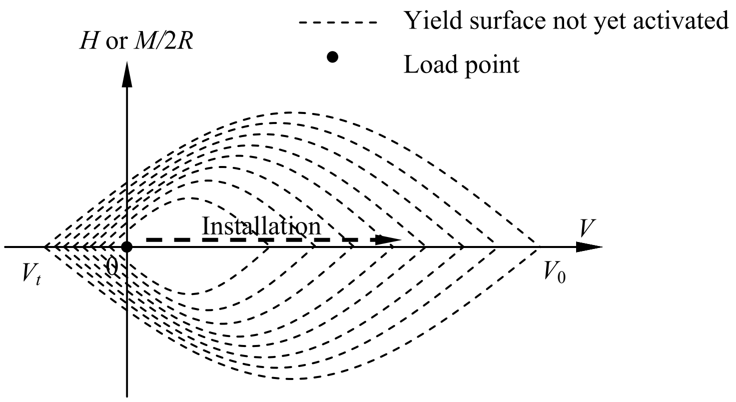

(a) Initial yield surface system

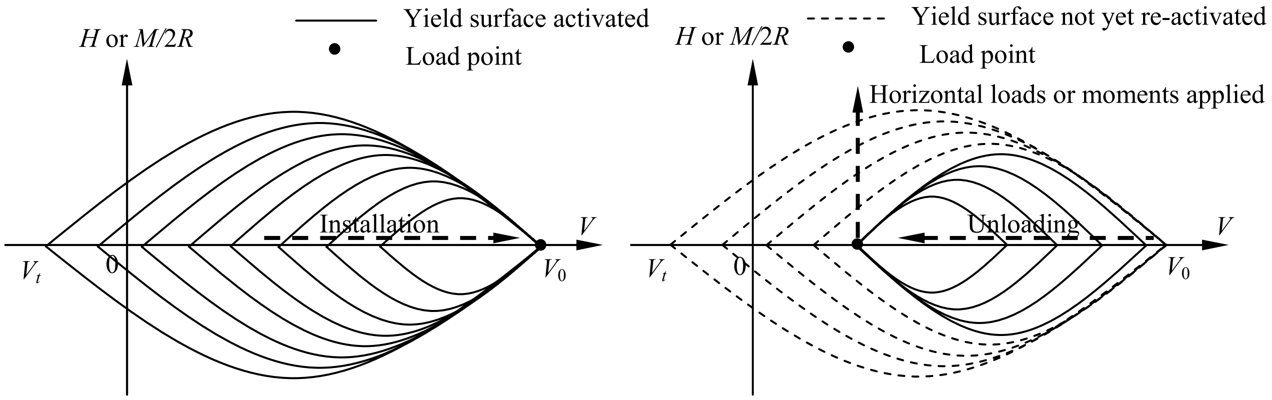

(b) Installation (vertical loading)

(c) Vertical unloading to the serviceability condition

Figure 5.18 Installation and elasto-plastic vertical unloading process to the serviceability condition

In the second possibility the installation process also starts with purely elastic behaviour and reaches the fully plastic state as shown in Figures 5.18a and 5.18b. However, the yielding occurs sooner since the size of the first yield surface is smaller than that in the case above. Furthermore, in the unloading process, due to the smaller first yield surface, there are some yield surfaces re-activated (Figure 5.18c). Consequently, the unloading process is elasto-plastic and causes the negative (upward) vertical plastic displacements in the analysis.

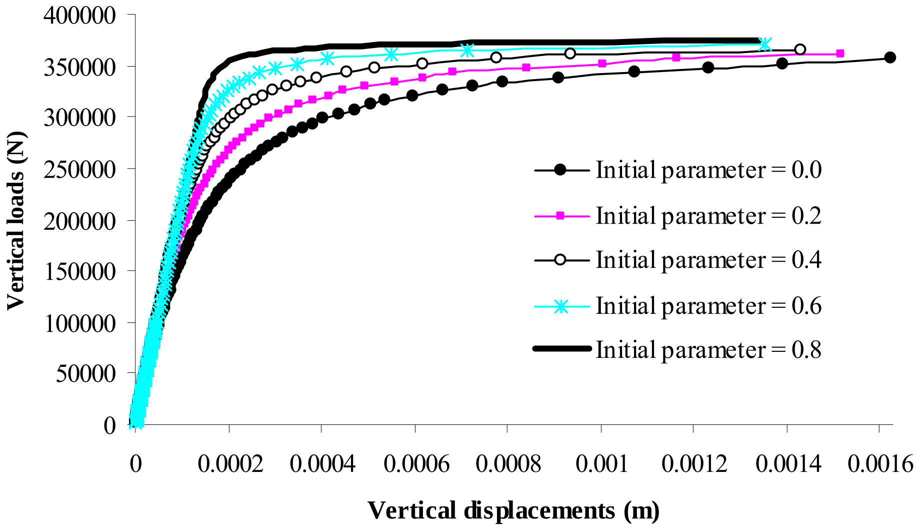

Figure 5.19 Vertical response from the elastic to the full plastic behaviours (at the beginning of the installation process)

In order to illustrate the above, numerical analyses have been implemented for the caisson footing which was introduced in Example 5 in section 4.5.1.3 with a variety of initial $\eta_0^{initial}$ parameter magnitudes of 0.0, 0.2, 0.4, 0.6 and 0.8. Figure 5.19 shows the beginning of the vertical responses from the start to the full plastic state. It is clear that the smaller the initial parameter used, the sooner the plastic behaviour occurrs. In addition, there are also differences between the curves using different initial parameters during the unloading process following installation. As shown in Figure 5.20, at the end of the unloading process the biggest upward displacement obtained corresponds to the smallest value of $\eta_0^{initial}$. In fact, the bigger the value of $\eta_0^{initial}$ used, the smaller the upward movement. In the case of $\eta_0^{initial} = 0.8$, the unloading is purely elastic and shown by the straight line in Figure 5.20. In the other case, there are a number of yield surfaces activated. Table 5.3 shows the numbers of yield surfaces activated at the end of the unloading process corresponding to different values of $\eta_0^{initial}$.

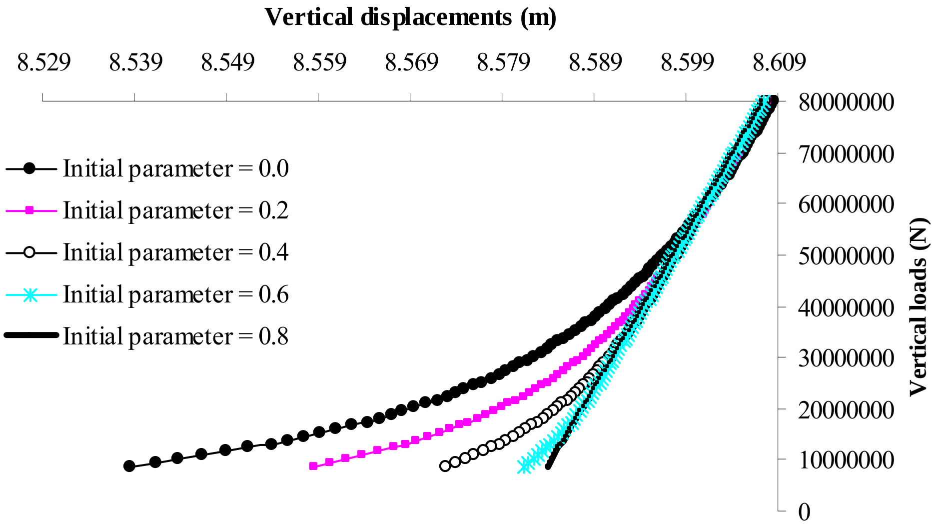

Figure 5.20 Vertical response during the vertical unloading process (after finishing the installation process)

Table 5.3 Number of yield surface activated after finishing the vertical unloading process (20 yield surfaces in total)

$\eta_0^{initial}$	0.0	0.2	0.4	0.6	0.8
Number of yield surfaces activated	16	15	13	9	0

Consequently, at the beginning of either horizontal loading or moment loadings, there is an initial elasto-plastic stiffness due to the number of yield surfaces activated at the end of the vertical unloading process. Therefore both the horizontal and rotational responses can be very different depending on the value of the initial parameter. Figure 5.21 shows the initial horizontal response of the caisson described above corresponding to 16, 15, 13, 9 and 0 yield surfaces activated as shown in Table 5.3.

From the numerical illustrations in section 4.5, the uniform distribution combined with the initial parameter, $\eta_0^{initial} = 0.8$, can be seen to be a reasonable choice for the multiple-yield-surface ISIS model. There are, however, many other choices for the distribution of the yield surfaces. The discussions in this section give a general idea about the mechanism by which the distribution of the yield surfaces affects the solutions which will be applicable to other options.

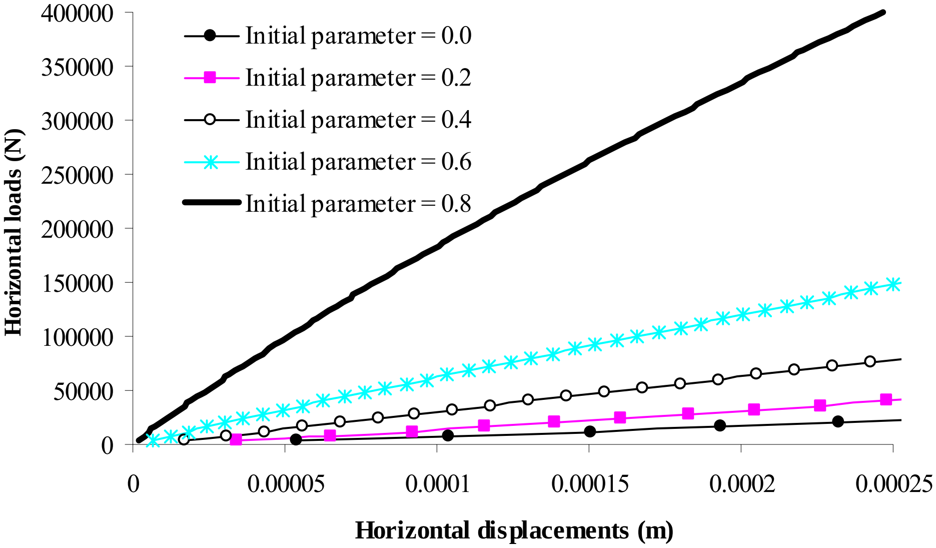

Figure 5.21 The first horizontal response at the constant vertical load of the serviceability condition (after finishing the unloading process)

5.5 Effects of kernel functions on the distribution of plastic displacements

In addition to the effect of the initial distribution of the yield surfaces on the transition from purely elastic behaviour to fully plastic behaviour, the form of kernel functions can also affect the shapes of the transition curves. Since the same kernel function is applied for all loading directions, this section focuses on the explanation of the effect of the kernel function on the vertical response as being representative of all other components.

Firstly, it is necessary to look back to the general formulation of the vertical kernel function, which was proposed in chapter 4 as follows:

$$H_1^{*(\eta_i)} = A_1 K_1 (b_1 - \eta_i)^{n_1} \qquad (5.24)(4.68bis)$$

In the multiple-yield-surface ISIS model, there is an assumption that, once the whole system of yield surfaces is activated, fully plastic behaviour has occurred. The fully plastic behaviour of the multiple-yield-surface version must be compatible with those of the single-yield-surface version of ISIS using isotropic hardening which has been verified by either Model B or Model C. Therefore, the parameter b_1 can be fixed as 1. It is clear that when the last (outer-most) yield surface is activated the internal coordinate η_i is equal to 1. Then, the term $H_1^{*(\eta_N)}$, as in Eq. (5.24), becomes zero. This means that there is no kinematic hardening applied for the outer most yield surface. This yield surface just expands or contracts without translation. In contrast, the inner yield surfaces have both actions.

Consequently, there are two changeable parameters, A_1 and n_1, in the kernel function. A_1 is the parameter controlling the initial slope of the hardening curve, while n_1 affects the curvature of this curve. In order to illustrate the effects of these parameters on the solution, the numerical analysis of the caisson described in section 5.4 will be used. The first stage of the installation process is analysed using different forms of the kernel function $H_1^{*(\eta_i)}$ corresponding to different values of the various parameters. The multiple-yield-surface model using 20 yield surfaces is used for these analyses.

There are two separate series of numerical analyses. Firstly, different values of the parameter A_1 are taken into account while the other parameters of the kernel function are kept constant. The second series considers the solution with different values of the parameter n_1.

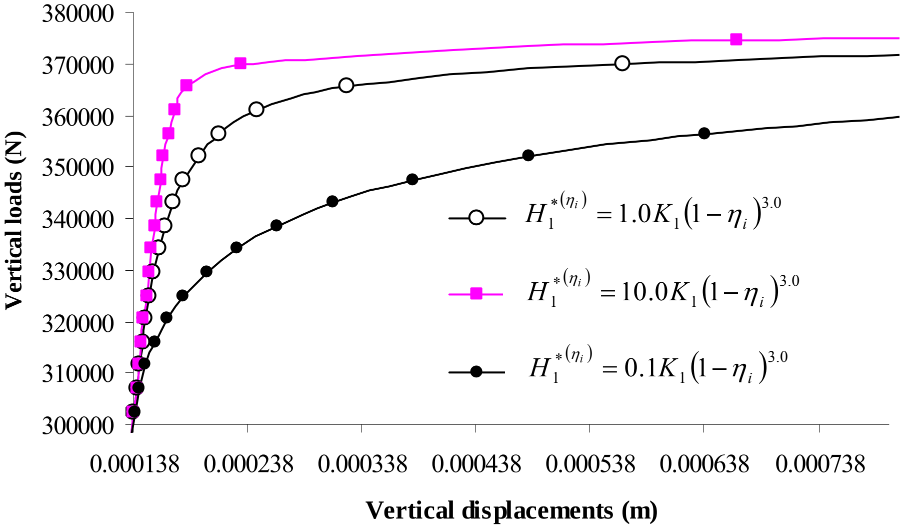

Figure 5.22 Vertical responses using different values of A_1 for the kernel function

Figure 5.22 shows the vertical responses corresponding to the magnitudes of A_1 of 1.0, 10.0 and 0.1 respectively. In this figure, the curves show the stage from the end of purely elastic behaviour to nearly full plastic behaviour. It is clear that, in the very initial part when the footing behaviour is still elastic, all the curves have the same slope. Afterwards, when the yielding occurs, the initial elasto-plastic slope of the curve increases significantly when A_1 becomes larger. As a result, the transition from purely elastic behaviour to fully plastic behaviour becomes more dramatic. The larger the value of A_1 used, the smaller the effects on the model behaviour obtained from the inner yield surfaces. In other words, the multiple-yield-surface solution will get closer to the single-yield-surface solution when A_1 is increased.

In addition, as shown in Figure 5.23, corresponding to the smaller values of A_1, the magnitudes of the internal variables which are accumulated in the inner yield surfaces are much larger. This implies that when A_1 is chosen to be smaller, there is a larger amount of energy dissipated in the model during partial plasticity.

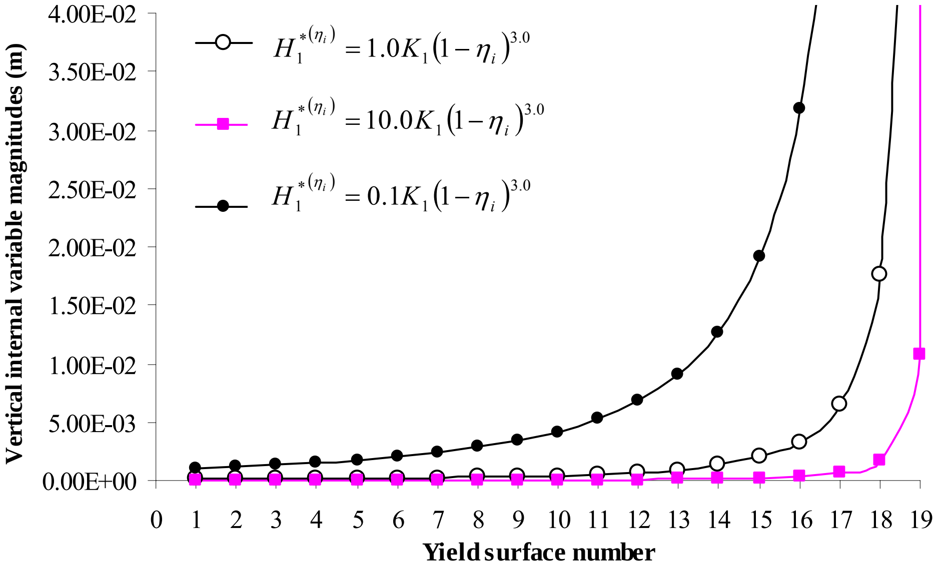

Figure 5.23 Vertical internal variable magnitude at each level of plasticity

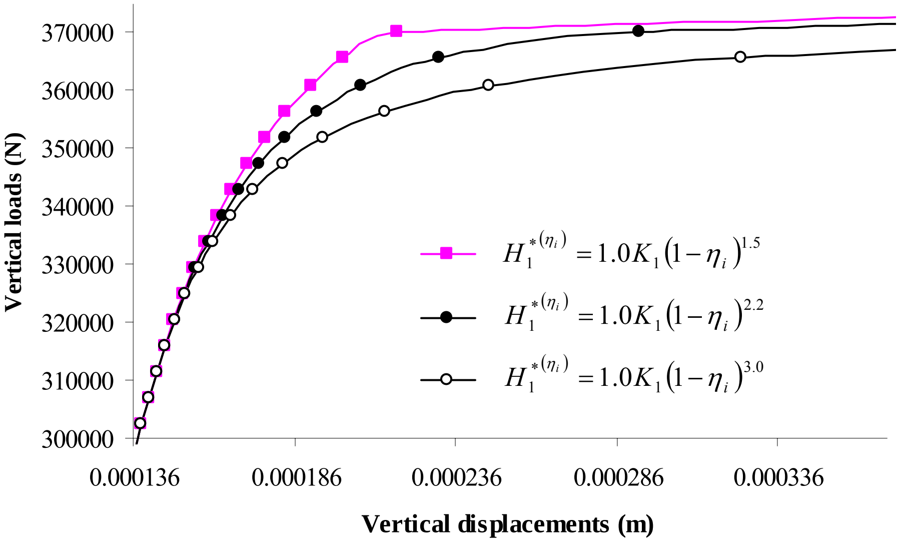

Figure 5.24 Vertical responses using different values of n_1 for the kernel function

The effects of changing the exponential parameter n_1 are shown in Figures 5.24 and 5.25. It can be seen that, by decreasing the magnitude of n_1, the transition between purely elastic behaviour and fully plastic behaviour becomes more dramatic. The changes in the magnitudes of the vertical internal variables accumulated in the inner yield surfaces, as shown in Figure 5.25, confirm this remark.

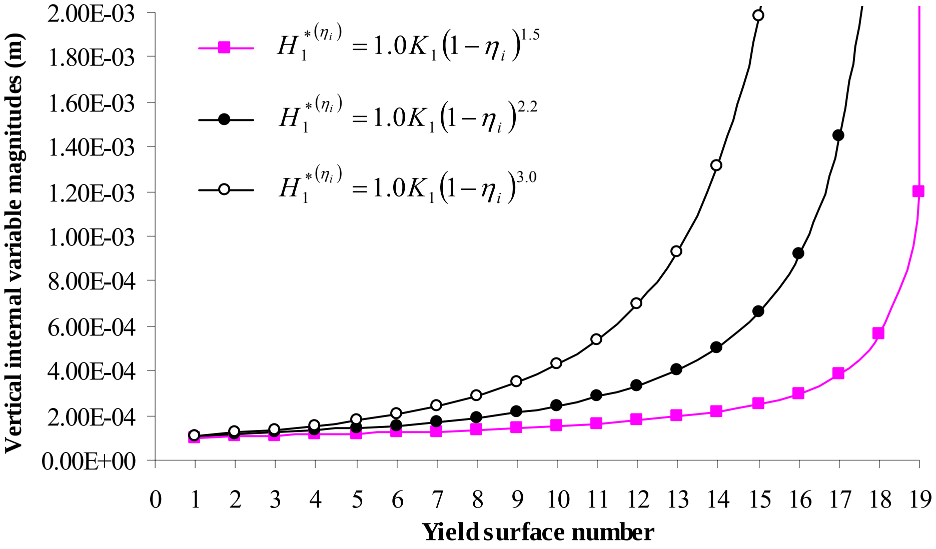

Figure 5.25 Vertical internal variable magnitude at each level of plasticity

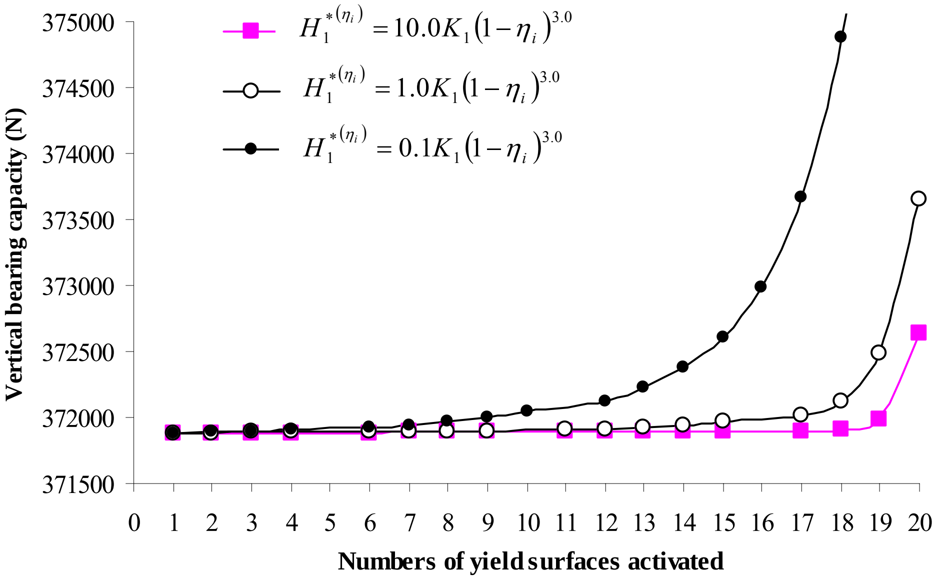

Figure 5.26 Developments of the vertical bearing capacity V_0 corresponding to the levels of plasticity

Finally, it is necessary to explain the mechanism of the effects of the kernel functions on the solution of the multiple-yield-surface ISIS model. The kernel functions play the key role of the kinematic hardening of the model. They determine the velocities of the inner yield surfaces moving inside the outer-most yield surface. At the same plastic displacement during the elasto-plastic loading, if the velocities of the inner yield surfaces are faster the larger numbers of yield surfaces are activated. This means that the fraction of the plastic work stored in the Gibbs free energy function (the term g_2) increases when the velocities of the inner yield surfaces increase and vice versa.

From the numerical analyses for the caisson introduced in the preceding paragraphs of this section, the changes of the vertical bearing capacity V_0, which represent the isotropic hardening corresponding to the number of yield surfaces activated have been shown in Figure 5.26. It can be found that, once the inner yield surfaces move slower corresponding to smaller value of A_1, the increase of V_0 becomes faster. This implies that there is increasing dissipative energy coming from the expansion of the yield surfaces when they move slower.

Therefore, it can be seen out that by changing the parameters of the kernel functions, the ISIS model can be adjusted to capture the hardening curves for the foundation response on many different kinds of soil. In particular for the case of loose sand as tested in Villalobos *et al.* (2004a), the kernel functions for caisson footing can be used as shown in equations from Eq. (4.120) to Eq. (4.124).

5.6 Relationship between viscosity factor, time increment and loading step in rate-dependent solution

In the use of rate-dependent solutions to simulate the rate-independent behaviour, there are two matters that should be investigated: the stability and the accuracy of the numerical solutions.

The matter of accuracy involves the difference between the rate-independent and the rate-dependent solution. This depends on the rates of loading or the rates of displacements applied. The slower the rate of loading applied, the more accurate a solution can be obtained, which means that the solution using the rate-dependent behaviour can get closer to the solution using the rate-independent solution. In order to decrease the rate of loading, there are options such as increasing the time increments for a given load or decreasing the load increments for a given time. Decreasing the viscosity factor can be shown to have an effect equivalent to that of slowing down the solution.

Since the numerical calculation is an approximate process, there always exist some numerical errors in the solution. These errors can accumulate either to make the solution divergent or to return the load point into the elastic zone, which causes the model response to be oscillate between elasto-plastic and purely elastic behaviour. These phenomena result in instability of the solution. A criterion to verify the stable condition before implementing the calculation is therefore required.

To satisfy the two criteria for accuracy and stability, a compromise with suitable choices of the time increments, load increments and the viscosity factor is required. Unfortunately, establishing rigorous mathematical derivations for these criteria for the sophisticated ISIS model is very difficult. Therefore, in the following expressions, there will not be an attempt to determine the universal criteria for the general cases. There are merely principal explanations for the choices of the parameters involved in the rate-dependent solution. The main purpose of this work is to give some advice in terms of the empirical formulations which come from the mathematical derivations for the simpler models.

5.6.1 Accuracy and stability conditions of the simplest one-dimensional kinematic hardening rate-dependent model

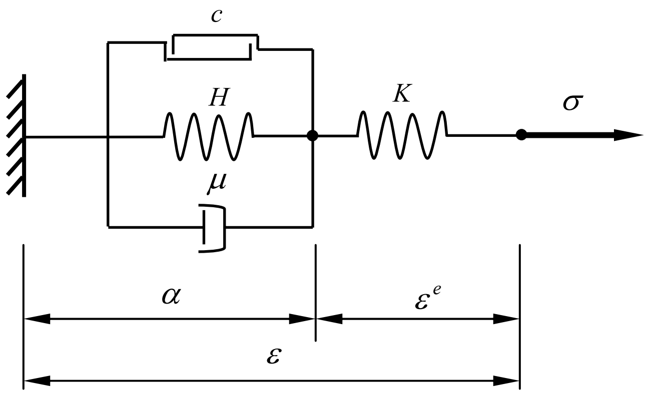

Figure 5.27 One-dimensional model

Considering a very basic one-dimensional model using kinematic hardening as shown in Figure 5.27, the two scalar functions of the model can be expressed as follows:

$$g = -\frac{\sigma^2}{2K} - \sigma\alpha + H\frac{\alpha^2}{2} \tag{5.25}$$

$$d = c\left|\dot{\alpha}\right| + \mu\dot{\alpha}^2 \tag{5.26}$$

In which: K is the elastic stiffness; H is the hardening factor; c is the threshold stress and μ is the viscosity factor.

The force potential function can be defined as:

$$z = c\left|\dot{\alpha}\right| + \mu\frac{\dot{\alpha}^2}{2} \tag{5.27}$$

The generalised stresses $\overline{\chi}$ and the dissipative generalised stresses χ can be defined as:

$$\overline{\chi} = -\frac{\partial g}{\partial \alpha} = \sigma - H\alpha \tag{5.28}$$

$$\chi = \frac{\partial z}{\partial \dot{\alpha}} = c\,\mathrm{sgn}\left(\dot{\alpha}\right) + \mu\dot{\alpha} \tag{5.29}$$

By using Ziegler's orthogonality condition (Puzrin and Houlsby, 2001a), $\overline{\chi} = \chi$, the rate of changes of the internal variable α can be derived as:

$$\dot{\alpha} = \frac{\sigma - H\alpha - c\,\mathrm{sgn}\left(\dot{\alpha}\right)}{\mu} \tag{5.30}$$

The stress-strain relationship can be written as follow:

$$\varepsilon = \frac{\sigma}{K} + \alpha \tag{5.31}$$

Then, in an elasto-plastic response with σ, $d\sigma$ and $\dot{\alpha}$ all positive, the incremental response can be expressed as follows:

$$d\sigma = Kd\varepsilon - K\left(\frac{\sigma - H\alpha - c}{\mu}\right)dt \tag{5.32}$$

There are two separate analysed that are required. Firstly, the accuracy condition is considered for both stress-controlled and strain-controlled cases. Secondly, the stability of the calculation is investigated.

Accuracy in stress-controlled problems

In this case, the stress rate $\dot{\sigma}$ can be assumed as constant. The stress can thus be explained as:

$$\sigma = c + \dot{\sigma}\, t \tag{5.33}$$

In which we assume that at the beginning of the plastic behaviour, when $t = 0$, the magnitude of the stress is equal to the threshold stress c. The incremental response in Eq. (5.32) can be rewritten as follows:

$$\frac{d\sigma}{dt} = K\frac{d\varepsilon}{dt} - \frac{K}{\mu}\left(\left(c + \dot{\sigma}\, t\right) - H\alpha - c\right) \tag{5.34}$$

From Eq. (5.31) combined with the definition of σ in Eq. (5.33), the plastic strain can be expressed as follows:

$$\alpha = \varepsilon - \frac{c - \dot{\sigma}\, t}{K} \tag{5.35}$$

Substituting Eq. (5.35) into Eq. (5.34), the incremental response can be expressed as follows:

$$\dot{\sigma} = K\frac{d\varepsilon}{dt} - \frac{K}{\mu}\left(c + \dot{\sigma}\, t - H\left(\varepsilon - \frac{c + \dot{\sigma}\, t}{K}\right) - c\right) \tag{5.36}$$

Simplifying Eq. (5.36), one can get a first order ordinary differential equation with respect to ε and t as follows:

$$\frac{d\varepsilon}{dt} + \frac{H}{\mu}\varepsilon = +\frac{1}{\mu}\left(1 + \frac{H}{K}\right)\dot{\sigma}\, t + \frac{\dot{\sigma}}{K} + \frac{H}{K\mu}c \tag{5.37}$$

Integrating Eq. (5.37), the analytical rate-dependent solution using stress-control can be determined as:

$$\varepsilon = \left(\frac{K+H}{KH} \right) (\sigma - c) + \frac{c}{K} + \frac{\mu \dot{\sigma}}{H^2} \left(1 + e^{-\frac{H}{\mu} t} \right) \tag{5.38}$$

If the viscosity factor becomes $\mu = 0$, the Eq. (5.38) becomes the rate-independent solution $\varepsilon = \left(\frac{K+H}{KH} \right) (\sigma - c) + \frac{c}{K}$. Thus, the proportional errors between the rate-independent and rate-dependent solution can be expressed in the following form:

$$e_{acc} = \frac{\frac{\mu \dot{\sigma}}{H^2} \left(1 + e^{-\frac{H}{\mu} t} \right)}{\left(\frac{K+H}{KH} \right) (\sigma - c) + \frac{c}{K}} \tag{5.39}$$

At large time the exponential term tends to zero Eq. (5.39) can be simplified as:

$$e_{acc} = \frac{\mu \frac{d\sigma}{dt}}{H \left((\sigma - c) + \frac{H}{K} \sigma \right)} \leq f^{s}_{acc} \tag{5.40}$$

Where the proportional difference between the two solutions e_{acc} must be smaller than an accuracy factor f^{s}_{acc} proposed.

It can be seen that if H is much smaller than K, the accuracy factor can be approximately $f^{s}_{acc} \geq \frac{\mu \dot{\sigma}}{H(\sigma - c)}$ (5.40bis).

Accuracy in strain-controlled problems

In this case, the strain rate is assumed as constant and the strains can be expressed as:

$$\varepsilon = \frac{c}{K} + \dot{\varepsilon}\, t \tag{5.41}$$

(If again the time is measured from the onset of plasticity)

Eq. (5.32) can be rewritten as follows:

$$\frac{d\sigma}{dt} = K\dot{\varepsilon} - \frac{K}{\mu}\left(\sigma - H\alpha - c\right) \tag{5.42}$$

From Eq. (5.31) combined with Eq. (5.41), the plastic strain can be expressed as follows:

$$\alpha = \varepsilon - \frac{\sigma}{K} = \varepsilon - \frac{\frac{c}{K} + \dot{\varepsilon}\, t}{K} \tag{5.43}$$

Substituting Eq. (5.43) into Eq. (5.42), the incremental response can be rewritten as a first order ordinary differential equation as follows:

$$\frac{d\sigma}{dt} + \left(\frac{K}{\mu} + \frac{H}{\mu}\right)\sigma = \left(\frac{HK}{\mu}\dot{\varepsilon}\right)t + \left(K\dot{\varepsilon} + \frac{H}{\mu}c + \frac{K}{\mu}c\right) \tag{5.44}$$

By integrating Eq. (5.44), the analytical expression of the stress-strain relationship can be written as:

$$\sigma = \frac{KH}{K+H}\left(\varepsilon - \frac{c}{K}\right) + c + \left(\frac{K}{K+H}\right)^2 \mu\dot{\varepsilon}\left(1 - e^{-\frac{H+K}{\mu}t}\right) \tag{5.45}$$

By using a similar procedure to the stress-controlled solution, the proportional accuracy condition can be derived as:

$$e_{acc} = \frac{\mu \frac{d\varepsilon}{dt}}{\frac{(K+H)}{K}\left(c + H\varepsilon\right)} \le f_{acc}^{e} \tag{5.46}$$

If H is much smaller than K, Eq. (5.46) simplifies to $f_{acc}^{e} \geq \frac{\mu \overset{\bullet}{\varepsilon}}{c}$ (5.46bis). This means that for a given $\overset{\bullet}{\varepsilon}$, it can be able to choose μ to control the accuracy of the solution.

Stability condition

In order to consider the stability of the numerical solution, it is necessary to start from an initial state of the model with a certain error. Then, by considering the relation between the initial error and the next error after an increment of loading, the stability condition can be derived.

At the initial state, it can be assumed that the model is at the stress level of σ_1, the total strain ε_1 and the error e_1 compared with the correct rate-dependent solution as shown in Figure 5.28. In the correct solution, the yield function can be written as follows:

$$y = \sigma - H\alpha - c = 0 \tag{5.47}$$

Therefore, the stress increment can be calculated as:

$$d\sigma = Hd\alpha \tag{5.48}$$

In the approximate solution, the yield function can be written as follows:

$$y = \sigma - H\alpha - c - e_1 = 0 \tag{5.49}$$

The incremental response becomes:

$$d\sigma = Kd\varepsilon - K\left(\frac{\sigma - H\alpha - c - e_1}{\mu}\right)dt \tag{5.50}$$

In a correct solution, $d\sigma = Hd\alpha$. Thus, the value of $Hd\alpha$ can be calculated as follows:

$$Hd\alpha = Kd\varepsilon - K\left(\frac{\sigma - H\alpha - c - e_1}{\mu}\right)dt \tag{5.51}$$

This leads to the following derivation:

$$\sigma - H\alpha - c = -\frac{\mu H d\alpha}{Kdt} + \frac{\mu d\varepsilon}{dt} + e_1 \tag{5.52}$$

Substituting Eq. (5.52) into Eq. (5.32), the result can be:

$$d\sigma = Hd\alpha - \frac{Kdt}{\mu}e_1 \tag{5.53}$$

The error updated at the end of the increment can be:

$$e_2 = e_1 + d\sigma - Hd\alpha = e_1 - \frac{Kdt}{\mu}e_1 = e_1\left(1 - \frac{Kdt}{\mu}\right) \tag{5.54}$$

The relation between e_1 and e_2 can be chosen depending on the quality of the stress-train curve required. There are three possibilities which can be used as the guidance for the choices of the relations between them.

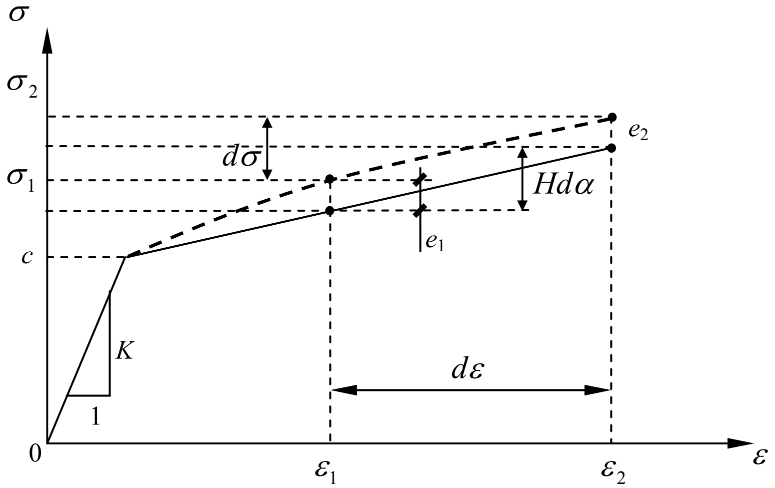

Figure 5.28 One-dimensional incremental response with its errors

The first possibility is that if $e_2 > e_1$, the solution is divergent and the stress-strain curve will continue to diverge from the correct results. This is an unstable solution. The second possibility is when $|e_2| \le fe_1$. In this case, the absolute value of e_2 must be smaller than or equal to e_1, multiplied by a factor of f (where $f \le 1$). By using this relation, the solution can converge smoothly if $e_2 > 0$. Otherwise, if $e_2 < 0$, the solution may oscillate slightly but can be quasi-stable. Figure 5.28 shows the shape of the stress-strain curve (the dashed line) compared with the correct solution curve (the continuous line) and the errors for the second possibility with $e_2 > 0$. The third possibility is the case of $e_2 \le -fe_1$. The solution in this case will oscillate and will either become stable more slowly than the second possibility or go unstable depending on how much e_2 is smaller than $-fe_1$. The more negative the value of e_2, the more oscillation occurs in the solution.

Whenever the value of e_2 becomes negative, there will be oscillations occurring in the stress-strain curve of the results. The reason is that, for a negative value of e_2, after a load increment the load point will return into the elastic zone which means that, in the next increment, the behaviour of the model will become purely elastic. The model then shows a much stiffer response than the elasto-plastic response expected. The amplitudes of these oscillations depend on the ratio of $\frac{|e_2|}{e_1}$. Therefore, if there is either too big a value of f chosen or a larger value of $|e_2|$ compared with fe_1, the solution will become unstable and oscillation in the stress-strain curve will occur.

In this simple model, the second case is used as the guideline to determine the stable condition. The following relation between e_1 and e_2, is therefore required:

$$\frac{|e_2|}{e_1} \le f \tag{5.55}$$

By substituting Eq. (5.54) into Eq. (5.55), the stability condition can be found as:

$$\frac{1}{1+f} \le \frac{\mu}{Kdt} \le \frac{1}{1-\min(f, 1.0)} \tag{5.56}$$

It should be noted that e_1 is supposed as a positive error. Furthermore, if negative values of e_2 are not accepted, i.e. $\frac{\mu}{Kdt} \ge 1.0$, the solution will be stable with every stress or strain increment applied.

5.6.2 Accuracy and stability conditions for ISIS model

For a much more sophisticated model such as ISIS, unfortunately, it is very difficult to derive explicit formulations for both accuracy and stability conditions. However, the characteristics of accuracy and stability described in the previous simple model can still exist in the ISIS model. Therefore, based on the form of these criteria in the one-dimensional model in section 5.6.1, empirical formulations for the accuracy and stability criteria are suggested for vertical component.

In order to verify whether the solution is correct or not, the first condition which must be satisfied is that it must be stable to give reasonable results. Afterward, the accuracy of the solution will be considered. Therefore, in the following sections, the stability condition is addressed first.

5.6.2.1 Stability conditions for ISIS model

Since it is too difficult to establish the explicit formulation for the stability condition, it could be easier to investigate the vertical component as the starting point.

In the ISIS model, since the mixed kinematic-isotropic hardening is used, the stability condition must involve the vertical bearing capacity V_0 which determines the isotropic hardening in the model behaviour.

Based on the expression of the rate-dependent ISIS model presented in chapter 3, an incremental plastic vertical displacement can be expressed as follows:

$$d\alpha_V = \frac{\langle y \rangle}{\mu} \frac{\partial y}{\partial \chi_V} dt \tag{5.57}$$

Thus, the viscosity factor μ can be defined as follows:

$$\mu = \frac{\langle y \rangle}{d\alpha_V} \frac{\partial y}{\partial \chi_V} dt \tag{5.58}$$

In Eq. (5.58), the value of the yield function y is dimensionless; the incremental plastic displacement has the dimension of length (m); the partial differential $\frac{\partial y}{\partial \chi_V}$ has the dimension of 1/force (1/N); the time increment dt has the dimension of time (s). Therefore, the viscosity must have the dimension of (s/Nm).

Applying the form of the stability condition of the simple model in Eq. (5.56), the stability condition taken into account the dimension of μ can be defined as follows:

$$\frac{\mu V_0^2 C_V}{\delta t} \geq f_{stab}^V \tag{5.59}$$

In which C_V is the elastic factors corresponding to vertical components in the diagonal of the compliance matrix $\left[C\right]$ which is the inversed matrix of the elastic stiffness matrix $\left[K\right]$.

After a series of tests, the empirical stability factor f_{stab}^{V} for the rate-dependent multiple-yield-surface ISIS model is suggested as 7.0 i.e. $\frac{\mu V_0^2 C_V}{\delta t} \geq 7.0$ (5.59bis)

It should be noted that this value of the stability factor is just valid with the accuracy of the solution of about 1%. In the vertical component, this accuracy can be seen by the ratio between V and V_0 i.e. $\left|\frac{V - V_0}{V_0}\right| \cong 0.01$. This is because the value of the yield function y that is not required to be zero in the rate-dependent solution increases with almost squares of the error $\left|\frac{V - V_0}{V_0}\right|$. This means that if the error is too large, the increase of y will be much faster than that of the error. This leads to the change of displacement rate, which is related to the differential of y with respect to χ_V. Meanwhile the stability condition was based on a constant strain rate in the simple model or constant displacement rate in the ISIS model. Therefore, the error $\left|\frac{V - V_0}{V_0}\right|$ must be kept small enough to ensure that the change of y does not lead to the big change of the displacement rate.

For other components, the horizontal and rotational components, the stability condition can be chosen in the similar form to the Eq. (5.59) corresponding to their stiffness factors.

5.6.2.2 Accuracy conditions for ISIS model

In addressing the accuracy conditions, it is impossible to integrate the differential equations of the force-displacement relationship analytically in either the rate-dependent or rate-independent solution cases. The only way that the accuracy of the solution can be determined is by repeating the rate-dependent solution with different parameters (time increments, load increments or displacement increments and viscosity factor) and observing the difference between solutions. Once there is only a small difference between the two trials, the solution can be considered as a correct answer.

Based on the form of either Eq. (5.40bis) or Eq. (5.46bis), the formulation of the accuracy criterion can be proposed in the ISIS model with the simple forms as follows:

In the case of a load-controlled solution:

$$\mu\left|\overset{\bullet}{\sigma}_i\right|\frac{V_0}{K_i} \le f^i_{acc\_s} \tag{5.60}$$

In the case of a displacement-controlled solution:

$$\mu\left|\overset{\bullet}{\varepsilon}_i\right|V_0 \le f^i_{acc\_e} \tag{5.61}$$

where σ_i represents the force components $(V, H_2, H_3, Q, M_2, M_3)$ and K_i is the corresponding elastic stiffness factor; ε_i represents the displacement components $(w, u_2, u_3, \omega, \theta_2, \theta_3)$; $f^i_{acc\_s}$ and $f^i_{acc\_e}$ are the accuracy factors in the load-control and displacement-control cases corresponding to each σ_i and ε_i. It is flexible to choose the values for these accuracy factors. This depends on how much of the accuracy that people need for the solution.

5.6.3 Discussion and advice for the use of rate-dependent solution

It is clear that the smaller the accuracy factors chosen, the more accurate results are obtained. However, the penalty of choosing the small accuracy factors is that, in order to keep the solution stable, the number of increments must be increased. For instance, as shown in Eq. (5.61), at a certain constant displacement rate, the viscosity factor μ must be decreased to make the solution more accurate. This leads to the decrease of the term in the right hand side of Eq. (5.59) and may cause the violation of this inequality. Thus, in order to satisfy this inequality, the value of the time increment dt must be decreased. This means that the number of displacement increments must be increased. Consequently, the calculation time can become longer.

Since the accuracy and stability criteria depend on the elastic stiffness factors, time increments, load increments, viscosity factor and the vertical bearing capacity of the footing, there is a common procedure proposed to make an input data file which can satisfy the accuracy and stability criterion without the need for running so many trials.

Firstly, some trial values of the load increments, the time increments and the viscosity factor are used to find a stable solution which is not required to be accurate. This process is implemented in case of applying purely vertical load (pushing installation). The stability factor in Eq. (5.59bis) can be used as the starting point.

Secondly, the difference between V and V_0 is considered as the error. If this error is lager than 1% then either the viscosity factor or the number of increments can be changed to get more accurate solution. During this process, the stability condition in Eq (5.59bis) must be satisfied.

Thirdly, after finishing the installation process with reasonable precision, the number of increments and either loading rates or displacement rates in other components can be chosen proportionally with the ratio between their elastic stiffness factors and the vertical elastic stiffness factor.

5.7 Concluding remarks

In this chapter, the explanations of the following matters have been discussed:

- The shapes of the yield surfaces and their shape parameters;
- The association factors and the suitable ranges of their magnitude;
- The initial distribution of the yield surfaces in force space;
- The kernel functions and their effects on the hardening process; and
- The general ideas and empirical advice for determining suitable input data for the use of the rate-dependent solution.

From the above issues, the model parameters can be selected reasonably for the application of the model in practice.

CHAPTER 6

MODEL APPLICATIONS

6.1 Introduction

This chapter presents numerical applications of the multiple-yield-surface rate-dependent ISIS model to predict the response of caisson foundations. There are two foundation options considered: a monopod caisson and a quadruped structure with four caissons. Three kinds of soil are used for these analyses: sand, soft clay and stiff clay. The numerical results are compared with the results of finite element analyses (Fugro, 2004) which determined the failure loads. In addition, the influences of the model parameters on the solution are addressed.

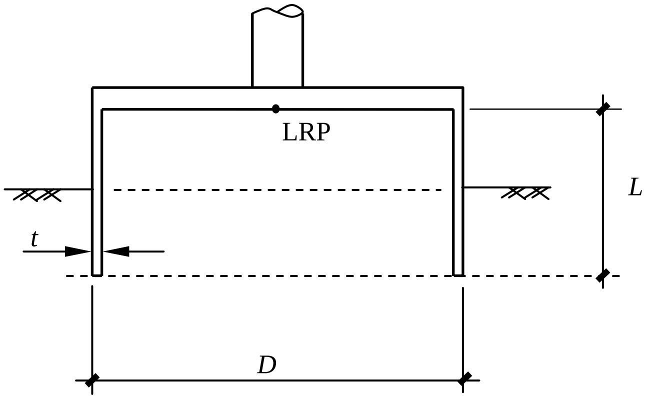

Figure 6.1 Outline of caissons

Table 6.1 Dimensions of caissons (after Fugro, 2004)

Case	Monopod	Quadruped
External diameter D (m)	19.0	6.0
Length of skirt L (m)	9.5	4.0
Wall thickness t (mm)	42.5	20.0

The outline and the dimensions of both monopod and quadruped caissons are presented in Figure 6.1 and Table 6.1. The soil properties are provided in Table 6.2.

Table 6.2 Soil properties (after Fugro, 2004)

Case	Sand	Soft clay	Stiff clay
Effective unit weight, γ' (kN/m^3)	10.0	10.0	10.0
Shear modulus, E (MPa)	25.0	(3.0 + 0.4 (z/m)) $G/s_u = 200$	30.0 $G/s_u = 200$
Poisson's ratio, ν	0.2	0.49	0.49
Angle of friction, ϕ' (^{o})	35	-	-
Undrained strength, s_u (kPa)	-	(15.0 + 2.0(z/m))	150.0

In this study, the shear modulus G will be determined using the formulation presented in Eq. (2.10) (Doherty *et al.*, 2004). Values of the exponential factor α are given as 0.0, 0.5 and 0.0 for sand, stiff clay and soft clay respectively. Values of the coefficient G_R are given as 25.0 MPa and 30.0 MPa for sand and stiff clay. For soft clay, G_R are given as 6.8 MPa in the case of monopod caisson and 4.6 MPa in the case of quadruped caisson.

Since the monopod caisson is a single foundation, it requires an analysis of a single loading combination for a given load case. However, the quadruped caisson may require several analyses which depend on the relative position of the caisson in the quadruped group for a given load direction. For a given load case, the different caissons are subjected to different load combinations. In this chapter, the two extreme loading combinations are applied for the analysis of the quadruped caisson: a windward caisson subjected to tensile loads and a leeward caisson to compression loads.

The extreme environmental conditions represented by the loading combinations in Table 6.3 are represented by planar loading. These data are provided in the reports of Fugro (2004). The strategies of the loading process for the two kinds of caisson foundation are presented below:

(i) Installation to full depth using suction;

(ii) Load to the vertical load (load point A) as given in Table 6.3;

(iii) Apply the load combination following the linear load path passing through the load point B (see Table 6.3) to failure load.

Table 6.3 Load cases (after Fugro, 2004)

Case		Monopod	Quadruped - leeward	Quadruped - windward
Load point A	Vertical load, *V* (kN)	8,772	1,987	1,987
	Horizontal load, *H* (kN)	0	0	0
	Momnet, *M* (kNm)	0	0	0
Load point B	Vertical load, *V* (kN)	8,772	4,729	-739
	Horizontal load, *H* (kN)	3,196	1,927	1,591
	Moment, *M* (kNm)	100,000	1,445	1,817

In the ISIS model, there are two ways to estimate the tensile capacity V_t of the caisson. The first way is expressing the tensile capacity as a fraction of the vertical bearing capacity V_0. The second way is calculating the tensile capacity on the basis of friction on the side of the caisson. In the examples of this chapter, the first way is used. Values of t_0 are given in Table 6.4.

The failure point of the solution can be determined in two cases: (1) the numerical solution fails or (2) the plastic displacement of the foundation is larger than the corresponding limit value defined in the model. The limitations of the displacements in the model are defined as 0.01*R*(m) for horizontal displacement.

6.2 Analysis of a monopod caisson

This section presents the analysis of a monopod caisson in three different kinds of soil. Figure 6.2 shows the load path for this case. During the application of the horizontal and moment loads, the vertical load that represents the self-weight of the wind turbine is kept constant. The model parameters are as given in Table 6.3.

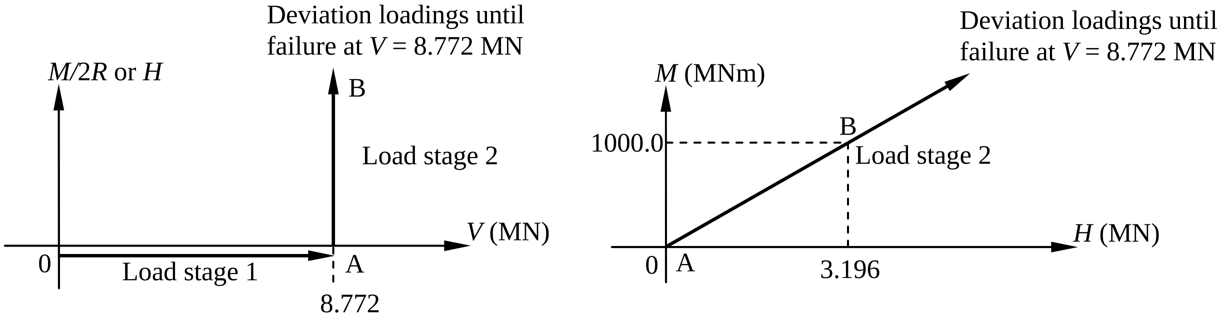

Figure 6.2 Load paths applied for the monopod caisson

Table 6.4 Model parameters for the analysis of the monopod caisson

<table>
<tr><th colspan="6">Model parameters (multiple-yield-surface ISIS model)</th></tr>
<tr><td rowspan="2">Association factors</td><td>a_{V1}</td><td>a_{V2}</td><td>a_H</td><td>a_M</td><td>a_Q</td></tr>
<tr><td>0.297 (sand)
0.645 (clay)</td><td>1.0 (sand)
0.645 (clay)</td><td>0.7 (sand)
1.0 (clay)</td><td>0.7 (sand)
1.0 (clay)</td><td>0.7 (sand)
1.0 (clay)</td></tr>
<tr><td rowspan="8">Shape factors of yield surface</td><td colspan="2">e_1</td><td colspan="3">-0.2 (for sand); 0.518 (for clay)</td></tr>
<tr><td colspan="2">e_2</td><td colspan="3">0.0 (for sand); -1.18 (for clay)</td></tr>
<tr><td colspan="2">t_0</td><td colspan="3">0.05 (for sand); 0.1 (for soft clay); 0.4 (for stiff clay)</td></tr>
<tr><td colspan="2">m_0</td><td colspan="3">0.15</td></tr>
<tr><td colspan="2">h_0</td><td colspan="3">0.337</td></tr>
<tr><td colspan="2">q_0</td><td colspan="3">0.2</td></tr>
<tr><td colspan="2">β_1</td><td colspan="3">0.99</td></tr>
<tr><td colspan="2">β_2</td><td colspan="3">0.99</td></tr>
<tr><td rowspan="2">Parameters for the rate-dependent solution</td><td colspan="2">Viscosity μ</td><td colspan="3">0.002</td></tr>
<tr><td colspan="2">Time increment dt</td><td colspan="3">Changed with the load incerements</td></tr>
<tr><td>Number of yield surfaces</td><td colspan="5">20 yield surfaces used</td></tr>
<tr><td>Bell width (w_{bell}) (m)</td><td colspan="5">0.012</td></tr>
</table>

6.2.1 Installation

In this example, the installation is implemented by using the suction technique. Figure 6.3 shows the initial penetration of the caisson under its self-weight and the installation during the suction process. In the soft clay, the caisson penetrates to a depth which is almost two third of the length of the caisson under its own weight. In the case of stronger soil (stiff clay and sand), the initial penetration of the caisson is much smaller.

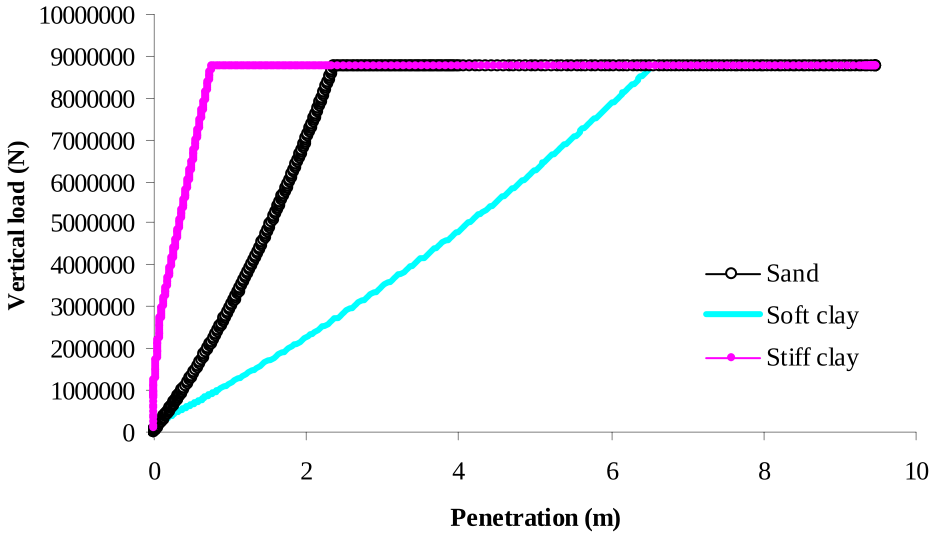

Figure 6.3 Vertical load during the suction installation of monopod caisson

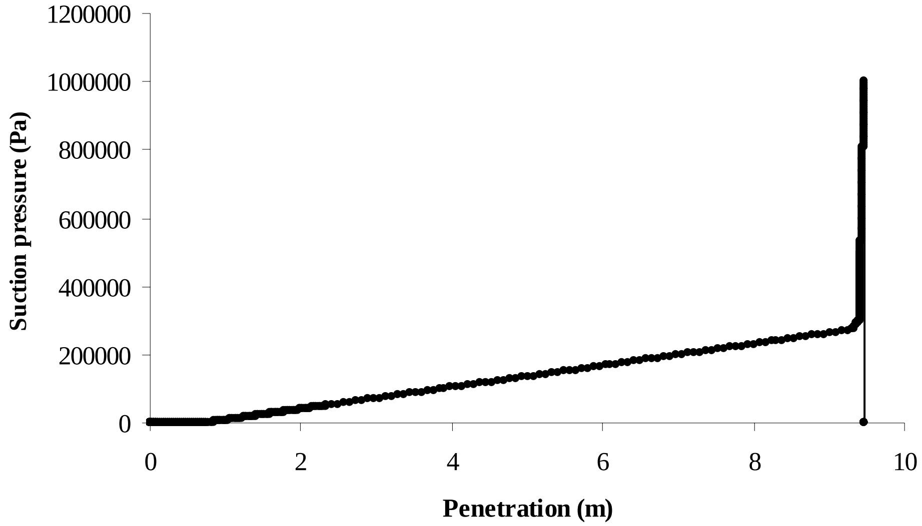

Figure 6.4 Suction pressures needed to install the monopod caisson to the full depth in stiff clay

After the self-weight penetration is finished, suction pressures are applied to install the caisson to the full depth. In the case of sand, the suction pressure plays the role of an additional vertical load and also causes the decrease of the effective stress of the soil inside the caisson, which leads to the decrease of the strength of the soil at the tip level of the caisson. In case of clay, since the permeability of clay is low, the suction pressure merely plays the role of the additional vertical load without any effect on the soil strength. This leads to the fact that installing the caisson by suction in clay may be harder than in sand, especially in the case of strong soil such as stiff clay. Figure 6.4 shows the prediction of the suction pressure needed to install the monopod caisson to the full penetration depth (L = 9.5m) in stiff clay. It can be found that in order to get to the full depth, a very high pressure must be applied at the end of the process, up to approximately 1.0 MPa. This would not be a possible value in practice at shallow water depth. Therefore, in this analysis, the caisson in the case of stiff clay is installed to a smaller depth (which is approximately 99% of the full depth) to avoid unrealistic behaviour.

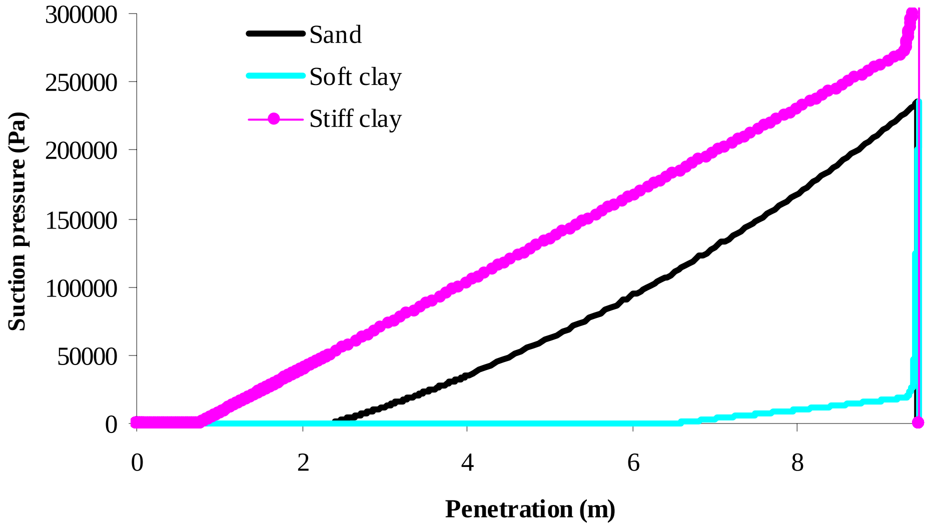

Figure 6.5 Suction installation of monopod caisson

Figure 6.5 shows the suction pressures required to install the caisson to the full depth in sand, soft clay and to 9.41m-depth in stiff clay. Again, it can be seen that in case of soft clay, the suction pressure must be increased dramatically at a few centimetres before the full depth. The precise position at which this increase occurs depends on the “bell width” parameter, which in part represents effects of heave of the soil within the caisson.

6.2.2 Horizontal and rotational responses

Figure 6.6 and 6.7 show the horizontal and rotational responses of the monopod caisson in all three cases of soil. In these figures, the curves of the caisson in stiff clay and soft clay are stopped at clearly defined failure load points. In the case of caisson in sand, the failure occurs when the horizontal displacement reaches the limiting displacement. Details of the failure loads are presented in Table 6.5.

It can be seen that the horizontal response of the caisson in stiff clay is stiffer than that in the case of sand and soft clay. In both components (horizontal and moment responses), the curves representing the behaviour of the caisson in sand are in the middle between the stiff clay and soft clay (at the beginning of the loading).

Figure 6.8 shows the vertical movements of the caisson under the horizontal and moment loading. In the cases of sand and stiff clay, the caisson moves slightly upward. In the case of soft clay, the upward movement of the caisson is larger than other cases.

The fact that the caisson lifts in the case of soft clay seems unreasonable. This is because the parallel points on the yield surfaces are not located correctly by the model parameters. In fact, the positions of the parallel points in the case of clay in these analyses are based on that in the cases of circular footing and spudcan (Model B). This needs to be corrected by using the additional experimental observations for clay, which are not available yet.

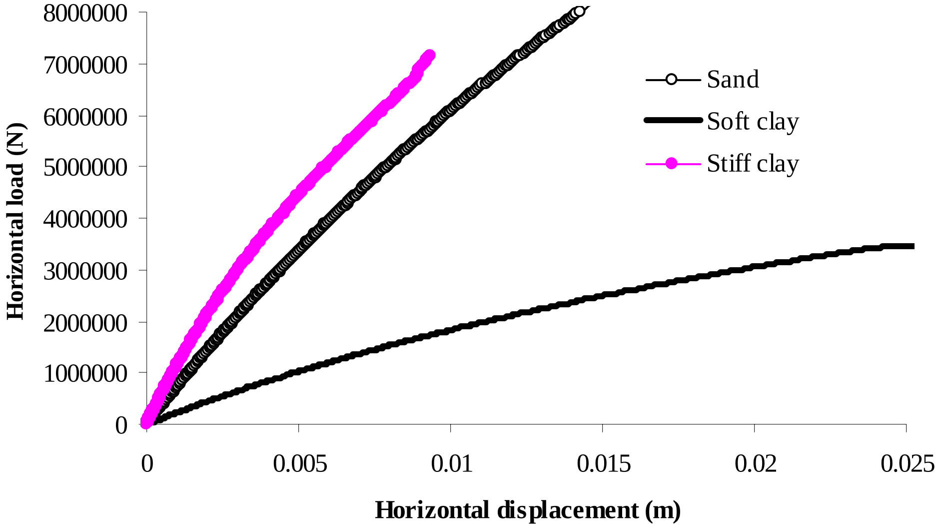

Figure 6.6 Horizontal response of monopod caisson

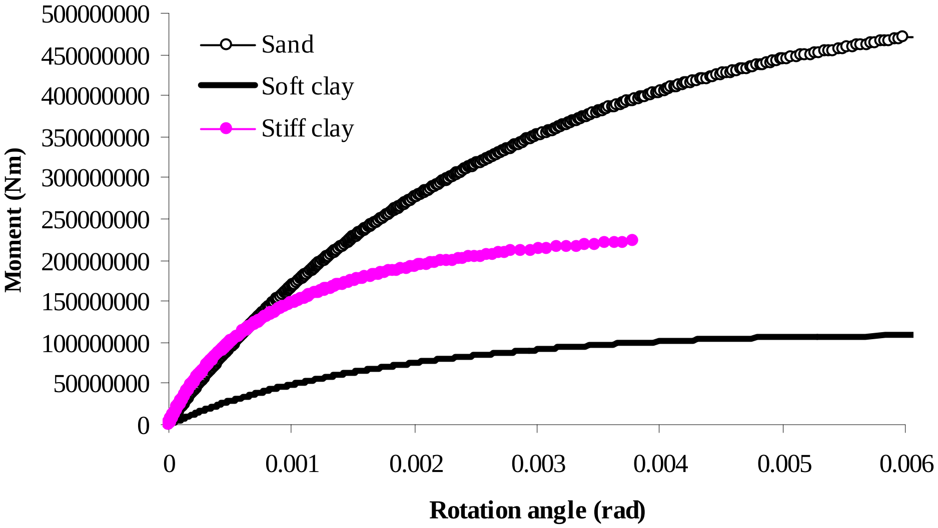

Figure 6.7 Rotational response of monopod caisson

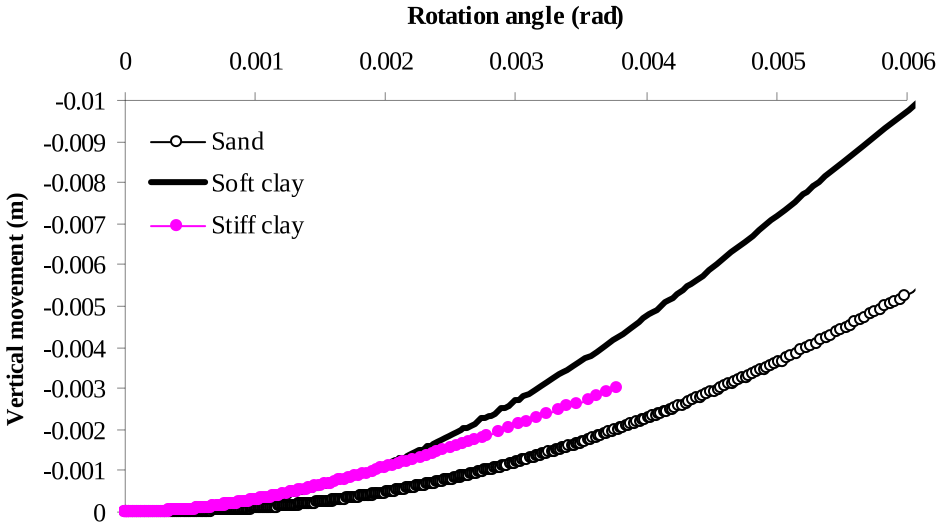

Figure 6.8 Vertical movement of monopod caisson
(until failure in soft clay)

6.2.3 Numerical results

Table 6.5 shows the failure load values of the monopod caisson in all three kinds of soil. The results of finite element analysis and extreme environmental loads (Fugro, 2004) are also given in Table 6.5 for comparison.

Table 6.5 ISIS results compared with Finite Element analysis (after Fugro, 2004)

Monopod caisson	Soil Profile	Loads			Percentage environmental load	Notes
		Vertical (MN)	Horizontal (MN)	Moment (MNm)		
Failure values (ISIS)	Sand	**8.772**	**15.873**	**496.67**	496.67	B
	Soft clay	**8.772**	**3.467**	**108.50**	108.50	A
	Stiff clay	**8.772**	**7.127**	**223.00**	223.00	A
Failure values (FE)	Sand	8.800	15.400	481.50	481.6	
	Soft clay	8.800	3.200	99.00	99.3	
	Stiff clay	8.800	25.500	797.00	797.2	
Point A		8.772	0.000	0.000		
Point B		8.772	3.196	100.0		

Note A: clearly defined failure (case 1)

Note B: failure considered as horizontal plastic displacement $u = 0.01R$ (case 2)

As shown in Table 6.4, the FE analyses give significantly higher failure values in the case of stiff clay. Meanwhile, in the case of soft clay, the ISIS failure loads are larger than FE values. In the case of sand, the ISIS model gives failure values which are close to the FE results. The differences between the two solutions may be due to the following points:

(i) In the FE analyses, the footings were assumed to be in place without consideration of the installation process. However, the method of installation can significantly affect the foundation response during the horizontal and moment loadings. Different methods can cause different stress histories in the soil, and different responses of the footing after installation are therefore expected. This matter will be discussed in more detail in section 6.4.

(ii) The ISIS solution is rather sensitive to the choice of the parameters. In particular, the tensile capacity t_0 (which represents the tensile capacity of the footing) has strong effect on the results, especially in cases of applying small vertical loads. Detailed expressions will be given in section 6.5.

(iii) In the cases of soft clay and stiff clay, the shape parameters of the yield function have the same values as those for sand since there is limited experimental data available for clay. This can cause some inaccuracy in the ISIS solution.

(iv) In stiff clay, according to the ISIS analysis, it is difficult to install the caisson to the full depth by suction because of the required high pressure. The analyses of the monopod caisson in stiff clay have been implemented at 99% of its depth. This means that the V_0 value, which determines the sizes of yield surfaces, is smaller than that at the full depth. This leads to the smaller failure loads obtained. The calculation principle of this matter is similar to that of the heave inside the caisson discussed in section 6.6.

(v) The finite element analyses may themselves be subject to errors and inaccuracies.

6.3 Analysis of a quadruped caisson

This section presents the analysis of a quadruped caisson in the two extreme load cases of a leeward leg and a windward leg. Figures 6.9 and 6.10 show the load paths of these examples. The corresponding extreme environmental loads are given in Table 6.3 and shown as point B in Figures 6.9 and 6.10.

The dimensions of the caisson are provided in Table 6.1. The model parameters used in this example are the same as in the analysis of the monopod caisson (see Table 6.4).

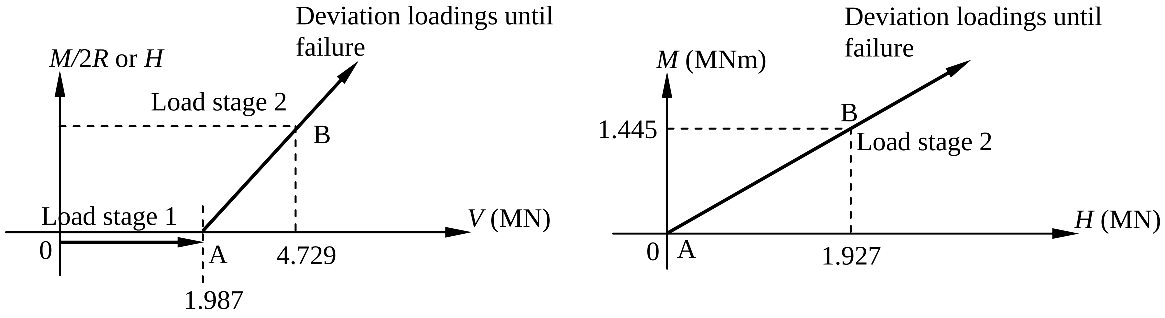

Figure 6.9 Load paths applied for the quadruped caisson – leeward leg

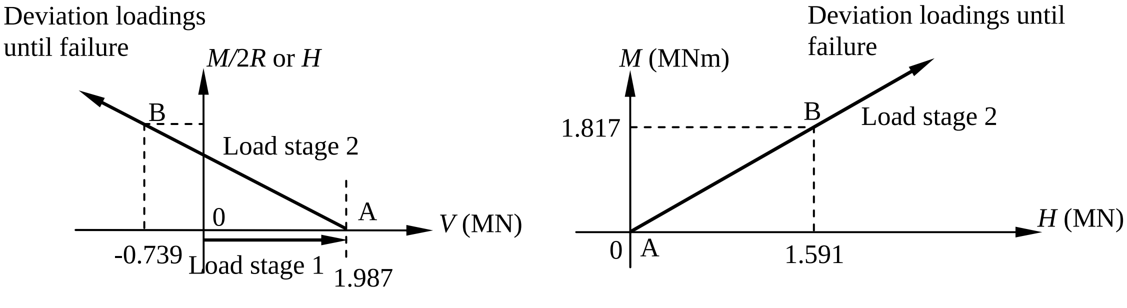

Figure 6.10 Load paths applied for the quadruped caisson – windward leg

6.3.1 Installation

As with the monopod caisson, the analysis in this section also commences with the prediction of the installation process. Figure 6.11 shows the suction pressures required to install the caisson to its full depth in sand and stiff clay. Since the suction process of the caisson in soft clay has a different scale compared with that in the case of sand and stiff clay, it is presented in a separate figure (Figure 6.12).

Again, in the case of stiff clay, the suction pressure required increases dramatically near the full penetration depth. Thus, the analysis for this case is implemented at a slightly smaller depth at which the suction process is stopped (see Figure 6.11). The approximate depth is 3.96m (99% of the full value). In the case of soft clay, the caisson penetrates to almost the full depth by its self-weight. However, in order to complete the installation, it still needs a further suction pressure of approximately 170 kPa. In contrast, in the case of sand, since the initial penetration by the self-weight is rather big, the suction pressure needed to assist the installation is small.

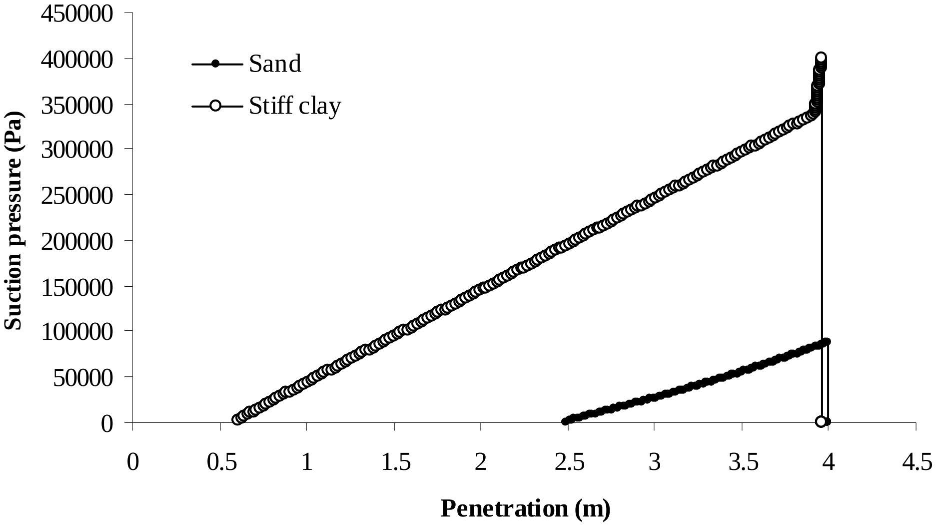

Figure 6.11 Suction pressure needed for the installation of the quadruped-leeward caisson in sand and stiff clay

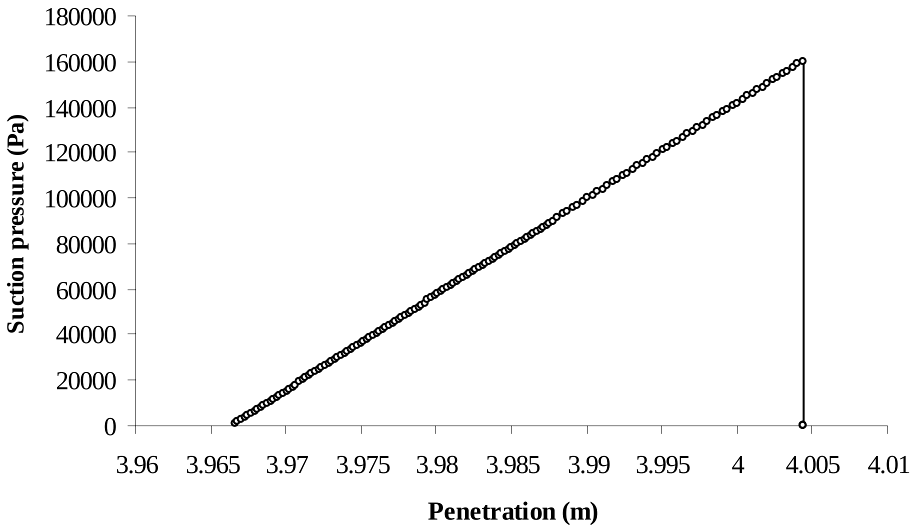

Figure 6.12 Suction pressure needed for the installation of the quadruped-leeward caisson in soft clay

6.3.2 Horizontal and rotational responses

This section presents the horizontal and rotational responses of the quadruped caisson in both cases: the leeward-leg load case and the windward-leg load case.

Quadruped caisson at leeward leg

Figures 6.13 and 6.14 show the horizontal and rotational responses of the caisson. Figure 6.15 shows the further vertical displacement of the caisson under the combined loading. Figure 6.16 shows the vertical movement versus rotation displacement of the caisson during the loading process.

In all three kinds of soil, the caisson responses under the leeward-leg load case fail as the plastic displacements become larger than the limit values. In this particular example, the horizontal displacements are larger than the corresponding limit value, which is 0.03m (0.01*R*).

As shown Figure 6.15, the vertical movements of the caisson, regardless of the soil profile, are downward. This means that under the leeward load case, the caisson is penetrating into the soil.

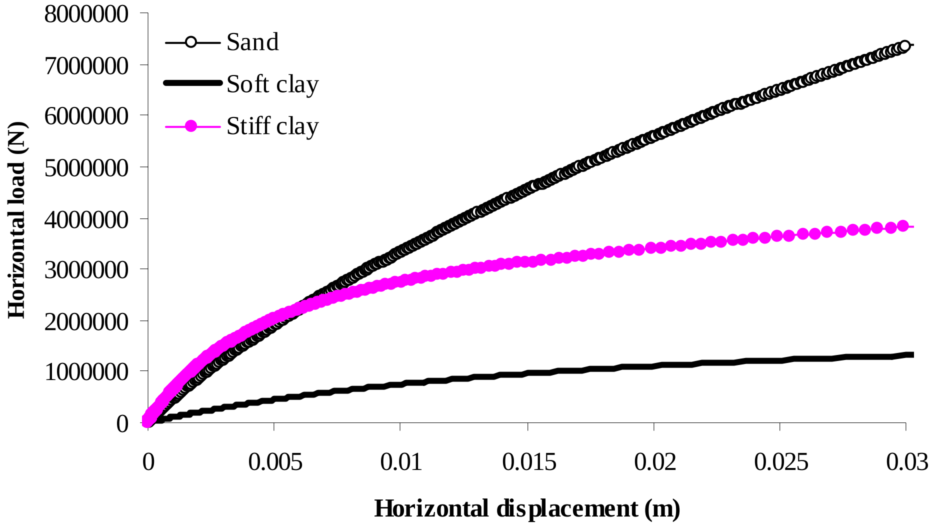

Figure 6.13 Horizontal response of the quadruped-leeward caisson until failure

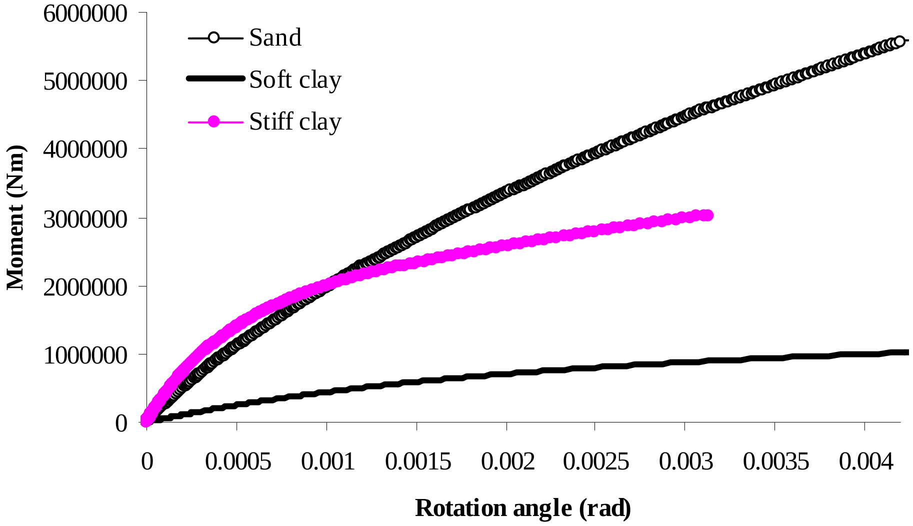

Figure 6.14 Rotational response of the quadruped-leeward caisson until failure

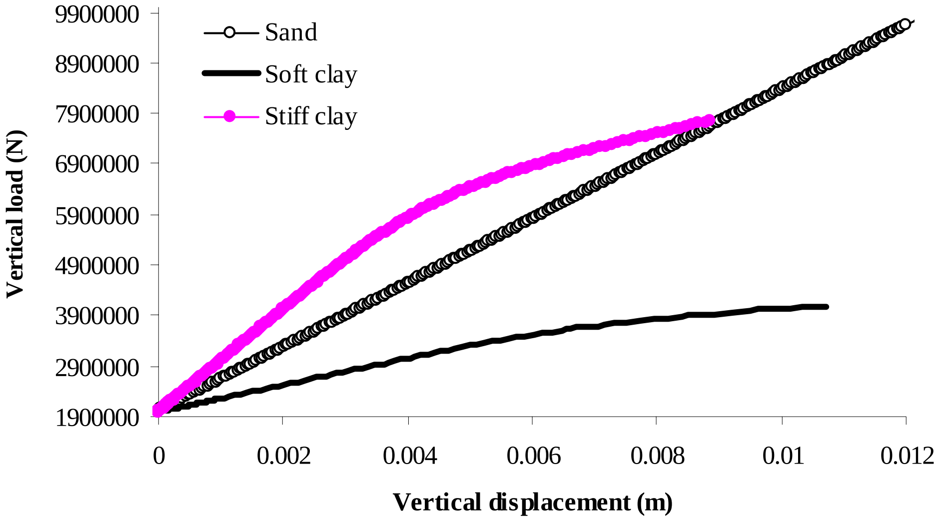

Figure 6.15 Vertical displacement of the quadruped-leeward caisson during compressive loading

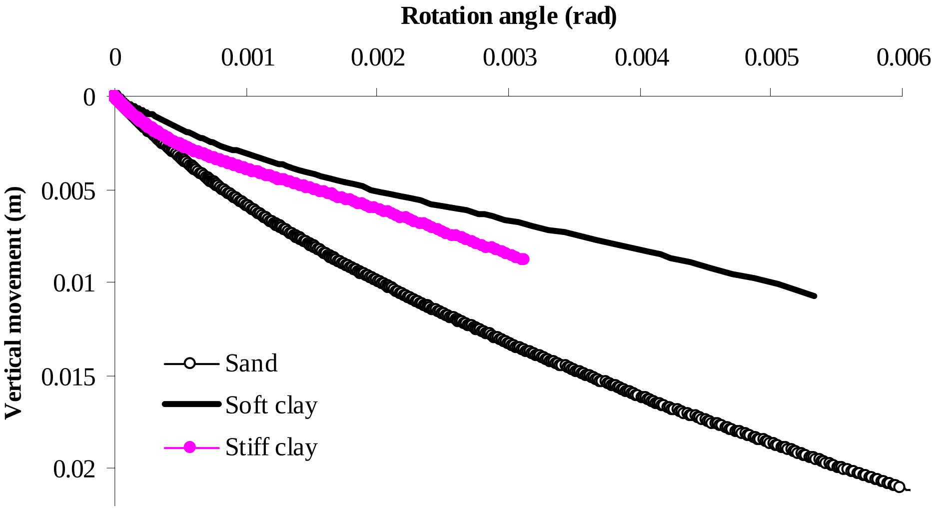

Figure 6.16 Movement of the quadruped-leeward caisson during compressive loading

In all the components, the analysis of the caisson in stiff clay, which is the strongest soil in this example, gives much smaller failure loads than in the case of sand. This contradiction is due to the effect of the incomplete penetration. The value of the vertical bearing capacity V_0, which affects the plastic response, increases quickly in the area near the full penetration depth. The model is therefore very sensitive to the depth of caisson near the full penetration position. Consequently, the 1% of the depth (0.04m) which has not been reached causes a significant decrease of the footing capacity. This matter is discussed in more detail in section 6.6.

Quadruped caisson at windward leg

As shown in Figure 6.10, the quadruped caisson at the windward leg is subjected to a combination of a horizontal load, a moment and a tensile vertical load. Figures 6.17, 6.18 and 6.19 show the horizontal, rotational and vertical responses of the caisson in all three kinds of soil.

In this load case, the analyses of the caisson in sand and soft clay fail when the horizontal displacements become larger than the limit values (failure case (2)). In stiff clay, the analysis is terminated since the numerical solution fails, which implies the failure of the foundations (failure case (1)).

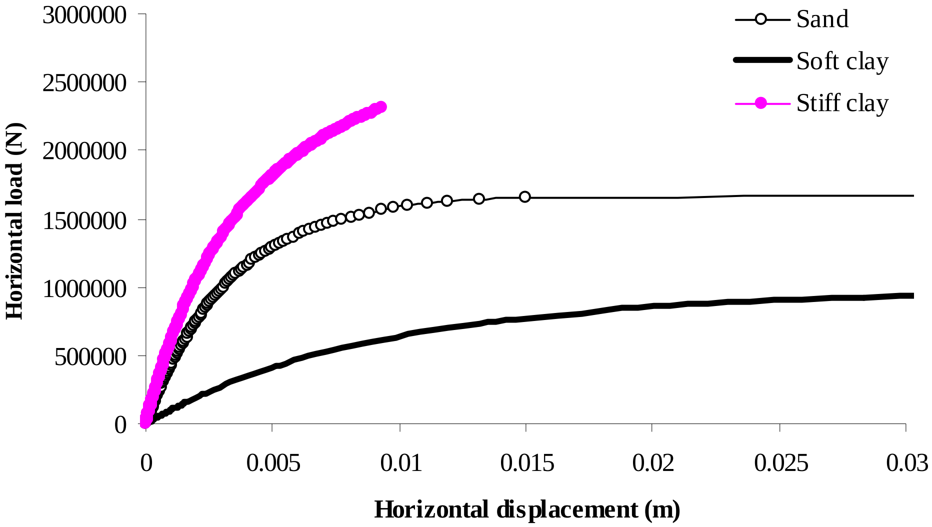

Figure 6.17 Horizontal response of the quadruped-windward caisson until failure

As shown in Figure 6.19, the caisson is pulled out of the soil. In the case of stiff clay, the vertical response is much stiffer than in other soil profiles. The upward displacement at failure in the case of soft clay is largest.

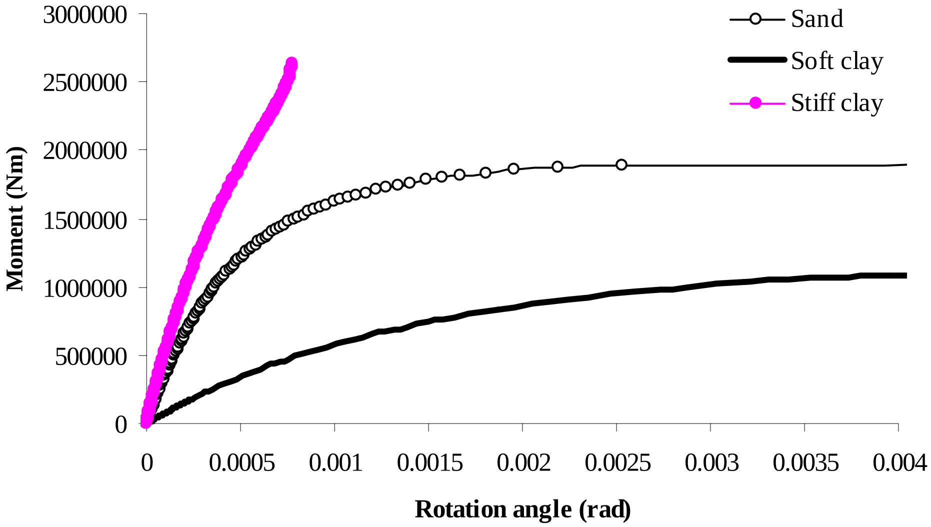

Figure 6.18 Rotational response of the quadruped-windward caisson until failure

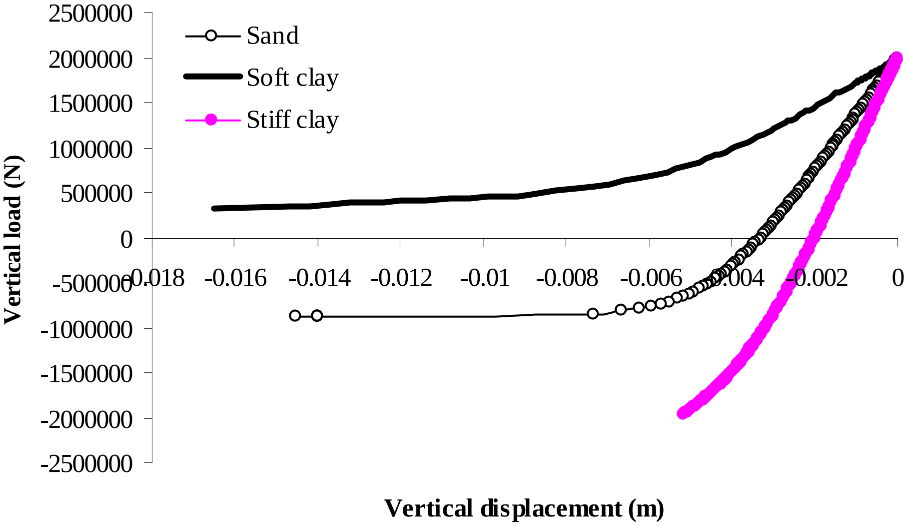

Figure 6.19 Vertical displacement of the quadruped-windward caisson during tensile loading

In the case of caisson in soft clay, the response shows the failure point at a positive value of vertical load. This means that in soft clay, the caisson cannot withstand the tensile vertical force. This matter depends on the value of the tensile capacity factor t_0. With a larger t_0, the model response can show a small tensile capacity of the caisson.

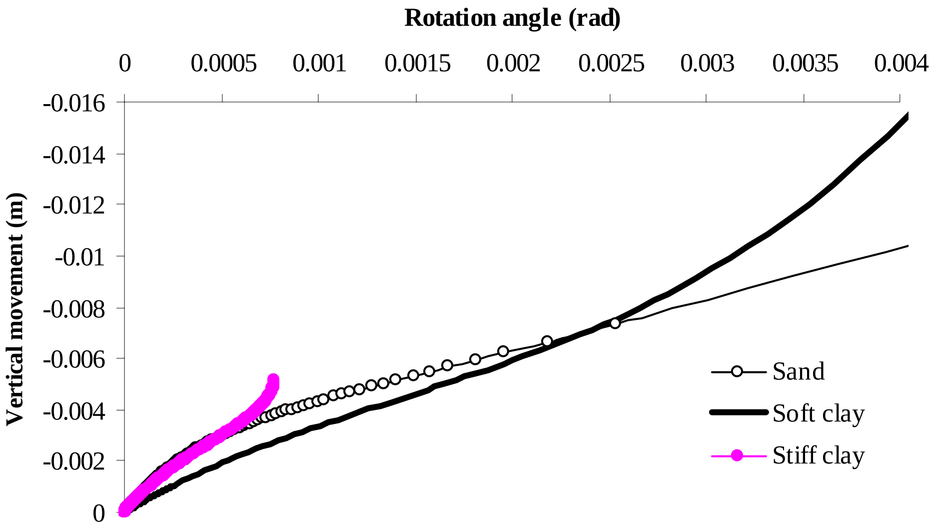

Figure 6.20 Movement of the quadruped-windward caisson during tensile loading

Figure 6.20 shows the vertical movement of the caisson versus the rotational displacement. It can be seen that the movement of the caisson in the case of stiff clay has the similar shape as in the case of soft clay but much smaller.

6.3.3 Numerical results

This section presents the numerical results showing the failure loads of the foundation in both leeward and windward load cases. The results of ISIS are compared with FE analysis results reported in Fugro (2004). Tables 6.6 and 6.7 show the results for the leeward load case and windward load case respectively.

In the leeward load case, the ISIS model gives failure values, which are close to the FE results in the case of sand. This is similar to the case of the monopod caisson in sand. The model parameters used in this study are from experiments with the caisson at a ratio of V/V_0, which is in the range from 0.0 to 0.2 (Villalobos *et al.*, 2003b, 2004a and 2004b). Therefore, among these examples, the failure loads predicted in the cases of monopod and quadruped-leeward caissons in sand can be expected to be the most reliable results. In the cases of stiff clay and soft clay, the ISIS results are approximately one half of the FE results. This means that the ISIS solution gives much more conservative results.

Table 6.6 ISIS results compared with Finite Element analysis (after Fugro, 2004) – quadruped caisson – leeward leg

Quadruped caisson (leeward)	Soil Profile	Loads			Percentage environmental load	Notes
		Vertical (MN)	Horizontal (MN)	Moment (MNm)		
Failure values (ISIS)	Sand	**12.406**	**7.322**	**5.491**	380.0	B
	Soft clay	**3.852**	**1.310**	**0.982**	67.98	B
	Stiff clay	**7.443**	**3.835**	**2.876**	199.03	B
Failure values (FE)	Sand	17.100	10.600	7.900	550.8	
	Soft clay	6.200	3.000	2.200	154.3	
	Stiff clay	20.200	12.800	9.600	664.2	
Point A		1.987	0.000	0.000		
Point B		4.729	1.927	1.445		

Note A: clearly defined failure (case 1)

Note B: failure considered as horizontal plastic displacement $u = 0.01R$ (case 2)

Table 6.7 ISIS results compared with Finite Element analysis (after Fugro, 2004) – quadruped caisson – windward leg

Quadruped caisson (windward)	Soil Profile	Loads			Percentage environmental load	Notes
		Vertical (MN)	Horizontal (MN)	Moment (MNm)		
Failure values (ISIS)	Sand	**-0.873**	**1.669**	**1.906**	113.3	B
	Soft clay	**0.378**	**0.938**	**1.072**	62.6	B
	Stiff clay	**-1.965**	**2.307**	**2.634**	146.9	A
Failure values (FE)	Sand	-3.700	3.300	3.800	208.3	
	Soft clay	-1.500	2.000	2.300	127.4	
	Stiff clay	-7.800	5.700	6.500	358.8	
Point A		1.978	0.000	0.000		
Point B		-0.739	1.591	1.817		

Note A: clearly defined failure (case 1)

Note B: failure considered as horizontal plastic displacement $u = 0.01R$ (case 2)

In the windward load case, the differences between the results of ISIS and FE are approximately 50%. Again, the ISIS results are sensitive to the tensile capacity factor t_0 as a result of the decreasing vertical load.

6.4 Effect of the simulation of suction installation on the solution

It is generally accepted that soils possessing different stress histories can exhibit different behaviours. In the case of caisson foundations, the installation of the caisson creates a stress history in the soil before the serviceability condition is analysed. In the ISIS model, two installation methods are mentioned: pushing installation and suction installation. This section presents the effect of these methods on the model response when they are taken into account.

Figure 6.21 shows the yielding process during the suction installation. Firstly, from the initial position (Figure 6.21a) which implies that there is no yield surface activated, the caisson is installed by its self-weight. This process usually reaches the full plastic state quickly (Figure 6.21b). This means that all the yield surfaces have been activated. After finishing the self-weight penetration, the suction is applied. During the suction process, the vertical bearing capacity V_0, which determines the sizes of the yield surfaces, does not increase with depth because of the influence of suction pressure. Thus the yield surfaces do not expand. Once the caisson reaches the full penetration depth, the suction is stopped. In the ISIS model, this leads to the fact that the foundation is returned to the “original” state at which there is no yield surface activated. The V_0 which has been a function of both depth and suction pressure is immediately returned to be a function of depth only and its current value is the value of the bearing capacity of the caisson at the full depth (without taking into account the suction). This sudden change of V_0 from a small constant value during the suction process to a great value of the vertical bearing capacity of the caisson at the full depth leads to the instantaneous redistribution of the yield surfaces. Figure 6.21c shows the redistribution of the yield surfaces after the suction is switched off. The relative position of the load point with respect to the positions of the yield surfaces is therefore changed. From being the intersection of the yield surface, the load point is now inside the yield surfaces. This means that all the yield surfaces are inactivate. Consequently, in the next stage of loading, the model response will start with elastic behaviour.

Figure 6.22 shows the yielding process during pushed installation. In this case, after the installation is completed, there must be an unloading process to return the vertical load to the self-weight of the caisson. During the pushing installation, kinematic hardening of the yield surfaces occurs. The yield surfaces move with the increase of the V_0 values. In the unloading process, since the self-weight is rather small compared with the vertical bearing capacity V_0, some inner yield surfaces are reactivated (see Figure 6.22c) and cause a slight uplift displacement of the footing as well as the contraction of the yield surfaces. This means that in the next stage of loading, the model response will start with the elasto-plastic behaviour.

It is clear that the response of the caisson installed by suction is different to that of the caisson installed by pushing. Using the formulation of the ISIS model, the caisson installed by suction may give a stiffer response. This may, however, be unrealistic as experiments show that suction installation may give a more flexible response (Villalobos *et al.*, 2005).

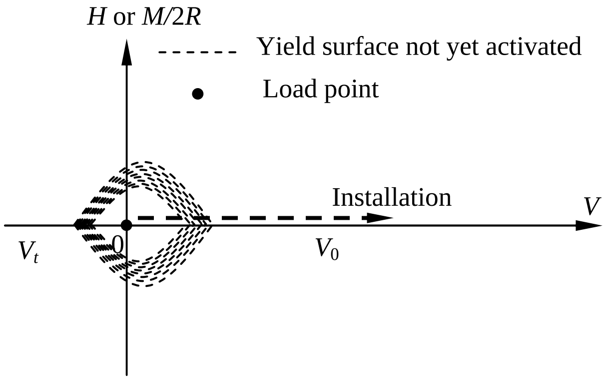

(a) Initial yield surface system

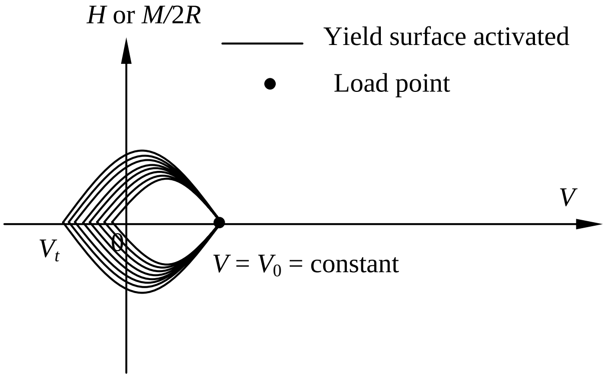

(b) Fully plastic state without expansion of the yield surfaces during the suction installation

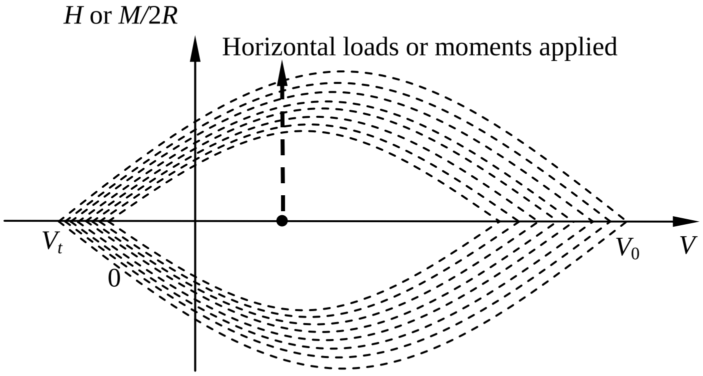

(c) Yield surface system after finishing the installation

Figure 6.21 Yielding process during suction installation

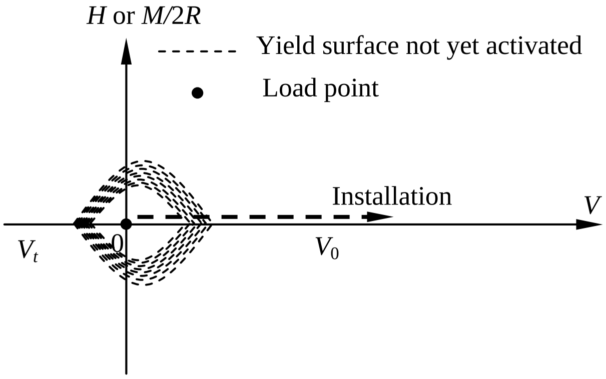

(a) Initial yield surface system

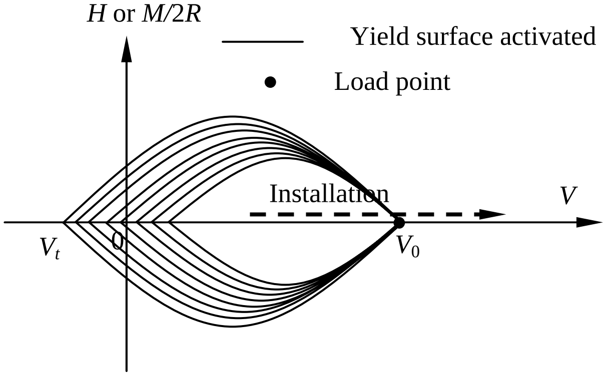

(b) Fully plastic state during the installation

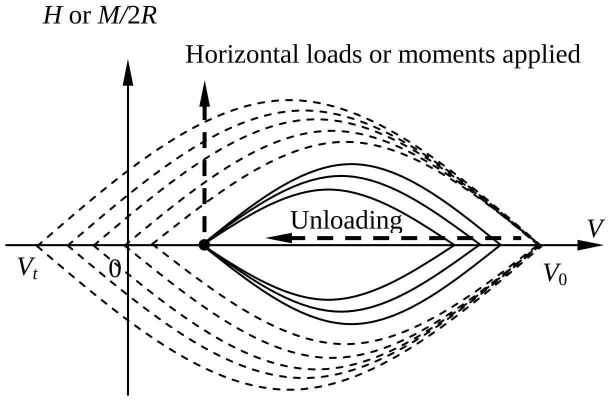

(c) Yield surface system after finishing the installation

Figure 6.22 Yielding process during pushing installation

Figures 6.23, 6.24 and 6.25 show the comparison between the responses of the monopod caisson in sand installed by pushing and that installed by suction. It can be seen that the response in the case using suction installation is much stiffer than that using pushing installation. In Figure 6.25, the difference between the vertical displacements at the beginning is caused by the softening during the unloading process of the caisson installed by pushing.

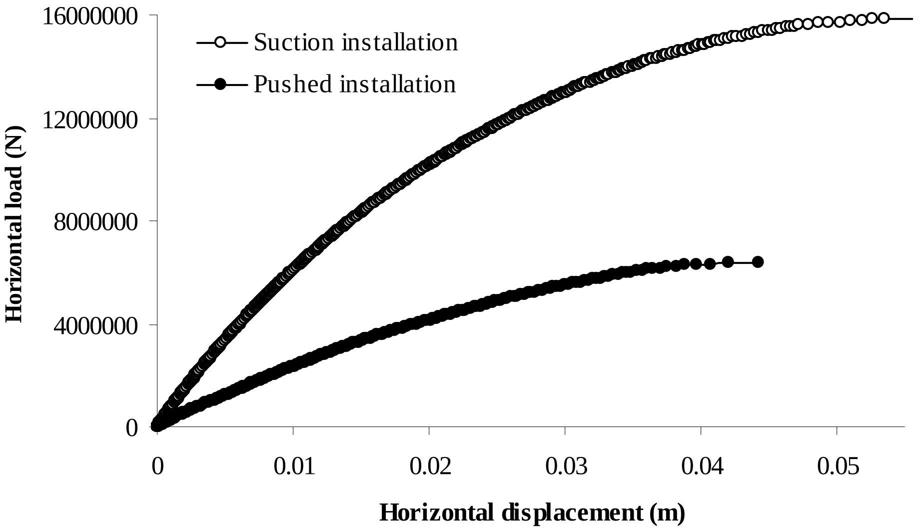

Figure 6.23 Effect of the installation method to the horizontal response of the monopod caisson in sand (t_0 = 0.05)

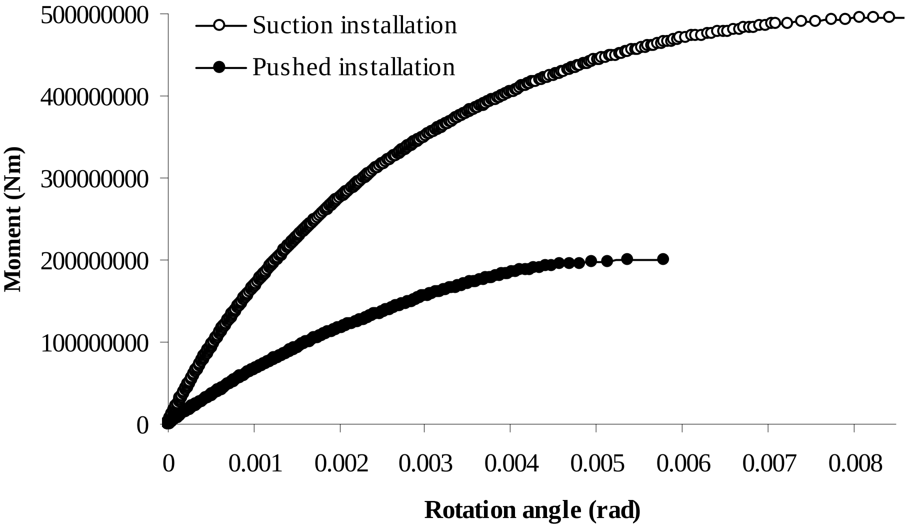

Figure 6.24 Effect of the installation method to the rotational response of the monopod caisson in sand (t_0 = 0.05)

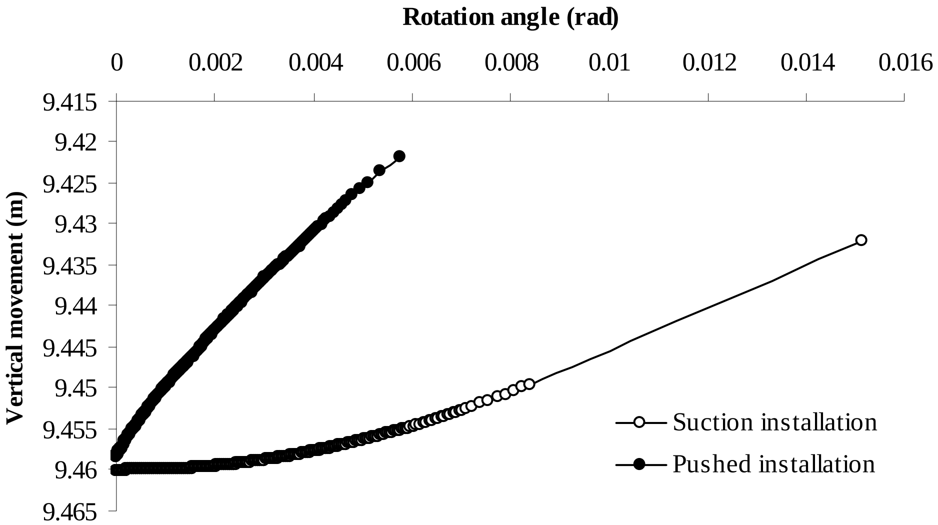

Figure 6.25 Effect of the installation method to the vertical movement of the monopod caisson in sand ($t_0 = 0.05$)

The above discussion about the effect of installation method on the foundation response as far as the theory is concerned. This feature needs further experimental work. A more rational way of distributing the yield surfaces at the end of suction installation may be required.

6.5 Effect of the tensile capacity factor on the caisson response

This section presents the influence of the tensile capacity factor t_0 on the model response. Two main effects of t_0 are illustrated:

(i) Effect on the model response after installation; and

(ii) Effect on the difference between the model response using suction installation and that using pushing installation.

(i) *Effect on the model response after installation*

By using the model parameters, the geometry and the load case of the monopod caisson presented in section 6.2, another numerical example is implemented with a different value of tensile capacity factor t_0: $t_0 = 0.1$.

Figures 6.26 and 6.27 show the comparison between the two results in horizontal and moment responses. It is clear that with the larger t_0, the model response become stiffer and the failure load values also become much higher. As shown in Figure 6.28, with a small t_0 the yield surfaces, especially at the small value of vertical load, are smaller than in the case of the large t_0. This means that in the next loading stage using the same decreasing vertical load, the load point in the case of small t_0 will touch the yield surfaces sooner. Therefore the elasto-plastic response of the model becomes softer.

The effect of t_0 on the solution essentially occurs in the negative and small positive part on the *V*-axis. If the next loading stage (after the installation) is implemented with increasing vertical load, the effect of t_0 on the solution can be reduced. This is because the sizes of the parts of the yield surfaces in the large value range of *V*-axis are not too sensitive to the change of t_0.

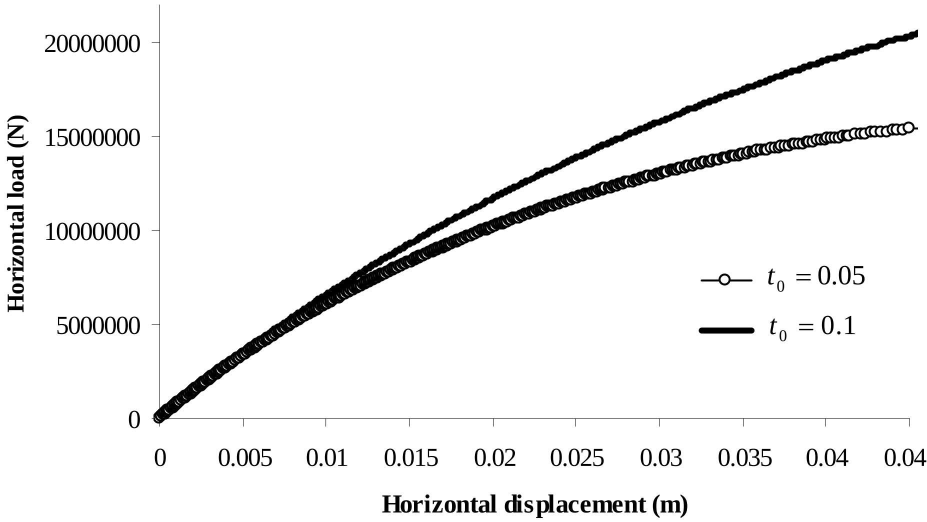

Figure 6.26 Effect of the tensile capacity factor t_0 to the horizontal response of the monopod caisson in sand

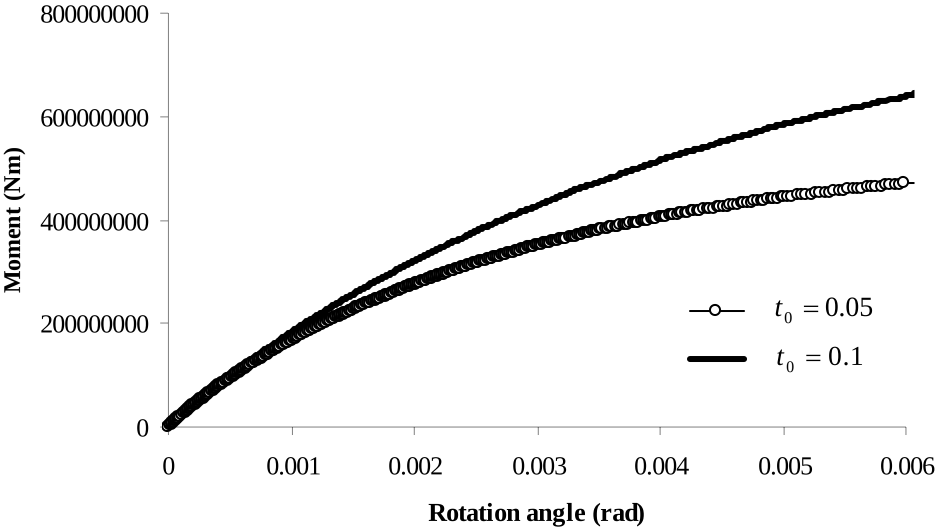

Figure 6. 27 Effect of the tensile capacity factor t_0 to the rotational response of the monopod caisson in sand

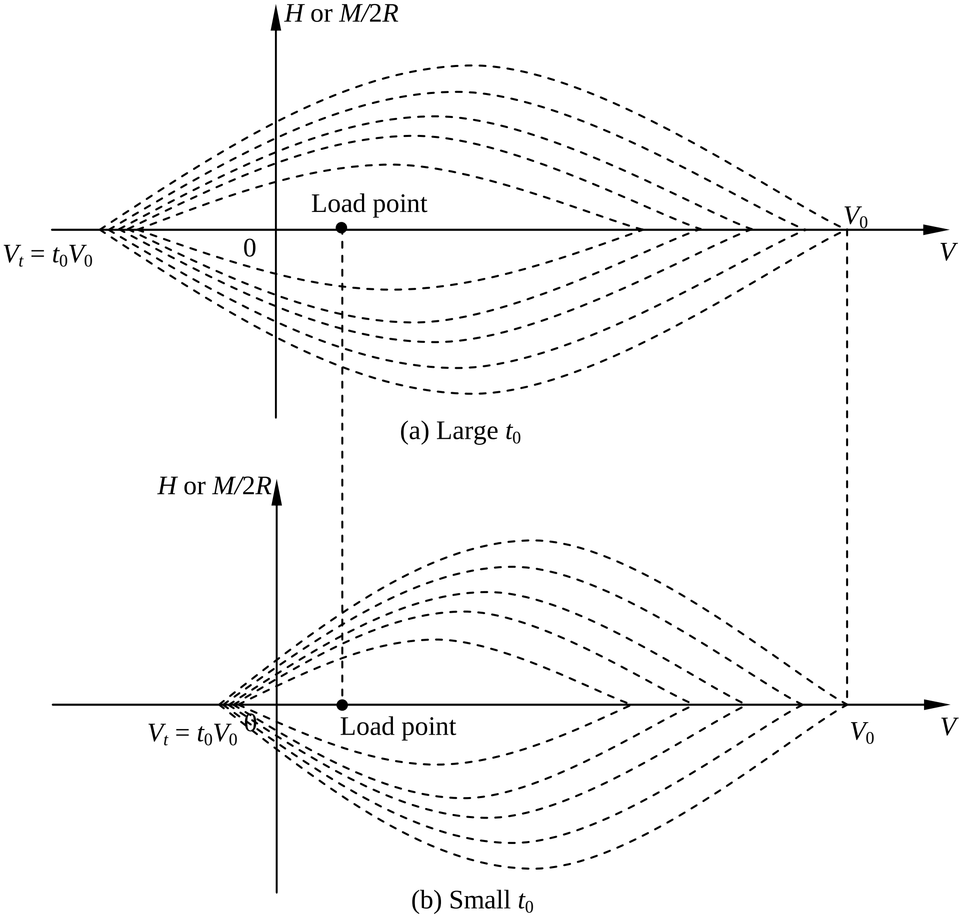

Figure 6.28 System of five yield surfaces in a full plastic vertical loading

(ii) *Effect on the difference between the model response using suction installation and that using pushing installation*

In this section, another example using the data of the monopod caisson in section 6.2 is analysed but with a larger value of t_0 ($t_0 = 0.1$). The two installation methods, suction and pushing, are used for comparison. Figures 6.29 and 6.30 show the comparison between the model response after the suction installation and that after the pushing installation.

Comparing the results in section 6.4 (Figures 6.23 and 6.24), the difference between the response of the caisson installed by suction and that by pushing on the solution is decreased when the value of the tensile capacity t_0 is increased. In fact, when t_0 increases, the yield surfaces become larger and the unloading process causes fewer yield surfaces to be activated. This means that the response of the model in the next loading stage will get closer to the elastic behaviour, which is the response in the case using suction installation.

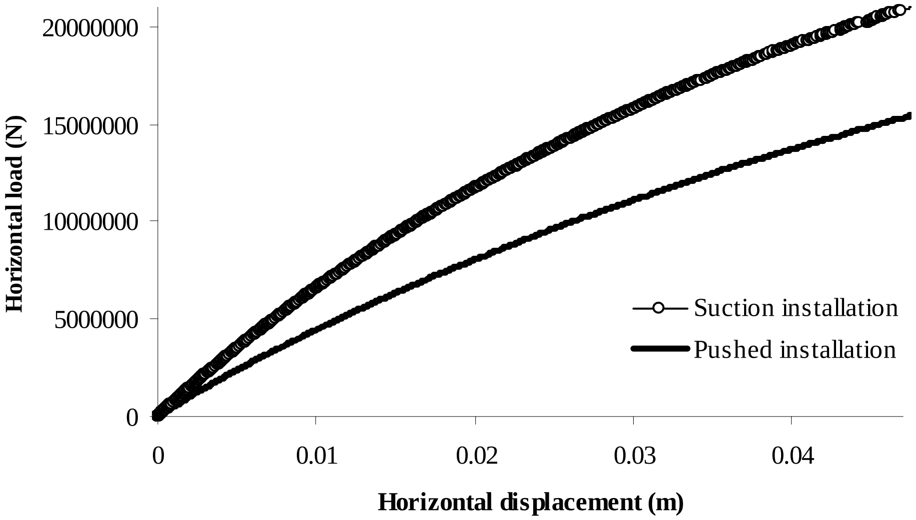

Figure 6.29 Effect of the installation method to the horizontal response of the monopod caisson in sand (t_0 = 0.1)

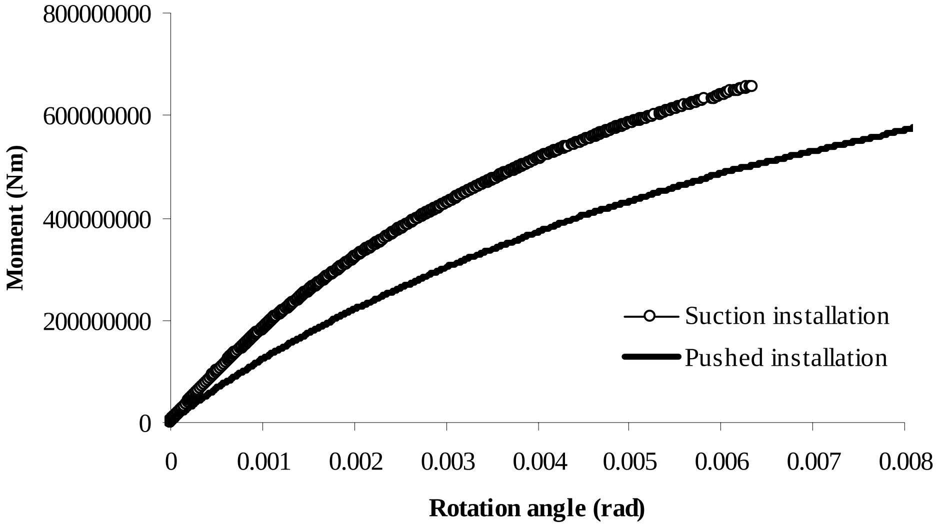

Figure 6.30 Effect of the installation method to the rotational response of the monopod caisson in sand (t_0 = 0.1)

6.6 Effect of the heave on the caisson response

In the numerical applications presented in sections 6.2 and 6.3, in order to compare with the FE results (which have not considered the effect of the heave inside the caisson) the ISIS solution takes into account a very small heave, represented by a very small bell width. However, the heave inside the caisson always exists and it may give serious problems for the design of caisson foundations in both the installation and the serviceability condition.

In section 3.5.1, the calculation procedure for the vertical bearing capacity V_0 taking into account the heave through a bell function with a certain bell width has been presented. In this current section, the effect of the heave represented by the bell width on the real foundation behaviour is illustrated numerically by an example.

A monopod caisson is used with the loads and the model parameters presented in section 6.2 (see Table 6.2) but with different t_0 and bell width values. In this section the tensile capacity t_0 is 0.1.

From the experimental observations by Villalobos *et al.* (2003a) for model test scale in loose sand as well as the results from the centrifugal tests of Manh Tran (University of Western Australia, 2004 – personal correspondence) in dense sand, the heave inside the caisson is approximately 8% to 10% the length of the caisson. Therefore, in this example, the penetration depth expected is approximately 8.7m. The bell width is chosen as 0.7m to give a vertical bearing capacity curve which looks similar to the test observations. Figure 6.31 shows the variations of V_0 corresponding to the two different values of the bell width.

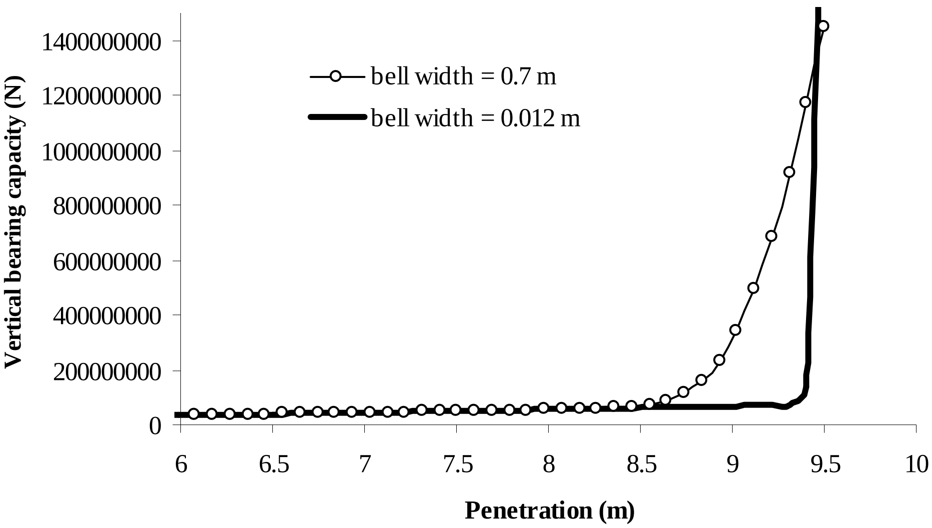

Figure 6.31 Variation of V_0 corresponding to different bell width

As mentioned above, the installation of the caisson in the case using the large bell width (0.7m) is stopped at the depth 8.7m (91.5% the full depth). At this depth, the caisson is predicted that it cannot penetrate further because of the heave. In the case using small bell width (0.012m), the caisson is installed to the full depth. Comparison between these two cases is presented to show how much the heave affects the caisson behaviour.

In the case when the heave is not taken into account (small value of bell width), the caisson can be installed to the full penetration depth corresponding to a very high value of V_0. Taking into account the heave, the installation must be stopped at a smaller depth (partial penetration) and the value of V_0 is much lower than in the previous case. This leads to a softer behaviour of the caisson when subjected to the load case of the serviceability condition. Figures 6.32 and 6.33 show the illustration for this feature in horizontal and rotational responses.

It can be found that when the heave is taken into account, the failure loads of the foundation become much smaller than the results of the analysis without the heave. Thus, in the design of a caisson foundation, it is necessary to pay attention to this matter to avoid the overestimation of the foundation capacity.

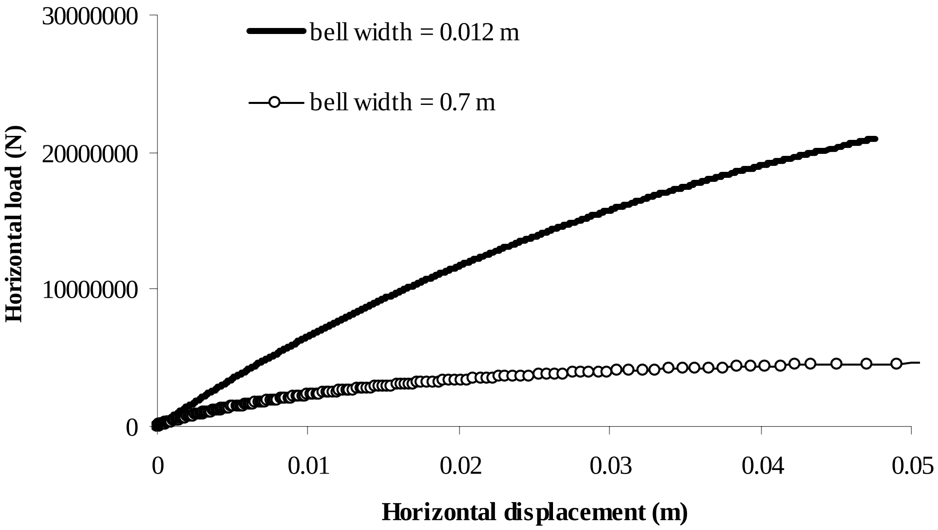

Figure 6.32 Horizontal response of the monopod caisson after installation with different bell width

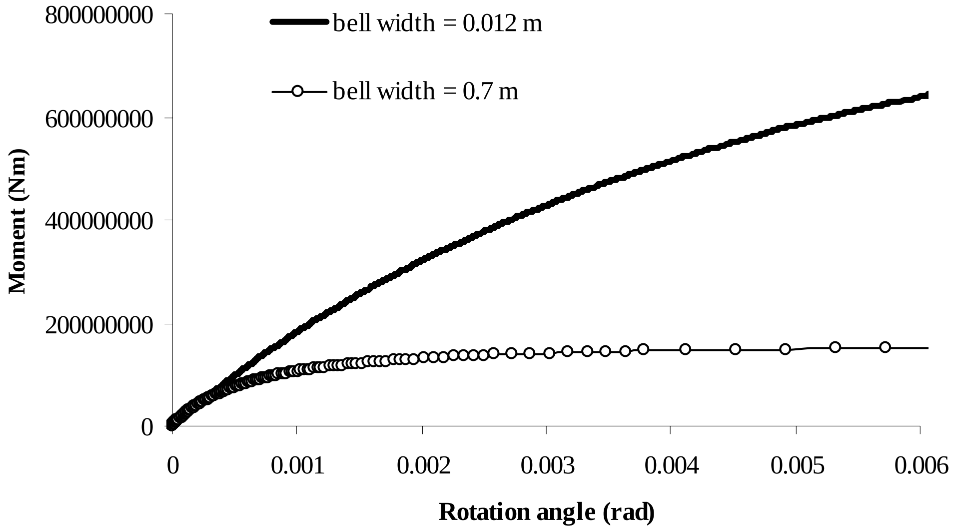

Figure 6.33 Rotational response of the monopod caisson after installation with different bell width

6.7 Confirmation for cyclic behaviour

In order to check the whether the model still has the ability to capture the cyclic behaviour in real load cases with real caisson footings, two examples are presented in this section: (i) a monopod caisson under cyclic loading and (ii) a quadruped caisson under vertical tension-compression loading.

(i) *Monopod caisson under cyclic loading*

A numerical example is implemented to analyse the monopod caisson presented in section 6.2. A cyclic loading based on the environmental loading given in Table 6.3 is applied in this example. Model parameters, suction pressures and loading process are given in Table 6.8.

Table 6.8 Input data – monopod caisson

<table>
<tr><th colspan="9">Model parameters (for ISIS model)</th></tr>
<tr><td colspan="3" rowspan="2">Association factors</td><td>a_{V1}</td><td>a_{V2}</td><td>a_H</td><td>a_M</td><td colspan="2">a_Q</td></tr>
<tr><td>0.297</td><td>1.0</td><td>0.7</td><td>0.7</td><td colspan="2">0.7</td></tr>
<tr><td colspan="3" rowspan="8">Shape factors of yield surface</td><td colspan="2">e_1</td><td colspan="4">-0.2</td></tr>
<tr><td colspan="2">e_2</td><td colspan="4">0.0</td></tr>
<tr><td colspan="2">t_0</td><td colspan="4">0.1</td></tr>
<tr><td colspan="2">m_0</td><td colspan="4">0.15</td></tr>
<tr><td colspan="2">h_0</td><td colspan="4">0.337</td></tr>
<tr><td colspan="2">q_0</td><td colspan="4">0.2</td></tr>
<tr><td colspan="2">β_1</td><td colspan="4">0.99</td></tr>
<tr><td colspan="2">β_2</td><td colspan="4">0.99</td></tr>
<tr><td colspan="3" rowspan="2">Parameters for the rate-dependent solution</td><td colspan="2">Viscosity μ</td><td colspan="4">0.002</td></tr>
<tr><td colspan="2">Time increment *dt*</td><td colspan="4">Changed with the load incerements</td></tr>
<tr><td colspan="3">Number of yield surfaces</td><td colspan="6">20 yield surfaces used</td></tr>
<tr><td colspan="3">Bell width (w_{bell}) (m)</td><td colspan="6">0.7</td></tr>
<tr><th colspan="9">Installation with suction</th></tr>
<tr><td>Load stage</td><td>Suction pressure (kPa)</td><td>V (MN)</td><td>H_2 (MN)</td><td>H_3 (MN)</td><td>Q (MNm)</td><td>M_2 (MNm)</td><td>M_3 (MNm)</td><td>Time increment dt (10^6)</td></tr>
<tr><td>1</td><td>0.0</td><td>0.0 to 0.1</td><td>0.0</td><td>0.0</td><td>0.0</td><td>0.0</td><td>0.0</td><td>10^{-3}</td></tr>
<tr><td>2</td><td>0.0</td><td>0.1 to 1.0</td><td>0.0</td><td>0.0</td><td>0.0</td><td>0.0</td><td>0.0</td><td>1.0</td></tr>
<tr><td>3</td><td>0.0</td><td>1.0 to 8.772</td><td>0.0</td><td>0.0</td><td>0.0</td><td>0.0</td><td>0.0</td><td>10^2</td></tr>
<tr><td>4</td><td>0.0 to 20.0</td><td>8.772</td><td>0.0</td><td>0.0</td><td>0.0</td><td>0.0</td><td>0.0</td><td>10^2</td></tr>
<tr><td>5</td><td>20.0 to 200.0</td><td>8.772</td><td>0.0</td><td>0.0</td><td>0.0</td><td>0.0</td><td>0.0</td><td>10^2</td></tr>
<tr><th colspan="9">Application of 1 cycle of horizontal and moment loadings</th></tr>
<tr><td>6</td><td>0.0</td><td>8.772</td><td>0.0</td><td>0.0 to 3.1960</td><td>0.0</td><td>0.0 to 100.0</td><td>0.0</td><td>5000.0</td></tr>
<tr><td>7</td><td>0.0</td><td>8.772</td><td>0.0</td><td>3.1960 to -3.8352</td><td>0.0</td><td>100.0 to -120.0</td><td>0.0</td><td>9000.0</td></tr>
<tr><td>8</td><td>0.0</td><td>8.772</td><td>0.0</td><td>-3.8352 to 4.1548</td><td>0.0</td><td>-120.0 to 130.0</td><td>0.0</td><td>11000.0</td></tr>
<tr><td>9</td><td>0.0</td><td>8.772</td><td>0.0</td><td>4.1548 to -4.6022</td><td>0.0</td><td>130.0 to -144.0</td><td>0.0</td><td>12500.0</td></tr>
<tr><td>10</td><td>0.0</td><td>8.772</td><td>0.0</td><td>-4.6022 to 5.1136</td><td>0.0</td><td>-144.0 to 160.0</td><td>0.0</td><td>12500.0</td></tr>
</table>

Figures 6.34 and 6.35 show the numerical results of the cyclic loading case compared with those of the monotonic loading case which is the extreme environmental load case given in Table 6.3. It is clear that the monotonic loading curves still play the role of the “backbone” curves in this example. This means that Masing’s rules are still followed.

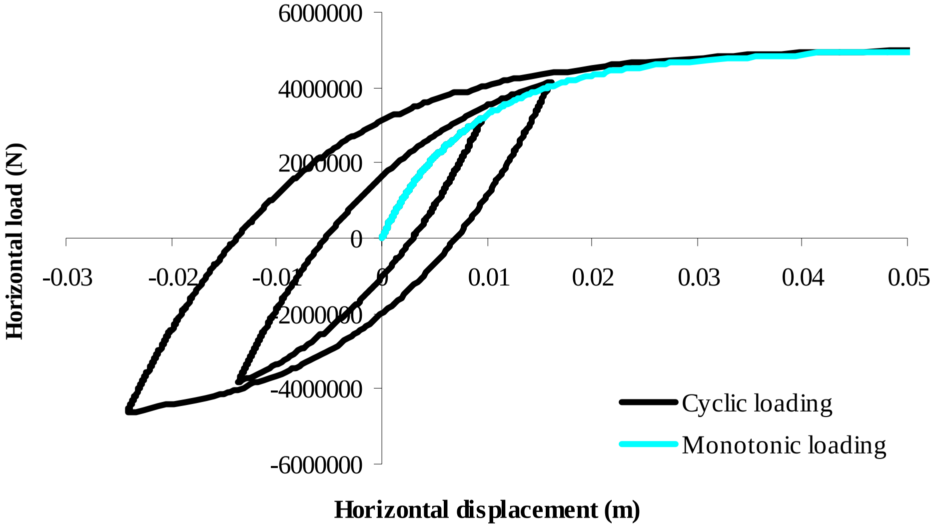

Figure 6.34 Horizontal cyclic and monotonic response of the monopod caisson in sand

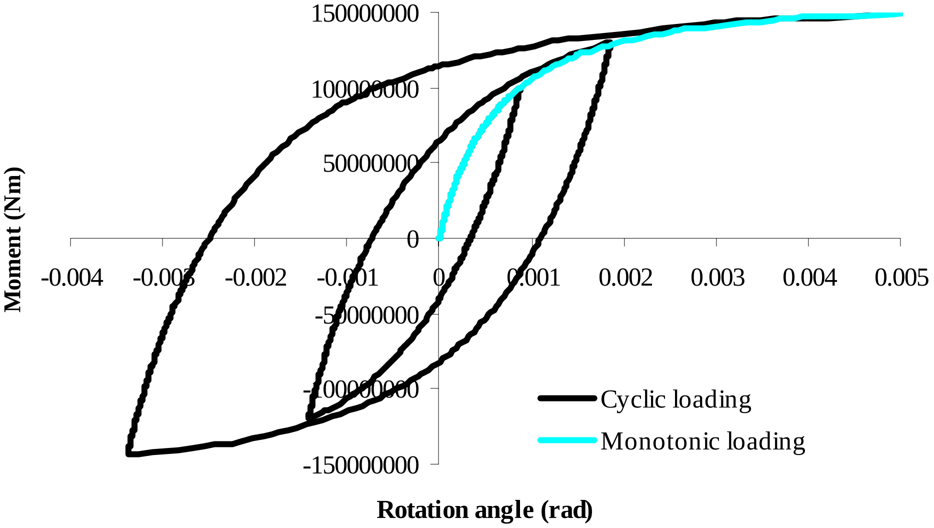

Figure 6.35 Rotational cyclic and monotonic response of the monopod caisson sand

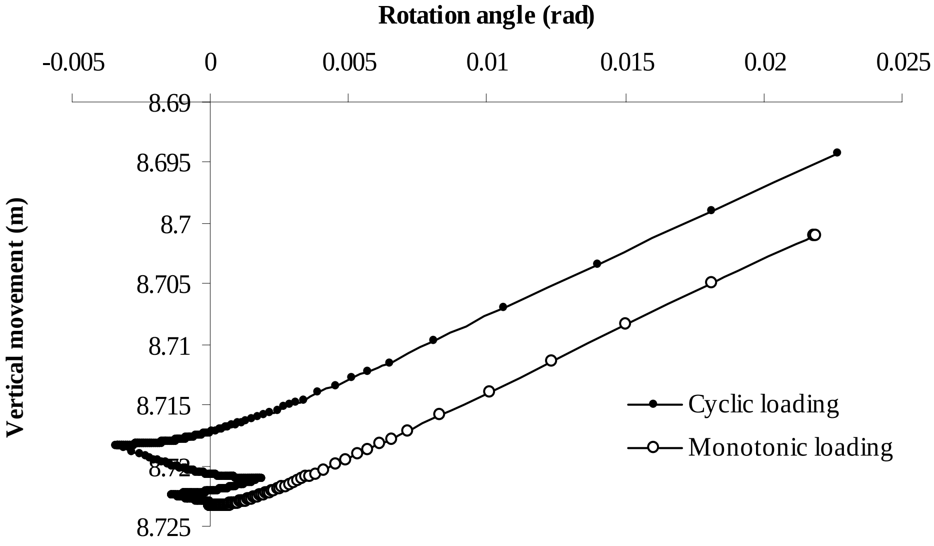

Figure 6.36 Vertical movement during cyclic and monotonic loading of the monopod caisson in sand

In addition, Figure 6.36 shows that under cyclic loadings, the caisson is uplifted faster than in monotonic loading. This is a reasonable observation.

(ii) *Quadruped caisson under tension-compression load*

Table 6.9 Input data – quadruped caisson

<table>
<tr><th colspan="9">Model parameters (for ISIS model)</th></tr>
<tr><td colspan="3" rowspan="2">Association factors</td><td>a_{V1}</td><td>a_{V2}</td><td>a_H</td><td>a_M</td><td colspan="2">a_Q</td></tr>
<tr><td>0.297</td><td>1.0</td><td>0.7</td><td>0.7</td><td colspan="2">0.7</td></tr>
<tr><td colspan="3" rowspan="8">Shape factors of yield surface</td><td colspan="2">e_1</td><td colspan="4">-0.2</td></tr>
<tr><td colspan="2">e_2</td><td colspan="4">0.0</td></tr>
<tr><td colspan="2">t_0</td><td colspan="4">Calculated from friction</td></tr>
<tr><td colspan="2">m_0</td><td colspan="4">0.15</td></tr>
<tr><td colspan="2">h_0</td><td colspan="4">0.337</td></tr>
<tr><td colspan="2">q_0</td><td colspan="4">0.2</td></tr>
<tr><td colspan="2">β_1</td><td colspan="4">0.99</td></tr>
<tr><td colspan="2">β_2</td><td colspan="4">0.99</td></tr>
<tr><td colspan="3" rowspan="2">Parameters for the rate-dependent solution</td><td colspan="2">Viscosity μ</td><td colspan="4">0.002</td></tr>
<tr><td colspan="2">Time increment *dt*</td><td colspan="4">Changed with the load incerements</td></tr>
<tr><td colspan="3">Number of yield surfaces</td><td colspan="6">20 yield surfaces used</td></tr>
<tr><td colspan="3">Bell width (w_{bell}) (m)</td><td colspan="6">0.012</td></tr>
<tr><th colspan="9">Installation with suction</th></tr>
<tr><td>Load stage</td><td>Suction pressure (kPa)</td><td>V (MN)</td><td>H_2 (MN)</td><td>H_3 (MN)</td><td>Q (MNm)</td><td>M_2 (MNm)</td><td>M_3 (MNm)</td><td>Time increment dt (10^6)</td></tr>
<tr><td>1</td><td>0.0</td><td>0.0 to 0.01</td><td>0.0</td><td>0.0</td><td>0.0</td><td>0.0</td><td>0.0</td><td>10^{-3}</td></tr>
<tr><td>2</td><td>0.0</td><td>0.01 to 0.2</td><td>0.0</td><td>0.0</td><td>0.0</td><td>0.0</td><td>0.0</td><td>1.0</td></tr>
<tr><td>3</td><td>0.0</td><td>0.2 to 1.987</td><td>0.0</td><td>0.0</td><td>0.0</td><td>0.0</td><td>0.0</td><td>10^2</td></tr>
<tr><td>4</td><td>0.0 to 96.0</td><td>1.987</td><td>0.0</td><td>0.0</td><td>0.0</td><td>0.0</td><td>0.0</td><td>10^2</td></tr>
<tr><th colspan="9">Application of 1 cycle of tension and copression loads</th></tr>
<tr><td>5</td><td>0.0</td><td>1.987 to -2.98</td><td>0.0</td><td>0.0</td><td>0.0</td><td>0.0</td><td>0.0</td><td>2000.0</td></tr>
<tr><td>6</td><td>0.0</td><td>-2.98 to 11.0</td><td>0.0</td><td>0.0</td><td>0.0</td><td>0.0</td><td>0.0</td><td>8000.0</td></tr>
</table>

In this example, the quadruped caisson presented in section 6.3 is used. The model parameters and loading process are given in Table 6.9. The tensile capacity factor is now calculated directly from the friction on the side of the caisson.

Figure 6.37 shows the results of the analysis. It can be seen that the vertical response of the caisson in the reloading stage (compression) is elastic until the vertical load reaches again the value of the vertical bearing capacity V_0 at the corresponding depth. This feature is different from test observations in Kelly *et al.* (2004). Figure 6.38 shows the outline of these tests.

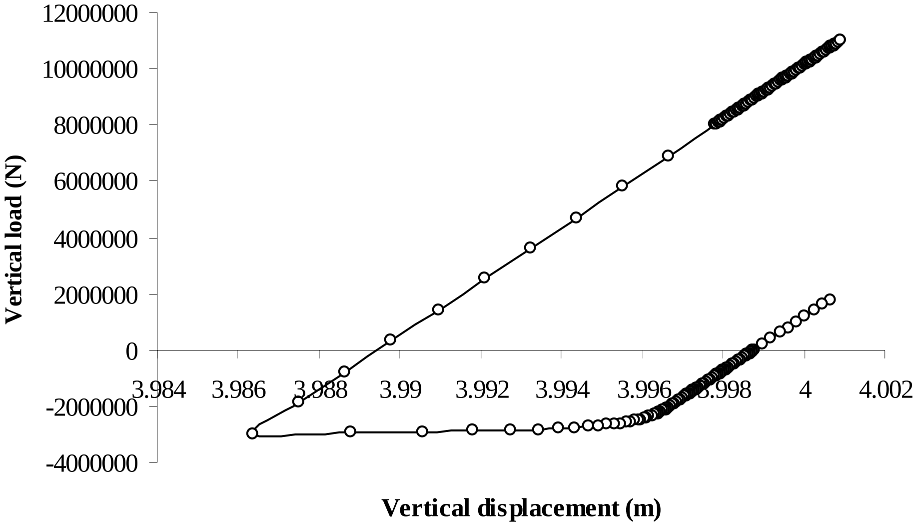

Figure 6.37 Tension – compression behaviour of the quadruped caisson in sand

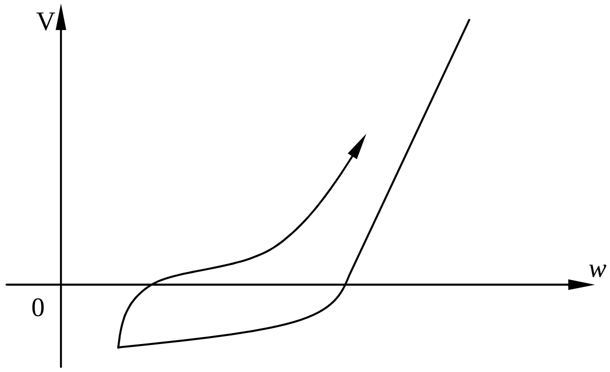

Figure 6.38 Vertical displacement in tension-compression test (after Kelly *et al.*, 2004)

The shape of the test curve shows that there might have some gaps between the caisson base and the soil occurring in the tensile loading. Thus, in the reloading stage, the foundation reveals the elasto-plastic response rather soon, then it tends to be elastic again. In the current version, the ISIS model has not taken into account the matter of the gaps existing between the caisson and the soil during cyclic loadings.

6.8 Concluding remarks

The application of the ISIS model to analyse the real caissons under extreme environmental loads has been presented in this chapter. Although there are significant differences between the ISIS solution and finite element analysis, the ISIS model, in general, gives the more conservative results.

In addition, the effects of the suction installation, tensile capacity factors and the heave inside the caisson on the model response have been addressed. These can be considered to be the reasons for the differences between the ISIS solution and finite element analysis results.

It is clear that choosing appropriate values for the model parameters is very important. By using the results obtained from experiments, suitable preliminary values of the model parameters can be selected. However, for any real caisson, it is also possible to carry out a FE analysis to calibrate important factors for the ISIS model. The ISIS model would then be used in combination with structural analysis, which will be very expensive if using finite element analysis.

CHAPTER 7

CONCLUDING REMARKS

7.1 Introduction

The development of a numerical model simulating the behaviour of shallow foundations of offshore structures under cyclic loading has been presented as the main achievement of this study. The applicability of the model for suction caisson foundations and their special characteristics is the main objective of this research. Several conclusions have been presented in previous chapters. In this final chapter, the important conclusions are summarised. In addition, some ideas for future developments are proposed.

7.2 Main Findings

Based on the thermodynamic framework (Puzrin and Houlsby, 2000), a hyperplasticity model, developed in chapters 3 and 4, has shown promising abilities to describe the cyclic behaviour of shallow foundations. A model which allows calculation of incremental plastic response including a non-associated plastic flow rule without the violation of thermodynamic principles has been achieved. This model is named ISIS.

A framework for the analysis of cyclic response of shallow foundations of offshore structures including a novel kind of footing called a suction caisson has been established within the ISIS model. Many options have been allowed in its development to be able to adjust the model behaviour for different cases of both footings and soils.

In chapter 3, by the use of the macro-element concept, a single-yield-surface hyperplasticity model (the preliminary version of ISIS) for shallow foundations has been developed. This model uses a different set of definitions and assumptions from those of conventional plasticity models. Numerical results have provided evidence of the capability of the model in capturing the results of the previous conventional plasticity models, such as Model B (Martin, 1992) and Model C (Cassidy, 1999).

The most important development of the ISIS model presented in chapter 4 is the introduction of the multiple-yield-surface concept for plastic behaviour. By the use of this concept, there are two aspects of foundation behaviour explained more rigorously. Firstly, the changes of elastic stiffness of the foundation depending on the level of displacements are described in a straightforward manner. Secondly, the hysteretic phenomenon of the foundation response during cyclic loading can be expressed clearly, both in physical and mathematical terms.

Based on a series of experiments on caisson models performed at the University of Oxford by Villalobos *et al.* (2003a, 2003b, 2004a and 2004b) and field tests by Kelly *et al.* (2005c), details of the numerical analysis for suction caisson foundations have been specified and applied in the ISIS model. A FORTRAN program has been written to perform retrospective simulations of the footing tests. In addition, the analyses of circular flat footings and spudcans have been discussed and illustrated.

The rate-dependent solution has been introduced as the way to mimic the rate-independent solution and to avoid numerical difficulties when using the multiple-yield-surface model.

In chapter 5, a number of investigations into the use of the model parameters have been discussed to give some useful hints and guidelines for model applications.

In chapter 6, the model has been used to analyse two real caissons, a monopod and a quadruped caisson, under extreme environmental loads. The numerical results of ISIS had been compared with those of Finite Element analysis (Fugro, 2004). In general, the ISIS model gives rather conservative results. However, the parameters of the ISIS model can be adjusted to give a less conservative solution, hence getting closer to the Finite Element results.

7.3 Suggestions for future research

In this dissertation, by using the macro-element concept, the analyses can be implemented in a much simpler fashion than the analyses using Finite Element procedures. However, this simplification leads to the need to use the results of many other investigations as tools or parameters for the model. The model, by itself, cannot cover all aspects of the foundation behaviour. The more the tools supplied for the model, the more reliable the results obtained in the solution. In particular, in the current version of the ISIS model, some features which have not been taken into account or have not given the correct answers are described as motivations for future research and presented in the following sections.

Firstly, the heave of the soil inside the caisson under suction-assisted penetration needs to be investigated in more detail. This phenomenon depends on the relative density of the soil, the thickness of the caisson skirt and the suction pressures applied during the installation process.

In the current research, the heave is partly taken into account by the use of the bell function presented in section 3.5.1 and the magnitude of the bell width is chosen empirically. It could be necessary to implement this in more detail.

Secondly, in the case of tension-compression loadings as shown in section 4.5.1, the current ISIS model has not been able to simulate this feature. The gap between the base of the footing and the soil which happens during this loading process has not been simulated in the model.

The third issue which could need some more information is that of the shape of the outer most yield surface depending on the ratio between the length and the diameter of the caisson. In this study, the information of the shapes of yield functions is mainly based on experiments with the ratio of *L*/*D* as 0.5 and 1.0. Obviously, this is not enough for a general analysis for all kinds of caisson foundations.

The model parameters such as the shape parameters of the yield function (m_0, h_0, t_0), the association factors ($a_{V1}, a_{V2}, a_M, a_H, a_Q$), the initial parameter of the distribution of yield surfaces ($\eta_0^{initial}$) and the hardening rule parameters (A_i, b_i, n_i) still need more experiments to find appropriate values for a variety of caisson types (with different *L*/*D*) as well as for different kinds of soil.

7.4 Conclusion

This dissertation has presented the modelling of the shallow foundations of offshore structures; especially the caisson foundation is a promising footing type for offshore wind turbines. By the introduction of the multiple-yield-surface concept, the ISIS model is capable of giving realistic predictions for the foundation behaviour.

REFERENCES

Atkinson, J. (1993). An introduction to the mechanics of soils and foundations. *McGraw-Hill*, London.

Bell, R. W. (1991). The analysis of offshore foundations subjected to combined loading. *MSc. thesis*, University of Oxford.

Brinch Hansen, J. (1961). A general formula for bearing capacity. Bull. No. 11, *Danish Geotechnical Institute*, Copenhagen, pp. 38-46.

Brinch Hansen, J. (1970). A revised and extended formula for bearing capacity. Bull. No. 98, *Danish Geotechnical Institute*, Copenhagen, pp. 5-11.

Butterfield, R. and Banerjee, P. K. (1971). A rigid disk embedded in an elastic half space. *Geotechnical Engineering.* , Vol. 2, pp. 35-52.

Butterfield, R. and Ticof, J., (1979). Design parameters for granular soils (discuss contribution). *Proc. 7 th European Conf. Soil Mech. Fndn. Engng.*, Brighton, Vol. 4, pp. 259-261.

Bycrof, R. N. (1956). Forced vibrations of a rigid circular plate on a semi-infinite elastic space and on an elastic spatrum. *Phil. Trans. Roy. Soc. A.* 248, pp.327-368.

Byrne, B. W. (2000). Investigation of suction caissons in dense sand. *D.phil Thesis*, University of Oxford.

Byrne, B. W., Houlsby, G. T., Martin, C. M. and Fish, P. (2002). Suction caisson foundations for offshore wind turbines. *Wind Engineering*, Vol. 26, No. 3, pp. 145-155.

Byrne, B. W. and Houlsby, G. T. (2004). Experimental Investigations of the Response of Suction Caissons to Transient Combined Loading. *Proc. ASCE, Journal of Geotechnical and Geoenvironmental Engineering*, Vol. 130, No. 3, pp 240-253

Byrne, B. W. and Houlsby, G. T. (2004a). Design Procedures for Installation of Suction Caissons in Clay and Other Materials. *Proc ICE - Geotechnical Engineering,* in press.

Byrne, B. W. and Houlsby, G. T. (2004b). Design Procedures for Installation of Suction Caissons in Sand. *Proc ICE - Geotechnical Engineering,* in press.

Cassidy, M. J., 1999. Non-linear analysis of Jack-Up structures subjected to random waves. *D. Phil. thesis*, University of Oxford.

Collins, I. F. and Houlsby, G. T., 1997. Application of Thermomechanical Principles to the Modelling of Geotechnical Materials. *Proc. Royal Society of London*, Series A, Vol. 453, pp. 1975-2001.

Dean, E. T. R., James, R. G., Schofield, A. S., Tan, F. S. C. & Tsukamoto, Y. (1992). The bearing capacity of conical footings on sand in the relation to the behaviour of spudcan footings of jack-ups. *Proc. Wroth Memorial Symp. “Predictive Soil Mechanics”*, Oxford, pp. 230-253.

Doherty, J. P., Houlsby, G. T. and Deeks, A. J. (2004). Stiffness of Flexible Caisson Foundations Embedded in Non-Homogeneous Elastic Soil. Submitted to *Proc. ASCE, Jour. Structural Engineering Division.*

Endley, S. N., Rapoport, V., Thompson, P. J. and Baglioni, V. P. (1988). Prediction of jack-up rig footing penetration. *Proc. 13th Offshore Technology Conf.*, Houston, OTC4133.

Fugro (2004). Analysis of suction caissons using alternative numerical methods. *Report to DTI*, Document No. 0216-G-RP-S-11051.

Fugro (2004). Numerical simulations of caisson foundations. *Report to DTI*, Document No. 0216-G-RP-S-11071.

Gazetas, G., Tassoulas, J. L., Dobry, R. and O’Rourke, M. J. (1985). Elastic settlement of arbitrarily shaped foundations embedded in half space. *Géotechnique*, Vol. 35, No. 3, pp. 339-416.

Gerrard, C. M. and Harrison, W. J. (1970). Circular load applied to a cross-anisotropic half space. *Technical Report* 8, C.S.I.R.O Aus. Div. App. Geomech.

Gottardi, G. and Houlsby, G. T. (1995). Model tests of circular footings on sand subjected to combined loads. *Report No. 2071/95*, Department of Engineering Science, University of Oxford.

Gottardi, G., Houlsby, G. T. and Butterfield, R. (1999). Plastic response of circular footings on sand under general planar loading. *Géotechnique*, Vol. 49, No 4, pp. 453-469.

Hansen, B. and Christensen, N. H. (1969). Discussion on theoretical bearing capacity of very shallow footings. *Proceedings ASCE, Journal of the Soil Mech. and Found. Division*, Vol. 95, No. SM-6, pp. 1568-1572.

Houlsby, G. T. (2003). Modelling of Shallow Foundations for Offshore Structures. Invited Theme Lecture, *Proc. International Conference on Foundations*, Dundee, 2-5 September, Thomas Telford, ISBN 0 7277 3244 7, pp. 11-26.

Houlsby, G. T. and Byrne, W. B. (2000). Suction caisson foundations for offshore wind turbines and anemometer masts. *Wind Engineering*, Vol. 24, No. 4, pp. 249-255.

Houlsby, G. T and Cassidy, M. J. (2002). A plasticity model for the behaviour of footings on sand under combined loading. *Géotechnique*, Vol. 52, No 2, pp. 117-129.

Houlsby, G. T. and Puzrin, A. M. (2000). A Thermomechanical Framework for Constitutive Models for Rate-Independent Dissipative Materials. *International Journal of Plasticity*, Vol. 16, No. 9, pp. 1017-1047.

Houlsby, G. T. and Puzrin, A. M. (2002). Rate-Dependent Plasticity Models Derived from Potential Functions. *Journal of Rheology*, Vol. 46, No. 1, January/February, pp. 113-126.

Houlsby, G. T., Kelly, R. B., Huxtable, J. and Byrne, B. W. (2005a). Field Trials of Suction Caissons in Clay for Offshore Wind Turbine Foundations. *Géotechnique*, in press.

Houlsby, G. T., Kelly, R. B., Huxtable, J. and Byrne, B. W. (2005b). Field Trials of Suction Caissons in sand for Offshore Wind Turbine Foundations. Submitted to *Géotechnique*.

Kelly, R. B., Byrne, B. W., Houlsby, G. T. and Martin, C. M. (2003). Pressure chamber testing of model caisson foundations in sand. *Proc. BGA International Conference on Foundations*, pp 421-432

Kelly, R. B., Byrne, B. W., Houlsby, G. T. and Martin, C. M. (2004). Tensile Loading of Model Caisson Foundations for Structures on sand. *Proc. 12th Int. Conf. On Offshore and Polar Engineering*, Toulon, Vol.2, pp 638-641

Kelly, R. B., Houlsby, G. T. and Byrne, B. W., (2005). A Comparison of Field and Laboratory Tests of Caisson Foundations in Sand and Clay. Submitted to *Géotechnique*.

Lemaitre, J. and Chaboche, J. L. (1990). Mechanics of solid materials. *Cambridge University Press*, Cambridge.

Luan, N.T. (1996). The analysis of offshore foundations subjected to combined loading. *D. Phil. thesis*, University of Oxford.

Masing, G. (1926). Eiganspannungen und Verfestigung beim Messing. *Proc., 2nd Int. Congress of Appl. Mech.*, pp. 332-335.

Martin, C. M. (1994). Physical and numerical modelling of offshore foundations under combined loads. *D. Phil. thesis*, University of Oxford.

Martin, C. M. and Houlsby, G. T. (2001). Combined loading of spudcan foundations on clay: numerical modelling. *Géotechnique*, Vol. 51, No. 8, pp. 687-699.

Maugin, G. A. (1992). The Thermodynamics of Plasticity and Fracture. *Cambridge University Press*, Cambridge.

Meyerhof, G. G. (1951). The ultimate bearing capacity of foundations. *Géotechnique*, Vol. 2, No. 4, pp. 267-334.

Meyerhof, G. G. (1953). The bearing capacity of foundations under eccentric and inclined loads. *Proc. 3 rd Int. Conf. Soil Mech. Fndn. Engng.*, Zurich, Vol. 1, pp. 440-445.

Meyerhof, G. G. (1961). The ultimate bearing capacity of wedge-shaped foundations. *Proc. 5 th Int. Conf. Soil Mech. Fndn. Engng.*, Paris, Vol. 2, pp. 446-449.

Muir Wood, D. (1991). Soil behaviours and critical state soil mechanics. *Cambridge University Press*, Cambridge.

Noble Denton and Associates. (1987). Foundation fixity of jack-up units: a join industry study. *Noble Denton and Associates*, London.

Nova, R. and Montrasio, L. (1991). Settlements of shallow foundations on sand. *Géotechnique*, Vol. 41, No. 2, pp. 243-256.

Poulos, H.G. (1988). Marine Geotechnics. *Unwin Hyman*, London.

Poulos, H. G. and Davies, E. H. (1974). Elastic solution for soil and rock mechanics. *John Wiley & Son*, New York.

Puzrin, A. M. and Houlsby, G. T. (2001a). Thermomechanical Framework for Rate-Independent Dissipative Materials with Internal Functions. *International Journal of Plasticity*, Vol. 17, pp. 1147-1165.

Puzrin, A. M. and Houlsby, G. T. (2001b). Fundamentals of Kinematic Hardening Hyperplasticity. *International Journal of Solids and Structures*, Vol. 38, No. 21, May, pp. 3771-3794.

Puzrin, A. M. and Houlsby, G. T. (2003). Rate Dependent Hyperplasticity with Internal Functions. *Proceedings of the American Society of Civil Engineers, Journal of the Engineering Mechanics Division*, Vol. 129, No. 3, March, pp 252-263.

Pyke, R. (1979). Nonlinear soil models for irregular cyclic loadings. *J. Geotech. Eng. Div., Am. Soc. Viv. Eng.*, Vol. 105, No. 6, pp. 715-726.

Roscoe, K. H. and Schofield, A. N. (1956). The stability of short pier foundations in sand. *British Welding Journal*, August, pp. 343-354.

SNAME (1994). Guidelines for site specific assessment of mobile jack-up units. *Society of Naval Architects and Marine Engineers*, Technical and Research Bulletin 5-5A, New Jersey.

Tan, F.S.C. (1990). Centrifuge and theoretical modelling of conical footings on sand. *Ph.D. Thesis*, University of Cambridge.

Vesic, A. S., 1975. Foundation Engineering Handbook. *Van Nostrand*, New York.

Villalobos, F., Byrne, B. W., Houlsby, G. T. and Martin, C. M. (2003a). Bearing capacity tests of scale suction caisson footings on sand: Experimental data. *Report Number FOT005/1*, Department of Engineering Science, University of Oxford

Villalobos, F., Byrne, B. W., Houlsby, G. T. and Martin, C. M. (2003b). Moment loading tests of scale suction caisson footings on sand: Experimental data. *Report Number FOT015/1*, Department of Engineering Science, University of Oxford

Villalobos, F., Byrne, B. W., Houlsby, G. T. and Martin, C. M. (2004a). Cyclic moment loading tests of suction caisson footings on sand: Experimental data. *Report Number FOT020/1*, Department of Engineering Science, University of Oxford.

Villalobos, F., Byrne, B. W., Houlsby, G. T. and Martin, C. M. (2004b). Moment loading tests of suction installed and pushed installed caissons in sand: Experimental data. *Report Number FOT021/1*, Department of Engineering Science, University of Oxford.

Villalobos, F., Houlsby, G. T. and Byrne, B. W. (2004c). Suction Caisson Foundations for Offshore Wind Turbines. *Proc. 5th Chilean Conference of Geotechnics* (Congreso Chileno de Geotecnia), Santiago, November, pp. 24-26.

Villalobos, F. (2004d). An experimental study of cyclically loaded monopod suction caisson foundations for offshore wind turbines. *Proc. Eight YGES*, BGA, Birmingham.

Villalobos, F. A., Byrne, B. W and Houlsby, G. T. (2005). Moment loading of caissons installed into saturated sand. *Proceeding of International Symposium on Frontiers in Offshore Geotechnics*, Perth, September, pp. 411-416.

Wroth, C. P. and Houlsby, G. T. (1985). Soil Mechanics – Property Characterization and Analysis Procedures. *Invited Paper, Proceedings of the 11th International Conference on Soil Mechanics and Foundation Engineering*, San Francisco, August 12-16, Vol. 1, ISBN 90-6191-561-9, pp 1-55.

Ziegler, H. (1977). An introduction to Thermomechanics, 2nd edition: 1983. *North Holland*, Amsterdam.